Structural and Electronic Investigations of In_2O_3 Nanostructures and Thin Films Grown by Molecular Beam Epitaxy

A thesis submitted to University of Oxford for
Doctor of Philosophy

(Kelvin) Hongliang Zhang

Inorganic Chemistry Laboratory
Department of Chemistry
University of Oxford

Abstract

Structural and Electronic Investigations of In_2O_3 Nanostructures and Thin Films Grown by Molecular Beam Epitaxy

Transparent conducting oxides (TCOs) combine optical transparency in the visible region with a high electrical conductivity. In_2O_3 doped with Sn (widely, but somewhat misleadingly, known as indium tin oxide or ITO) is at present the most important TCO, with applications in liquid crystal displays, touch screen displays, organic photovoltaics and other optoelectronic devices. Surprisingly, many of its fundamental properties have been the subject of controversy or have until recently remained unknown, including even the nature and magnitude of the bandgap. The technological importance of the material and the renewed interest in its basic physics prompted the research described in this thesis. This thesis aims (i) to establish conditions for the growth of high-quality In_2O_3 nanostructures and thin films by oxygen plasma assisted molecular beam epitaxy and (ii) to conduct comprehensive investigations on both the surface physics of this material and its structural and electronic properties.

It was demonstrated that highly ordered In_2O_3 nanoislands, nanorods and thin films can be grown epitaxially on (100), (110) and (111) oriented Y-stabilized ZrO_2 substrates respectively. The mismatch with this substrate is -1.7%, with the epilayer under tensile strain. On the basis of *ab initio* density functional theory calculations, it was concluded that the striking influence of substrate orientation on the distinctive growth modes was linked to the fact that the surface energy for the (111) surface is much lower than for either polar (100) or non-polar (110) surfaces. The growth of $In_2O_3(111)$ thin films was further explored on Y-$ZrO_2(111)$ substrates by optimizing the growth temperature and film thickness. Very thin In_2O_3 epilayers (35 nm) grew pseudomorphically under high tensile strain, caused by the 1.7% lattice mismatch with the substrate. The strain was gradually relaxed with increasing film thickness. High-quality films with a low carrier concentration (5.0×10^{17} cm^{-3}) and high mobility (73 $cm^2V^{-1}s^{-1}$) were obtained in the thickest films (420 nm) after strain relaxation. The bandgap of the thinnest In_2O_3 films

was around 0.1 eV smaller than that of the bulk material, due to reduction of bonding-antibonding interactions associated with lattice expansion.

The high-quality surfaces of the (111) films allowed us to investigate various aspects of the surface structural and electronic properties. The atomic structure of In_2O_3 (111) surface was determined using a combination of scanning tunnelling microscopy, analysis of intensity/voltage curves in low energy electron diffraction and first-principles *ab initio* calculations. The (111) termination has an essentially bulk terminated (1×1) surface structure, with minor relaxations normal to the surface. Good agreement was found between the experimental surface structure and that derived from *ab initio* density functional theory calculations. This work emphasises the benefits of a multi-technique approach to determination of surface structure.

The electronic properties of In_2O_3(111) surfaces were probed by synchrotron-based photoemission spectroscopy using photons with energies ranging from the ultraviolet (6 eV) to the hard X-ray regime (6000 eV) to excite the spectra. It has been shown that In_2O_3 is a highly covalent material, with significant hybridization between O and In orbitals in both the valence and the conduction bands. A pronounced electron accumulation layer presents itself at the surfaces of undoped In_2O_3 films with very low carrier concentrations, which results from the fact the charge neutrality level of In_2O_3 lies well above the conduction band minimum. The pronounced electron accumulation associated with a downward band bending in the near surface region creates a confining potential well, which causes the electrons in the conduction band become quantized into two subband states, as observed by angle resolved photoemission spectra (ARPES) Fermi surface mapping. The accumulation of high density of electrons near to the surface region was found to shrink the surface band gap through many body interactions.

Finally epitaxial growth of In_2O_3 thin films on α-Al_2O_3(0001) substrates was investigated. Both the stable body centred cubic phase and the metastable hexagonal corundum In_2O_3

phase can be stabilized as epitaxial thin films, despite large mismatches with the substrate. The growth mode involves matching small but different integral multiples of lattice planes of the In_2O_3 and the substrate in a domain matching epitaxial growth mode.

ACKNOWLEDGEMENTS

I would like to take this opportunity to express my deepest gratitude for all the help, support, discussions and encouragement I have received while staying in Oxford.

First and foremost, I would like to express my deepest gratitude to my supervisor Professor Russell George Egdell for his constant support and guidance over the past three years. I appreciate valuable discussions and helpful suggestions in "everyday" meetings with him, from which I learned quite a lot about how to do research. I appreciate his in-depth reviews of my every manuscript and also of this thesis word by word despite his busy schedule. I appreciate his introducing me to people in my research community and his strong letters of recommendation in development of my future professional career. I appreciate his enormous amounts of care and encouragement in my personal life. Thanks, Russ! My time at Oxford has been a successful and very happy one.

I am also grateful to Dr. David Payne and Dr. Robert Palgrave for their support and many useful discussions. Being experienced in spectroscopy and molecular beam epitaxy, they gave me a lot of suggestions and assistance in my research projects. I must also acknowledge my colleague and best friend Dr. Freddy Oropeza for his support and discussions. We are the best partners in research and the best buddies in life. I must also thank my lab mates: Henry, for help with experiments and discussions; Dongmyung, my MBE partner; Anna for a very good trip to the ESRF in France; Wanzhen, impressed by your dances; Debs, sorry I can't follow your English and all the other Part II students in our group. They made my research life enjoyable.

My research involved much collaboration. I must especially take this opportunity to express my great appreciation to them. Thanks to Dr. Aron Walsh and Professor Richard Catlow from UCL for their help in conducting theoretical simulations; thanks to Dr. Vlado Lazarov from York University for the TEM measurements; thanks to Professor Roger Cowley of the Oxford Physics Department for sharing his world-class HR-XRD technique; thanks to Dr. Philip King (St Andrews), Professor Chris McConville and Dr. Tim Veal from Warwick University for their help in surface physics; thanks to Dr. Vin Dhanak from Liverpool for his help in LEED and XPS/UPS; thanks to Dr. Danny Law

and Dr. Graham Beamson for help in XPS at the NCESS facility; thanks to Dr. Francesco Offi, Dr. Stefano Iacobucciv and Professor Giancarlo Panaccione for their help in synchrotron based XPS measurements; thanks to Professor Katariina Pussi from Finland for her LEED I-V calculations; thanks to Assist/Professor Wei Chen and Professor Andrew Wee for STM facilities. I would also like thank all the beamline scientists who helped us to conduct our synchrotron experiment.

I am grateful to my family for all their love, tolerance and encouragement. Their love and supports are the impetus that drives me to stick to my goals. I would also like to thank all of the friends who have shared daily life with me through these years. I have really enjoyed the time with them. Financial support from an Oxford Clarendon Scholarship is gratefully acknowledged.

Finally, this research work involved much collaboration. I must especially *acknowledge* the efforts of collaborators who have contributed to the project. Dr. Aron Walsh and Professor Richard Catlow from UCL conducted the *ab-initio* DFT calculations in Chapter 4, 5 and 6. Dr. Philip King (St Andrews) performed modified Thomas-Fermi approximation (MTFA) calculations for surface band bending in Chapter 7. Dr. Vlado Lazarov from York University conducted TEM imaging in this thesis. Professor Katariina Pussi performed LEED I-V calculations in Chapter 6.

Publications 2009 onward

(References in blue indicate publications from work included in this thesis)

1. **K. H. L. Zhang***, D.J. Payne, R.G. Palgrave, V.K. Lazarov, W. Chen, A.T.S. Wee, C.F. McConville, P.D.C. King, T.D. Veal, G. Panaccione, P. Lacovig, R.G. Egdell
   "Surface structure and electronic properties of $In_2O_3(111)$ single crystal thin films grown on Y- stabilised $ZrO_2(111)$"
   Chemistry of Materials **21**, 4353 (2009)

2. P. D.C. King, T. Veal, F. Fuchs, C.Y. Wang, D.J. Payne, A. Bourlange, **K.H.L. Zhang**, G.R. Bell, V. Cimalla, O. Ambacher, R.G. Egdell, F. Bechstedt, C. F. McConville
   "Band gap, electronic structure, surface electron accumulation of cubic and rhombohedral In_2O_3"
   Physical Review B **79** 205211 (2009)

3. **K. H. L. Zhang**, Wei Chen, Xue Sen Wang, Andrew T. S. Wee
   "Self-assembly of well-aligned Bi nanoribbons on Ag(111)"
   Applied Surface Science **256**, 460 (2009)

4. S.S. Kushvaha , H. Xu, W. Xiao, **K. H. L. Zhang**, A.T.S. Wee, and X.-S. Wang
   "Scanning tunneling microscopy investigation of growth of self-assembled indium and aluminium nanostructures on inert substrates"
   Thin Solid Films **517** 4540 (2009)

5. A. Bourlange, D. J. Payne, R.G. Palgrave, **K. H. L. Zhang**, J. S. Foord, R. G. Egdell, R.M. J. Jacobs, T.D. Veal, P.D.C. King and C.F. McConville
   "The influence of Sn doping on the growth of In_2O_3 on Y-stabilized $ZrO_2(100)$ by oxygen plasma assisted molecular beam epitaxy"
   Journal of Applied Physics **106** 013703 (2009)

6. **K. H. L. Zhang**, H. Li, H.Y. Mao, H. Huang, J. Ma, A. T. S. Wee and W. Chen
   "Control of 2-D Ordering of $F_{16}CuPc$ on Bi/Ag(111): Effect of Interfacial Interactions"

Journal of Physical Chemistry C. **114**, 11234 (2010)

7. I.M. McLeod, V. R. Dhanak, A. Matilainen, M. Lahti and K. Pussi, **K. H. L. Zhang**
   "Structure Determination of the p($\sqrt{3}\times\sqrt{3}$)R30°Bi-Ag(111) Surface Alloy Using LEED I-V and DFT Analysis
   Surface Science **604**, 1395 (2010)

8. **K. H. L. Zhang**, Aron Walsh, C. Richard A. Catlow, V. Lazarov and R.G. Egdell
   "Surface energies control self-organisation of oriented In_2O_3 nanostructures on cubic zirconia"
   Nano Letters **10**, 3740 (2010)

9. R. A. Cowley, A. Bourlange, J. L. Hutchison, **K. H. L. Zhang**, A. M. Korsunsky, and R. G. Egdell
   "*A study of island growth of In_2O_3 on Y-stabilised ZrO_2(001) by high resolution XRD"*
   Physical Review B **82** 165312 (2010)

10. **K. H. L. Zhang**, V. K. Lazarov, T. D. Veal, F. Oropeza, C. McConville, R. G. Egdell, A. Walsh, R. Catlow
    "Thickness dependence of the strain, band gap and transport properties of epitaxial In_2O_3 thin films grown on Y- ZrO_2(111)"
    Journal of Physics Condensed Matter **23**, 334211 (2011)

11. **K. H. L. Zhang***, I.M. McLeod, Y.H. Lu, V. R. Dhanak, A. Matilainen, M. Lahti, K. Pussi, R.G. Egdell, X.-S. Wang, A. T. S. Wee, and W. Chen
    "*Observation of a surface alloying-to-dealloying transition during growth of Bi on Ag(111)"*
    Physical Review B **83**, 235418 (2011)

12. **K. H. L. Zhang***, V.K. Lazarov, T.D. Veal, C.F. McConville, H.H.C. Lai, R.G. Egdell
    "Influence of Temperature on the Epitaxial Growth and Properties of In_2O_3 Thin Films on Y-ZrO_2(111)"
    Journal of Crystal Growth **318**, 345 (2011)

13. I.M. McLeod, V. R. Dhanak, A. Matilainen, M. Lahti and K. Pussi, **K. H. L. Zhang**
"LEED I-V and DFT Structure Determination of the (√3x√3)R30° Pb-Ag(111) Surface Alloy"
J. Phys. Condens. Matter. **318**, 345 (2011)

14. A. Walsh, R. C. Catlow, **K. H. L. Zhang** and R.G. Egdell
"Band gap control of metal oxides through epitaxial strain: the case of In_2O_3"
Physical Review B **83**, 161202(R) (2011)

15. V. K. Lazarov, Z. H. Cai, K.Yoshida, **K. H. L. Zhang**, M. Weinert, K. S. Ziemer, and P. J. Hasnip
"Polar oxide films growth: the case of MgO(111)"
Physical Review Letters **107**, 056101 (2011)

16. K. Pussi, A. Matilainen, V. R. Dhanak, A. Walsh, R.G. Egdell and **K. H. L. Zhang**
"Surface structure of In_2O_3(111) (1×1) determined by DFT calculations and LEED"
Surface Science **606**, 1 (2012)

17. **K. H. L. Zhang**, D. J. Payne and R. G. Egdell
"Cross section and resonance effects in photoemission from Sn doped In_2O_3(111)"
Solid State Communications **152**, 194 (2012)

18. **K. H. L. Zhang**, V.K. Lazarov, F.E. Oropeza, D. J. Payne, H.H.C. Lai, R.G. Egdell
"Domain matching epitaxial growth of In_2O_3 thin films on α-Al_2O_3(0001)"
Crystal Growth and Design (accepted)

19. **K. H. L. Zhang**, A. Regoutz, R.G. Palgrave, D.J. Payne, R.G. Egdell, S. P. Collins, D. Wermeille, A. Walsh, and R.A. Cowley
"Determination of the Poisson ratio of In_2O_3 by synchrotron based X-ray diffraction on strained thin films grown by molecular beam epitaxy"
Physical Review B **84**, 233301 (2011)

22. **K. H. L. Zhang***. I.M. McLeod, A. Matilainen, M. Lahti, K. Pussi, V. R. Dhanak

"Evolution of electronic structure at the Bi/Ag(111) interface studied by photoemission spectroscopy"
Submitted to Surface Science

20. **K. H. L. Zhang**, A. Regoutz, R.G. Egdell, D. Wermeille and R.A. Cowley
"Strain and tilt in In_2O_3 nanorods on Y-stabilised $ZrO_2(110)$ probed by high resolution X-ray diffraction"
(Manuscript in preparation)

21. **K. H. L. Zhang**, A. Bourlange, R.G. Egdell, S. P. Collins, R.J. Bean, I.K. Robinson and R.A. Cowley
"Size dependent shape and tilt transitions in In_2O_3 nanoislands grown on cubic Y-stabilised $ZrO_2(001)$ by molecular beam epitaxy"
(Manuscript in preparation)

Contents

Abstract i

Acknowledgements iv

Publications vi

Contents x

1. Introduction to Indium Oxide 1

1.1. Transparent Conducting Oxides: Background and Challenges 1

1.1.1. Electronic Structure of Metal Oxides 1

1.1.2. Transparent Conducting Oxides 5

1.2. Surface Science of Metal Oxides 12

1.2.1. Basic Concepts of Solid Surfaces 13

1.2.2. Metal Oxide Surfaces 17

1.3. Crystal Structures of In_2O_3 22

1.4. Electronic Structures of In_2O_3 and ITO 23

1.5. Organization of the Thesis 27

1.6. References 30

2. Background to Experimental Techniques 34

2.1. Molecular Beam Epitaxy 34

2.1.1. Concepts of Thin Film Growth 34

2.1.2. Molecular Beam Epitaxy 39

2.2. X-ray Diffraction 40

2.3. Transmission Electron Microscopy 41

2.4. Scanning Probe Microscopy (STM/AFM) 43

2.4.1. Scanning Tunnelling Microscopy (STM) 44

2.4.2. Atomic Force Microscopy (AFM) ... 48

2.5. Low Energy Electron Diffraction (LEED) ... 51

2.6. Photoelectron Spectroscopy (PES) ... 55

2.6.1. Introduction to PES ... 55

2.6.2. Theory of Photoemission Spectroscopy ... 59

2.6.3. Core Level and Satellites ... 61

2.6.4. Valence Band Spectra ... 66

2.6.5. Electron Mean Free Path ... 68

2.6.6. Photoionization Cross-sections ... 70

2.7. References ... 71

3. Experimental Apparatus and Techniques ... 73

3.1. Oxygen Plasma Assisted MBE ... 73

3.2. X-ray Diffraction ... 75

3.3. Transmission Electron Microscopy ... 75

3.4. Scanning Probe Microscopy ... 76

3.4.1. Scanning Tunnelling Microscopy ... 76

3.4.2. Atomic Force Microscopy ... 77

3.5. Low Energy Electron Diffraction ... 78

3.6. Photoelectron Spectroscopy (PES) ... 78

3.6.1. Scienta ESCA-300 spectrometer at Daresbury Laboratory, UK ... 79

3.6.2. Beamline ID16 at ESRF in Grenoble, France ... 81

3.6.3. Beamline I311 at the MAX II synchrotron MAX-lab, Lund, Sweden ... 83

3.6.4. Beamline BaDElPh at Elettra Synchrotron Light Source, Trieste, Italy ... 84

3.7. References 87

4. Surface Energies Control the Self-organisation of Oriented In_2O_3 Nanostructures on Cubic Zirconia 88

4.1. Introduction 88

4.2. Experimental and Theoretical details 90

4.2.1. MBE Growth 90

4.2.2. Structural and Morphological Characterizations 91

4.2.2. Density Functional Theory (DFT) Calculations 91

4.3. Results and Analysis 92

4.3.1. Growth of Oriented In_2O_3 Nanostructures and Thin Films 92

4.3.2. Surface Energies Calculations 98

4.3.3. Nanostructure Morphology Determined by Thermodynamics 101

4.4. Concluding Remarks 108

4.5. References 109

5. Temperature and Thickness Dependence of Strain, Band gap and Transport Properties of Epitaxial In_2O_3 Thin Films Grown on YSZ(111) 111

5.1. Introduction 111

5.2. Experimental Section 113

5.2.1. Thin Film Growth 113

5.2.2. Characterizations 113

5.3. Computational Details 114

5.4. Influence of Temperature on the Epitaxial Growth of In_2O_3 116

5.4.1. Surface Morphology: AFM studies 117

5.4.2. The Interface: Cross-sectional TEM studies 119

5.4.3. θ-2θ X-ray Diffraction: Evidence for Strain 120

5.4.4. Post-annealing Effects 122

5.4.5. Summary of Influence of Temperature on the Epitaxial Growth 123

5.5. Thickness Dependence of the Strain, Band gap and Transport Properties 124

5.5.1. Structure and Morphology 124

5.5.2. Evolution of Strain: X-ray Diffraction 125

5.5.3. Surface Morphology: AFM Studies 129

5.5.4. Electrical Transport Properties 131

5.5.5. Optical Bandgap 134

5.6. Concluding remarks 138

5.7. References 140

6. The Surface Atomic Structure of In_2O_3(111) Determined by STM, LEED and DFT 144

6.1. Introduction 144

6.2. Experimental Details 145

5.2.1. Thin Film Growth 145

5.2.2. Scanning Tunnelling Microscopy 145

5.2.1. Low Energy Electron Diffraction 146

6.3.Density Functional Theory Calculations on In_2O_3 (111) Terminated Surface 146

6.4. Results and Analysis 147

6.4.1. Surface Geometric Structures 147

6.4.2. Analysis of LEED Data 153

6.5. Conclusions ... 161

6.6. References ... 162

7. The Surface Electronic Structures of In_2O_3 Probed by Photoemission Spectroscopy ... 165

7.1. Introduction ... 165

7.2. Experimental Details ... 166

7.2.1. MBE samples ... 166

7.2.2. Photoemission Spectroscopy (PES) ... 166

7.3. Surface Electronic Structure of In_2O_3: Quantized Electron Accumulation States .. 168

7.3.1. The Valence Band Structures ... 166

7.3.2. Evidence of Surface Electron Accumulation layer ... 171

7.3.3 Quantized Electron Sub-states ... 176

7.4. The Influence of Sn Doping on the Electronic Structures ... 180

7.4.1. The Doping Effect on Valence Band Structures ... 181

7.3.2. In 3*d* Core Level ... 182

7.3.3 Resonance Effects in Photoemission from Sn-doped $In_2O_3(111)$ ... 185

7.5. Conclusions ... 188

7.6. References ... 189

Contents

8. Domain Matching Epitaxial Growth of In_2O_3 Thin Films on α-Al_2O_3(0001)...... 192

8.1. Introduction... 192

8.2. Experimental Details 195

8.3. Results and Discussion 196

8.3.1. Overview of the Growth Morphology 196

8.3.2. Characterization of *bcc*-In_2O_3 199

8.3.3 Characterization of *rh*-In_2O_3 204

8.3.3 Optical Absorption Spectra 207

8.4. Conclusions 208

8.5. References... 209

9. Concluding Remarks and Outlooks 211

9.1. Thesis Summary 211

9.2. Future Works and Outlooks 215

9.2.1. High Resolution X-ray Diffraction of In_2O_3 Nanostructures and Thin Film. 216

9.2.2. Surface Physics of Low Index ITO Surface 218

9.2.3 Optimizing the Energy Level Alignment at Organic Layer/ITO Interface.... 219

9.3. References... 220

Chapter 1

Introduction to Indium Oxide

1.1 Transparent Conducting Oxides: Background and Challenges

Most metals are thermodynamically stable as oxides under ambient conditions. Metal oxides are an exciting class of material whose electronic properties range from insulators such as Al_2O_3 and MgO, through semiconductors including $SrTiO_3$, TiO_2 and CeO_2 to metals like V_2O_3, Na_xWO_3 and ReO_3 and superconductors typified by $YBa_2Cu_3O_{7-x}$.[1-3] Not surprisingly, metal oxides are at the heart of many established and emerging technologies in electronics, data storage, and energy and environmental applications. The diverse electronic properties of the metal oxides are largely determined by the nature and occupancy of the valence and conduction bands. For example, stoichiometric In_2O_3 is an insulator with a dipole forbidden bandgap of 2.8 eV, but it becomes the famous transparent conductive oxide indium tin oxide (ITO) when electrons are introduced into the conduction band by doping with Sn. This section reviews the key concepts needed to understand the electronic structures of metal oxides and transparent conductive oxides.

1.1.1 Electronic Structure of Metal Oxides

Two complementary approaches are selected to rationalize the electronic structures of metal oxides: the *ionic model* and *band theory,* based on the tight binding model. The *ionic model* concentrates on the energy levels associated with individual ions. Figure 1.1

illustrates the derivation of a schematic energy level diagram for MgO using the ionic model. The 3*s* level of neutral Mg ($3s^2$) sits above the O *2p* level of neutral O ($2p^4$), as O is more electronegative than Mg (Figure 1.1a). However these levels are reversed for O^{2-} and Mg^{2+} ions (Figure 1.1b). The second electron affinity of an O atom is negative so the *2p* level of O^{2-} sits above the vacuum level. The Madelung potential in the lattice sites of MgO stabilizes the ionic configuration and reverses the energy levels for O^{2-} and Mg^{2+} ions (Figure 1.1c). The bandgap of MgO estimated from the Madelung potential is however around 24 eV, much larger than the experimental value of 7.8 eV. Two further effects need to be considered to reduce the bandgap. The first is electrostatic polarization, resulting from the deformation of electron distribution in an electric field. It lowers the energy of added electrons and raises the energy of occupied O *2p* level, as shown in Figure 1.1d. The other is the bandwidth. The overlap and interaction of orbitals on the neighbouring ions give rise to appreciable Mg *3s* conduction and O *2p* valence bandwidth (Figure 1.1 e). It is estimated that the O *2p* bandwidth for MgO is 6 eV.

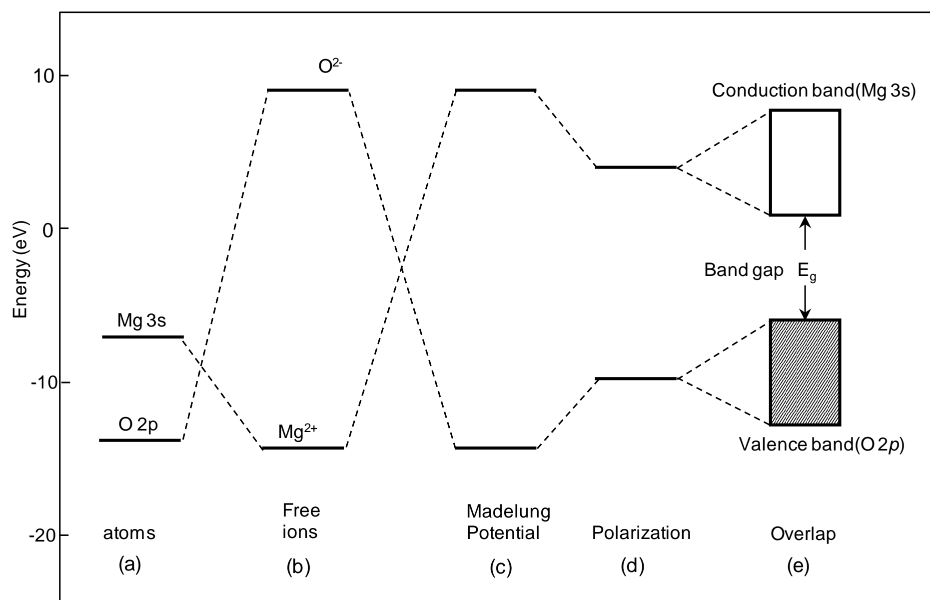

Figure 1.1. Derivation of the bandstructure of MgO using *ionic model* (Adapted from reference[1]).

The second approach is based on the *band model.* In the so-called perturbed free electron approach electrons move in the potential of a periodic lattice to give periodic states: bandgaps arise when the wavelength of the periodic states matches the lattice periodicity. This approach is adopted by standard textbooks on solid state physics but is unsuited to developing a qualitative understanding of the electronic structure of metal oxides. Alternatively, the occupied and unoccupied periodic Bloch states may be constructed as linear combination of atomic orbitals (LCAO). A typical "ionic" band structure for a non-transition metal oxide with the metal in its maximum oxidation state would have an occupied (valence) band composed of combinations of O 2*p* and deeper 2*s* orbitals and an unoccupied (conduction) band made up of combinations of metal orbitals: for example Mg *3s* and *3p* in the case of MgO. The band structure can incorporate hydridization or mixing between these states and band energy dispersion as function of wave-vector in *k* space.

The structures of metal oxides are based on an array of metal cations surrounded by doubly charged O^{2-} anions, most often in an octahedral (6 coordinate) or a tetrahedral (4 coordinate) configuration. There are a wide variety of crystallographic structures for binary oxides, including rocksalt-MO (MgO, CdO, CaO, NiO, CoO 6:6 coordinate), corundum-M_2O_3 (Al_2O_3, V_2O_3, Cr_2O_3, Fe_2O_3, Ti_2O_3 6:4 coordinate), rutile-MO_2 (TiO_2, SnO_2, RuO_2 6:3 coordinate), wurtzite-MO (ZnO 4:4 coordinate), fluorite-MO_2 (CeO_2, UO_2 8:4 coordinate). Common structures for ternary or more complex oxides include perovskite ABO_3 ($SrTiO_3$, $BaTiO_3$, $La_{1-x}Sr_xMnO_3$, NaW_xO_3) and spinel AB_2O_4 ($MgAl_2O_4$ and Fe_3O_4). It is convenient to divide electronic structures of metal oxides into two categories: non-transition metal oxides (the cation valence orbitals are of *s* or *p* type) and transition metal oxides (the cation valence orbitals have *d* symmetry). The band structure for both kinds of oxides may be constructed according to the models discussed

above. In general one expects a filled valence band based predominantly on O 2*p* orbitals, separated by a gap from a metal-based conduction band. However, the complex bonding properties of the transition metal *d* atomic orbitals give rise to a variety of complicating phenomena, including variable oxidation states, electron-electron and electron-phonon interactions, and crystal-field splitting. It is from these complexities that the wide ranging electronic properties of transition metal oxides emerge, including localisation of the *d* electrons by Coulomb repulsion or electron-phonon coupling, ferromagnetic and antiferromagentic ordering of localised spins, metal-insulator transitions and superconductivity.[2]

Non-transition metal oxides can be divided into two groups:

(i) Pre-transition metal oxide such as alkaline-earth oxides (MgO) and Al_2O_3, which are wide bandgap insulators, because of the large difference in electronegativity between the metal and oxygen.

(ii) Post-transition metal oxides such as ZnO, SnO_2 and In_2O_3, which have intrinsic bandgaps around 3-4 eV, but can become *n*-type semiconductors by donor impurity doping.

Compared with pre-transition metal oxides, the post-transition metal oxides have less ionic character, since the O 2*p* orbitals are closer in energy to the metal n*s* and n*p* orbitals and so hybridize more strongly. The filled shallow core *d* orbitals can mix with the O 2*p* valence band orbitals to some extent. Another difference with post-transition metal oxides is the existence of different oxidation states. For example, Sn and Pb have oxidation states of +4 and +2, and As, Sb have oxidation states of +5 and +3. The post-transition metal oxides are an interesting and diverse class of materials, which find many technological and industrial uses. For example, ZnO is a direct bandgap semiconductor

with applications in catalysis and optoelectronics,[4, 5] PbO_2, is found in the lead/acid battery used in all motor vehicles, and In_2O_3,[6] the main subject of this thesis, is used as transparent electrode materials in liquid crystal displays and many other areas.[7]

1.1.2 Transparent Conducting Oxides

Transparent conducting oxides (TCOs) combine optical transparency in the visible region with a high electrical conductivity, making them essential components as an electrode material in liquid crystal displays (LCD), touch screen displays, electroluminescent display device, solar cells and other optoelectronic devices.

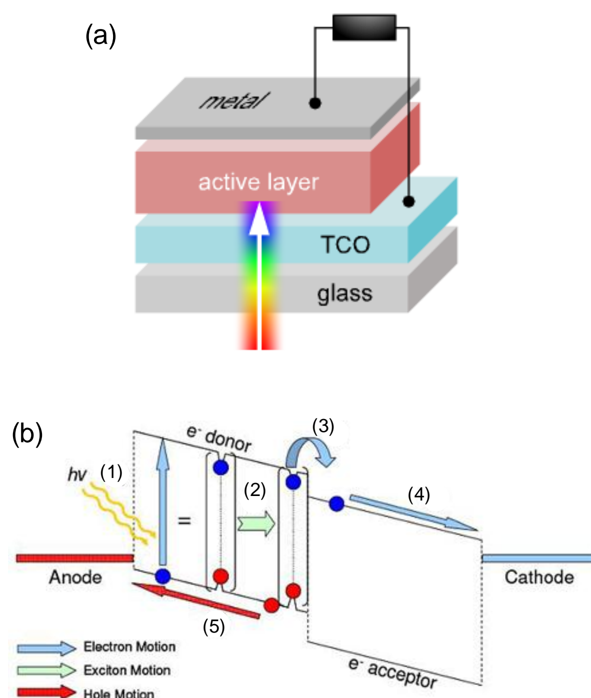

Figure 1.2. (a) Device structure of a typical organic solar cell; (b) the energy diagram for the process of harvesting solar power as electricity: (1) Solar light shines into the solar cell through a TCO and is absorbed by a donor material to generate excitons (electron-hole pairs); (2) Excitons diffuse to the interface; (3) Excitons are split into free electrons and holes by interfacial potential; (4) Electrons are collected by cathodes with low work function; (5) holes are collected by a TCO . (http://www2.warwick.ac.uk/fac/sci/chemistry/research/jones/jonesgroup/research/organicsemiconductors/organicpv/)

Figure 1.2 depicts the typical usage of a TCO in an organic solar cell, where it acts to collect holes generated by the photoexcitation in the organic active layer. The technology of the *n*-type TCOs is more mature than that of *p*-type and we focus on *n*-type materials.

In general, TCO thin films in practical use exhibit a conductivity of the order of 10^4 S·cm^{-1} and an average transmittance above 80% in the visible region.[7-10] TCOs suitable for thin film electrodes should have a carrier concentration of the order of 10^{20} or 10^{21} cm^{-3}, mobilities up to 100 cm^{2}V^{-1}S^{-1}, and also an optical bandgap above approximately 3 eV. From the bandstructure point of view, the combination of the two properties in the same materials is apparently contradictory: to be transparent, a material needs to be an insulator which possesses completely filled valence and empty conduction bands; whereas metallic conductivity requires the Fermi level lies within a band with a large density of states. Such requirements can however be satisfied by degenerately doping several conventional post-transition metal oxides, in particular In_2O_3, ZnO, SnO_2 and CdO. The post-transition metals of these oxides have an $(n\text{-}1)d^{10}ns^2np^x$ electronic configuration (x=0 for Zn and Cd, x=1 for In and x=2 for Sn) and densely packed structures with four or six coordinate metal ions. In the undoped stoichiometric state, these materials are transparent insulators with wide optical bandgap of around 2-3 eV or greater. The valence band is primarily derived from filled oxygen $2p^6$ states and the conduction band derives from metal *n*s states, as shown in Figure 1.3a. To become conducting, the transparent oxide hosts must be degenerately doped, with the Fermi level sitting above the bottom of the conduction band. This requires these oxide hosts to have a relatively high electron affinity. Thus In_2O_3 has an electron affinity of 4.4 eV but the electron affinity of MgO is only 1.4 eV. The metal *ns* states in general give rise to a highly dispersive conduction band giving a low electron effective mass. *N*-type dopants introduce energy levels just below the conduction band minimum at low doping level.

The donor level moves toward the conduction band with increasing doping level so that the activation energy for conduction ΔE decreases according to:

$$\Delta E = \Delta E_0 - \beta n^{1/3}$$

where n is the carrier concentration; ΔE_0 is the activation energy at very low doping level and β is constant. Ultimately, the TCOs exhibit a free electron like metallic behaviour described by Drude model. The critical carrier concentration n_c for the transition from an insulating to metallic phase is defined by the Mott criterion $(n_c)^{1/3}$ a_0*>0.26, where a_0* is Bohr radius. Taking ITO for example, literatures suggest that the static dielectric constant ε(0) = 8.9, an electron effective mass m* = 0.17m_0 (where m_0 is the electron rest mass), giving an effective Bohr radius a_0* = 2.78 nm. Thus the Mott critical carrier density n_c for ITO is calculated to be 1×10^{18} cm^{-3}.

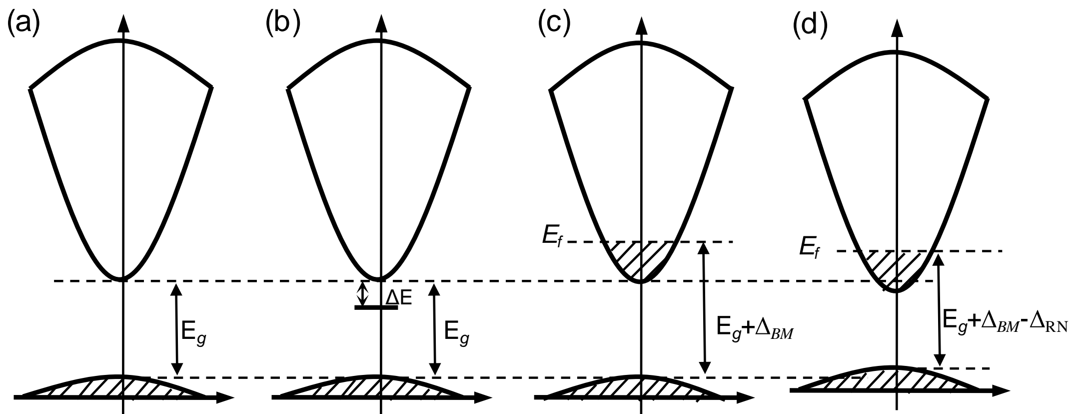

Figure 1.3. Schematic bandstructures of: (a) TCO host-a wide bandgap E_g and with a dispersive conduction band band derived from metal ns states; (b) low doping level before onset of degeneracy; (c) degenerate doping displaces the Fermi level (E_f) above conduction band minimum, making the system conducting; the filling of conduction band increases the optical bandgap by a Burstein-Moss shift; (d) band-gap renormalization shrinks the band gap. (Figure adapted from reference[3])

For doping levels above that set by the Mott criterion, one can consider TCOs to have a full valence band and a parabolic conduction band partially filled by a degenerate free

electron gas up to Fermi energy. The partial filling of the conduction band leads to blocking of the lowest states and hence increasing of the observed optical transition energy. This is the well documented Burstein-Moss shift, as shown in Figure 1.3b. The magnitude of the shift Δ_{BM}, under free-electron theory, is given by:

$$\Delta_{BM} = \frac{\hbar}{2m^*}(3\pi^2 n)^{2/3}$$

which indicates that it is inversely proportional to the reduced effective mass m* ($1/m^*=1/m_c^*+1/m_v^*$), assuming parabolic downward valence band dispersion and upward conduction band dispersion. The shift is proportional to $n^{2/3}$, where n is the electron carrier concentration. However, the carrier dependence of the bandgap shift is generally much less than that expected from the free-electron model, because bandgap renormalization or shrinkage (Δ_{RN}) should be considered. This is associated in part with the increased attractive potential associated with donor centres, and in part with mutual screening of repulsions between valence and conduction electrons by the conduction electron gas itself. This leads to an increase in the energy of the VBM and decrease in the energy of the CBM as shown in Figure 1.3c. Therefore the net change in E_g can therefore be taken as a difference of the two contributions:

$$\Delta E_g = \Delta_{BM} - \Delta_{RN}$$

The free electrons in the conduction band can oscillate with an applied field, like the free electrons in metals (plasma oscillations). Below the plasma energy any material exhibits a high reflectivity. The plasma frequency, ω_p given by:

$$\omega_p^2 = \frac{ne^2}{m^* \varepsilon(\infty)\varepsilon_0}$$

where n is the free carrier density, m* is the electron effective mass and ε_0 is the permittivity of free space. The plasma frequency depends on the carrier concentration in TCOs. For a TCO with a carrier concentration of order 10^{21} cm^{-3}, the plasma energy is typically in the near-infrared (NIR) region at around 0.5-1 eV. Therefore the "optical window" for typical TCOs is set at short wavelengths by its optical bandgap (considering the Burstein-Moss and renormalization) and at longer wavelengths by its reflectivity plasma edge ($\hbar\omega_p$), as shown in Figure 1.4.

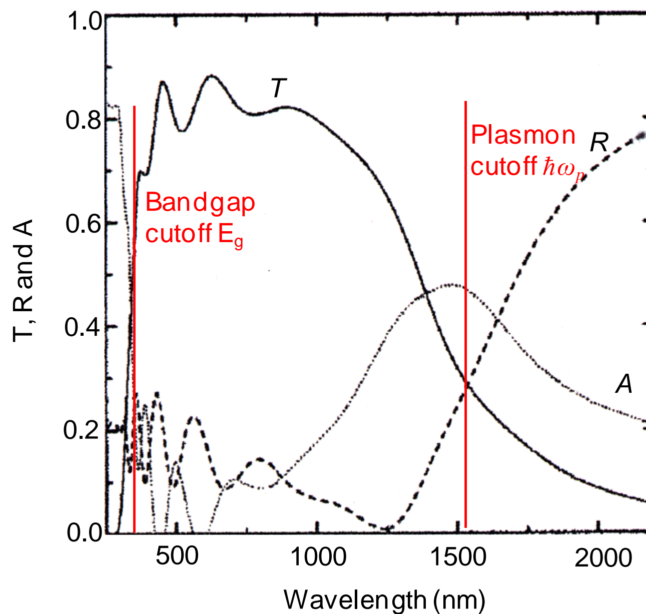

Figure 1.4. "Optical window" of TCOs with high ***Transmission*** in visible region between onset of strong ***Absorption*** in UV set by bandgap (shorter wavelengths) and onset of high ***Reflectivity*** in near IR below plasmon ($\hbar\omega_p$) at lower energy (longer wavelengths). (Figure adapted from reference[66])

Table 1 lists various TCO materials have been developed. Most of the TCOs documented are *n*-type, such as the doped binary compounds like Sn-doped In_2O_3 (indium tin oxide or ITO), Al or Ga-doped ZnO (AZO or GZO) and F-doped SnO_2 (FTO). Among them, ITO is the most widely used TCO,[7-10] because of its intrinsically facile dopability, high

conductivity, excellent transparency and easy processability. It accounts for more than 90% of the TCO market and is expected to be the dominant materials in the following decade,[11] as a report by NanoMarkets which was one of best received reports to date. On the other hand as the rapid expansion in market for liquid crystal displays, solar cells and touch screens has led to a rapid increase in the price of In. There is thus some incentive to develop alternatives to ITO. Al or Ga-doped ZnO (AZO or GZO) and F-doped SnO_2 (FTO) are likely replacement materials and now share 5% of the TCO market. In particular, AZO thin films are composed of inexpensive and non-toxic source materials and are comparable in performance to ITO film with resistivity of the order of 10^{-5} Ω cm. In addition to the binary TCOs mentioned above, multi-component oxides based of combinations of these binary compounds are of interest. Candidate materials include $(ZnO)_{1-x}(In_2O_3)_x$, $(In_2O_3)_x(SnO_2)_{1-x}$, $(ZnO)_{1-x}(SnO_2)_x$.[12]

Table 1. TCO semiconductors for thin-film transparent electrodes (adapted from reference[9]).

Materials	Dopant	Type
In_2O_3	Sn, Ge, Mo, F, Zr, Ta, W, Hf, Te	*n*
SnO_2	Sb, F, As, Nb, Ta	*n*
ZnO	Al, Ga, In, B, Y, F, Ge, Ti, Zr, Hf	*n*
CdO	In, Sn, Y	*n*
$In_4Sn_3O_{12}$	Excess Sn	*n*
Zn_2InO_5, $Zn_3In_2O_6$	Excess In	*n*
Zn_2SnO_4, $ZnSnO_3$	Excess Sn	*n*
Cu_2O	N	*p*
$CuAlO_2$	Mg, Zn	*p*
$CuCrO_2$	Mg, Zn	*p*
$SrCu_2O_2$	K	*p*

On the other hand, the growing interest in electronic or optoelectronic devices based on transparent *p-n* junctions has led to exploration of potential *p*-type TCOs. To date the most promising materials are Cu (I) oxides. In the parent binary oxide cuprite Cu_2O the upper valence-band states are of dominant Cu $3d^{10}$ atomic character. *P*-type doping can be achieved by introducing defect level close to valence band. Thus creation of holes involves oxidation of valence $3d^{10}$ Cu (I) to $3d^9$ Cu (II). However the bandgap of Cu_2O is only 2.17 eV, and still lies in the visible region.[13] The relatively small band gap for Cu_2O is due to the fact that a large Cu $3d$ bandwidth arises from strong Cu-Cu interactions, e. g. each Cu ion has 12 next-nearest Cu neighbours. A growing family of ternary Cu (I) oxides with the general formula $Cu^{I}T^{III}O_2$ such as $CuAlO_2$, $CuInO_2$ and $CuCrO_2$ have wider bandgaps.[14-16] These oxides have a delafossite structures with reduced dimensionality in next-nearest-neighbor Cu-Cu interactions, thus giving rise to larger bandgap, i.e. 3.5 eV for $CuAlO_2$.[15] However, the achievement of a high conductivity in *p*-type TCOs still remains challenging owing to low hole mobility. Most current research on *p*-type TCOs concentrates on Cu (I) compounds.[17]

In spite of the undoubted technological importance of ITO, many basic physical properties of the material have been the subject of ongoing controversy. For example it was only in 2008 that it was established that In_2O_3 has a direct, but dipole forbidden, bandgap of around 2.8 eV, almost 1 eV lower than the value of 3.75 eV widely quoted for over 40 years.[18] Revision of the value for the bandgap led in turn to the realisation that electron accumulation may be observed on In_2O_3 surfaces with low bulk doping levels.[19] An ongoing problem lies in the difficulty in obtaining high quality In_2O_3 thin films or nanostructures that exhibit the intrinsic properties of In_2O_3.[20-23] The renewed interest in the bulk and surface physics of In_2O_3 prompts our attempts to growing high quality single crystal thin films of In_2O_3 both for detailed physicochemical property

investigations and for electronic device applications. It is hoped that the results will provide the insights for the continuous improvement of the properties of ITO and in turn ITO-related device performances.

In summary the objectives of this research are (i) to establish the conditions for growth of high-quality In_2O_3 single crystal thin films by using by oxygen plasma assisted molecular beam epitaxy (OP-MBE) system; (ii) to investigate the surface structural and electronic properties of the high-quality In_2O_3 thin films using techniques such as scanning tunnelling microscopy (STM), high resolution transmission electron microscopy (HR-TEM) and synchrotron based photoemission spectroscopy, coupled with *initio* density functional theory (DFT) calculations to supplement our experimental results.

1.2 Surface Science of Metal Oxides

The surfaces and interfaces of solids play a crucial role in an extremely wide range of phenomena. In many instances, the properties of a metal-oxide surface or of the interface between metal oxides and other materials are key to device performance. This is because the surface/interface is the very place where materials growth or free carrier tunnelling/scattering occurs.[24-30] Another urgent issue is to understand and ultimately design better heterogeneous catalysts. The reactions in heterogeneous catalysis largely occur on the surfaces, so understanding surfaces is obviously important. Thus the control of the surface/interface physics of oxides is of key interest in many technological areas and is now emerging as an important frontier in surface science.[26, 27, 30] For examples, in the photoelectrochemical water splitting, the conduction-band level of the photoanode (e.g. TiO_2) must be high enough to make the chemical reduction of H^+ to H_2

thermodynamically favourable, while to utilize ITO as transparent hole collecting anodes for organic photovoltaic devices, the Fermi level of ITO must be as low as possible to maximize the open-circuit voltage.[31-33] The geometric and electronic structures of In_2O_3(111) surface will be particularly studied in this thesis. In the following sections, a brief introduction to the surface science of oxides will be introduced.

1.2.1 Basic Concepts of Solid Surfaces

The termination of a crystal at a surface leads breaking of bonds. The atoms at the surface will rearrange themselves to minimize the *surface energy (γ)* and often the resulting structure is very different from a simple truncation of the bulk. The surface energy is defined as the excess energy at the surface of a material compared to the bulk, and thus depends on the energy required to break the bonds of the surface. It is reduced through the *surface relaxation* and *reconstruction* processes. Adjustment in the positions of atoms in the topmost layers perpendicular to the surface is called *surface relaxation*. The atomic rearrangement may also involve change of the periodicity parallel to the surface within the topmost atomic layer (the 2-dimensional lattice). This is called *surface reconstruction*. Reconstruction may also include surface atomic configurations in which atoms or a whole row of atoms are missing in comparison with the bulk.

The surface atomic rearrangements generally are different for metals and semiconductors. In metals, the electrons are strongly delocalized and the chemical bonds are not directional, whereas in most semiconductors significant directional covalent bonding is present. Thus one commonly observes relaxation for metal surfaces.[34] In the case of many semiconductors, surface reconstruction happens to reduce the numbers of dangling bonds on the surfaces. For example, the formation of a Si(100) surface requires

breaking the bonds between the Si atoms that form the new surface and those that were in the layer immediately above.[35] This leaves two "dangling bonds" per surface Si atom. Pairs of Si atoms in the topmost layer move together to form surface "Si dimers" in order to reduce the number of dangling Si bonds. This process leads to a change in the surface periodicity: the period of the surface structure is doubled in one direction giving rise to a so-called (2×1) reconstruction observed on Si(100) surface.

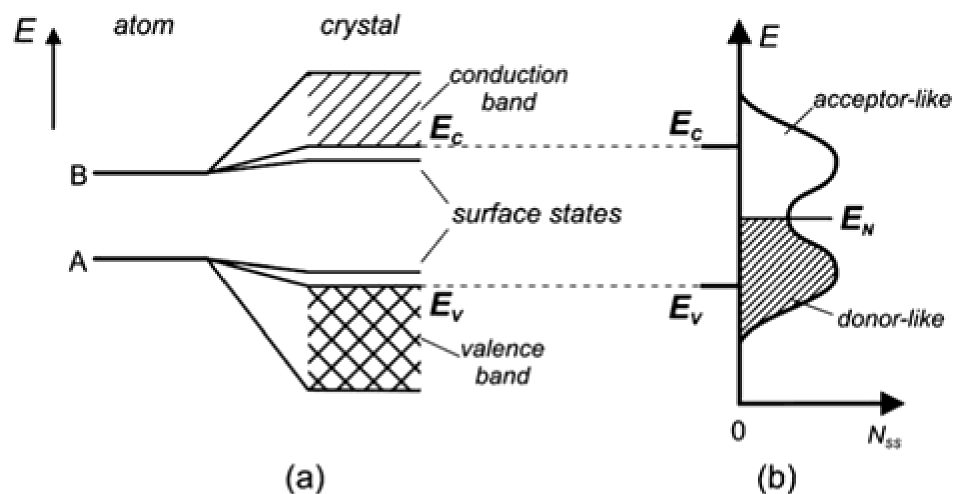

Figure 1.5. Qualitative explanation the origin of surface states: (a) Two atomic levels A and B form the bulk valence and conduction bands, respectively; surface atoms have fewer bonding neighbours than bulk atoms, thus giving rise to electronic energy levels that are closer to those of the free atoms, i.e. surface states levels are split off from the bulk bands; (b) Depending on their origin, these surface states have acceptor- or donor-like charge character; mostly the intrinsic surface states having the periodicity of 2-dimensional (2D) surface show dispersion in the surface 2D reciprocal space which results in broader bands. (Figure taken from reference[36])

The breakup of the translational symmetry by the surface invariably results in surface electronic states distinct from those of the bulk, namely *intrinsic surface electronic states*.[36] The microscopic origin for such states involves interplay between dangling bonds, relaxation and reconstruction at the surface. Surface atoms have fewer bonding

neighbours than bulk atoms and thus give rise to electronic energy levels that are closer to those of free atoms, i.e. surface state levels are split off from the bulk bands, as shown in Figure 1.5. Depending on their origin, surface states have donor-like or acceptor-like character, where the surface state wave functions have predominantly valence band or conduction band character, respectively. A good example of the simple case in Figure 1.5 is that of partly ionic materials like GaAs. The bulk valence and conduction bands are derived from As (atom A) and Ga (atom B), respectively. Thus the As-derived surface states have more donor character, whereas the Ga-derived surface states are more acceptor-like.

The charge neutrality level (CNL) of surface states is the position for the Fermi level which renders the surface without a net charge. The surface states remain neutral with occupied donor-like or unoccupied acceptor-like states, when the Fermi level coincides with CNL.[37] When the Fermi level is above the CNL, the surface is negatively charged (occupied acceptor-like states). When the Fermi level is below the CNL, the surface is positively charged (unoccupied donor-like states). In the presence of charged surface (with a charge density of Q_{ss}), carriers with opposite charge will accumulate in the near surface region inside the semiconductor in order to screen the surface charge, which are called the space charge Q_{sc}. To maintain charge neutrality,

$$Q_{ss} = -Q_{sc}$$

For an n-type material, negatively charged surface states are balanced by a positive space-charge region to maintain charge neutrality, whereas positively charged surface states requires a negative space charge region. This is achieved by an upward (downward) bending of the bands in order to decrease (increase) the electron concentration at the surface with respect to the bulk values, resulting in depletion (accumulation) of electrons

at the surface. Figure 1.6 presents an example of a space charge layer, in which a positive charge density of Q_{ss} of unoccupied donor-like surface states is compensated by accumulation of electrons near the surface region (Q_{sc}). The formation of the space charge layer accordingly induces downward band bending.

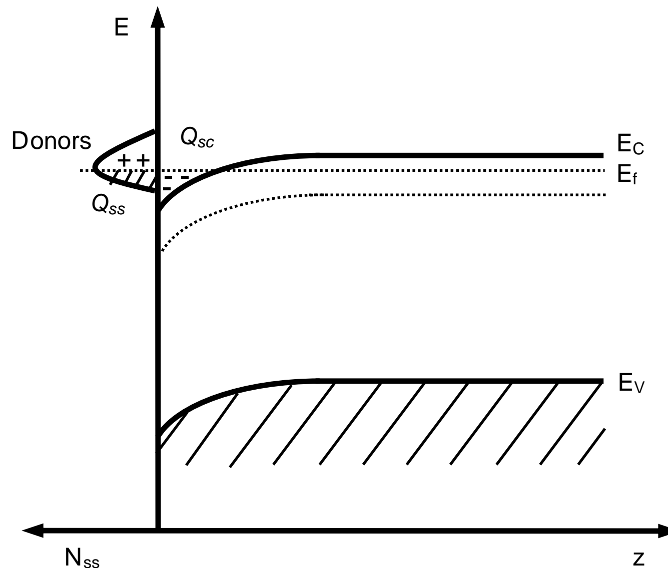

Figure 1.6. Band scheme for n-doped semiconductor with positively charged donor-like surface states and electron accumulation layer (band energy E versus z coordinate normal to the surface z=0); Partially unoccupied donor-like surface states (Q_{ss}) is compensated by the space charge region Q_{sc}. E_c, E_f and E_v is conduction, Fermi and valence band energy. (Figure taken from reference[36])

In addition to *intrinsic surface electronic states,* there are other electronic states localized at the surface, which are related to imperfections (for example defects or adatoms), called *extrinsic surface electronic states.* A missing surface atom causes a change in the geometry of surrounding atoms, thus giving rise to changes in electronic surface states. In particular, for crystals with partly ionic bonds, it is easily seen how a missing surface atom, i.e. ion affects the electronic structure in the vicinity. If a negatively charged O^{2-} ion in ZnO is missing in the surface, then a finite area of the surrounding surface contains

more positive charge due to Zn^{2+} ions than do other stoichiometric areas of the surface. This enhanced positive charge near the defect acts as a trap for electrons, i.e. the localized defect state can be occupied by electrons, leading to a donor-like state.

1.2.2 Metal Oxide Surfaces

The surface chemistry of metal oxides is inherently complex due to the effect of surface polarity, stoichiometry and surface defects as well as the difficulties in preparing well-controlled single crystal surfaces.[38] The coordination number of the surface ions is lower than those in the bulk, leading to reduced Madelung potential, smaller polarization and bandwidths, and the possibility of "dangling bond" state in more covalent materials. These effects could lead to reduced bandgaps and various surface enhanced gap states. Surface relaxations and reconstructions also are important, as they change the ionic bonding length and coordination numbers. The concentration of defects such as cation or anion vacancies or adatoms on metal oxide surfaces may be higher than in the bulk, since the formation energies are in general lower on surfaces. The defects further change the coordination of the surface atomic, and hence dramatically change the local atomic and electronic structures. This leads to further influence on the overall electrical properties in a way which depends on the energy levels of the defects and on their polarity, as discussed above. Surface defects are associated with space charge layers involving change in surface carrier concentration and band bending. For example the formation of surface oxygen vacancies may leave extra electrons in the surface region, leading to the surface electron accumulation layer and downward band bending.

Because of the ionic bonding feature, the polarity is a key concept in the surface science of metal oxides. Surfaces that possess a net dipole moment are called *polar surfaces* and are intrinsically unstable, whereas surfaces whose atomic planes are charge neutral are referred to as *non-polar surfaces*. Tasker classified the surfaces of ionic crystals into three types.[39] "Type I" surfaces consist of layers of cations and anions which are charge neutral within the individual layers. These layers generate no net dipole moment, and the resulting non-polar surfaces are often quite stable. For example, the (110) surface of fluorite oxides (e.g. UO_2) remain neutral by containing metal cations (U^{4+}) and O^{2-} anions with a ratio of 1:2 within one atomic layer,[40] see Figure 1.7a.

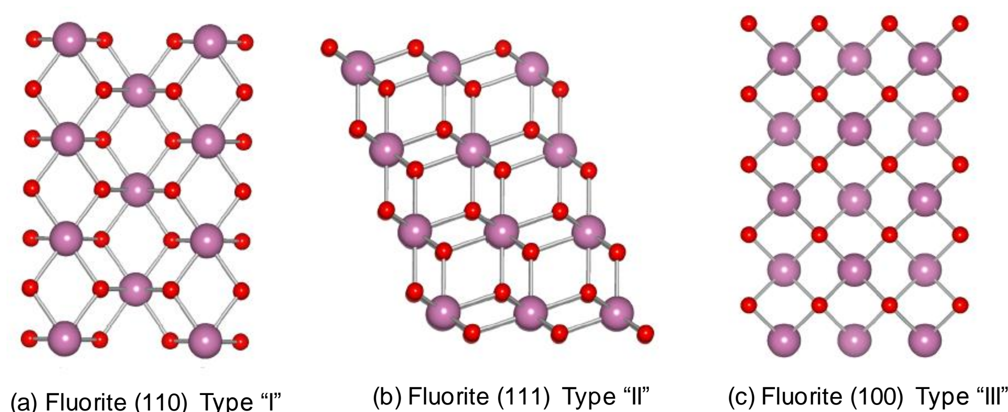

Figure 1.7. Schematic side views of the fluorite oxide (e.g. UO_2) surface structures, which are labelled according to the Tasker surface notation for polar compounds. The cations and anions are represented by large and small spheres, respectively.

"Type II" surfaces comprise trilayers containing the same total number of positive and negative charges, but with an excess of one type of charge on each side of the trilayer structure. This results in a quadrupolar unit with two opposing dipoles, which cancel each other. The resulting surfaces are also often quite stable; one classic example is the fluorite oxide (111) surfaces, shown in Figure 1.7b. For fluorite the (111) surface is the most thermodynamically stable surface. Structural studies on this surface also indicate it

has a near ideal bulk termination with very little relaxation.[40] "Type III" surfaces are polar, with repeating cationic and anionic bilayers, as shown by the (111) surface of rocksalt oxides (MgO)[41] and (100) of fluorite oxide (Figure 1.7c). Each bilayer gives rise to a dipole moment. The electrostatic potential causes the surface energy to diverge to infinity with increasing thickness of a crystal. Thus the polar surface is normally not stable. However the polar surface can undergo stabilization by a pronounced modification of the surface electronic structure, to provide a macroscopic depolarization field. Stabilizing atoms may be achieved by total or partial filling of surface states, sometimes leading to surface metallization; or by changes in the surface stoichiometry involving spontaneous desorption of atoms, faceting, development of large cell reconstructions, or adsorption of foreign species like hydroxyl ions.[42] These processes dramatically affect the surface chemistry of metal oxides, and new electronic surface states may appear in the gap of the oxide. As a result, surface oxygens and cations may present an enhanced basic or acid character. A more complete review on polar surfaces was provided by Noguera[42] and was recently updated by Goniakowski *et al.*[43] The polarity largely determines the thermodynamic stability of surfaces i.e. surface free energy. This normally gives rise large anisotropy in surface energies of metal oxides, i.e. polar surfaces have the largest surface energy, whereas the others are much lower. The anisotropy in surface energy plays a significant role in determining the equilibrium shape of nanoparticles by Wulff construction: the equilibrium shape a crystal adopts during growth is determined by the directional dependence of surface energy i.e. lower surface energy planes are preferred over others.[37]

The other important issue for metal oxide surfaces is the role *defects* of many oxides such as cation or anion vacancies or adatoms. The predominant d*efects* are oxygen vacancies. The removal of surface O further reduces the coordination number of cations

and leaves behind two electrons. One well studied example is the (110) surface of rutile TiO_2.[44, 45] Rutile is the most stable polymorph of TiO_2 an important material for heterogeneous photocatalysis.[46] The surface has a bulk-terminated TiO_2(110)-(1×1) structure with some relaxations.[47, 48] A model of this surface is shown in Figure 1.8a. The truncation of the crystal invariably results in surface atoms with fewer co-ordinations than those in the bulk. Thus the surface consists of row of fivefold coordinated Ti_{5c} atoms (sixfold coordinated in bulk) along the [001] direction, separated by twofold coordinated bridging surface O_{2c} atoms (threefold coordinated in bulk). The surface atomic structure can be directly imaged by scanning tunnelling microscopy (STM) in the empty states (Figure 1.8b). The image contrast is dominated by electronic effects: the conduction band consists mostly of Ti states and the Ti_{5c} atoms appear brighter lines in the STM, while the valence band consists of O 2*p*-derived states and appear as dark lines. The ultrahigh vacuum surface preparation procedure also induces bridging O_{2c} vacancies, which can be directly observed as the fainter bright spots in the image. It has been shown that the defect-mediated dissociation of water molecules could be directly monitored: i.e. one water molecule dissociates at the O_{2c} vacancies (Figure 1.8a), resulting in two hydroxyls in the bridging row with the green O atom from the water and the red one from the surface O_{2c}.[49] Meanwhile, the surface electronic structure of modified by the defects (e.g. absorption of hydroxyls) can be studied by photoemission spectroscopic techniques. As indicated in Figure 1.8c, a Ti *3d*-derived gap state at approximately 1 eV below Fermi energy presents on non-stoichiometric TiO_2 surface.[45, 50] When this surface is exposed to water at room temperature, the gap state increases in intensity and shifts to somewhat higher binding energies, indicating the absorption of surface hydroxyl groups on the surface.

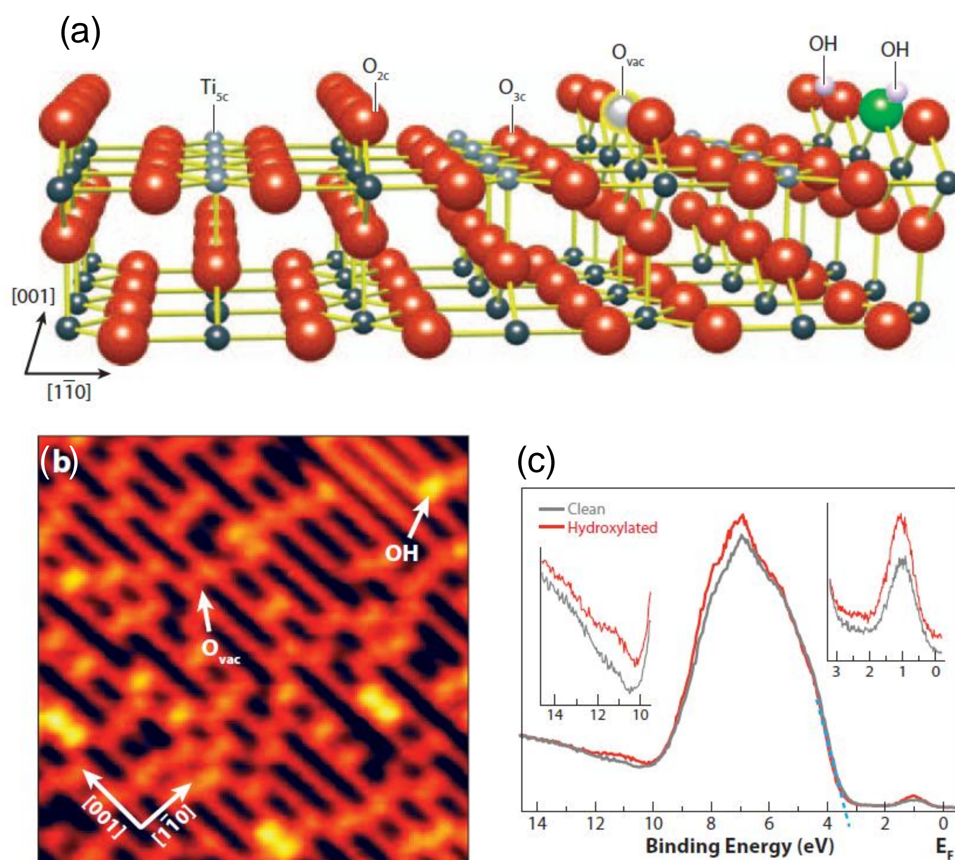

Figure 1.8. Rutile $TiO_2(110)$ surface: (a) Geometric model with O vacancies (O_{vac}) and OH groups. The OH group with the green O atom stems from the water molecule that has filled a vacancy, and the red one represents a lattice O_{2c} atom that has received a proton upon water dissociation; (b) Empty state STM image of (10 nm × 10 nm, $V_{sample} = +1.48$ V, $I_{tunnel} = 0.08$ nA);[51] (c) Photoemission spectrum taken with a photon energy of 47 eV. The right and left insets show the gap state and the region of the OH 3σ states, respectively, and the dashed blue line marks the position of the valence band maximum. Figures are taken from reference.[27]

The research on oxide surface science is just in its initial stage. Whereas many important issues such as the surface structures and the stabilization of polar oxide surfaces have been addressed to some extent, even more remain open or even unknown, such as the effects of surface defects or intentional dopants on the catalytic activity, e. g. the exotic 2D electron gas at the $LaAlO_3/SrTiO_3$ interface.[52] The ultimate goal is to control and design the surface or interface of metal oxides. Recent efforts on enhancing the power conversion efficiency (PCE) of organic photovoltaic by interfacial engineering[32, 53] and

significant improvement of the energy conversion efficiency for solar hydrogen production of TiO_2 by controlling introducing localized surface electronic states[30] provide good paradigms for surface science to engineer the device performance.

1.3 Crystal Structures of In_2O_3

The thermodynamically stable phase of In_2O_3 adopts a body-centred cubic bixbyite structure, with space group $Ia\overline{3}$ and lattice parameter a = 1.01170 nm.[54] The structure may be regarded as a 2×2×2 superstructure of fluorite with ordered removal of O from ¼ of the anion sites, as shown in Figure 1.9a. There are 80 atoms in one unit cell, with 32 sites occupied by cations on two non-equivalent sixfold coordinated sites and 48 oxygen ions on fourfold coordinated sites. The two cation sites occupy 8b and 24d positions according to international notation.[55]

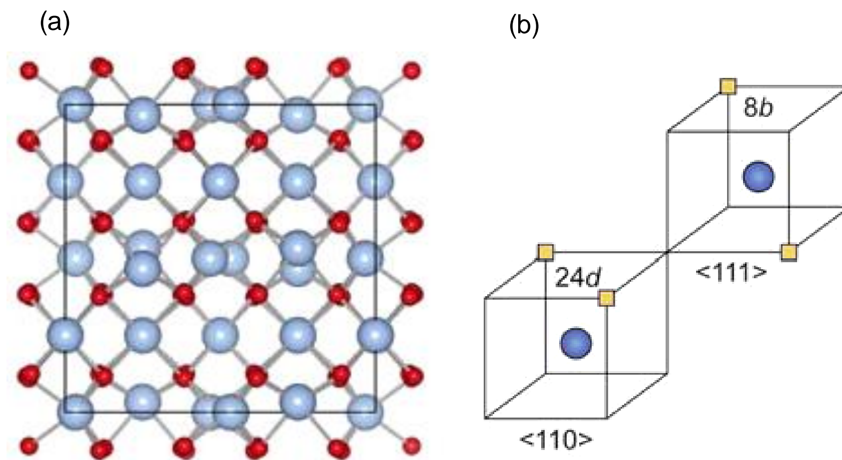

Figure 1.9. (a) Crystal structure representations of the bixbyite In_2O_3 unit cell; In is coloured blue (large balls), with red reserved for oxygen (small balls); (b) The structural anion vacancy configurations (yellow squares) around both types of In sites 8b and 24d. (Figures from Dr. A. Walsh from University of College London)

Figure 1.9b illustrates the anion vacancy configuration around In cations. Each cation sites at the centre of a distorted cube, with six corners occupied by oxygen anions, while two corners are empty. One quarter of the cations (8b cations) are coordinated by six oxygen anions with the same In-O bond length of 2.19 Å. The oxygen anions are nearly at the corners of the distorted cube with two anions vacancies along one face diagonal. The remaining three quarter 24d cations occupy sites of lower symmetry, as they are coordinated to six oxygen anions at three distances (2.13, 2.19, and 2.23 Å). All 48 oxygen anions occupy the same symmetry sites and are coordinated by 4 cations. It was found that the doping Sn atoms preferentially replace the In cations at 8b sites.[55] The other polymorph of In_2O_3 adopts the metastable corundum-type structure with space group $R\bar{3}c$, No. 167.[56] The hexagonal corundum In_2O_3 is a high pressure phase with lattice parameters of a=5.478 Å and c=14.51 Å.[57] This structure is the same as that adopted by α-Al_2O_3 (corundum). It contains of one type of In atom (surrounded by oxygen in trigonal antibiprism coordination) and one type of O atom occupying 12c and 18e Wyckoff positions, respectively.

1.4 Electronic Structures of In_2O_3 and ITO

Despite the technological importance of In_2O_3 and ITO, the basic physical properties of these materials remain contentious. Thus even the nature and magnitude of the band gap has been debated. Optical absorption measurements performed on single crystals of In_2O_3 by Weiher and Ley in 1966 showed that In_2O_3 had a direct band gap of about 3.75 eV marking the onset of strong optical absorption and a weaker absorption onset around 2.62 eV which was presumed to be due to indirect transition.[58-61] Photoemission experiments

showed that the valence band onset of nominally undoped In_2O_3 is found about 2.8 eV below the Fermi below the Fermi level (which is usually situated within the lower part of the conduction band), in agreement with the indirect bandgap hypothesis.[62-65] Nevertheless for many years the band gap has been presumed to be direct and quoted to be 3.75 eV.[54, 66] *Moreover* bandstructure calculation results have been inconsistent with the indirect bandgap hypothesis, which required about 1 eV upward dispersion in the upper valence band.[67-71]

Guinness *et al.* measured synchrotron radiation excited O K emission spectra on a series of transparent conducting oxides including In_2O_3, CdO, ZnO and SnO_2, which directly reveal significant hybridization between O 2*p* partial density of states and shallow-core metal *d* states for In_2O_3, CdO and ZnO.[65] It was therefore proposed that the indirect gap could arise from mixing of O 2*p* and shallow-core In 4*d* states away from the Γ point within the centrosymmetric crystal structure of In_2O_3, similar to the situation in rocksalt CdO. It has been proved by photoemission spectra that the Cd 4*d* level is quite shallow (10.7 eV relative to E_f).[72] Inversion symmetry in the rocksalt structure prevents hybridization of O 2*p* states with Cd 4*d* states at the zone centre, but O 2*p* – Cd 4*d* mixing is allowed away from Γ.[73] The indirect gap is proved to be a consequence of the hybridization of O 2*p* derived orbitals with Cd 4*d* states.[65] As such the band structures calculated by density functional theory (see Figure 1.10) involve a conduction band minimum at Γ and a dispersive valence band, giving rise to a direct band gap of 1.61 eV at the Γ point and indirect bandgaps of 0.39 eV and 0.47 eV away from Γ point.[72, 74, 75] These values are slightly less than experimental values (2.16 eV for direct and 0.55 for indirect bandgap).[74, 75] Note that density functional theory usually underestimates the bandgaps.

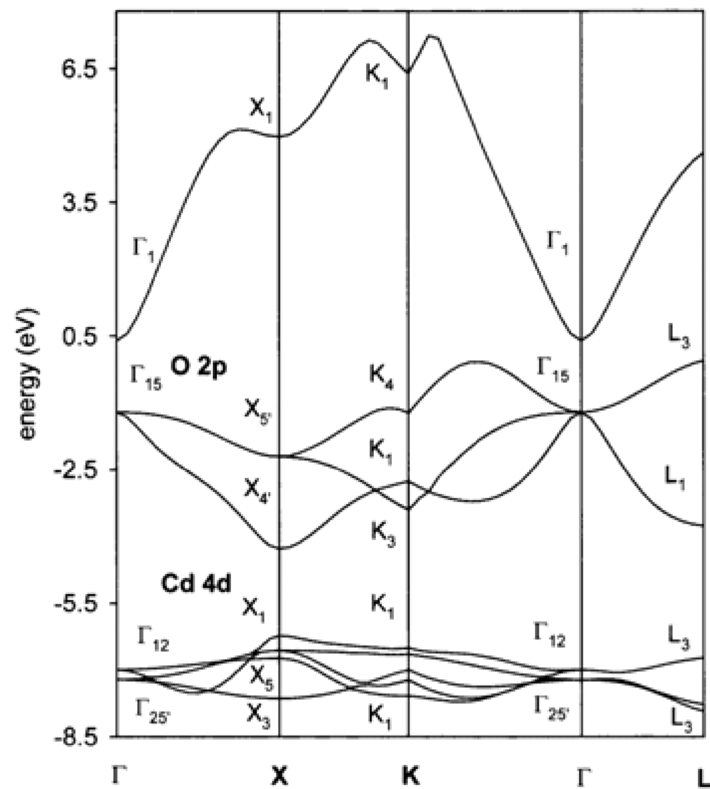

Figure 1.10. The bandstructure of CdO calculated by density functional theory. Symmetry labels for some of the bands at high-symmetry points are given. Figure is taken from refence.[72]

It is also true that the bixbyite In_2O_3 has a centrosymmetric crystal structure. Previous O K X-ray emission spectra also provided evidence that In 4*d* mixed with O 2*p* at the valence band.[65] However the binding energy of In 4*d* shallow core level in In_2O_3 (about 17 eV) is much larger than that of Cd 4*d* level in CdO.[65, 76, 77] Thus it is expected as the binding energy increases the metal 4*d* – oxygen 2*p* interaction decreases. Odaka *et al.* have performed first principles calculations which included the In 4*d* orbitals localized at 12.5 eV.[68] They did find some evidence of In 4*d* – O 2*p* mixing at the top of the valence band away from Γ in the Brillouin zone. However upward dispersion of the valence band to a maximum at the H point was only 0.079 eV, with the conduction band minimum at Γ. The dispersion is much lower than the dispersion energy required by the experimental

difference (around 1 eV). The absolute value of the bandgap and the binding energy of the In 4*d* shallow core level was underestimated in this study due to the nature of the calculations. Erhart *et al.*[78] have recently performed extensive density functional theory calculations using the local density approximation (LDA+U) and generalised gradient approximation (GGA+U), where U is a self-interaction correction, to correct against the underestimation of the shallow core In 4*d* binding energy observed with density functional methods. It was found that there was an indirect band gap, but the upward dispersion of the valence was always less than 0.05 eV away from the Γ point. Thus *bandstructure calculations* do not support the indirect bandgap hypothesis.

It was only in 2008 that the long-term experimental and theoretical controversy was reconciled based on X-ray photoemission spectroscopies coupled with *ab initio* density functional theory.[18] It was established that In_2O_3 has a direct, but dipole forbidden, bandgap of around 2.9 eV. The bandstructure is shown in Figure 1.11. The weak nature of optical absorption around the onset energy can be attributed to the fact that transitions between states in the upper part of the valence bands and the conduction band minimum are dipole forbidden or carry very low dipole intensity. The onset of fully optical transitions is from states about 0.8 eV lower that the valence band maximum.

The surface electronic properties of In_2O_3 have also proved to be controversial or largely ignored. A pronounced depletion of carriers with an upward band at the surface of In_2O_3 was suggested as a way of reconciling a gap of 3.75 eV with photoemission mearsurements.[64] However the revised value for the bandgap led to the realisation that electron accumulation may be observed at the In_2O_3(100) surfaces with low bulk doping levels,[19] similar to that observed on CdO,[74] and the other In containing compound, InN[79] and InAs[80]. The surface electron accumulation layer is attributed to the highly dispersive conduction band as shown in Figure 1.11 and the CNL of In_2O_3 lies well above the

conduction minimum to give rise a unoccupied donor-like surface states, which induce an electron accumulation layer near surface region to maintain charge neutrality.

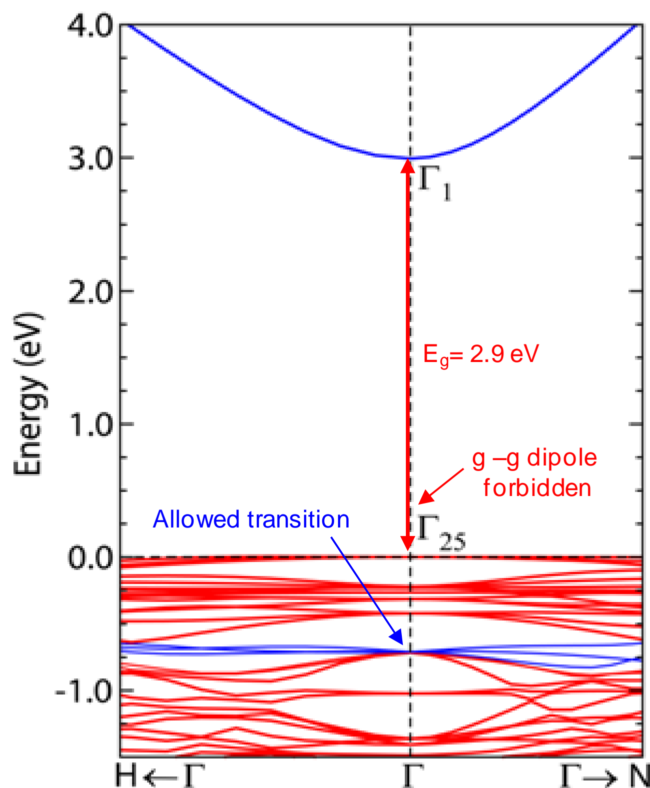

Figure 1.11. Band structure of In_2O_3 (along the H-Γ-N lines), showing it has a direct bandgap of around 2.9 eV; however the transition from the valence band maximum to conduction band minimum is dipole forbidden; the allowed transition locates about 0.8 eV lower that the valence band maximum (blue lines), which marks the strong onset absorption at 3.7 eV in the optical absorption measurements. Figure is taken from reference.[18]

1.5 Organization of the Thesis

This chapter has presented an introduction to the key idea in the surface science of metal oxides, and a background on the crystal and electronic structures of In_2O_3. Chapters 2 and 3 describe the background and details respectively of the key experimental techniques used throughout this thesis. Topics considered include molecular beam

epitaxy, transmission electron microscopy, scanning probe microscopy, photoemission spectroscopy, optical absorption and so on. Chapter 4 demonstrates the self-organization of In_2O_3 nanostructures grown on (100), (110) and (111) oriented Y-stabilised ZrO_2 substrates. It is shown that the large surface energies of In_2O_3(100) and (110) prompt the growth of pyramid islands and nanorods structure on the respective surfaces, while the lowest energy In_2O_3(111) surface favours the growth of flat thin films. In Chapter 5, the influence of the growth temperature and film thickness on the physical properties (strain, morphology, bandgap and transport properties) of the epitaxial In_2O_3(111) thin films is systematically investigated using a combination of experimental and computational methods. It was established that the In_2O_3(111) thin film grown at 700°C with a thickness of 200 nm has the highest quality for subsequent surface structural and electronic studies. Following the achievement of high-quality surfaces, chapter 6 investigates in detail the surface atomic structure of In_2O_3(111) as determined by low energy electron diffraction, scanning tunnelling microscopy and density functional theory. These techniques reveal a bulk-terminated (1×1) surface with relatively minor inward relaxations. In Chapters 7, the electronic structures of Sn doped and undoped In_2O_3(111) are examined by synchrotron-based photoemission spectra excited with a wide range of photon energies between 9 eV and 6000 eV. It is shown that a pronounced electron accumulation layer presents itself at the surfaces of undoped In_2O_3 films with very low carrier concentrations. The pronounced electron accumulation associated with a downward band bending in the near surface region creates a confining potential well, which causes the electrons in the conduction band become quantized into two subband states, as observed by angle resolved photoemission spectra (ARPES) Fermi surface mapping. The accumulation of high density of electrons near to the surface region was found to shrink the surface band

gap through many body interactions. Chapter 8 moves on to consider the epitaxial growth of In_2O_3 thin films on α-Al_2O_3(0001). The mismatch is now 15%. It is shown that both the stable body centred cubic phase and metastable hexagonal corundum In_2O_3 phases can be stabilized in epitaxial thin films by the domain matching epitaxy mechanism by matching the integral multiples of lattice planes of the In_2O_3 and substrate. Finally, the main concluding remarks and outlooks of this work are summarised in Chapter 9.

1.6 References:

1. P. A. Cox, *Transition Metal Oxides:: An Introduction to Their Electronic Structure and Properties* (Oxford University Press, Oxford, 2010).
2. V. E. Henrich and P. A. Cox, *The Surface Science of Metal Oxides* (Cambridge University Press, Cambrige, 2000).
3. A. Facchetti and T. J. Marks, *Transparent Electronics: From synthesis to applications* (Wiley, Chippenham, 2010).
4. U. Ozgur, Y. I. Alivov, C. Liu, A. Teke, M. A. Reshchikov, S. Dogan, V. Avrutin, S. J. Cho and H. Morkoc, J. Appl. Phys. **98**, 041301 (2005).
5. C. Klingshirn, ChemPhysChem **8**, 782 (2007).
6. T. L. Blair, J. Power Sources **73** (1), 47 (1998).
7. C. G. Granqvist and A. Hultaker, Thin Solid Films **411**, 1 (2002).
8. C. G. Granqvist, Solar Energy Materials and Solar Cells **91**, 1529 (2007).
9. H. Y. Liu, V. Avrutin, N. Izyumskaya, U. Ozgur and H. Morkoc, Superlattices Microstruct. **48**, 458 (2010).
10. H. Hosono, Thin Solid Films **515**, 6000 (2007).
11. Transprant Conductor Markets 2010: ITO and the Alternatives; NanoMarkets Report (2010).
12. C. A. Hoel, T. O. Mason, J. F. Gaillard and K. R. Poeppelmeier, Chem. Mat. **22**, 3569 (2010).
13. H. Raebiger, S. Lany and A. Zunger, Phys. Rev. B **76**, 045209 (2007).
14. H. Kawazoe, M. Yasukawa, H. Hyodo, M. Kurita, H. Yanagi and H. Hosono, Nature **389** (6654), 939 (1997).
15. H. Yanagi, T. Hase, S. Ibuki, K. Ueda and H. Hosono, Appl. Phys. Lett. **78**, 1583 (2001).
16. T. Arnold, D. J. Payne, A. Bourlange, J. P. Hu, R. G. Egdell, L. F. J. Piper, L. Colakerol, A. Masi, P. A. Glans, T. Learmonth, K. E. Smith, J. Guo, D. O. Scanlon, A. Walsh, B. J. Morgan and G. W. Watson, Phys. Rev. B **79**, 075102 (2009).
17. S. Sheng, G. Fang, C. Li, S. Xu and X. Zhao, Phys. Stat. Sol. (a) **203**, 1891 (2006).
18. A. Walsh, J. L. F. Da Silva, S. H. Wei, C. Korber, A. Klein, L. F. J. Piper, A. DeMasi, K. E. Smith, G. Panaccione, P. Torelli, D. J. Payne, A. Bourlange and R. G. Egdell, Phys. Rev. Lett. **100**, 167402 (2008).
19. P. D. C. King, T. D. Veal, D. J. Payne, A. Bourlange, R. G. Egdell and C. F. McConville, Phys. Rev. Lett. **101**, 116808 (2008).
20. O. Bierwagen, M. E. White, M. Y. Tsai and J. S. Speck, Appl. Phys. Lett. **95**, 262105 (2009).

21. A. Bourlange, D. J. Payne, R. G. Egdell, J. S. Foord, P. P. Edwards, M. O. Jones, A. Schertel, P. J. Dobson and J. L. Hutchison, Appl. Phys. Lett. **92**, 092117 (2008).
22. A. Bourlange, D. J. Payne, R. G. Palgrave, J. S. Foord, R. G. Egdell, R. M. J. Jacobs, A. Schertel, J. L. Hutchison and P. J. Dobson, Thin Solid Films **517**, 4286 (2009).
23. T. Koida and M. Kondo, J. Appl. Phys. **99**, 123703 (2006).
24. E. W. Plummer, Ismail, R. Matzdorf, A. V. Melechko and J. D. Zhang, Prog. Surf. Sci. **67**, 17 (2001).
25. R. Schaub, E. Wahlstrom, A. Ronnau, E. Laegsgaard, I. Stensgaard and F. Besenbacher, Science **299**, 377 (2003).
26. U. Diebold, Nat. Mater. **9**, 185 (2010).
27. U. Diebold, S. C. Li and M. Schmid, in *Annual Review of Physical Chemistry, Vol 61* (Annual Reviews, Palo Alto, 2010), Vol. 61, pp. 129.
28. H. G. Yang, C. H. Sun, S. Z. Qiao, J. Zou, G. Liu, S. C. Smith, H. M. Cheng and G. Q. Lu, Nature **453**, 638 (2008).
29. A. Fujishima, X. T. Zhang and D. A. Tryk, Surf. Sci. Rep. **63**, 515 (2008).
30. X. B. Chen, L. Liu, P. Y. Yu and S. S. Mao, Science **331**, 746 (2011).
31. N. R. Armstrong, P. A. Veneman, E. Ratcliff, D. Placencia and M. Brumbach, Accounts Chem. Res. **42**, 1748 (2009).
32. S. Braun, W. R. Salaneck and M. Fahlman, Adv. Mater. **21**, 1450 (2009).
33. H. Hoppe and N. S. Sariciftci, J. Mater. Res. **19**, 1924 (2004).
34. A. M. Rodriguez, G. Bozzolo and J. Ferrante, Surf. Sci. **289**, 100 (1993).
35. D. J. Chadi, Phys. Rev. Lett. **43**, 43 (1979).
36. H. Lüth, Solid Surfaces, Interfaces and Thin Films, Springer (2001).
37. H. Lüth, *Solid Surfaces, Interfaces and Thin Films* 4th ed. (Springer-Verlag, Berlin, 2001).
38. P. A. C. V.E.Henrich, The Surface Science of Metal Oxides, Cambrige, (2000).
39. P. W. Tasker, Journal of Physics C-Solid State Physics **12**, 4977 (1979).
40. P. W. Tasker, Surf. Sci. **87**, 315 (1979).
41. A. Pojani, F. Finocchi, J. Goniakowski and C. Noguera, Surf. Sci. **387**, 354 (1997).
42. C. Noguera, J. Phys.-Condes. Matter **12** (31), R367 (2000).
43. J. Goniakowski, F. Finocchi and C. Noguera, Rep. Prog. Phys. **71**, 016501 (2008).
44. C. L. Pang, R. Lindsay and G. Thornton, Chem. Soc. Rev. **37**, 2328 (2008).
45. U. Diebold, Surf. Sci. Rep. **48**, 53 (2003).
46. A. L. Linsebigler, G. Q. Lu and J. T. Yates, Chemical Reviews **95** (3), 735-758 (1995).
47. R. Lindsay, A. Wander, A. Ernst, B. Montanari, G. Thornton and N. M. Harrison, Phys. Rev. Lett. **94**, 246102 (2005).

48. G. Cabailh, X. Torrelles, R. Lindsay, O. Bikondoa, I. Joumard, J. Zegenhagen and G. Thornton, Phys. Rev. B **75**, 241403 (2007).
49. O. Bikondoa, C. L. Pang, R. Ithnin, C. A. Muryn, H. Onishi and G. Thornton, Nat. Mater. **5**, 189 (2006).
50. E. Bertel, R. Stockbauer and T. E. Madey, Phys. Rev. B **27**, 1939 (1983).
51. U. Diebold, J. F. Anderson, K. O. Ng and D. Vanderbilt, Phys. Rev. Lett. **77**, 1322 (1996).
52. A. Ohtomo and H. Y. Hwang, Nature **427**, 423 (2004).
53. H. Ma, H. L. Yip, F. Huang and A. K. Y. Jen, Adv. Funct. Mater. **20**, 1371 (2010).
54. M. Marezio, Acta Crystallographica **20**, 723 (1966).
55. G. B. Gonzalez, T. O. Mason, J. P. Quintana, O. Warschkow, D. E. Ellis, J. H. Hwang, J. P. Hodges and J. D. Jorgensen, J. Appl. Phys. **96**, 3912 (2004).
56. S. Z. Karazhanov, P. Ravindran, P. Vajeeston, A. Ulyashin, T. G. Finstad and H. Fjellvag, Phys. Rev. B **76**, 075129 (2007).
57. M. Sorescu, L. Diamandescu, D. Tarabasanu-Mihaila and V. S. Teodorescu, J. Mater. Sci. **39**, 675 (2004).
58. R. L. Weiher and R. P. Ley, J. Appl. Phys. **37**, 299 (1966).
59. H. Kostlin, R. Jost and W. Lems, Phys. Status Solidi A-Appl. Res. **29**, 87 (1975).
60. I. Hamberg, C. G. Granqvist, K. F. Berggren, B. E. Sernelius and L. Engstrom, Phys. Rev. B **30**, 3240 (1984).
61. K. L. Chopra, S. Major and D. K. Pandya, Thin Solid Films **102**, 1 (1983).
62. P. A. Cox, W. R. Flavell and R. G. Egdell, J. Solid State Chem. **68**, 340 (1987).
63. V. Christou, M. Etchells, O. Renault, P. J. Dobson, O. V. Salata, G. Beamson and R. G. Egdell, J. Appl. Phys. **88**, 5180 (2000).
64. Y. Gassenbauer, R. Schafranek, A. Klein, S. Zafeiratos, M. Havecker, A. Knop-Gericke and R. Schlogl, Phys. Rev. B **73**, 245312 (2006).
65. C. McGuinness, C. B. Stagarescu, P. J. Ryan, J. E. Downes, D. F. Fu, K. E. Smith and R. G. Egdell, Phys. Rev. B **68**, 165104 (2003).
66. I. Hamberg, C. G. Granqvist, K. F. Berggren, B. E. Sernelius and L. Engstrom, Phys. Rev. B **30**, 3240 (1984).
67. E. A. Albanesi, S. J. Sferco, I. Lefebvre, G. Allan and M. Lannoo, Solid State Commun. **86**, 27 (1993).
68. H. Odaka, S. Iwata, N. Taga, S. Ohnishi, Y. Kaneta and Y. Shigesato, Jpn. J. Appl. Phys. Part 1 - Regul. Pap. Short Notes Rev. Pap. **36**, 5551 (1997).
69. I. Tanaka, M. Mizuno and H. Adachi, Phys. Rev. B **56**, 3536 (1997).
70. O. N. Mryasov and A. J. Freeman, Phys. Rev. B **64**, 233111 (2001).

71. P. Erhart, A. Klein, R. G. Egdell and K. Albe, Phys. Rev. B **75**, 153205 (2007).
72. Y. Dou, R. G. Egdell, D. S. L. Law, N. M. Harrison and B. G. Searle, J. Phys.-Condes. Matter **10**, 8447 (1998).
73. J. E. Jaffe, R. Pandey and A. B. Kunz, Phys. Rev. B **43**, 14030 (1991).
74. L. F. J. Piper, L. Colakerol, P. D. C. King, A. Schleife, J. Zuniga-Perez, P. A. Glans, T. Learmonth, A. Federov, T. D. Veal, F. Fuchs, V. Munoz-Sanjose, F. Bechstedt, C. F. McConville and K. E. Smith, Phys. Rev. B **78**, 165127 (2008).
75. L. F. J. Piper, A. DeMasi, K. E. Smith, A. Schleife, F. Fuchs, F. Bechstedt, J. Zuniga-Perez and V. Munoz-Sanjose, Phys. Rev. B **77**, 125204 (2008).
76. P. D. C. King, T. D. Veal, A. Schleife, J. Zuniga-Perez, B. Martel, P. H. Jefferson, F. Fuchs, V. Munoz-Sanjose, F. Bechstedt and C. F. McConville, Phys. Rev. B **79**, 205205 (2009).
77. P. D. C. King, T. D. Veal, F. Fuchs, C. Y. Wang, D. J. Payne, A. Bourlange, H. Zhang, G. R. Bell, V. Cimalla, O. Ambacher, R. G. Egdell, F. Bechstedt and C. F. McConville, Phys. Rev. B **79**, 205211 (2009).
78. P. Erhart, A. Klein, R. G. Egdell and K. Albe, Phys. Rev. B **75**, 153205 (2007).
79. I. Mahboob, T. D. Veal, C. F. McConville, H. Lu and W. J. Schaff, Phys. Rev. Lett. **92**, 036804 (2004).
80. M. Noguchi, K. Hirakawa and T. Ikoma, Phys. Rev. Lett. **66**, 2243 (1991).

Chapter 2:

Background to Experimental Techniques

Throughout this thesis, molecular beam epitaxy is used to grow In_2O_3 and tin-doped indium oxide (ITO) thin films on single crystal substrates. The techniques of X-ray diffraction, transmission electron microscopy, scanning tunnelling microscopy/atomic force microscopy, low electron energy diffraction and photoemission spectroscopy are used extensively to characterize the structural and electronic properties of the films. This chapter presents a brief introduction to the background of these techniques.

2.1 Molecular Beam Epitaxy

2.1.1 *Concepts of Thin Film Growth*

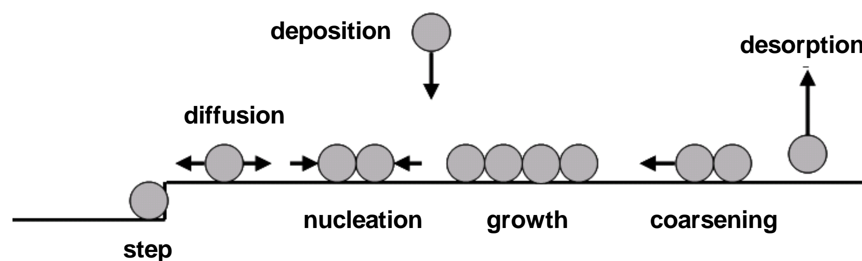

Figure 2.1. Schematic illustrations of atomic processes in film growth on a solid surface.

The epitaxial growth of thin films on lattice mismatched surfaces is a complex process largely governed by the competition between kinetics and thermodynamics.[1-3] Figure 2.1 illustrates the individual atomic processes that occur during material growth on substrate surfaces. Once an atom has condensed from the vapor phase on the surface, there are three things that may happen: (i) it can form a strong bond to the surface where it is trapped, particularly at special sites likes steps or other defects; (ii) it may diffuse across a terrace to find an energetically preferred location prior to being trapped, i.e. this process leading to nucleation, coarsening and thin film growth; or (iii) it may evaporate away from the surface i.e. desorb. In all these processes, characteristic activation energies have to be overcome,[4] i.e. the number of atoms being able to participate in a particular process is given by an Arrhenius-type exponential law. The diffusion rate, for example, is given by:

$$D \propto \exp -(E_{act}/kT)$$

where E_{act} is the activation energy for diffusion, k is Boltzmann's constant, and T is the growth temperature. The corresponding activation energies for adsorption or diffusion depend on the atomic details of the particular process. High substrate temperatures during growth in general allow activation barriers to be overcome. If surface diffusion is facile more than one atom will be incorporated into each nucleation centre.

The reduction of the total free energy of the system is the overall driving force for nucleation and growth. The condensation from the gas phase into the solid phase reduces the overall Gibbs free energy. However, this energy reduction is counter balanced by the introduction of surface and interface energies. Thus the change of total energy resulting from the formation of a nucleation centre, ΔG, is given by:

$$\Delta G = \Delta\mu_v + \Delta\mu_s = (4/3)\pi r^3 \Delta G_v + 4\pi r^2 \gamma$$

where $\Delta\mu_v$ is the change of Gibbs cohesive free energy which is negative and decreases as the cube of the radius of nucleation centre r^3, $\Delta\mu_s$ is surface free energy, which is positive and increases as r^2. Thus ΔG passes through a maximum, denoted by ΔG^*, at some value of $r = r^*$. This nucleus with the maximum ΔG is called the critical nucleus. Only nucleus larger than the critical size can be stable and further grow into large islands. In the atomistic view, the high concentration of adatoms or monomers diffusing on the surface initially results in a high probability of island nucleation. The density of nucleation centres continues to increase with coverage, until the probability of a diffusing adatom finding an island is much higher than the probability of finding another adatom. The number of nucleation events is substantially reduced as the adatom diffusion length becomes large relative to the average island spacing. Thus the majority of events occurring involve adatoms attaching to the existing islands, hence defining the aggregation regime. With further growth within the aggregation regime, the island density remains relatively constant while the islands continue to grow in size. Eventually, the islands will begin to merge with each other and one enters into the coalescence regime, which is characterized by a decrease in the island density with increasing coverage.

As an alternative to the atomistic approach, a microscopic point of view can provide a phenomenological description of thin film growth.[5] In general, three markedly different growth modes can be distinguished, depending on the surface and interfacial energies as well as lattice mismatch between the deposited materials and substrate. Figure 2.2 illustrates the three growth modes. When the lattice mismatch is small and the interface binding is strong, the film grows in a layer-by-layer (Frank-Van der Merwe) mode. If the interface bonding is weak, the deposited material grows in 3D islanding

(Volmer-Weber) mode. If the interface binding is strong but the lattice mismatch is relatively large, the film will grow in the layer-by-layer mode initially, followed by 3D-islanding. This process is known as the Stranski-Krastanov (S-K) mode. The initial wetting layer grows pseudomorphically with the same lattice constant of substrate, with a misfit strain which can be accommodated elastically below a critical thickness. The strain energy increases with film thickness. At certain point, it becomes energetically favourable to generate misfits and threading dislocations to relieve the build-up of strain within the film. The growth temperature on the other hand provides thermal energy for atom diffusion and defect formation.

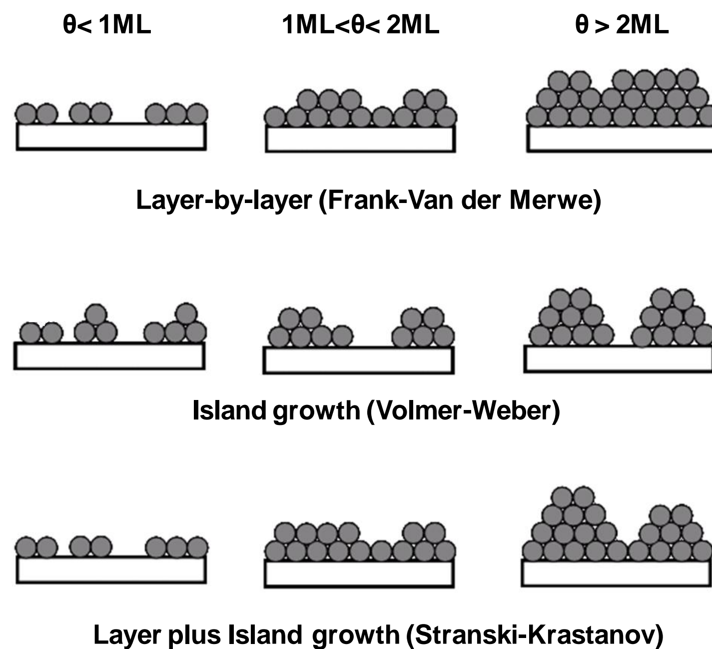

Figure 2.2. Schematics of of three growth modes of a film for different coverage (θ) regimes.

In dynamic material growth processes, the thin-film is not in general under thermodynamic equilibrium.[2, 4] Thus, one needs to consider the kinetics of processes occurring on the surface, including the adsorption, diffusion, desorption, coarsening and nucleation of atoms, as well as the inter-layer migration of the atoms, as discussed above.

The former factors can affect the lateral uniformity of the film, while the latter factor can lead to a 2-D layer-by-layer or a 3-D growth mode. If the material favours a 2-D growth mode, sufficient inter-layer atomic transport is necessary. An important quantity this process is the Ehrlich-Schwoebel barrier (ES), which is the additional barrier for an adatom to jump down (or up) a step edge. If the ES barrier is large, it is hard for atoms to transport between layers. This will result to the 3-D growth. On the other hand, if the ES barrier is small, it is easy for atoms to undergo atomic inter-layer-transport. This will result in 2-D growth. Thus three kinetically controlled growth modes are step-flow growth, layer-by-layer growth, and multilayer growth.[2]

In Chapter 4 and 5, the basic concepts on thin film growth will be applied to guide the growth of In_2O_3 nanostructures and thin films, considering both the kinetic and thermodynamic (surface/interface and strain energies) factors.

2.1.2 Molecular beam epitaxy

Molecular beam epitaxy (MBE) is a versatile technique for epitaxial growth of thin films of semiconductors, metals and insulators by thermal evaporation of molecular or atomic beams in ultra-high vacuum (UHV) environments.[6] An important aspect of MBE is that the slow growth rate usually employed allows one to steer the epitaxial growth layer by layer with nearly atomic precision.

Figure 2.3 show a simple schematic diagram of an MBE growth chamber. Ultra-pure elements (99.99% purity) such as In and Sn are thermally heated in Knudsen effusion cells (K-cells) until they begin to slowly evaporate into gaseous molecular or atomic beam directed onto the substrate. In an oxide MBE system there is in addition an atomic oxygen source typically involving an oxygen plasma. The gaseous elements then condense on the substrate where they may react with each other, leading to epitaxial

growth of a compound overlayer. Reflection high energy electron diffraction (RHEED) is often used for monitoring the growth of the crystal layers. The oscillation of the RHEED signal exactly corresponds to the time needed to grow a monolayer and the diffraction pattern gives direct indication over structures of the surface. A computer controls shutters in front of each K-cells, allowing precise control of the thickness of each layer, down to a single layer of atoms. Intricate structures of layers of different materials may be fabricated this way. Such control has allowed the development of nanostructures where the electrons can be confined in space, giving quantum wells, nanorods or quantum dots.[7, 8]

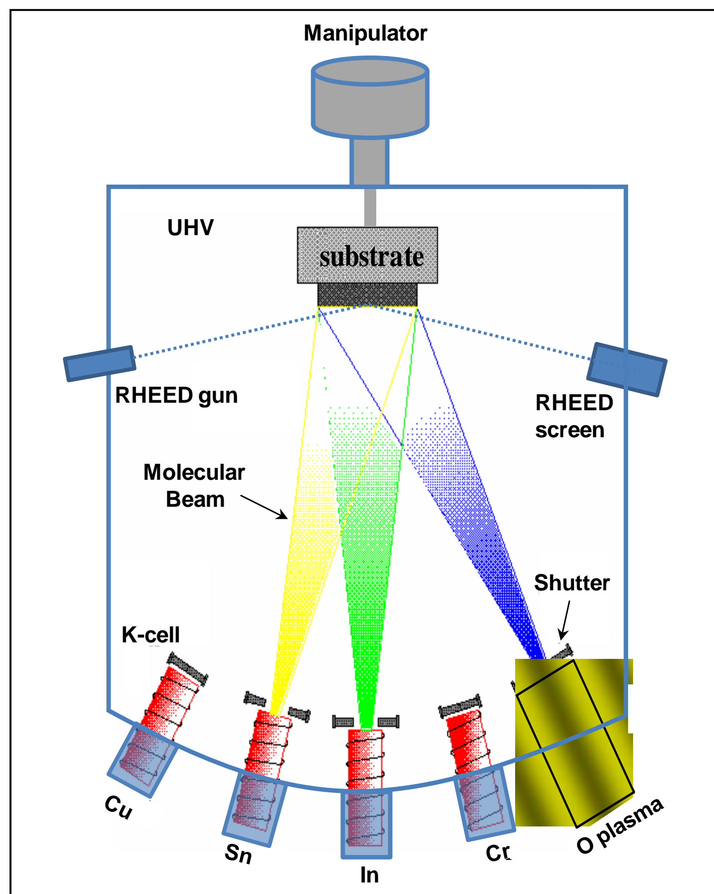

Figure 2.3. Schematic illustrations of molecular beam epitaxy (MBE) systems. (Image adapted from *http://www.nber.org/~tanwinc/DissertationDefense/1_Introduction/mbe.html*).

2.2 X-ray Diffraction

X-ray diffraction (XRD) is a non-destructive technique used to find the thickness, lattice parameters, strain and defect densities of epitaxial thin films and device structures.[9-11] It involves probing a crystal with X-ray radiation having a wavelength λ (typically ranging from 0.7 to 2 Å) of the same order as the crystal lattice spacings. X-rays are generated by bombarding a metal (typically Cu) with electrons in a vacuum tube or high intensity. Alternatively X-rays may be derived from a synchrotron. These X-rays are elastically scattered by the electrons surrounding each atom in the crystal.

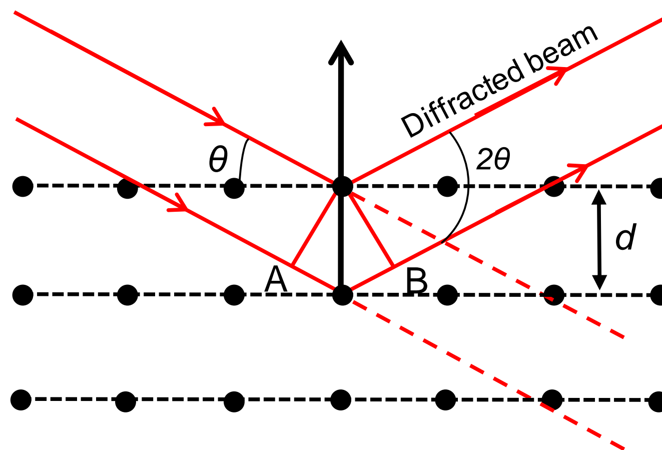

Figure 2.4. Schematic of the conditions required for Bragg diffraction to occur.

As shown in Figure 2.4 constructive interference occurs if the path length difference AB = $2d\sin\theta$ between the scattered X-rays is equal to $n\lambda$. This leads to the basis of Bragg's law which relates the lattice spacing to the angle (θ) of the incidence beam:

$$2d\sin\theta = n\,\lambda$$

where λ is the wavelength of the X-ray and θ is the angle at which incidence beam meets a crystal plane and d the interplanar spacing of a set of planes with Miller indices hkl.

2.3 Transmission Electron Microscopy

Electron microscopy exploits the short wavelength of high energy electrons to achieve spatial resolution superior to that of optical microscopy.[12] In transmission electron microscopy (TEM) electrons generated by thermionic emission are accelerated to a kinetic energy of around 100 keV or higher (up to 1 meV) and projected onto a very thin specimen (thickness less than 100 nm) by means of condenser lens system, as shown in Figure 2.5.

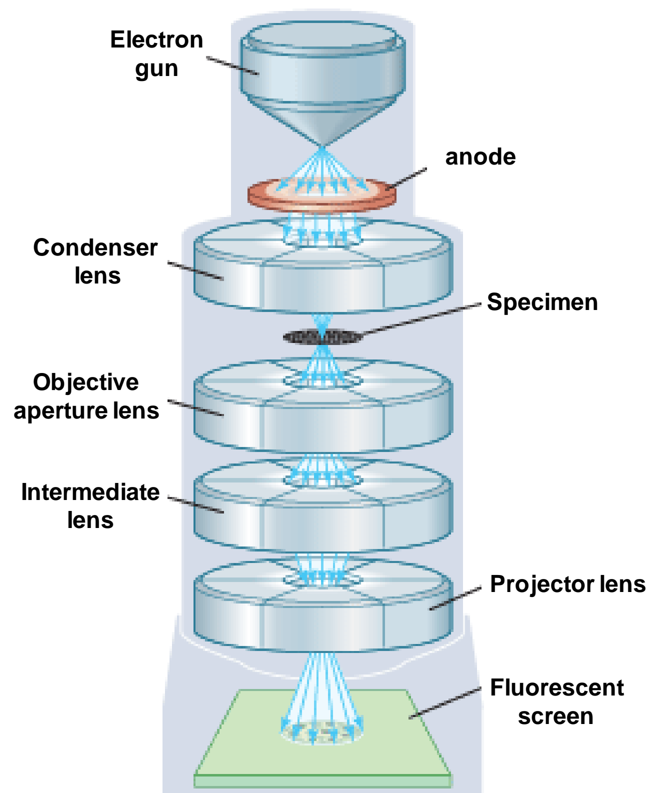

Figure 2.5. Layout of the components of transmission electron microscopy and basic work principles (Image from *http://www.britannica.com/EBchecked/media/110686/Transmission-electron-microscope*).

The electrons are scattered by the potentials associated with the periodic atoms in the specimen. A diffraction pattern can form after transmitting through the specimen. The pattern can be directly transformed into real space images by a series of electrostatic and magnetic lenses. The greatest advantages of TEM are the high magnification and its ability to provide both real space images and reciprocal space diffraction information from a single sample. The high magnification or resolution of TEM is a result of the small effective electron wavelengths λ, which is given by the de Broglie relationship:

$$\lambda = \frac{h}{\sqrt{2meV}}$$

where *m* and *e* are the electron mass and charge, *h* is Planck's constant, and *V* is the potential difference through which electrons are accelerated. For example, electrons with a kinetic energy of 100 keV have wavelengths of 0.037 Å. Typically, high voltage TEM instruments (e.g. 400 kV) can achieve a resolution better than 1 Å, which is limited by lense aberrations but is enough to obtain atomically resolved images of the sample. Thus TEM is the most powerful tool for investigation of the cross-sectional atomic structure of epitaxial interfaces. Figure 2.6 show high resolution cross-sectional TEM images of a $La_{0.7}Sr_{0.3}MnO_3/SrTiO_3$ superlattices grown by pulsed laser deposition. The atomic image in the right shows atomically sharp interfaces between the two materials.[13]

Selected-area diffraction (SAD) also offers a unique capability to determine crystal structures. In SAD, the condenser lens is defocused to produce parallel illumination at the specimen and a selected-area aperture is used to limit the diffraction volume. SAD patterns are often used to determine the Bravais lattice and lattice parameters of materials in a manner analogous to XRD.

One limitation of TEM is the difficulty in sample preparation which is critical to obtaining high resolution images. Samples need to be mechanically sliced and polished,

followed by ion milling to around 100 nm thick in order to achieve sufficient electron transmission. This process is very time consuming and requires significant efforts to accomplish. Optimal instrumental setting such as defocus, sample alignment and illumination are also important to get high resolution images.

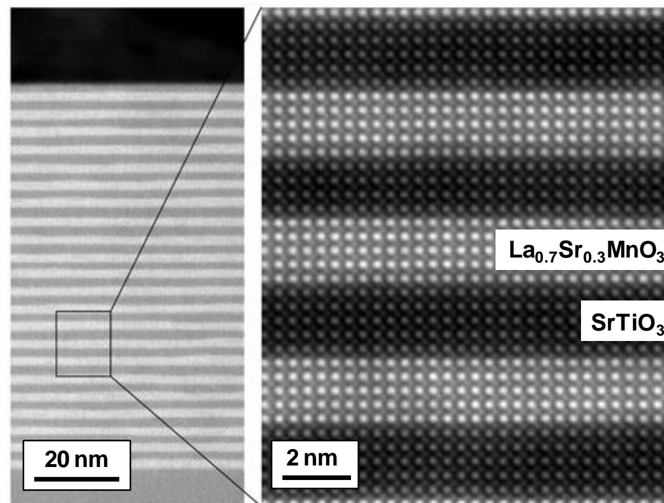

Figure 2.6. High resolution cross-sectional TEM images of a $La_{0.7}Sr_{0.3}MnO_3/SrTiO_3$ superlattices grown by pulsed laser deposition. The atomic image in the right shows atomically sharp interfaces between the two materials. (Images adapted from reference[13])

2.4 Scanning Probe Microscopy

Scanning Probe Microscopy (SPM) is a branch of microscopy that allows imaging of a surface with high resolution by recording the probe-surface interaction as a function of position during scanning a sharp probe over the surface.[14] In the early 1980's G. Binnig and H. Rohrer (Nobel Laureates in 1986) at the IBM Zürich Research Laboratory,[15] developed scanning tunnelling microscopy (STM) as a new technique for studying surface structure with atomic resolution. This invention was quickly followed by the development of a whole family of related techniques such as atomic force microscopy (AFM),[16] which together with STM have become the increasingly important in the field

of surface science in recent years, and opened up many new areas of science and engineering at the atomic and molecular level.

2.4.1. Scanning Tunnelling Microscopy (STM)

An STM system is usually based on a scanning tip, piezoelectric controlled *xyz* scanner, coarse sample-to-tip controller, vibration isolation system, and a computer for data storage and display.[14] The schematic drawing in Figure 2.7 shows the setup of a typical STM.[17]

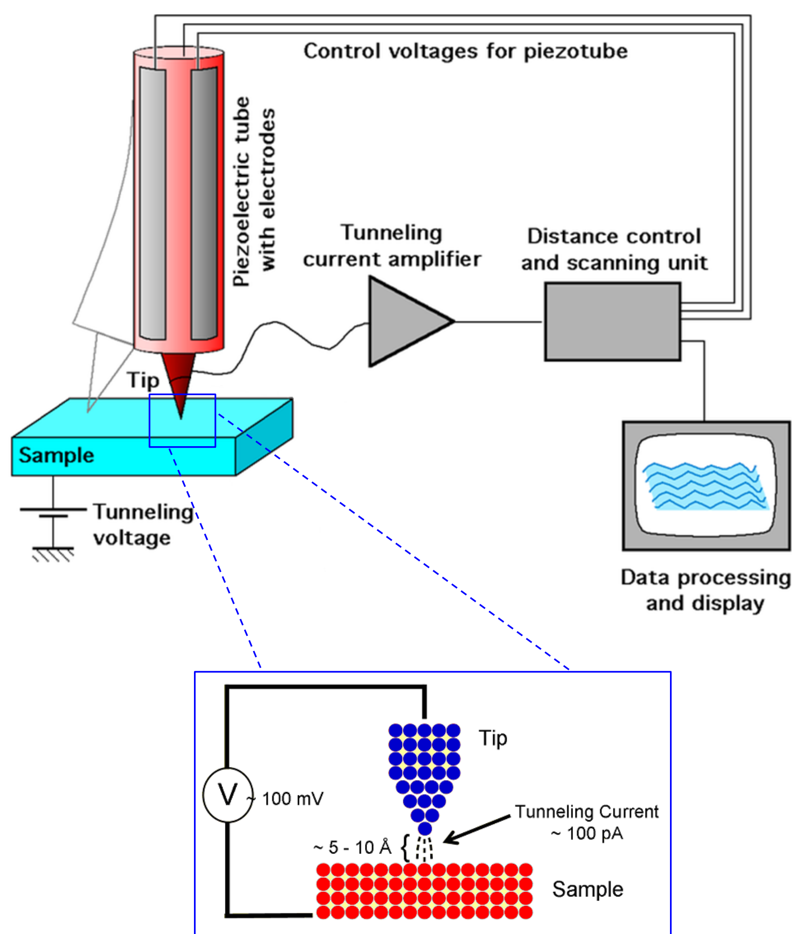

Figure 2.7. STM system setup and working principle, including an atomic sharp metallic tip mounted on a piezoelectric tube with electrodes, voltage control circuit, feedback control circuit, signal amplifier, data processing and display terminal and a sample. (Image from *http://www.iap.tuwien.ac.at/www/surface/stm_gallery/stm_schematic by M. Schmid, TU Wien*)[17]

STM is based on quantum mechanical tunnelling between a sharp tip and a conducting surface. The idea is to bring an atomically sharp metallic tip (usually an etched tungsten wire as shown in Figure 2.8) in close proximity (a few Å) to a conductive sample without actual physical contact. By applying a bias voltage (tens of mV to several V) between the tip and the sample, small tunnelling currents (0.01 nA-50 nA) can flow from the sample to the tip or vice versa (Figure 2.9).

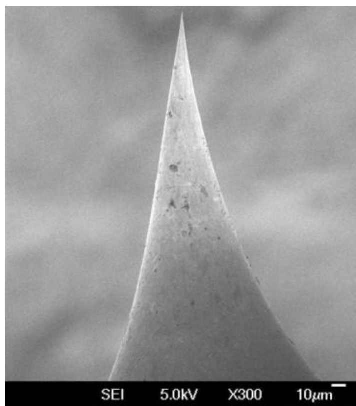

Figure 2.8. Scanning electron microscopy of a very sharp tungsten tip produced by electrochemical etching process in NaOH. (Imaged by S. Kushvaha and KHL Zhang in National University of Singapore)

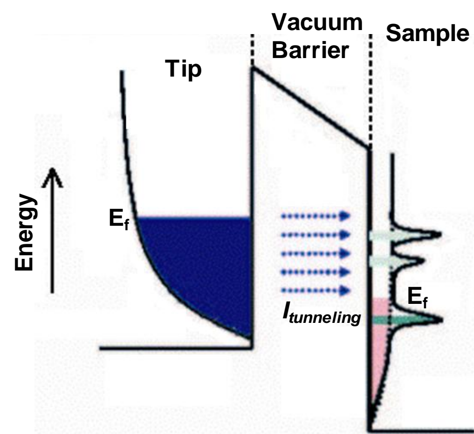

Figure 2.9. Energy level diagram between tip and sample where electrons tunnel from tip to empty state of the sample. (Image: http://www.physics.berkeley.edu/research/crommie/research:stm)

If the distance between the tip and sample is d and a bias voltage V is applied, the tunnelling current I can be written as:

$$I = e^{-kd} \int_0^{eV} d\varepsilon \; \rho_{Sample}(\varepsilon + E_f - eV)$$

where k is a constants; ρ_{sample} is the local density of states of the sample. It can be seen that the current I decreases exponentially with d, which leads to the high resolution of STM in the z direction. The precise positioning and scanning of the tip is often controlled by a piezoelectric tube, which can expand or contract in response to applied electric fields. The tube scanner moves the tip in the z direction for control of the tip-sample

distance (*d*) and in the *x* and *y* directions for lateral scanning. The lateral (*x* and *y* directions) resolution is typically about 1 Å whereas a vertical resolution down to 0.01 Å can be achieved. Figure 2.10 shows a typical atomic scale image of an ultra thin film of NaCl deposited on Ag surface.

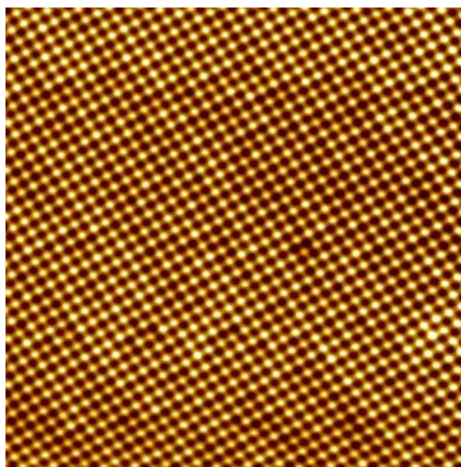

Figure 2.10. Atomic structure of NaCl on Ag(111) surface (Image size: 20 nm × 20nm; Parameters: V_{tip}= 2.6 V; I_t = 0.2 nA) (Imaged by KHL Zhang in National University of Singapore)

There are two approaches to STM imaging involving the *constant current* and *constant height* modes, as illustrated in Figure 2.11. In the *constant current mode* a feedback system keeps the tunnelling current at a preset constant value. If lateral motion leads the current to increase, the distance (*d*) between tip and sample will increase in response to maintain a constant tunnelling current. Conversely if the current begins to fall as a result of lateral motion, the feedback loop will reduce the tip-sample distance (*d*). Thus the tip is scanned line by line above the surface and an image of the surface is built up. In this way the image of the sample surface can be obtained. In the *constant height mode* the vertical position of the tip is not changed, which is equivalent to a slow or disabled feedback. The current as a function of lateral position is used to construct a surface image. This mode is only appropriate for atomically flat surfaces as otherwise a tip crash

would be inevitable. One of its advantages is that it can be used at high scanning frequencies: images may be acquired up to 10 kHz. In comparison, the scanning frequency in the constant current mode is usually less than 1 image per second.

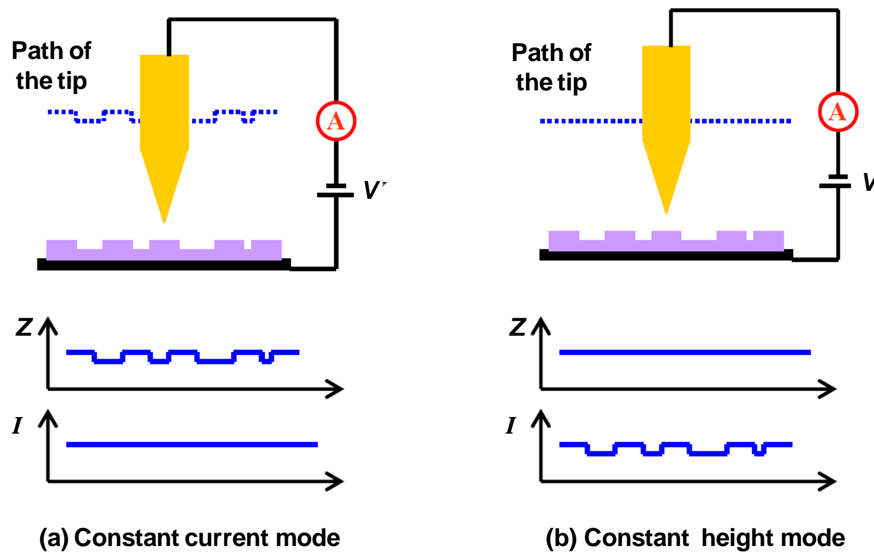

Figure 2.11. Two operation modes in STM system: (a) constant current mode and (b) constant height mode. (Image taken from reference[18])

It has to be mentioned that the image cannot be simply interpreted as a topographic map since the tunnelling current depends on the local density of states of the sample surface as well as the tip-sample separation d . While the dependence of current on position reveals the geometric structure of the surface, the dependence of current on voltage gives information about electronic structure. As shown above, the tunnelling current is approximately proportional to the integral of all the electronic states between the Fermi Energy and the tunnelling bias. The first derivative of the tunnelling current with respect to voltage (dI/dV) is thus proportional to the local density of electronic states below the tip, at the given tunnelling voltage:

$$\frac{dI}{dV} \propto \rho_{sample}(E_f - eV)$$

Thus by measuring *dI/dV* as a function of voltage, one can probe the electronic states at that particular point on the surface, giving rise to scanning tunnelling spectroscopy (STS). The advantage of STS over other measurements of the density of states lies in its ability to make extremely local measurements: for example, the density of states at an impurity site can be compared to the density of states far from impurities

2.4.2. Atomic Force Microscopy (AFM)

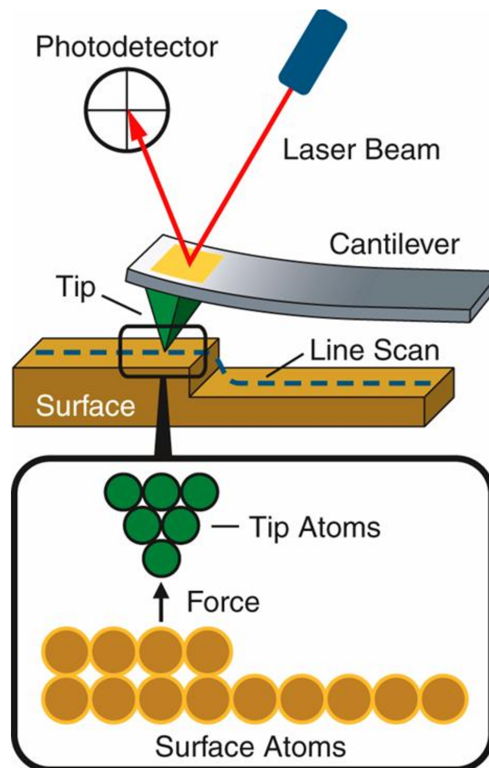

Figure 2.12. Schematic of setup and working principle of AFM. (Image taken from http://www.home.agilent.com/agilent/editorial.jspx?cc=IT&lc=ita&ckey=1774141&nid=-33986.0&id=1774141)

AFM is another scanning probe microscopy which was invented by Binnig, Quate, and Gerber in 1985 soon after STM was established.[19] The important difference between the AFM and the STM is that the AFM does not record the tunnelling current, but the small force between the tip and the surface.[16] AFM overcomes a basic drawback of STM that it can only image conducting or semiconducting surfaces. AFM, however, has the advantage of being able to image almost any type of surface, including polymers, ceramics, composites, glass, and biological samples.

Figure 2.12 shows the basic principle of AFM. Typically, the AFM tip is attached to a very small leaf spring, the cantilever, which is typically silicon or silicon nitride with a low spring constant. When a tip is brought into the proximity of a sample surface, forces between tip and surface lead to the deflection of the cantilever according to Hooke's law. The deflection is measured using a laser spot reflected from the top surface of the cantilever into an array of photodiodes. Depending on the situation, forces that are measured in AFM include the mechanical contact force, van der Waals forces, magnetic forces (magnetic force microscope, MFM), chemical bonding, electrostatic forces, *etc.* The xyz position and scanning of the tip is controlled by a piezoelectric tube, as in STM. There are three primary AFM operation modes: *contact mode*, *non-contact mode* and *tapping mode*.

Contact mode

As the name suggests, in *contact mode* tip scans the sample in close contact with the surface as the scanning proceeds. “Contact” represents the repulsive regime of the intermolecular force with a mean value of 10^{-9} N. The cantilever is "dragged" across the surface of the sample and the contours of the surface are measured directly using the deflection of the cantilever. One of the drawbacks of the tip remaining in contact with the

sample is that large lateral forces can be exerted on the sample as the tip is dragged over the specimen. These large forces can result in deformed images and damaged samples. However this mode works quite well for rigid materials with rough surface.

Non-contact mode

In this mode, the tip does not contact the sample surface. Instead the cantilever is forced to oscillate at a frequency slightly above its resonant frequency with an amplitude of a few nanometers (<10 nm). The resonant frequency of cantilever is reduced by van der Waals forces when the tip is close to the surface. The decrease in resonant frequency causes the amplitude of oscillation to decrease. This variation in resonant frequency is coupled with a feedback loop system to maintain a constant oscillation amplitude or frequency by adjusting the average tip-to-sample distance. Measuring the tip-to-sample distance at each (x,y) data point allows the scanning software to construct a topographic image of the sample surface. *Non-contact mode* AFM does not suffer from tip or sample degradation effects that are sometimes observed after taking numerous scans with contact AFM. This makes non-contact AFM preferable to contact AFM for measuring soft samples.

Tapping mode

In *tapping mode*, the cantilever is also driven to oscillate at near its resonance frequency similar to *non-contact mode*. However, the amplitude of this oscillation is typically in the range from 100 to 200 nm, which much greater than a range of around 10 nm used in the non-contact mode. The tip lightly taps on the sample surface during scanning, making direct contact with the surface at the bottom of its swing. The interaction of forces acting on the cantilever when the tip comes close to the surface also cause the amplitude of this

oscillation to decrease as the tip gets closer to the sample. A *tapping* image is therefore produced by imaging the force of the intermittent contacts of the tip with the sample surface. Because the contact time is a small fraction of its oscillation period, the average lateral forces are reduced dramatically.

The choice of which mode to use is based on the surface characteristics of interest and on the hardness/stickiness of the sample. *Contact mode* is most useful for hard surfaces; a tip in contact with a surface, however, is subject to contamination from removable material on the surface. Excessive force in contact mode can also damage the surface or blunt the probe tip. *Tapping mode* is well-suited for imaging soft biological specimen and for samples with poor surface adhesion (DNA and carbon nanotubes). *Non-contact mode* is another useful mode for imaging soft surfaces, but its sensitivity to external vibrations and the inherent water layer on samples in ambient conditions often causes problems in the engagement and retraction of the tip. Throughout this thesis, *contact mode* was used to study the surface morphology of In_2O_3 epilayers.

2.5 Low Energy Electron Diffraction (LEED)

Low Energy Electron Diffraction (LEED) is used as the standard technique to check the crystallographic quality of a surface. A typical experimental arrangement used in a LEED experiment is illustrated in Figure 2.13. An electron gun is used to produce a well collimated mono-energetic electron beam. Usually the energies of electrons range from 20 eV to 500 eV with de Broglie wave-lengths from 2.74 Å to 0.55 Å, which is optimal for crystallographic studies on the surfaces. Moreover for electrons within this energy range, the inelastic mean free path is 5 Å to 10 Å, which are equivalent to about 3-5

atomic layers. Hence LEED is an excellent surface sensitive tool for crystallographic studies.

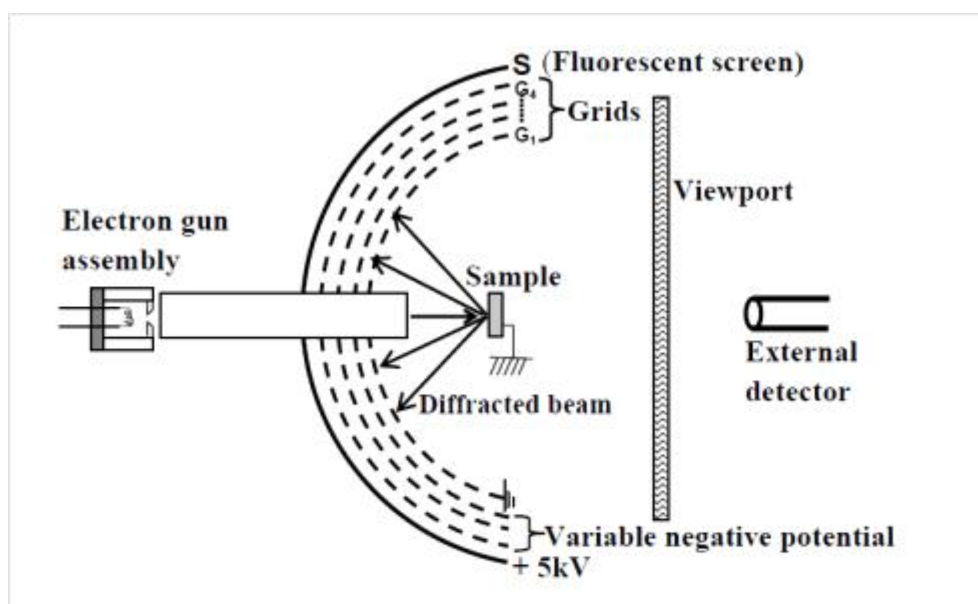

Figure 2.13. Schematic drawing of four grids LEED device. (Image adapted from reference[1])

The electrons beam is usually incident normally on the surface. These electrons are scattered mainly from the first few layers of the crystalline sample following the Bragg diffraction equation: $a sin\theta = n\lambda$, where a is the periodicity of the pattern, θ is the angle of diffraction, n is the diffraction order, and λ is the incident electron wavelength. The backscattered electrons are of two types; elastically scattered electrons forming a set of diffracted beams which create the LEED pattern, and inelastically scattered electrons, which may make up 99% of the total flux, but they are not required. After reaching the first grid G_1, which is earthed, the elastically scattered electrons are accelerated towards the fluorescent screen S, which carries a high positive potential (of the order of 5 kV). This provides the electrons in the diffracted beams with enough energy to excite the fluorescence in the screen, so that a pattern of bright LEED spots is seen. The grids G_2,

G_3 and G_4 are held at an adjustable negative potential and are used to reject the majority of the electron flux, which is made up of inelastically scattered electrons, and which otherwise contribute to a bright, diffuse background across the whole of the LEED screen. The potential on these grids is adjusted to minimize the diffuse background to the LEED pattern. The LEED pattern displayed on the phosphor screen gives information on the surface reconstruction in reciprocal space and the atomic structures of reconstruction can be determined. The LEED pattern must exhibit sharp spots with high contrast and low background intensity. Random defects or crystallographic imperfections can broaden the LEED pattern spots and increase the background intensity due to scattering from these defects. Figure 2.14 presents an example of using LEED to study the structure of Bi on Ag(111), where a $(\sqrt{3} \times \sqrt{3})R30°$ Bi_2Ag alloy superstructure was indentified embedded in Ag(111) lattice.[20]

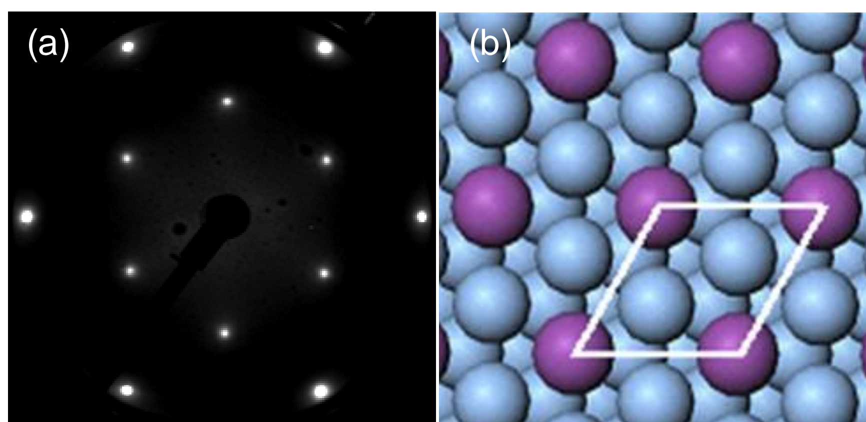

Figure 2.14. (a) LEED pattern (with an electron beam energy of 42 eV) of the $(\sqrt{3} \times \sqrt{3})R30°$ superstructure of Bi embedded in Ag(111) lattice; (b) corresponding schematic model: Bi (pink ball) and Ag(navy ball). (Figure by KHL Zhang[19])

LEED may be used in one of two ways: qualitatively and quantitatively.[21] In qualitative analysis, the diffraction pattern is recorded and analysis of the spot positions yields information on the size, symmetry and rotational alignment of the surface unit cell with respect to the substrate unit cell. The inspection of the LEED pattern gives a qualitative picture of the surface periodicity i.e. the size of the surface unit cell and to a certain degree of surface symmetries. A more quantitative analysis of LEED experimental data can be achieved by analysis of so-called I-V curves, which are measurements of intensity curves from diffracted spots as a function of incident electron energy. The I-V curves can be recorded by using a CCD camera connected to computer controlled data handling. The experimental curves are then compared to computer calculations based on the assumption of a particular model structure. These highly demanding calculations involve multiple scattering of the incident electrons: important parameters in the calculations are the amplitudes and phase shifts produced by scattering from individual atoms as well as the amplitudes of thermal oscillations of the atoms as reflected in Debye temperatures. The model is changed in an iterative process using the so-called Tesnor LEED code until a satisfactory agreement between experimental and theoretical curves is achieved. A quantitative measure for this agreement is the so called *reliability*- or R-factor. A commonly used reliability factor is the one proposed by Pendry, the so-called R_P-factor.[22] In this approach emphasis is given to fitting the positions of maxima and minima in the individual I/V curves, rather than the intensities of the maxima and minima. Specifically the Pendry R factor considers logarithmic derivatives of the intensity of a LEED beam as a function of energy $I(V)$ [22]:

$$L(V) = \frac{d(log_e I(V))}{dV}$$

and introduces a so-called Y function defined by:

$$Y(V) = \frac{L(V)^{-1}}{L(V)^{-2} + V_{oi}^2}$$

where V_{oi} is the imaginary part of the electron self energy which determines the widths of peaks in LEED I/V curves. The Y function is an oscillating function which can take both positive and negative values. The Pendry R_P function is then defined by[22]:

$$R_P = \sum_g \frac{\int_{V_{g1}}^{V_{g2}} \{Y(V)_g^{th} - Y(V)_g^{exp}\}^2 \, dV}{\int_{V_{g1}}^{V_{g2}} \{[Y(V)_g^{th}]^2 + [Y(V)_g^{exp}]^2\} dV}$$

where the summation is taken over g LEED beams; V_{g1} and V_{g2} define the energy range of each beam; and the superscripts exp and th denote experiment and theory. If R_p=0 there is perfect correlation between the experimental and theoretical I-V curves. R_p=1 means that experiment and theory are uncorrelated. The lower the final R_p factor achieved, the more reliable is the structural determination. In generally $R_p < 0.2$ is considered as a good agreement, $0.2 < R_p < 0.3$ is considered mediocre and $0.3 < R_p < 0.5$ is considered a bad agreement.

2.6 Photoelectron Spectroscopy (PES)

2.6.1 Introduction to PES

Photoemission spectroscopy (PES), also known as photoelectron spectroscopy, involves measurement of the kinetic energy (E_k) of electrons emitted from solids, gases or liquids under irradiation with fixed frequency high energy photon.[23] Since its invention by Kai

Siegbahn (Nobel Prize 1981),[24] it has been established as one of the most important methods for the study the chemical and electronic structures of molecules, solids and surfaces. Thus it is also the central technique used to study the electronic structures of (Sn-) In_2O_3 thin films in this work.

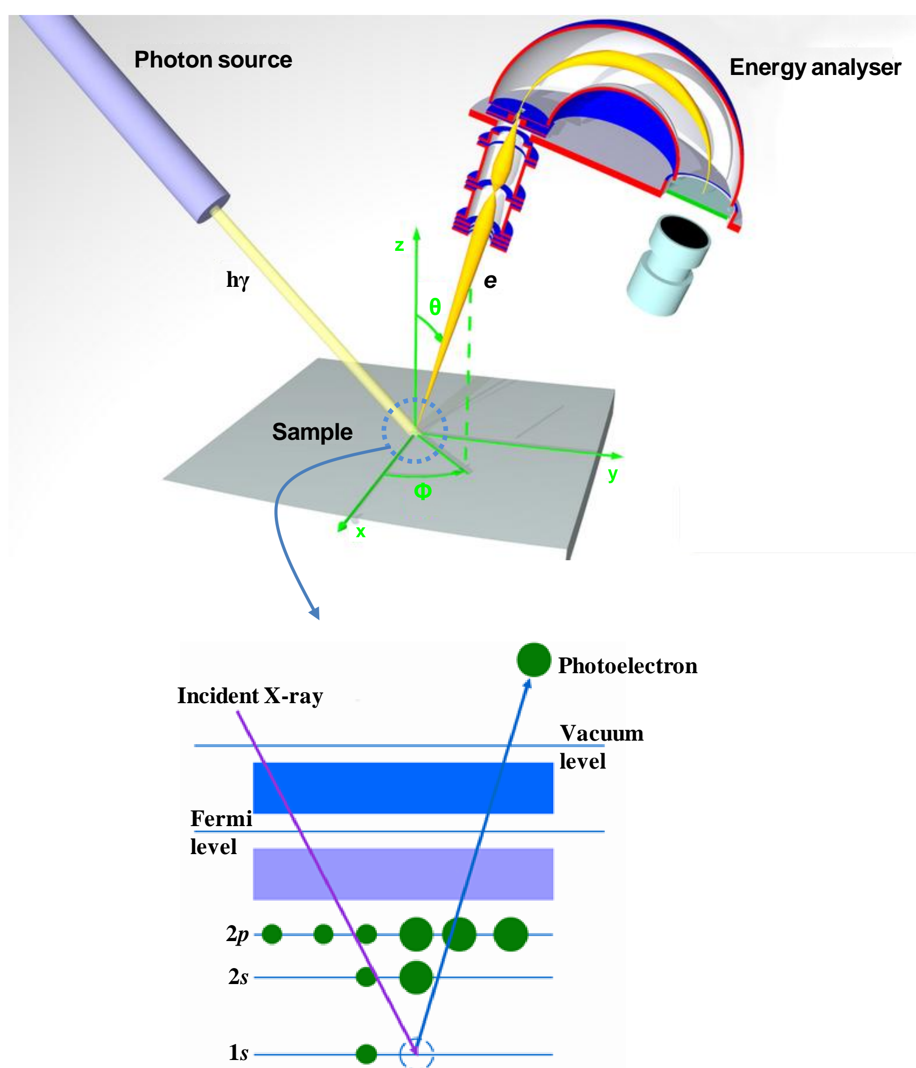

Figure 2.15. Schematic representation of PES showing the angle of photoelectron emission referenced to the sample coordinate system (top) and photoemission from core and valence states (bottom). (Image: http://en.wikipedia.org/wiki/Photoemission_spectroscopy)

At its simplest, the fundamental principle of PES is based on the well-known photoelectric effect, first discovered by Hertz in 1887 and explained by Einstein in 1905 (Noble prize 1921),[25] whereby an electron is emitted from a solid upon light-matter interaction. As shown schematically in Figure 2.15 a material is illuminated with a flux of photons with a specific energy (designated hγ in this figure, although more conventionally the photon energy is designated as hν) from an x-ray tube, gas discharge lamp or a synchrotron radiation source. The electrons in the materials that occupy a certain initial energy state (E_i) can absorb the photon and are excited as free electrons by the photoelectric effect. The photoelectrons are then analyzed with respect to their kinetic energy (E_k) and their momentum $\boldsymbol{p}$ in an electrostatic analyzer.

The relationship between E_k and binding energy (E_b) of emitted photoelectrons can be expressed according to energy conservation as:

$$E_b = h\gamma - E_k - \emptyset$$

where $\emptyset$ is the spectrometer work function, assuming the sample and spectrometer share the same ground. The binding energy relative to the Fermi energy E_b is given by the energy difference of total energies between the final state N-1 electrons after ejection of the photoelectron and the initial N electron ground state of the system:

$$E_b = E_{f,tot\,(N-1)} - E_{i,tot\,(N)}$$

The momentum $\boldsymbol{p}$ of the photoemitted electron is determined from its kinetic energy by:

$$E_k = \frac{p^2}{2m}$$

$$p = \sqrt{2mE_k}$$

The direction of momentum is obtained from polar (θ) and azimuth (φ) angles of the electron detected.

Figure 2.16 shows schematically the relation between energy levels and electron distribution in a solid state sample, which consists of core levels and a valence band. Thus PES basically reflects the electronic eigenstates of the solid.

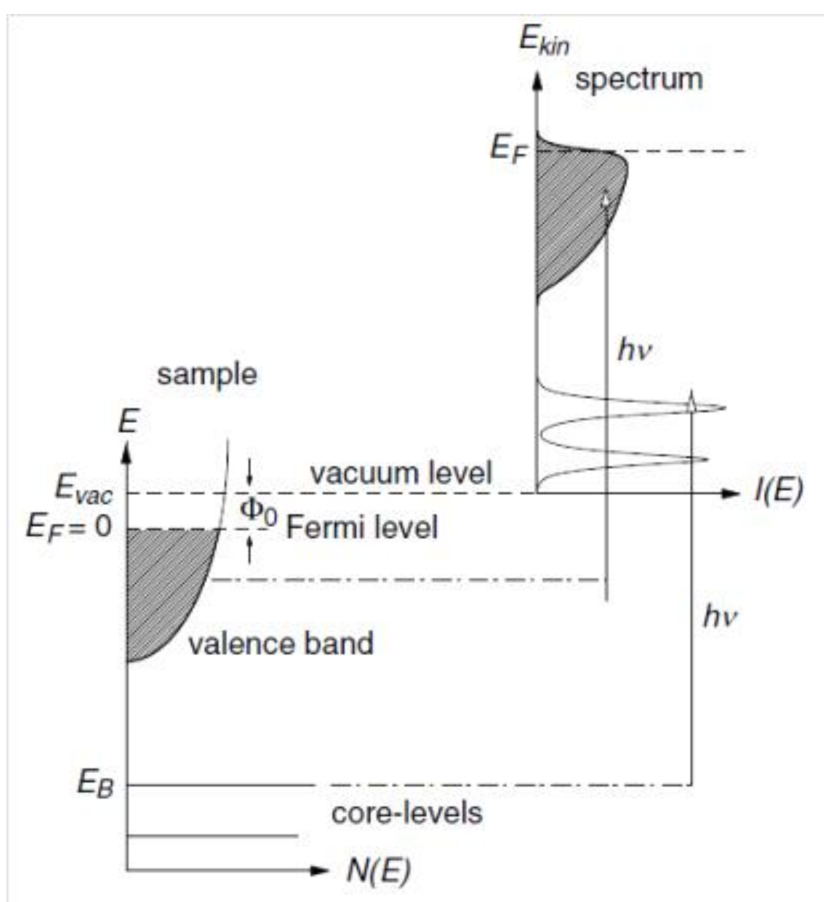

Figure 2.16. Schematic view of the photoemission process in the single-particle picture. Electrons with binding energy E_b can be excited above the vacuum level E_{vac} by photons with energy $h\gamma > E_b + \Phi_0$. The photoelectron distribution $I(E_{kin})$ can be measured by the analyser and is an image of occupied density of states $N(E_b)$ in the sample. (Figure adapted from reference[26])

2.6.2 Theory of Photoemission Spectroscopy

The photoemission process is actually a complicated process, always involving many-body interactions such as electron-electron, electron-phonon and electron-ion interactions. However, the simplified single electron "*sudden approximation*" has been widely accepted as a simplifying model, which assumes that the response of the system to the creation of the photohole is instantaneous and that there is no interaction between the escaping photoelectron and the remaining system.[27] The photoexcitation of an electron is described by the Fermi Golden rule, involving transitions from a ground state with wave function $|\Psi_i>$ to a final state with wave function $|\Psi_f> = |\Psi_{k,s}>$ under the interaction of the electron with the electromagnetic field $\boldsymbol{A}$, resulting in a photoelectron with momentum $\boldsymbol{\kappa}$ and kinetic energy $E_k = \hbar^2\kappa^2/2m_e$. The photocurrent can be described by:

$$J_k(h\gamma) = \frac{2\pi}{\hbar}\sum_s |<\Psi_{k,s}|H_{PE}|\Psi\mathrm{i}>|^2 \delta(\epsilon_k - \epsilon_s - h\gamma)$$

The index s refers to a set of quantum numbers that contains all possible excitations of the final state, including phonons, plasmons, electron–hole pairs and multiple excitations. The perturbation operator H_{PE} describes the interaction of an electron in the system with the electromagnetic field $\boldsymbol{A}$:

$$H_{PE} = \frac{e}{2m_e c}(\boldsymbol{A}\cdot\boldsymbol{p} + \boldsymbol{p}\cdot\boldsymbol{A}) + \frac{e^2}{2m_e c^2}A^2$$

where $\boldsymbol{A}$ is the vector potential of the incident light and $\boldsymbol{p}$ the momentum operator. Further approximations can be made since the quadratic term in $\boldsymbol{A}$ becomes relevant only

for extremely high photon intensities:

$$H_{PE}^{vol} = \frac{e}{m_e c}(\boldsymbol{A} \cdot \boldsymbol{p})$$

which is an appropriate perturbation operator for most photoemission process.

In the *sudden approximation*, the final state is decoupled from the remaining solid, so that all extrinsic interactions are neglected. The photocurrent J can be further described by:

$$J_k(h\gamma) = \frac{2\pi}{\hbar}\sum_k |\Delta_{kk}|^2 \mathrm{A_k}\,(\epsilon_k - h\gamma)$$

The matrix element $\Delta_{kk} = \langle \Psi_k | H_{PE} | \Psi \mathrm{i} \rangle$, describing the transition probability of a single electron from $|\Psi_i\rangle$ state into the final state $|\Psi_k\rangle$. The one-electron spectral function $\mathrm{A}_k(h\gamma) = \sum_s |\langle N-1, s | c_k | N \rangle|^2 \cdot \delta(h\gamma - \epsilon_s)$ can be related to the single-particle Green's function of the system:

$$\mathrm{A}_k(k,E) = \frac{1}{\pi}\Im\{G(k,E)$$

$$G(k,E) = \frac{1}{E - E_k^0 - \sum(k,E)}$$

For a non-interacting system, $|\Psi_f(N-1)\rangle = |\Psi_i(N-1)\rangle$, and the spectral function is simply a delta function at $E = E_k^0$, where E_k^0 is the one-electron energy of the system. Consequently, the binding energy observed in the photoemission spectrum would be that of the non-interacting system. This is known as the Koopmans' energy, although it is

never observed in practice. The self energy term $\sum(k, E)$ contains all the contributions from many-body interactions like electron-electron or electron-phonon interactions that determine the photoemission line shape. For core-levels of metals for example, the spectral function for the description of low-energy electron–hole excitations in the conduction band gives an asymmetric quasi-particle peak with a power-law singularity (the Mahan–Doniach–Šunjić (MDS) line shape. For a weakly interacting system, the Green's function can be recast into a so-called coherent part, which is very similar to the non-interacting system but with a slightly renormalized mass, a so-called quasi-particle, and an incoherent part. These can approximately be considered as the main photoemission line and satellite features occurring at higher binding energy due to screening by plasmons in the material, respectively.

2.6.3 Core Levels and Satellites

Spin-orbit splitting

For a non-interacting system the PES consists of the photoexcitation of an electron from the core level of a material labelled by its principal and orbital angular momentum quantum number (labelled *s, p, d, f, for l =0, 1, 2, 3 etc.*). The *s* core-level spectra consist of one single line broadened by the lifetime of the electronic states and the instrumental width. For core-levels with $l \neq 0$, the spectra lines exhibit a doublet structure due to spin-orbit coupling which originates from the interaction of the spin magnetic moment ($\hat{s}$) of an electron with the orbital magnetic momentum ($\hat{l}$) around nucleus. As the final state of the atom is singly ionized in photoemission, the *j-j* coupling scheme is appropriate for use, where $\hat{j}$ is the total angular momentum,

$$\hat{\boldsymbol{j}} = \hat{\boldsymbol{l}} + \hat{\boldsymbol{s}}$$

This coupling breaks the spin degeneracy of electrons in a particular orbital to produce two states with $|j| = |l \pm 1/2|$ each of which has $2j + 1$ degenerate substates characterized by m_j values $j, j-1 \ldots -j$. For $l = 0$ (s state), the only permitted value of j is $j = 1/2$ and the only source of angular momentum is the spin moment. In contrast, for $l \geq 1$, $j = l \pm 1/2$. This spin-orbit coupling causes a shift of the energy level by amount:

$$\Delta E_{SO} \propto \xi(nl)[j(j+1) - l(l+l) - s(s+1)]$$

where $\xi(nl)$ is the spin-orbit coupling constant. Therefore, spin-orbit doublets are observed in the core-level spectra with the lower j level occurring at higher binding energy. For example, for $l = 1$ (p orbital), j is either 3/2 or 1/2 , producing 4-fold degenerated $p_{3/2}$ and 2-fold degenerated $p_{1/2}$, respectively, and thus the intensity ratio of the spin-orbit split components, must be equal to the 2:1. Figure 2.17 shows the In 3d spectrum of In_2O_3, where the $3d_{5/2}$ and $3d_{3/2}$ give rise to intensity ratio of 3:2.

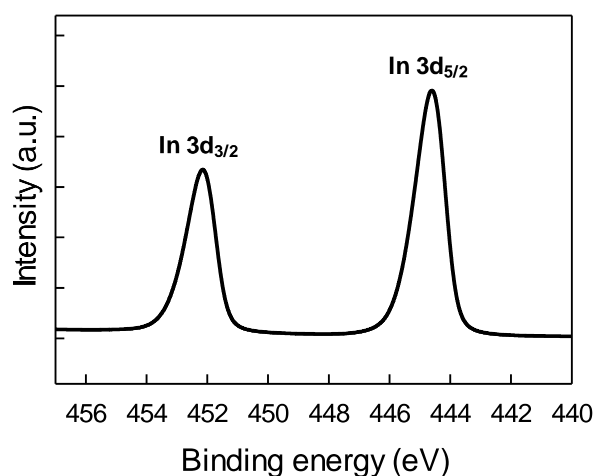

Figure 2.17. XPS core level of In $3d$ spectrum consists of spin-orbital doublet with binding energies of 444.7 eV for In $3d_{5/2}$ and 452.3 eV for in $3d_{3/2}$. (Figure by KHL Zhang)

As an alternative to treating spin orbit splitting as a final state effect it is often helpful to think in terms of spin-orbitals with characteristic *j* values in the initial state of the system. This allows different *j* states to have different ionisation cross-sections and different lifetimes.

Chemical shift

A very interesting aspect of core-level binding energies is that they are sensitive to the exact local chemical environment and charge state of the atom. In general binding energies increase with the formal oxidation state of the atom. Even within a given oxidation state there can be a range of binding energies depending on the electronegativity of the ligand atoms. Thus binding energies for fluorides are often higher than for oxides. In ionic solids differences in Madelung site potentials can also contribute to the chemical shift: for many post transition metal oxides site potential effects can largely cancel shifts due to changes in oxidation state. Overall, chemical shifts provide a very useful way to probe the chemical nature of the surface of materials.

Core level satellites

The ideal of a non-interacting system is rarely realised. Electrons interact with each other via Coulomb and exchange interactions and the emission of one electron in the photoemission process leads to excitations in the remaining system ("*final-state effect*"). These excitations require energy and therefore lead to signals in the PES spectrum with smaller kinetic energy (larger binding energy) than that corresponding to the ground state of the ionised system. In this case additional lines ("*satellites*") show up in the spectrum together with the main line (representing the ground state after photoexcitation). In principle, there are two sources for "*satellite*" in the PES spectrum: an *intrinsic satellite*

created synchronously in the photoemission process and an *extrinsic satellite* created during the travel of the photoexcited electron in a solid to the surface.

An often observed *intrinsic satellite* arises from splitting of core-levels resulting from the coupling of the spin and angular momenta of the core-hole with the spin and orbital angular momenta of valence shells with an open shell configuration. This can be clearly illustrated by the O 1*s* spectra lines for a mixture of gaseous O_2 and H_2O shown in Figure 2.18.[26]

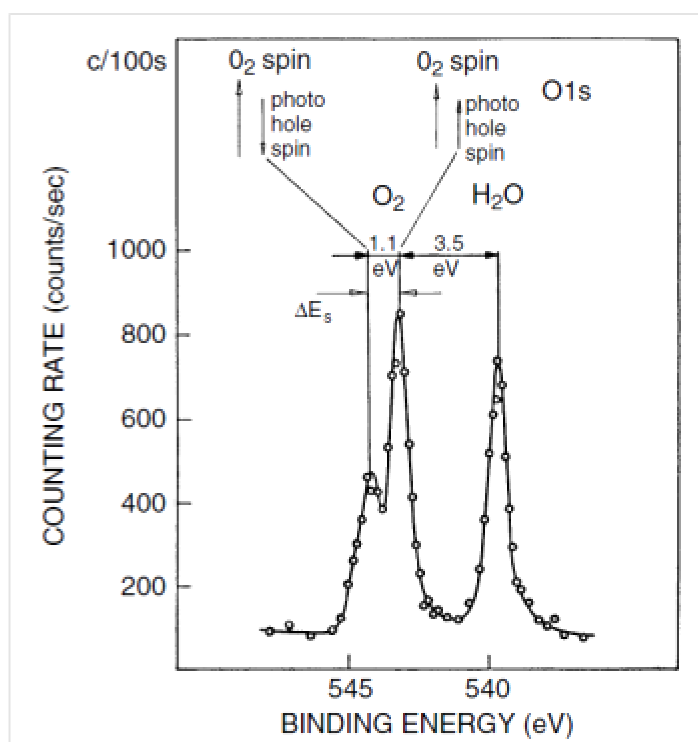

Figure 2.18. Oxygen 1*s* core-level of O_2 and H_2O as free molecules. In paramagnetic O_2, the spin of the photo-hole can be parallel or antiparallel to the spin of the valence orbital. The two final-state configurations have an energy difference of E_s = 1.1 eV; the relative intensity is given by the spin multiplicity. In the case of diamagnetic water molecules, the two final states are degenerate. (Figure adapted from reference[26])

A chemical shift of 3.5 eV is observed between the two species. However the line from H_2O is a singlet, while that from O_2 exhibits a splitting. O_2 in its ground state has one unpaired electron in each of the two valence orbitals, resulting in a total valence spin of S=1. Thus, after photoionization in the O 1*s* shell, the spin S=1/2 of the core-hole can

couple to the spin S = 1 of the valence-shell, producing two final state with total spins J=1/2 or J=3/2, depending on the spin of the core-hole parallel or antiparallel to the valence spin. The two states are separated by 1.1 eV determined by the energy of the exchange interaction. One may expect that the intensities reflect the (2J+1)-degeneracy of the total angular momentum of the states. H_2O however has a closed-shell valence band configuration and the total spin is zero (S=0). Therefore, the energy of the O 1*s* photo-hole is degenerate with respect to spin, i.e. the energy of the spin-up and the spin-down state is identical and no splitting is observed for the O 1*s* line of this molecule. Exchange splitting has also been observed extensively for the *s*-levels of many compounds of 3*d* transition metal[28] and rare-earth elements[29]. In these systems, the spin of the *s* core-hole couples with the spins of the open valence shell (e.g. 3*d* or 4*f*), resulting in the exchange splitting in the spectra. The situation becomes more complex for core levels with $l > 0$ as coupling of both spin and orbital angular momenta becomes important. In addition there may be charge transfer effects. Consider an ion with a ground state configuration d^nL, where L specifies a full ligand shell. One can observe two final states after the creation of a core-hole (e.g. $3s^{-1}$) associated with d^nL and $d^{n+1}L^{-1}$ final states. The latter is produced by charge transfer from the ligand shell L to the open metal *d* shell. Figure 2.9 presents the 3*s* core level spectrum of CuO ($3d^9$ initial-state configuration).[23] It shows that the main line (lower binding energy) has no splitting and is therefore attributed to a charge transfer state $3d^{10}L^{-1}$ final state. The satellite line (higher binding energy) has a splitting due to the spin coupling between the $3s^{-1}$ core hole and $3d^9L$ final state. Even more complex spectra are observed in the Cu 2*p* region.

Further satellites are produced by coupling with plasmons in nearly-free-electron metals. In this case, the incipient core-hole excites collective oscillations of the free electrons at the Fermi level relative to the system of positive lattice ions to produce

intrinsic plasmon satellites. *Extrinsic plasmons* can also be excited by the outgoing photoelectron during its travel from the ionised atom to the surface. In Chapter 8, the effect of Sn doping on the electronic structure of In_2O_3 will be investigated by core level XPS. The plasmon satellite on the In 3*d* core level will be discussed in detailed, since Sn doping effectively introduces free electrons at Fermi level.

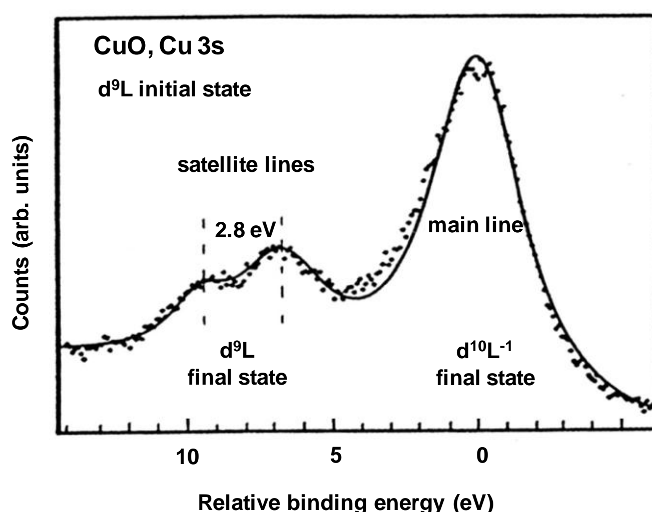

Figure 2.19. 3*s* core line in CuO; the main line is $d^{10}L^{-1}$(no exchange interaction possible) and the satellite line is d^9L and therefore exhibits and exchange interaction. (Figure adapted from Reference[23])

2.6.4 Valence Band Spectra

As shown in Figure 2.16, photoemission spectra also probe the valence electronic states. Valence band photoemission basically involves two important aspects. The first is that the electronic states are characterised by both energy and wavevector *k*; and the photoemission process involves *k* conservation.[30] Assuming perfect two-dimensional translational symmetry in the plane of the surface, parallel momentum must be conserved

in this step, up to a parallel reciprocal lattice vector, $\boldsymbol{G}_{//}$, and so the momentum of the final electron in vacuum $\boldsymbol{k}_{f//}$ satisfies:

$$\boldsymbol{k}_{f,//} = \boldsymbol{k}_{i,//} + \boldsymbol{G}_{//}$$

Assuming a free electron dispersion of the final state bands, the parallel wavevector of the initial state can therefore be determined from:

$$k_{i,||} = k_{f,||} = sin\theta\sqrt{\frac{2m_e E_k}{\hbar^2}}$$

where θ is defined as the emission angle as shown in Figure 2.15. The measurement of the valence band spectra by continuously varying the emission angle gives rise to the electronic dispersion curves in k-space e.g. along Γ-X or Γ-K. This is the central concept of angle resolved photoemission spectroscopy (ARPES) with excitation energy ranging from 10 eV-100 eV. Semiautomized methods with state-of-art high intensity synchrotron light allow an efficient measurement of spherical cuts through the Fermi surface, usually called Fermi surface mapping,[31] where the photoemission intensity at E_f is mapped as a function of the electron emission angles θ and φ. However, the wavevector is not simply conserved normal to the surface. Consequently, ARPES is most effective for looking at electronic features characteristic of two-dimensional solids, including both layered materials and surface states on metals or semiconductors.

However, if high energy X-ray photons are used, several other factors become important. Firstly for photoelectrons with high kinetic energies, small angles of emission still correspond to high values of wavevector, and so even for relatively modest

acceptance angles, it extends to the entire Brillouin zone. Secondly the influence of phonon scattering at higher energies can become very significant, meaning that transitions are no longer direct. It should also be noted that the wavevector of the photon can no longer be considered negligible for X-rays, resulting in the breakdown of the dipole approximation. Considering all the factors, valence-band spectra excited by x-rays approximate reasonably well to the initial density of states of the material, with the partial contributions to the total density of states weighted by ionisation cross sections for the orbitals involved. In Chapter 7, the surface electronic structures of In_2O_3 and Sn-doped In_2O_3 are studied by ARPES and X-ray photoemission.

2.6.5 Electron Mean Free Path

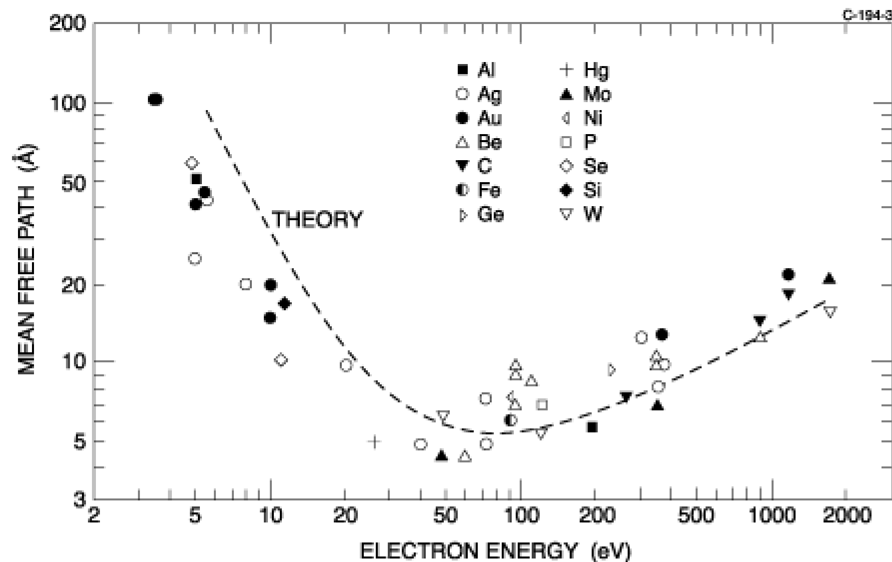

Figure 2.20. Mean-free paths in different elements as a function of kinetic energy. The general trend is called "universal curve" since the data shows no systematic dependence on the nature of the solid.[32]

Photoelectrons may be inelastically scattered as they propagate toward the surface. The scattering mainly involves interaction with other electrons and the consequent excitation of valence or conduction electron plasmons with energies typically of the order of 20 eV. Phonon or impurity scattering may also be important at lower kinetic energies. Such inelastic scattering events cause the photoelectron to be emitted from the solid with a lower energy than would be expected from its initial state and these therefore contribute to the background of photoemission spectra. The electron mean free path λ is a measurement of the mean distance that an electron travels before suffering an inelastic scattering event inside a solid.[32] The photoelectron flux is attenuated from a value I_0 at a distance d beneath the surface to a value I at the surface according to a Beer Lambert type attenuation law:

$$I = I_0 e^{-d/\lambda sin\theta}$$

where θ is the polar angle that the detector makes to the surface, so that $d/sin\theta$ is the effective path length to the surface. Consequently, PES is a surface specific technique. In normal emission geometry, 65% of the photoemission signal originates from within λ of the surface and 95% from within 3λ of the surface. Seah and Dench[33] showed that the electron mean free paths for a very large number of elements and compounds all fit approximately on a "universal curve" as shown in Figure 2.20.[32] It shows a pronounced minimum λ = 5 Å for electron kinetic energies around 30-70 eV, with a marked increase towards both lower and higher kinetic energies. The valence photoelectrons excited by a laboratory based Al Kα source (1485.6 eV) have a λ of about 15 Å. Thus PES measurements made in this energy range are the quite surface sensitive. However, the use of either the hard X-rays (e.g. 5000 eV) or very low energy UV radiation gives rise to

larger λ values of the order of 50 Å, from which information about bulk based electronic states can be extracted. In Chapter 7, we also employ the concept of "universal curve" to extract the bulk and surface electronic states of In_2O_3 thin film by comparing the valence band spectra excited with hard (6000 eV) and soft (1485.6 eV) X-rays.

2.6.6 Photoionization Cross-sections

The photoionization cross-sections are determined by the matrix elements discussed above, and so will clearly vary significantly with atomic number and core level. The relative ratio between the cross sections for different core-levels also shows a marked dependence on photon energy. A detailed discussion of this can be found in reference 29.[30] Yeh and Lindau have calculated atomic subshell photoemission cross-sections for all elements, assuming one-electron wavefunctions.[34] In practice their effect on measured spectra can be incorporated using tabulated sensitivity factors, making quantitative analysis possible.

2.7 **References:**

1. H. Lüth, *Solid Surfaces, Interfaces and Thin Films* 4th ed. (Springer-Verlag, Berlin, 2001).
2. Z. Y. Zhang and M. G. Lagally, *Morphological organization in epitaxial growth and removal* (World Scientific, Singapore, 1998).
3. R. M. Tromp and J. B. Hannon, Surf. Rev. Lett. **9**, 1565 (2002).
4. Z. Y. Zhang and M. G. Lagally, Science **276**, 377 (1997).
5. I. V. Markov, *Crystal growth for beginners: fundamentals of nucleation, crystal growth and epitaxy* (World Scientific, Singapore, 2003).
6. M. A. Herman and H. Sitter, *Molecular beam epitaxy: fundamentals and current status* (Springer, Berlin, 1996).
7. J. V. Barth, G. Costantini and K. Kern, Nature **437**, 671 (2005).
8. J. W. Evans, P. A. Thiel and M. C. Bartelt, Surf. Sci. Rep. **61**, 1 (2006).
9. C. Hammond, *The Basics of Crystallography and Diffraction* 2nd ed. (Oxford University Press, Oxford, 2001).
10. M. A. Moram and M. E. Vickers, Rep. Prog. Phys. **72**, 036502 (2009).
11. P. F. Fewster, *X-Ray Scattering from Semiconductors* 2nd ed. (Imperial College Press, London, 2003).
12. D. B. Williams and C. B. Carter, *Transmission electron microscopy: a textbook for materials science* 2nd ed. (Springer, New York, 2007).
13. L. F. Kourkoutis, J. H. Song, H. Y. Hwang and D. A. Muller, Proc. Natl. Acad. Sci. U. S. A. **107**, 11682 (2010).
14. E. Meyer, H. J. Hug and R. Bennewitz, *Scanning probe microscopy: the lab on a tip* (Springer-Verlag, Berlin Heidelberg, 2004).
15. G. Binnig and H. Rohrer, Helv. Phys. Acta **55**, 726 (1982).
16. F. J. Giessibl, Rev. Mod. Phys. **75**, 949 (2003).
17. http://en.wikipedia.org/wiki/Scanning_tunneling_microscope
18. Y. L. Huang, Two-dimensional Molecular Self-assemblies on Surfaces Studied by Low-Temperature Scanning Tunneling Microscopy, PhD thesis, Department of Physics, National University of Singapore (2010).
19. G. Binnig, C. F. Quate and C. Gerber, Phys. Rev. Lett. **56**, 930 (1986).
20. K. H. L. Zhang, I. M. McLeod, Y. H. Lu, V. R. Dhanak, A. Matilainen, M. Lahti, K. Pussi, R. G. Egdell, X.-S. Wang, A. T. S. Wee and W. Chen, Phys. Rev. B (83) (2011).
21. Y.-W. Chung, Practical guide to: surface science and spectroscopy (Academic Press, San Diego, CA, 2001.).

22. J. B. Pendry, Journal of Physics C-Solid State Physics **13**, 937 (1980).
23. S. Hüfner, *Photoelectron Spectroscopy: Principles and Applications*, 3rd ed. (Springer-Verlag, Berlin, 2003).
24. K. Siegbahn, Rev. Mod. Phys. **54**, 709 (1982).
25. A. Einstein, Ann. Phys. **17**, 132 (1905).
26. F. Reinert and S. Hufner, New J. Phys. **7**, 97 (2005).
27. L. Hedin, J. Michiels and J. Inglesfield, Phys. Rev. B **58** (23), 15565 (1998).
28. S. Hufner and G. K. Wertheim, Phys. Rev. B **7**, 2333 (1973).
29. F. R. McFeely, Kowalczy.Sp, L. Ley and D. A. Shirley, Phys. Lett. A **A 49**, 301 (1974).
30. S. Hüfner, *Photoelectron Spectroscopy: Principles and Applications*, 3rd ed. (Springer-Verlag, Berlin, 2003).
31. J. Osterwalder, T. Greber, E. Wetli, J. Wider and H. J. Neff, Prog. Surf. Sci. **64**, 65 (2000).
32. A. Zangwill, P*hysics at Surfaces* (Cambridge University Press, England, 1988).
33. M. P. S. a. W. A. Dench, Surf. Interface Anal. **1**, 2 (1979).
34. J. J. Yeh and I. Lindau, Atom. Data Nucl. Data Tables **32**, 1 (1985).

Chapter 3:

Experimental Apparatus and Techniques

This chapter describes the apparatus and techniques used to generate the data presented in subsequent chapters.

3.1 Oxygen Plasma Assisted Molecular Beam Epitaxy

Indium oxide films were grown in an oxide molecular beam epitaxy (MBE) system (SVT, USA)[1] with a base pressure of of 5×10^{-9} mbar housed in the Department of Chemistry, University of Oxford, as shown in Figure 3.1.[2]

Figure 3.1. The setup of the oxide MBE system at Oxford (Photo taken by R. G. Egdell).

The vacuum is maintained by combination of turbomolecular pumps and mechanical dry pumps. The pressure is measured by using ion gauges. The system consists of a fast entry load lock, a growth chamber and an analysis chamber. All the chambers are separated by gate valves but connected by a transportation arm for sample transfer. Substrates are held by gravity in a recessed Mo mounting plate. The fast entry load lock is used for introduction of substrates into the system without breaking the vacuum. The growth chamber incorporates liquid nitrogen cooled cryopanels, several effusion cells (Cu, In, Sn, Cr and Ga *etc.*), an oxygen plasma source and a manipulator with a stage heater. Oxygen atoms are generated in a radio frequency (RF) plasma source operated at 200 W RF power with an oxygen background pressure of 3×10^{-5} mbar. The substrate is heated radiatively using a graphite filament. The substrate temperature is measured by a chromel-alumel thermocouple which terminates behind the cradle holding the sample mounting plate. Before growth, substrates were cleaned by annealing for one hour with a measured substrate temperature of 900 °C followed by exposure to the oxygen atom beam for 5 minutes. Films were then grown over a range of substrate temperatures between room temperature and 1000 °C, with different durations of growth runs ranging from a few minutes to a few hours. The In effusion cell was operated at a temperature of 780°C which gave a deposition rate of 0.01 nm s^{-1} for In metal in the absence of an O flux as monitored by a quartz crystal monitor offset from the substrate position. The true growth rate of In_2O_3 on the substrate was found to be about 0.035 nms^{-1} at a substrate temperature of 700 ^{o}C. The films grown at high substrate (or low) temperature may appear to be thinner (or thicker) due the low (or high) sticking coefficient of the In and O species. For growth of Sn-doped In_2O_3, the Sn effusion cell was operated at temperature ranging from 650 ^{o}C to 800 °C, depending on the Sn doping level required. The start and

termination of growth runs were controlled by the shutters in front of effusion cells. During growth runs, the cryopanels of the growth chamber were filled with liquid nitrogen. After growth was complete, the samples could be transferred to analysis chamber equipped with LEED and XPS to conduct *in-situ* analysis.

3.2 X-ray Diffraction

θ-2θ X-ray diffraction patterns were measured using a PANanalytical X'pert PRO diffractometer housed in the Department of Chemistry, University of Oxford. It incorporates a monochromatic Cu $K\alpha_1$ X-ray source and an X'Celerator detector placed in a standard Bragg-Brentano (θ-2θ) geometry. The voltage on the anode was fixed at 40 KV and the emission current was set to 45 mA. X-rays were monochromated using a curved Ge (111) crystal. The slit which defines the incident beam was programmed so that X-rays irradiated the whole sample throughout the scan, but the slit for the diffracted X-rays was kept fixed at 0.25 mm.

3.3 Transmission Electron Microscopy

To make specimens for cross-sectional high resolution TEM, the samples were firstly cut into stripes with width of 900 μm by a diamond saw; then the two stripes were glued face-to-face together; and were mechanically polished down to 5–10 μm with diamond papers; finally specimens were further thinned down to electron transparency (10 nm) by Ar ion beam milling using a Gatan 691 Precision Ion Polishing System (PIPS). The energy of the Ar ion was 3.5 keV and the ions were incident at an angle of 6°. Cross-sectional TEM images were collected using a JEOL3000F microscope operating at 300 KeV housed in the Department of Materials University of Oxford. Digital Micrograph

image software was used to process the TEM images. Bragg filtering was applied to the TEM images in order to remove some of the background noise and contrast adjustment was applied uniformly across the images where necessary to enhance the display quality.

3.4 Scanning Probe Microscopy

3.4.1 Scanning Tunnelling Microscopy

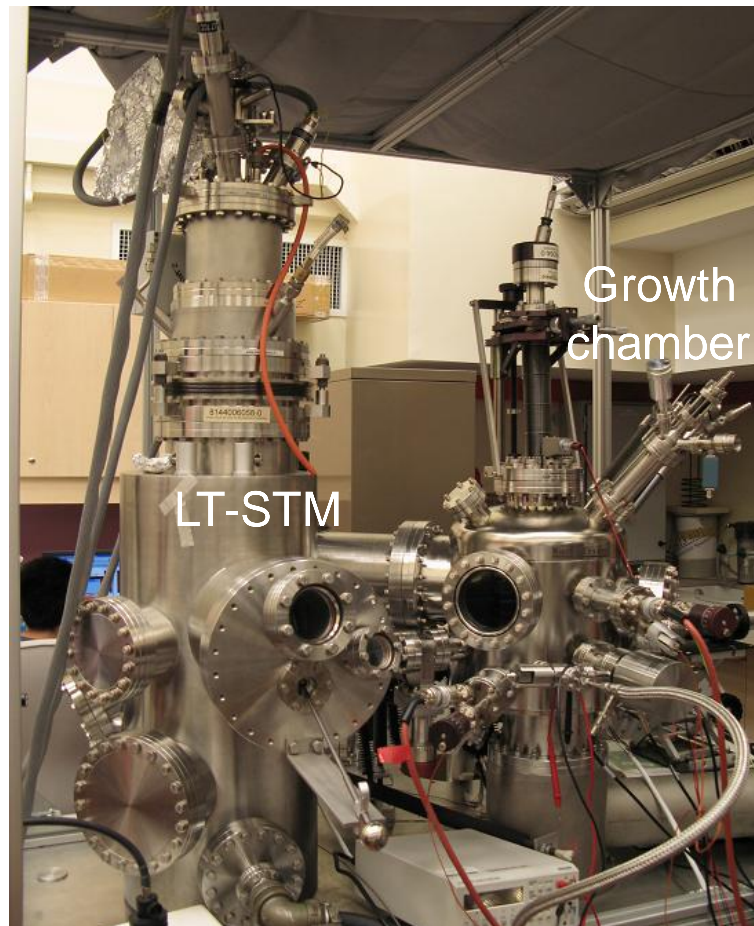

Figure 3.2. The setup of LT-STM chamber and the attached growth chamber (Photo taken by KHL Zhang in National University of Singapore).

The scanning tunnelling microscopy (STM) experiments were carried out in a home-built multichamber ultra-high vacuum system with a base pressure better than 2×10^{-10} mbar incorporating a fast entry load lock chamber, a sample preparation chamber and an Omicron low temperature STM (LT-STM) stage. This instrument is housed in the Surface Science Laboratory, National University of Singapore. A schematic of the apparatus is shown in Figure 3.2. The vacuum is maintained by a combination of turbomolecular pumps and ion pumps. Repeated cycles of argon ion bombardment followed by annealing were used as a standard procedure for the preparation of clean surfaces in the sample preparation chamber. Tungsten wires were used in the manipulators for the radiative sample heating up to 700 °C. For temperature above 700 °C, electron beam bombardment heating was utilized. An infrared pyrometer was used to monitor the sample temperature. The LT-STM stage is equipped with a cryostat for liquid N_2 or He, which can cool the sample down to 77 K or 4 K respectively for STM imaging. The STM was operated with a Nanonis controller (Nanonis, Switzerland). A chemically etched tungsten wire was used as tip and the scanner was calibrated by an atomic image of graphite. All the STM images were obtained in constant-current mode at liquid nitrogen temperature (77 K).

3.4.2 Atomic Force Microscopy

The AFM images were recorded with a Digital Instruments Multimode SPM instrument. This was operated in contact mode with “J” and “E” scanners having a lateral range of approximately 100 μm and 10 μm, respectively. Silicon nitride probes (Nascatec GmbH model NST NCHFR), with a thin coating of gold to act as a mirror for the laser beam, were used. The microscope is calibrated by scanning a 10 mm pitch 200 nm 3D reference from Digital Instruments. Digital Nanoscope software (version 5.12) was used to analyse

and process the AFM topographic images. All the images were treated with the 'flatten' command and are presented using one of the standard colour palettes of the Nanoscope software.

3.5 Low Energy Electron Diffraction

The LEED experiments were conducted in a standard multi-chamber UHV surface science system (Omicron, Germany) housed in the Surface Science Centre, University of Liverpool. It contains an analysis chamber equipped with a PSP Vacuum Technology electron energy analyser, dual anode X-ray source, rear view LEED optics from OCI Vacuum Microengineering and an Omicron scanning tunnelling microscopy module operating at room temperature. The base pressure of the system was less than 2×10^{-10} mbar, with hydrogen as the main residual gas in the chamber. A clean surface was prepared by cycles of Ar ion bombardment and annealing to approximately 600 ^{o}C by tungsten wires using radiative heating. The sample was considered clean when the LEED pattern showed sharp integer order spots and XPS did not show any traces of contamination. The intensities of the diffraction spots as a function of the energy of the incident electrons (LEED I-V spectra) were measured at normal incidence of the primary beam using a camera connected to computer controlled data handling system, or by direct measurement with a movable Faraday cup. The spectra were background subtracted and normalised with respect to the primary beam current. The intensities of the symmetrically equivalent spots were averaged in order to reduce experimental noise.

3.6 Photoemission Spectroscopy

3.6.1 Scienta ESCA-300 Spectrometer at Daresbury Laboratory, UK

The laboratory based high resolution X-ray photoelectron spectra were performed using a Scienta ESCA300 spectrometer housed in the National Centre for Electron Spectroscopy and Surface Analysis at Daresbury Laboratory, UK. The system incorporates an analysis chamber, a preparation chamber and a fast entry lock. The analysis and preparation chambers are pumped by separate oil diffusion pumps connected to their respective chambers through liquid nitrogen cooled traps, whilst the entry lock is pumped by a turbomolecular pump. The base pressure of the analyser and analysis chambers is 8×10^{-10} mbar, and the preparation chamber 2×10^{-9} mbar.

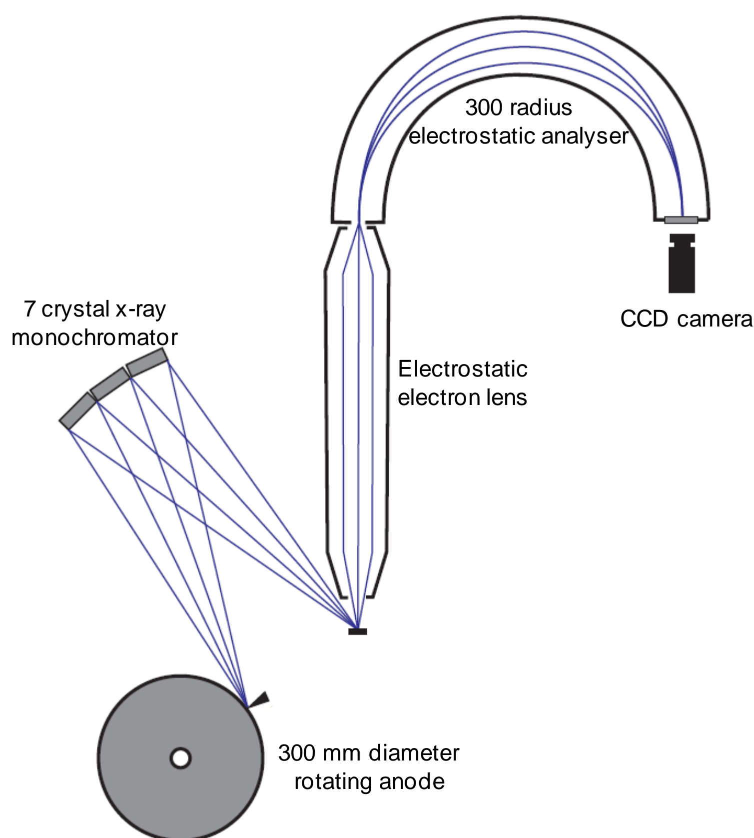

Figure 3.3. Schematic of the Scienta ESCA-300 spectrometer at Daresbury Laboratory (Figure adapted from reference[3])

The spectrometer consists of a high intensity rotating anode Al Kα X-ray source, a 7-crystal monochromator, a 300 mm mean radius hemispherical electron energy analyser, and a multi-channel CCD detection system, as shown schematically in Figure 3.3.[3] The rotating anode X-ray source contains an electron gun focussed on an Al band around the edge of a water-cooled titanium alloy disc, which rotates at about 1000 rpm. The X-rays (predominantly Al Kα $h\gamma$ = 1486.6 eV) source is run with 200 mA emission current and 14 kV anode bias. The X-ray passes into the monochromator chamber through a thin beryllium window that prevents secondary high energy electrons from bombarding the crystals of the monochromator. The wide-angle monochromator consists of seven toroidally bent α-quartz $(10\bar{1}0)$ crystals, arranged on a Rowland circle of 650 mm diameter. The combination of the finite width of the electron beam on planes the anode and the diffraction width of the quartz crystals yields monochromated Al Kα X-ray with a total linewidth of the X-ray source of about 0.26 eV.

The samples are mounted on a high precision manipulator to allow adjustments in the X, Y, Z and θ planes. The manipulator axis, electron lens axis and monochromated X-ray beam all lie in the same plane with the latter two at 45° to each other. An electron flood gun with energy up to 9 eV is incorporated into the analysis chamber, which can be used to compensate the charging effect if the sample is insulating. Note that the In_2O_3 and ITO samples investigated here were conducting but were grown on insulating (Y-ZrO_2) substrates. Electrical contacts were made on the top of the sample to ensure that In_2O_3 and ITO film were properly grounded.

Photoelectrons are collected by a 300 mm mean radius hemispherical electron energy analyser with 100 mm electrode gap. The analyser can be operated with pass energies in the range between of 20 eV and 1000 eV, with eight different slit widths between 0.2 mm and 4 mm. All spectra presented in this work were obtained with 150

eV pass energy and 0.8 mm slits, giving a good compromise between resolution and count rates. The overall instrumental resolution of about 0.40 eV is derived from the convolution of the analyser broadening and the linewidth of the X-ray source.

3.6.2 Beamline ID16 at ESRF in Grenoble, France

High energy X-ray photoelectron spectroscopy (HXPS) measurements were performed on beamline ID16 of the European Synchrotron Radiation Facility (ESRF) in Grenoble (France) using the spectrometer developed under the European Volume Photoemission project (VOLPE).[4] The ESRF is a third generation light source with a circumference of 844 m and storage ring energy of 6 GeV. There are 40 beamlines, incorporating bending magnets, focusing magnets and undulators.

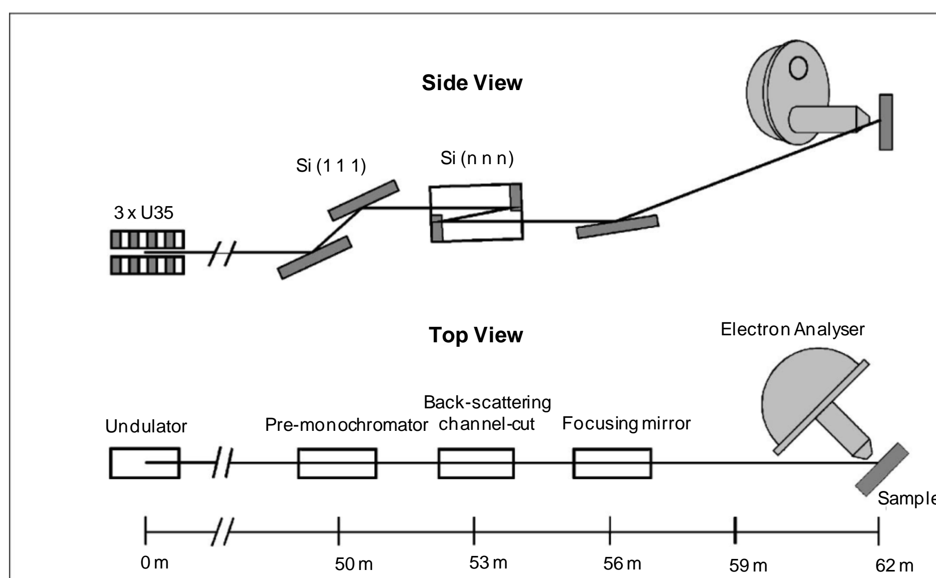

Figure 3.4. Schematic layout of the high energy photoemission experimental setup on ID16 beamline of ESRF (Figure adapted from reference[4]).

ID16 is a multi-operational beamline with high resolution inelastic x-ray scattering available, as well as HXPS. The layout of beamline ID16, in the configuration used for high energy photoemission experiments is sketched in Figure 3.4. ID16 is currently equipped with three undulators, each of them 1.6 m long and with a period of 35 mm. For our experiments, we used the first and third harmonics of the undulators to produce X-rays in the range 6–10 keV. The x-ray beam, with an angular divergence of 20 (vertical) and 40 (horizontal) μrad^2 full width half maximum (FWHM), is pre-monochromatized to a relative bandwidth ($\Delta E/E$) of 1.4×10^{-4} by a Si (1 1 1) double crystal fixed-exit monochromator. The two Si (1 1 1) crystals are liquid nitrogen cooled in order to extract the heat load from the beam. The premonochromatized beam impinges on a Si channel-cut crystal operating at the Si(*nnn*) reflection (*n* is 3 for ~6 keV and 4 at ~8 keV) and at Bragg angle of 88.1°.[4] After monochromatization a Rh coated toroidal mirror focuses the beam on the sample to a spot size of 50 µm (vertical) ×120 µm (horizontal). A 200 µm thick beryllium window separates the vacuum of the beamline with the UHV of the experimental chamber.

The experimental endstation consists of analysis chamber, preparation chamber and a fast-entry lock. The base pressure is in ~ 10^{-10} mbar range. The chamber is equipped with a XYZΘ manipulator and sample translations are performed with a remotely controlled stepper motor. The whole chamber can be aligned with respect to the beam in both the horizontal and vertical directions with a precision of 5 µm and 0.1 µm respectively. The sample stage is fitted with a ceramic heater, for gentle annealing of samples, with a maximum temperature of 130 °C.

The electron energy analyser is composed of a hemispherical dispersing element and an electrostatic input lens. The two hemispheres have a 200 mm mean radius. A

carousel provides a choice of nine entrance slits, ranging from curved aperture of 0.2 × 25 mm, to a rectangular one of 3.6 × 25 mm. The static input lens is composed of seven independent electrodes with a total length of 732 mm and a working distance of 40 mm. This lens system allows an extended range of values of the retardation ratio R, from 0.2 to 600. The electron analyser is equipped with a cross delay wire anode detector. The detector is 30 mm × 30 mm, and has been modified to permit floating operation up to 10 kV. The detector is fitted with 'home-built' acquisition electronics.

3.6.3 Beamline I311 at the MAX II Synchrotron MAX-lab, Lund, Sweden

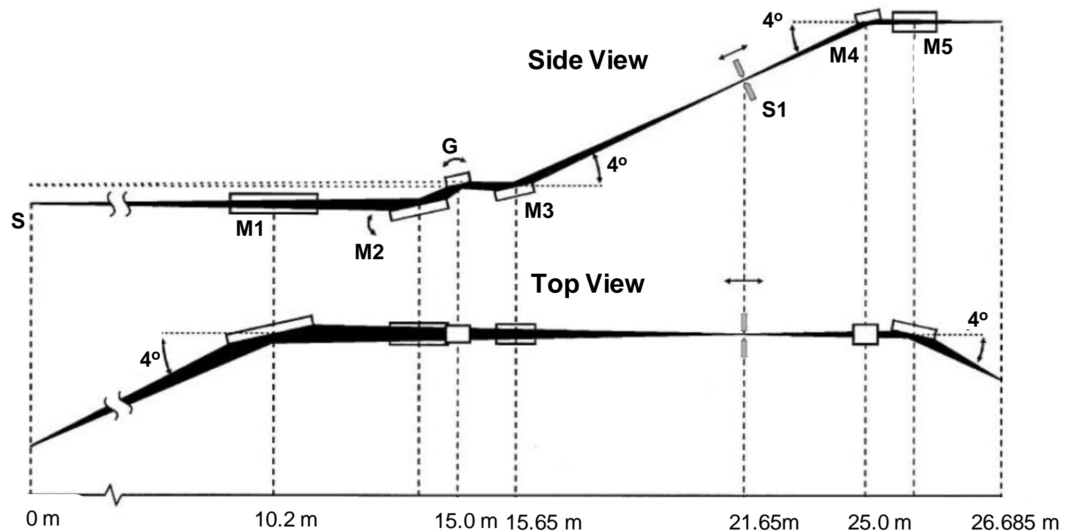

Figure 3.5. Schematic layout of the I311 beamline at MAX II synchrotron MAX-lab. The optical elements are: M1, horizontally ocusing pre-mirror; M2, rotatable plane mirror; G, plane grating; M3, spherical focusing mirror; M4 and M5, spherical re-focusing mirrors. S1 is a movable exit slit. The real source is at S. (Figure adapted from reference[5])

The soft X-ray and UV photoemission spectra measurements were performed on beamline I311 at the 1.5 GeV third generation MAX II synchrotron housed at MAX-lab, Lund, Sweden.[5] The beamline I311 is based on a 48.5 period undulator and operates in an energy range between 30 eV and 1500 eV. The undulator is of the hybrid permanent magnet type with 77 poles and a period length of 66 mm. The overall layout of the beamline is shown in Figure 3.5, consisting of a horizontally focusing pre-mirror, a plane-grating monochromator, a re-focusing mirror system and an end-station for high resolution photoemission.

The experimental endstation incorporates a sample preparation chamber including facilities for sample heating and rearview LEED optics, whilst the analysis chamber houses a Scienta SES200 spherical sector electron energy analyser. The samples were cleaned by radiative heating at 700 °C for several hours. Cleanness of the surfaces was confirmed by (1×1) LEED pattern and no trace of C 1s signal from XPS. PES spectra were collected at normal emission with an energy resolution of about 4 meV at 30 eV increasing to 1.4 eV at 1500 eV.

3.6.4 Beamline BaD ElPh at Elettra Synchrotron Light Source, Trieste, Italy

High-resolution angle-resolved photoemission spectroscopy (ARPES) in the low photon energy regime (4.6–40 eV) was carried out on the beamline BaD ElPh (Band Dispersion and Electron-Phonon coupling) at the Elettra Synchrotron Light Source, Trieste, Italy.[6] This synchrotron is a third generation light source with storage ring energy of 2.4 GeV. There are 23 beamlines, incorporating bending magnets, focusing magnets and undulators. BaD ElPh is especially designed for low-energy, high-resolution ARPES experiments. The radiation source of the beamline is the same Figure-8 undulator of the

IUVS beamline. This undulator has 2 sections with a total of 32 periods of NdFeB magnets with a 140 mm period length. The overall layout of the beamline is shown in Figure 3.6. The beamline is based on a 4 m normal-incidence monochromator (NIM) and consists of a silicon switching mirror to transfer the photon beam in the BaD ElPh branch, a spherical prefocusing mirror which focuses the beam into an entrance slit, a NIM with a moveable exit slit, and a gold coated toroidal mirror which refocuses the beam onto the sample in the experimental chamber. The monochromator has three (Al/MgF_2, SiC, Pt) interchangeable spherical gratings to cover the photon energy range 4.6-40 eV at 2.0 GeV of electron ring energy. The prefocusing mirror has two different parts: the bare Si portion of the surface is used for photon energies up to 13 eV while the Pt-coated part is suitable for higher photon energies.

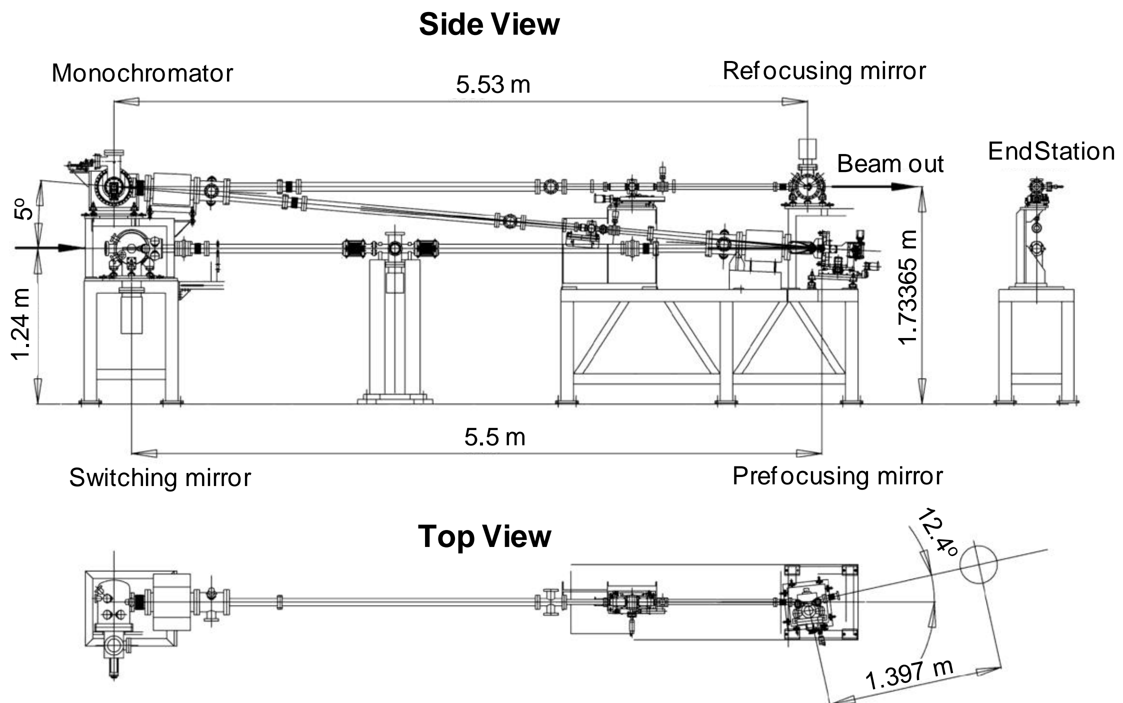

Figure 3.6. Schematic layout of BaD ElPh beamline at Elettra Synchrotron Light Source, Trieste. (Figure adapted from reference[6])

The experimental endstation consists of three independent ultra-high vacuum chambers and a load-lock chamber. The base pressure is 5×10^{-11} mbar. The preparation chambers are equipped with a ion sputter gun and with several free flanges to mount the needed tools for sample preparation (cleavage, scraping, gas treatment) and for UHV in-situ growth of thin films. The analysis chamber houses a SPECS Phoibos 150 analyzer with a 2D-CCD detector system, a high-intensity vacuum ultraviolet source, a conventional X-ray source, LEED and a residual gas analyzer. The SPECS Phoibos 150 is a 150 mm hemispherical analyzer and is mounted on a fixed geometry with an angle of 50° relative to the synchrotron radiation direction. It has a typical energy resolution of 5 meV, and an angular resolution of 0.1^{o}. The use of a 2D-CCD detector offers the possibility of simultaneous acquisition of the energy as well as the angular distributions of the photoelectrons. The surfaces of In_2O_3 and Sn-doped samples were cleaned by repeated cycles of Ar^+ sputtering and annealing at 600 ^{o}C in UHV for 1 hour. Well ordered (1×1) LEED pattern and no trace of C 1s signal from XPS confirmed the cleanness of the surfaces. Measurements were performed at room temperature with pressure better than 5×10^{-11} mbar.

3.7 References:

1. http://www.svta.com/.
2. A. Bourlange, D. J. Payne, R. G. Egdell, J. S. Foord, P. P. Edwards, M. O. Jones, A. Schertel, P. J. Dobson and J. L. Hutchison, Appl. Phys. Lett. **92**, 092117 (2008).
3. G. Beamson, D. Briggs, S. F. Davies, I. W. Fletcher, D. T. Clark, J. Howard, U. Gelius, B. Wannberg and P. Balzer, Surface and Interface Analysis **15**, 541 (1990).
4. P. Torelli, M. Sacchi, G. Cautero, M. Cautero, B. Krastanov, P. Lacovig, P. Pittana, R. Sergo, R. Tommasini, A. Fondacaro, F. Offi, G. Paolicelli, G. Stefani, M. Grioni, R. Verbeni, G. Monaco and G. Panaccione, Rev. Sci. Instrum. **76**, 023909 (2005).
5. R. Nyholm, J. N. Andersen, U. Johansson, B. N. Jensen and I. Lindau, Nucl. Instrum. Methods Phys. Res. Sect. A-Accel. Spectrom. Dect. Assoc. Equip. **467**, 520 (2001).
6. L. Petaccia, P. Vilmercati, S. Gorovikov, M. Barnaba, A. Bianco, D. Cocco, C. Masciovecchio and A. Goldoni, Nucl. Instrum. Methods Phys. Res. Sect. A-Accel. Spectrom. Dect. Assoc. Equip. **606**, 780 (2009).

Chapter 4:

Surface Energies Control the Self-organisation of Oriented In_2O_3 Nanostructures on Cubic Zirconia

4.1 Introduction

Despite the fact that ITO finds widespread application in liquid crystal displays, solar cells and other optoelectronic devices,[1-10] the basic physical properties of the material have been the subject of ongoing controversy,[11-14] including the nature and magnitude of the bandgap[11-13]. For many years the bandgap has been presumed to be direct and quoted to be 3.75 eV.[11, 16] However, bandstructure calculations are inconsistent with assignment of a weak optical onset observed at 2.69 eV to an indirect gap.[12] It was only in 2008 that it was established that In_2O_3 has a direct, but dipole forbidden, bandgap of around 2.8 eV, almost 1 eV lower than the widely quoted value of 3.75 eV which marks the onset of fully allowed optical transitions.[13] Revision of the value for the bandgap led in turn to the realisation that electron accumulation may be observed on In_2O_3 surfaces with low bulk doping levels.[17, 18] An ongoing problem is that it is difficult to obtain high quality In_2O_3 thin films that exhibit intrinsic properties because native defects almost invariably act as adventitious *n*-type donors, to the extent that nominally undoped films may in fact support a degenerate electron gas. The technological importance of the material and the renewed interest in the basic physics prompted work in our group on growth of high quality single crystal thin films of In_2O_3.[19-22] The motivations here are twofold: (i) to obtain high-quality In_2O_3 thin films that exhibit intrinsic properties for detailed fundamental investigations;[13, 17, 18] and (ii) to explore the use of In_2O_3 thin films as the

active layer in transparent electronics and short wavelength optoelectronic devices.[4-7, 23, 24] Moreover an improved understanding of key aspects of the bulk and surface physics would open the possibility of rational design of nanostructured materials with potential applications in gas sensing, field emission devices and transparent electronics. Self-organisation arising from lattice mismatch during heteroepitaxial growth provides a well-established approach to the preparation of "quantum dots" in conventional semiconductor systems such as Ge on Si and InAs on GaAs: the morphology of the dots is determined by an interplay between elastic strain and surface energies.[25, 26] Much less effort has been devoted to the controlled self-assembly of oxide nanostructures during epitaxial growth.[27] Oxides and other polar materials are however of particular interest because in general there are large differences between the energies of different low index surfaces.

In this chapter, we firstly explore the influence of substrate orientation in the epitaxial growth of In_2O_3 on (100), (110) and (111) single crystal faces of Y-stabilised cubic ZrO_2 (YSZ). In_2O_3 adopts a body-centred cubic bixbyite structure, with space group $Ia\overline{3}$ and lattice parameter a = 1.01170 nm.[16] The structure may be regarded as a 2×2×2 superstructure of fluorite with ordered removal of O from ¼ of the anion sites. YSZ adopts a fluorite structure belonging to the space group $Fm\overline{3}m$ with lattice parameter a = 0.51423 nm at the 17% Y doping level of the substrates used in the current work. Thus, there is a mismatch of only 1.6% between $2a$ for Y-doped ZrO_2 (1.02846 nm) and a for In_2O_3. Moreover, the cation arrays within the two materials are very similar, minimizing the chemical mismatch at the interface. We demonstrate the spontaneous formation of highly directional 1D nanorods during high temperature epitaxial growth of In_2O_3 on (110) oriented YSZ. By contrast growth on (100) surfaces leads to truncated square pyramidal islands, whilst atomically flat mesa or continuous

thin films develop on (111) oriented substrates. On the basis of *ab initio* quantum chemical simulations, it is shown that the different growth modes and the striking azimuthal orientation of the rods and pyramids on (110) and (100) surfaces are determined by large differences in the energies of the three low index surfaces.

4.2 Experimental and Theoretical details

4.2.1 MBE Growth

The In_2O_3 thin films were grown on (100), (110) and (111) oriented 1 cm × 1 cm YSZ substrates (PiKem, UK) in an ultrahigh vacuum oxide MBE system (SVT, USA) with a base pressure of 5×10^{-10} mbar. This incorporated a hot lip indium effusion cell and a radio frequency (RF) plasma oxygen atom source operated at 200 W RF power with an oxygen background pressure of 3×10^{-5} mbar. Substrates were heated radiatively using a graphite filament. The nominal growth rate was 0.035 nm s^{-1} calibrated using the thickness from high resolution transmission electron microscopy (HRTEM) measurements and atomic force microscopy (AFM) images. The YSZ substrates were cleaned by exposure to the oxygen atom beam at a nominal substrate temperature of 900 °C. We explored a wide range of growth conditions in terms of film thickness and growth temperature, which ranged between 550 °C and 1000 °C. Most of the data reported here relate to a deposition time of 3000 s which corresponds to a film thickness of 100 nm assuming a layer growth mode. *In situ* low energy electron diffraction (LEED) was carried out in an analysis chamber connected to the growth chamber.

4.2.2 Structural and Morphological Characterizations

AFM images were recorded *ex situ* with a Digital Instruments Multimode SPM instrument. This was operated in contact mode with a 'J' scanner having a lateral range of approximately 100 μm and a vertical range of 6 μm. Silicon nitride probes (Nascatec GmbH model NST NCHFR), with a thin coating of gold to act as a mirror for the laser beam were used. Calibration of the AFM was accomplished by scanning a 10 mm pitch 200 nm 3D reference from Digital instruments. Digital Nanoscope software (version 5.12) was used to analyze and process the AFM topographic images. All the images were treated with the "flatten" command and are presented using one of the standard colour palettes of the Nanoscope software. Specimens for cross-sectional TEM were prepared by cutting and mechanical grinding down to 5-10 μm, followed by thinning to electron transparency by Ar ion beam milling using a Gatan 691 Precision Ion Polishing System (PIPS). It proved very difficult to obtain sections with a uniform thickness across the ZrO_2/In_2O_3 interfaces because the epilayer etched at a much higher rate than the substrate. Cross-sectional TEM images were collected using a JEOL3000F microscope operating at 300 keV. Digital Micrograph image software was used to process the TEM images. Bragg filtering was applied to the TEM images in order to remove some of the background noise and contrast adjustment was applied uniformly across the images where necessary to enhance the display quality.

4.2.3 Density Functional Theory (DFT) Calculations

The bulk and surface electronic structure and total energies were calculated using density functional theory within the generalized gradient approximation (PBE),[28] as implemented

in the VASP package.[29, 30] The computational work was carried out by Dr. A. Walsh in University of College London. The plane-wave kinetic energy threshold (500 eV) and *k*-point density (4×4×4) were both well-converged for the bulk system. Starting from the relaxed bulk bixbyite lattice (a = 1.030 nm), 2D surface models were constructed using a periodic arrangement of slabs, separated with a 2 nm vacuum region. Convergence of γ with respect to slab thickness resulted in models containing 32, 32 and 48 formula units for the (100), (110) and (111) surfaces, respectively. In all cases, the top two ionic layers were allowed to relax, while all other layers were held at their bulk lattice positions. Simulated annealing was performed to assess the stability of the resulting structures at 750 K and no further relaxations or reconstructions were found.

4.3 Results and Analysis

4.3.1 Growth of Oriented In_2O_3 Nanostructures and Thin Films

Figure 4.1 show θ-2θ X-ray diffraction (XRD) profiles of In_2O_3 films grown on (100), (110) and (111) oriented YSZ substrates with a nominal thickness of 100 nm with a growth temperature of 750°C: samples grown at higher temperatures gave similar XRD profiles. In each case there is near perfect texture in the films and the atomic planes in the epilayer faithfully follow those of the substrate. On the (100) oriented substrate (Figure 4.1a), the epilayer In_2O_3(400) and (800) peaks with doubled Miller indices appear very close to the (200) and (400) peaks of the substrates, owing to the close match between $2\boldsymbol{a}_{YSZ}$ (1.02846 nm) for the YSZ with $\boldsymbol{a}_{\mathrm{In2O3}}$(1.01170 nm) for the epilayer. In addition, the body centred cubic structure of In_2O_3 allows for the appearance of a very weak (600) epilayer peak with no nearby (300) substrate peak owing to the face centred cubic

structure of stabilised zirconia. For (110) substrate orientation, a single (440) epilayer peak is observed close to the substrate (220) reflection as shown in Figure 4.1b.

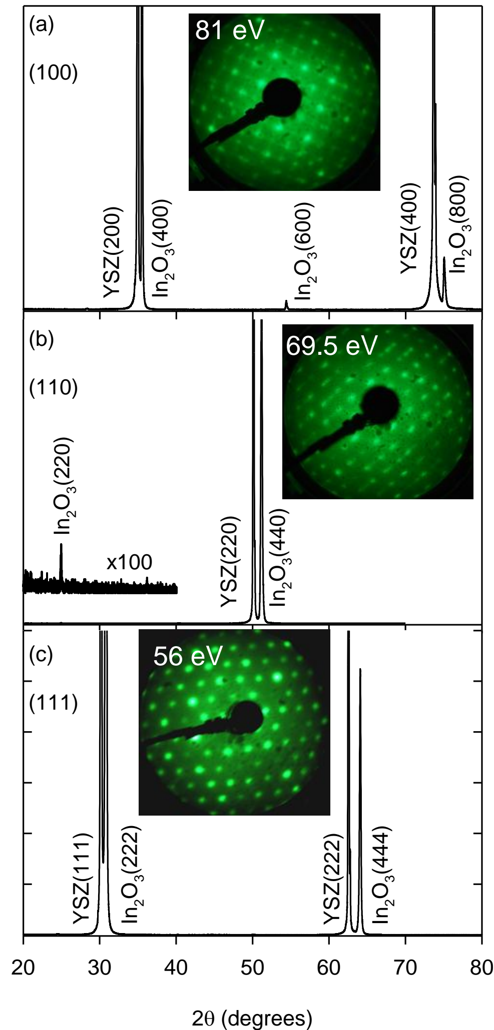

Figure 4.1. θ-2θ X-ray diffraction profiles of In_2O_3 films with a nominal thickness of 100 nm grown on (a) YSZ(100); (b) YSZ(110) and (c) YSZ(111) substrates respectively. The insets show corresponding LEED patterns measured *in situ* in the MBE growth system.

Within the space group $Ia\overline{3}$ $(hk0)$ reflections with $h = k$ are systematically absent unless with $h = 2n$, so that the (110) and (330) epilayer peaks are not observed but the (220) peak is just observable above the baseline noise. Finally for the (111) orientation (Figure

4.1c), (222) and (444) epilayer peaks appear close to substrate (111) and (222) peaks but the intermediate (333) epilayer reflection is forbidden due to the body centring in In_2O_3. The insets in Figure 4.1 show low energy electron diffraction (LEED) patterns from the differently oriented films measured *in situ* in the MBE system. As expected the patterns from (100), (110) and (111) surfaces show 4-fold, 2-fold and 3-fold rotational symmetries respectively. However the patterns from (100) and (110) oriented films show evidence of streaking and spot splitting that varies strongly with beam energy. This is indicative of extensive faceting at the surface.

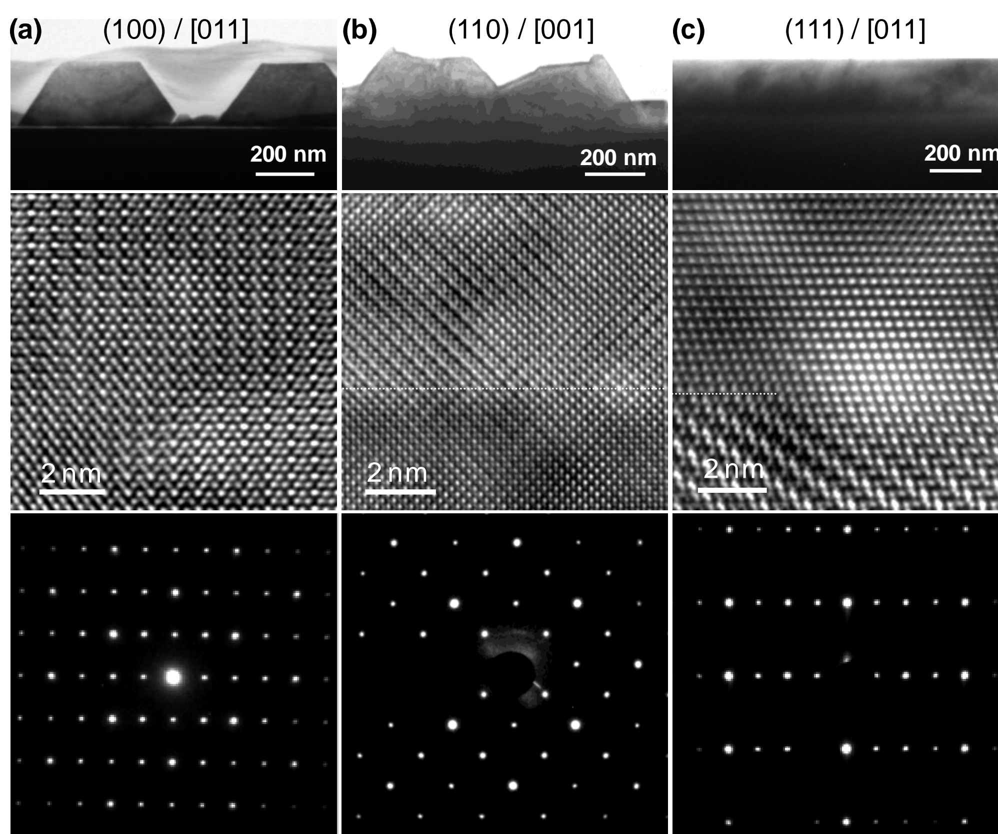

Figure 4.2. Panel (a), (b) and (c): cross-sectional TEM of In_2O_3 grown on (100), (110) and (111) oriented YSZ substrates at 700 °C, viewed down [011], [001] and $[1\bar{1}0]$ directions respectively; low magnification (top row); high resolution TEM (middle row); and corresponding electron diffraction pattern at interface region (bottom), confirming the epitaxial relationship in each case.

The epitaxial growth relationships for each substrate orientation were further examined by cross-sectional HRTEM. High resolution images such as those as shown in Figure 4.2 confirm the excellent crystalline order in the films grown on the three differently oriented substrates and also demonstrate the formation in each case of sharp interfaces between the substrate and the epilayer. The expected "*cube-on-cube*" epitaxial relationship for each case can be clearly observed.

However very pronounced morphological differences between films grown on the different low index substrates are apparent on a larger length scale. The differences are most obvious in large area AFM images, such as those shown in Figure 4.3. The (100) oriented epilayer grown at 750 °C (Figure 4.3a) is seen to consist of an array of square or rectangular islands with lateral dimensions typically of the order of 100 nm and with edges all aligned parallel to the [011] directions of the substrate. Elongation of the islands takes place along both [011] and $[1\bar{1}0]$ directions. The (110) epilayer (4.3b) shows a similar island structure but in this case the islands are *all* rectangular and oriented with edges along $[1\bar{1}0]$ and [001] directions. The elongation is exclusively along the $[1\bar{1}0]$ direction. By contrast the (111) epilayer consists of larger loosely connected mesa (shown in 3c) with dimensions up to about 5 µm, dissected occasionally by deep troughs which extend down to the substrate. These mesa have a distinctive serrated "autumn leaf" morphology and flat surfaces on which it is possible to resolve atomic scale steps with a height of 0.29 nm. This distance is equal to $a/2\sqrt{3}$ where a is the cubic lattice parameter of In_2O_3 and corresponds to the separation between successive cation containing planes within the bixbyite structure. The morphological differences between (100) and (110) surfaces become even more pronounced for samples grown at 900 °C, as shown in Figure 4.3d and e. Here the islands on the (100) surface have developed a more uniform square

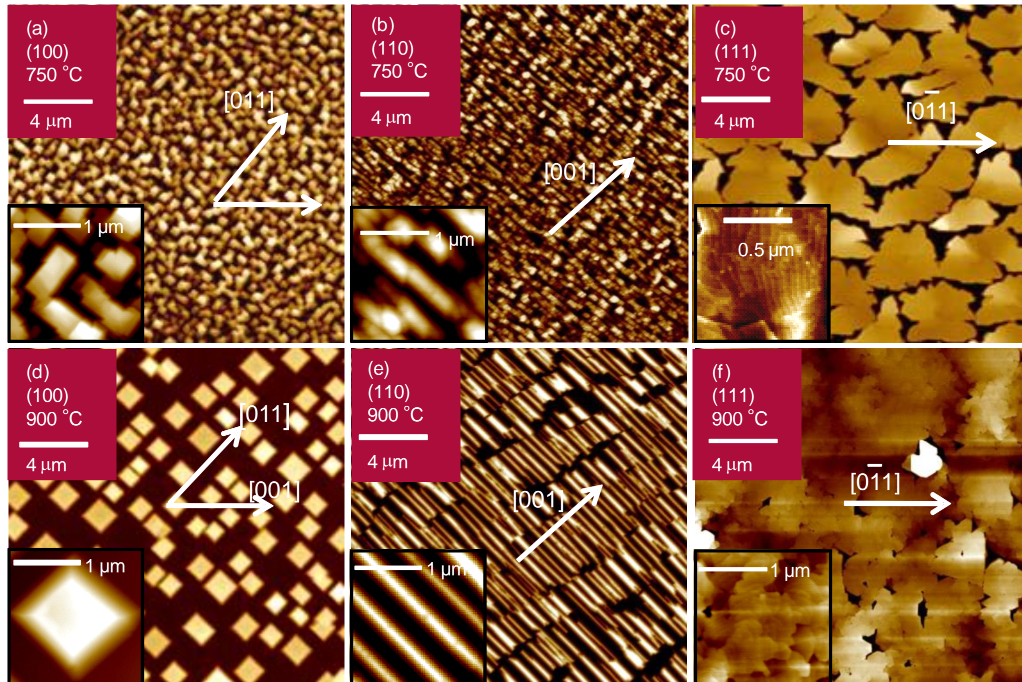

Figure 4.3. Atomic force microscopy (AFM) images of In_2O_3 grown on oriented Y-stabilised zirconia substrates. The images in (a), (b) and (c) are for samples grown at 750 °C substrate temperature on (100), (110) and (111) oriented substrates respectively, whilst the images in (d), (e) and (f) are for samples grown at 900 °C substrate temperature. The main images are scanned over an area of 20 µm × 20 µm and give an indication of the overall topology. The insets show scans over a smaller area of 1 µm × 1 µm, except for the inset to (c) which shows a scan over a smaller area of 0.5 µm × 0.5 µm in order to highlight atomic scale steps.

shape. The typical edge size of the islands is now about 1 µm (Figure 4.3d), which is around a factor of ten bigger than for films grown at 750 °C. The lateral sizes and heights of In_2O_3 islands can be controlled between 200 nm and 30 nm up to 1000 nm and 250 nm by varying the deposition time, as shown in Figure 4.4. In all cases, the islands remain aligned with edges parallel to <110> directions and maintain the square shape. The cross-sectional TEM (Top image in Figure 4.2a) and high-resolution AFM image inset in Figure 4.3d of an island clearly demonstrate that the (100) island has a truncated pyramid shape with a flat (100) top surface and sloping side facets with inclined at 54.7° to the surface plane.[31] The characteristic angle and the azimuthal orientation allows us to identify the side facets as being of {111} origin.

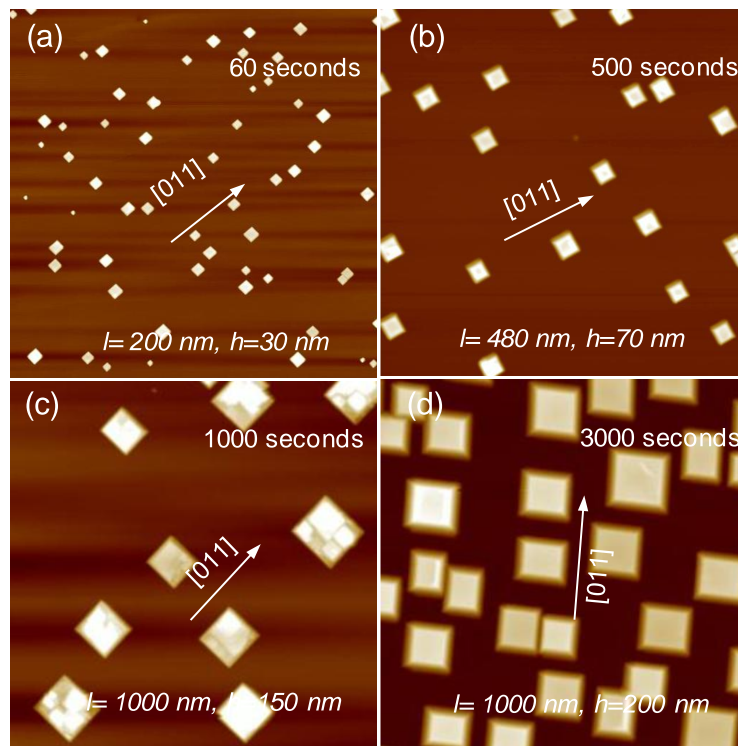

Figure 4.4. (a)-(d) AFM images (image size: 10 μm × 10 μm) of In_2O_3 nanoislands with different sizes on YSZ(100) at 900 °C substrate temperature for different deposition time as indicated in the images; The average crystal sizes: length *l* and height *h* are indicated; The in-plane crystal direction may be different due to the rotational scanning during AFM imaging; The edges of the islands aligned along [011] directions in order to expose the low surface energy (111) facets.

At higher growth temperature (Figure 4.3e), the surface the anisotropy on the (110) face between $[1\bar{1}0]$ and [001] directions becomes much more apparent and the islands assume a "rod-like" appearance with typical lengths between 2 μm and 5 μm along the $[1\bar{1}0]$ direction but with widths of around only 100 nm along the [001] direction. The spontaneous development of highly oriented nanorods on (110) surfaces prompted us to explore growth at yet higher temperatures. Panels in Figure 4.5 show AFM images of a layer grown with a lower nominal coverage (50 nm) at 1000 °C. The rods are now further elongated with lengths in excess of 20 μm and a width restricted to about 100 nm. As

with the square islands on (100) surfaces, the rods have sloping side facets and the predominant facets parallel to the $[1\bar{1}0]$ direction are of $\{111\}$ nature.

In contrast to films grown on (100) and (110) substrates, those grown on (111) substrates showed very little change on increasing the growth temperature from 750 °C to 900 °C (Figure 4.3f). The film consists of very smooth terraces and the cross sectional HRTEM confirm the growth of continuous thin films.

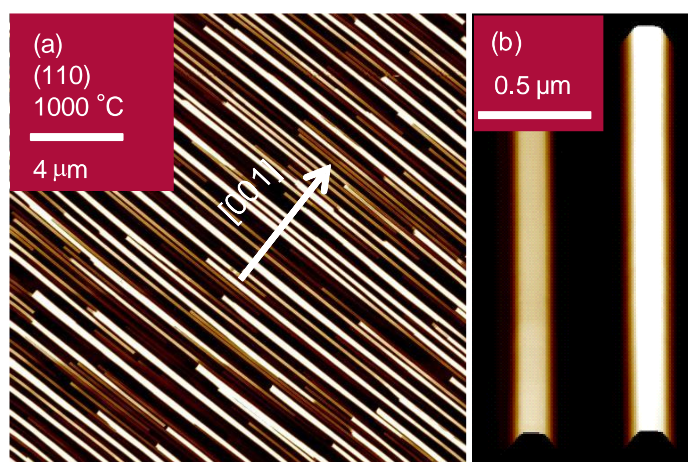

Figure 4.5. AFM images of nanorods grown on (110) oriented substrates at 1000 °C with a nominal coverage of 50 nm; (b) a 3D view of the two nanorods with high resolution.

4.3.2 Surface Energies Calculations

The morphology of growth in mismatched epitaxial systems depends on a complex interplay between the kinetics of nucleation and surface diffusion and the minimisation of surface and interface energies and elastic strain. The very pronounced changes with substrate temperature indicate that at low temperatures kinetic factors must be important and it is not clear that even at the highest temperatures that growth morphology is determined by purely thermodynamic factors. Nonetheless, many aspects of the experimental observations can be rationalised by considering the energies of the low

index surfaces of In_2O_3 computed using *ab initio* total energy calculations. The surface energy (γ) is defined as the energy per unit area required for forming the surface relative to the bulk, and is calculated according to:

$$\gamma = (U_{slab} - U_{bulk})/2A$$

where U_{slab} is the total energy of the 2D surface slab with a 2 nm vacuum region and U_{bulk} is the energy of the corresponding number of bulk In_2O_3 formula units; A represents the surface area, which is created on each side of the slab and is repeated periodically. The (100), (110) and (111) surfaces were modelled using $a \times a$, $a \times a\sqrt{2}$, and $a\sqrt{2} \times a\sqrt{2} \times \frac{\sqrt{3}}{2}$ expansions, respectively.

Side view ball and stick models of the three bixbyite surfaces are shown in Figure 4.6 along with corresponding views of the low index fluorite surfaces. The computed relaxed surface energies and associated relaxation energies are given at the bottom of the figure. The (100) surface of fluorite is a classic example of a "Type III" ionic surface within the Tasker classification[32] and contains alternating cation and anion planes. These give rise to a surface dipole and cause the surface energy to diverge to infinity for sufficiently thick slabs.[33, 34] The polar surface may be stabilised in a simple manner through microfaceting, i.e. by transferring half the ions in the outermost ionic layer to the other side of the slab.[33-36] Either cations or anions may be transferred allowing for two dissimilar polar surfaces.

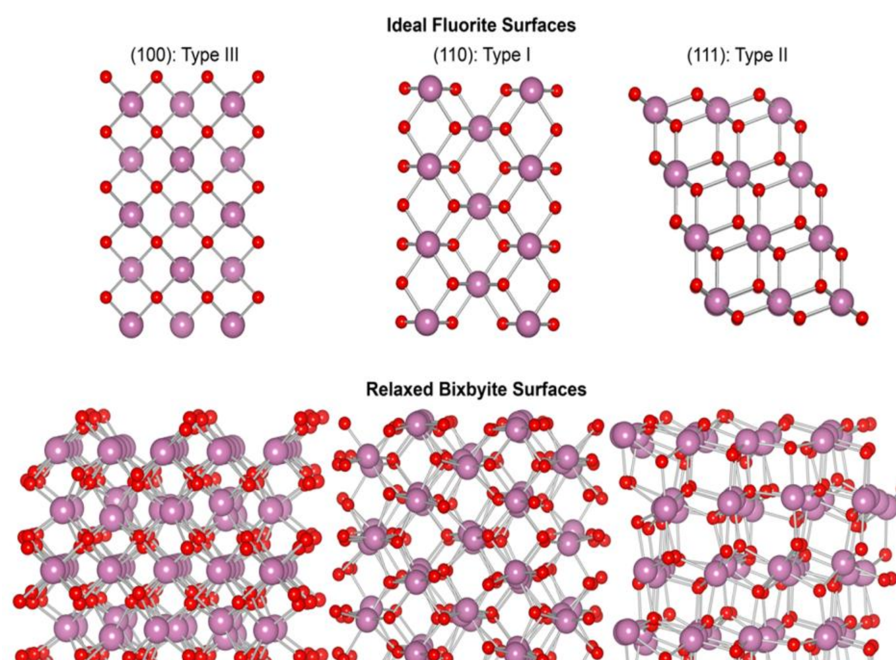

Surface	Tasker type	Bulk terminated surface energy	Relaxed surface energy
100 - In	Type III (polar)	2.721	2.088
100 - O	Type III (polar)	2.449	1.759
110	Type I (neutral)	1.595	1.070
111	Type II (quadrupolar)	1.522	0.891

Figure 4.6. Ball and stick representations of the pristine low index terminations of the fluorite (AB_2) and the relaxed In_2O_3 bixbyite (A_2B_3) surface structures, which are labelled according to the Tasker surface notation for polar compounds. The anions and cations are represented by large and small spheres, respectively. The bottom table show the corresponding bulk terminated and relaxed surface energies for each surface.

By contrast, the (110) surface of fluorite is a stable "Type I" surface containing charge neutral ionic layers. Finally the (111) surface is "Type II" and contains repeating quadrupolar grouping of anionic and cationic layers. The bixbyite surfaces of In_2O_3 are very similar in appearance to those of the parent fluorite structure, although there is minor rumpling within the cation layers due to the relaxations in atomic positions associated with the intrinsic vacant oxygen sites within the structure and the (110) surface is no longer rigorously "Type II". The bulk terminated surface energies follow a

sequence $\gamma(100)_{In} > \gamma(100)_{O} > \gamma(110) > \gamma(111)$, although the difference between (111) and (110) surfaces is rather small. However, the relaxation energy for the (111) surface is significantly bigger than for the (110) surface so that the relaxed surface energy for the (111) surface is about 0.18 J/m^2 lower than the (110) surface energy. Cleavage of the (111) surface breaks a single long In-O bond (0.24 nm) separating the charge neutral In_2O_3 units; efficient relaxation is then achieved primarily through a concerted contraction of the <111> In-O bond in the subsurface layers by *ca.* 9 %. The order of surface energies is the same as found for oxides with the fluorite structure such as UO_2[35] and indeed our substrate material cubic Y-stabilised ZrO_2[15, 37]. Thus for 24% Y doped ZrO_2, Ballabio *et al.*[15] found relaxed surface energies $\gamma(100) = 1.75$ J/m^2, $\gamma(110) = 1.44$ J/m^2 and $\gamma(111) = 1.04$ J/m^2. Note however that the order of surface energies for In_2O_3 is different to that proposed by Hao *et al.* who suggested a sequence $\gamma(110) > \gamma(100) > \gamma(111)$ on the basis of the morphologies In_2O_3 nanocrystals prepared by vapour transport.[38]

4.4.3 Nanostructure Morphology Determined by Thermodynamics

The present results establish unambiguously that the surface energies of In_2O_3 have a direct influence on the morphology of single crystal thin films. Continuous or near continuous epilayers which are atomically flat on the micron length range can be grown under a wide range of conditions on (111) oriented substrates because the (111) surface energy for In_2O_3 is the lowest amongst the three low index surfaces and $\gamma(111)_{In2O3} < \gamma(111)_{Y\text{-}ZrO2}$. By contrast on (100) and (110) surfaces an island growth mode is preferred. The thermodynamically favoured (111) termination is found to occur through spontaneous development of sloping side facets on the islands. Although this increases

the surface area of side facets by a factor of cosecθ (where θ is the contact angle with the surface), this is energetically favourable because higher energy {110} or {100} edge walls are replaced by lower energy {111} facets. In addition there is a reduction in the surface energy associated with the island top and with the bare substrate, at the minimal expense of increasing the overall contribution of the interface energy.

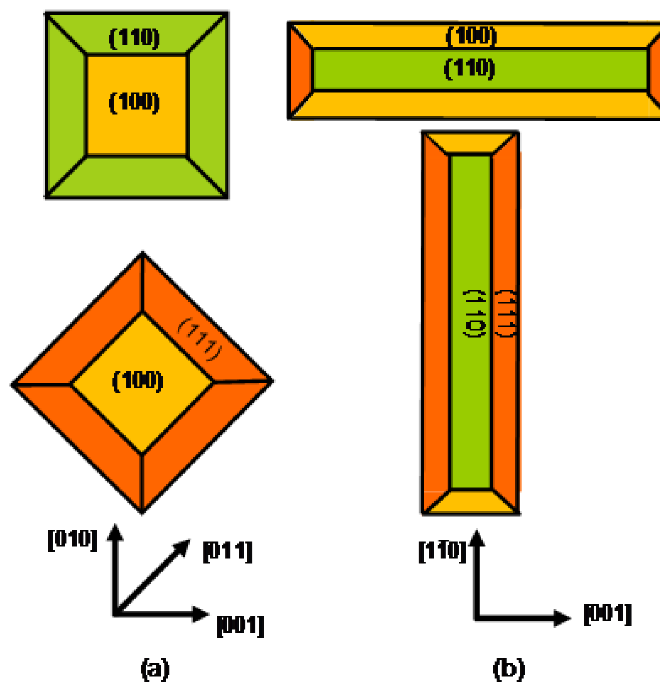

Figure 4.7. Schematic plan view illustrating the influence of azimuthal orientation on the facets which can develop on In_2O_3 islands grown on (a) (100) and (b) (110) oriented Y-ZrO_2 substrates. The preferred orientations shown in the two lower schematics allow development of thermodynamically favoured {111} side facets.

The propensity for the sloping side facets of the islands to have {111} orientation in turn determines the azimuthal orientation of the square islands found on (100) substrates and the elongation of islands along the [1$\bar{1}$0] direction to give rod-like structures on (110) oriented substrates. This is illustrated in Figure 4.7 which shows that {111} side facets can form on (100) islands provided the island edges align along <110> directions:

alignment with edges parallel to <100> directions would be associated with higher energy {110} side facets. Similarly on (110) surfaces, elongation of islands to give rod like structures with the long axis along the $[1\bar{1}0]$ direction allows for the development of extended {111} side facets whereas elongation along the [001] direction would demand formation of extended sloping {100} facets.

In the following, we will use a thermodynamic model developed by Tersoff and Tromp[39] to analyse the morphologies of the self-organized nanostructures. We considered rectangular islands with width w, length l and height h making contact with the substrate with a contact angle θ to give a truncated pyramidal morphology with sloping side facets as shown schematically in Figure 4.8. For large islands, the trade-off between strain energy and interface energy eventually drives a "shape" transition on the (100) surface of a cubic material and the islands assume a rectangular shape with $l>w$[39, 40]. For the current (100) islands, we are in the regime where $l = w$.

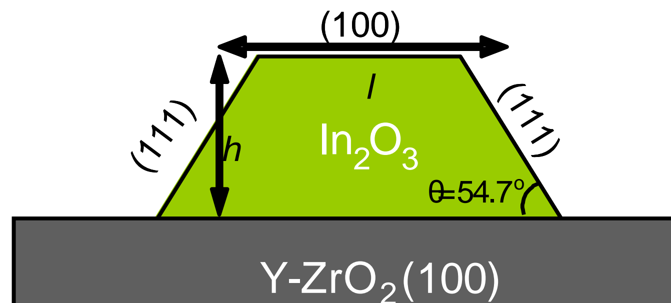

Figure 4.8. Definition of the parameters l, h and θ used in analysis of island orientation on (100) substrates.

Neglecting corners, the sum of surface and interface energies for islands oriented with edges parallel to <110> directions of the substrate is given by:

$$E_{<110>} = 4\Gamma_1 lh + \Gamma_3 l^2$$

Whilst for an island with edges parallel to <100> directions we have:

$$E_{<100>} = 4\Gamma_2 lh + \Gamma_3 l^2$$

Where:

$$\Gamma_1 = \gamma_{e(111)}\mathrm{cosec}\theta_1 - \frac{1}{2}(\gamma_{s(100)} + \gamma_{e(100)} - \gamma_{i(100)})\cot\theta_1$$

$$\Gamma_2 = \gamma_{e(110)}\mathrm{cosec}\theta_2 - \frac{1}{2}(\gamma_{s(100)} + \gamma_{e(100)} - \gamma_{i(100)})\cot\theta_2$$

$$\Gamma_3 = \gamma_{i(100)} + \gamma_{e(100)} - \gamma_{s(100)}$$

Where γ are surface and interface energies: the subscripts *e, s* and *i* denote the epilayer, substrate and interface respectively and the numbers in brackets specify the crystal plane. The contact angle $\theta_1 = 54.7°$ for {111} side facets, whilst $\theta_2 = 45°$ for {110} side facets. Neglecting the possible influence of island orientation on the strain energy, the energy difference ΔE between the two island orientations is given by:

$$\Delta E = E_{<110>} - E_{<100>} = 4lh(\Gamma_1 - \Gamma_2)$$

Inserting the values of surface energies for In_2O_3 derived in the present work along with those for Y-ZrO_2 obtained by Ballabio *et al.*[15] we obtain:

$$\Delta E = 4lh(0.09\text{-}0.15\gamma_i(100))\ \mathrm{J}$$

The interface energy has not been calculated in the present work but must have a small positive value. We thus see that orientation of islands with edges parallel to <110> directions is favoured over orientation with edges parallel to <100> directions provided that γ_i is greater than 0.6 Jm^{-2}.

Similar considerations for nanorods grown on (110) oriented substrates by the sum of surface and interfaces energies leads to the expression:

$$E_{R(110)} = 2\Gamma_4 lh + 2\Gamma_5 wh + \Gamma_6 lw$$

where the subscript R denotes a rod. Assuming {111} side facets form along the long edges and sloping {100} facets at the ends of the rod we have:

$$\Gamma_4 = \gamma_{e(111)}\text{cosec}\theta_3 - \frac{1}{2}(\gamma_{s(110)} + \gamma_{e(110)} - \gamma_{i(110)})\cot\theta_3$$

$$\Gamma_5 = \gamma_{e(100)}\text{cosec}\theta_4 - \frac{1}{2}(\gamma_{s(110)} + \gamma_{e(110)} - \gamma_{i(110)})\cot\theta_4$$

$$\Gamma_6 = \gamma_{i(110)} + \gamma_{e(110)} - \gamma_{s(110)}$$

Where the contact angles are now $\theta_3 = 35.3°$ and $\theta_4 = 45°$.

Minimising (110) subject to the constraint of constant area we obtain an aspect ratio l/w given by:

$$l/w = \Gamma_5/\Gamma_4$$

The aspect ratio is plotted as a function of the interface energy (110) in Figure 4.9. It can be seen that the aspect ratio diverges toward infinity as the interface energy approaches a

value of about 0.4 Jm^{-2}. This is because Γ_5 is always positive but the sum of terms $\gamma_{e(111)}\mathrm{cosec}\theta_3 - \frac{1}{2}(\gamma_{s(110)}+\gamma_{e(110)})\cot\theta_3$ appearing in the expression for Γ_4 has a negative value of -0.29 Jm^{-2}.

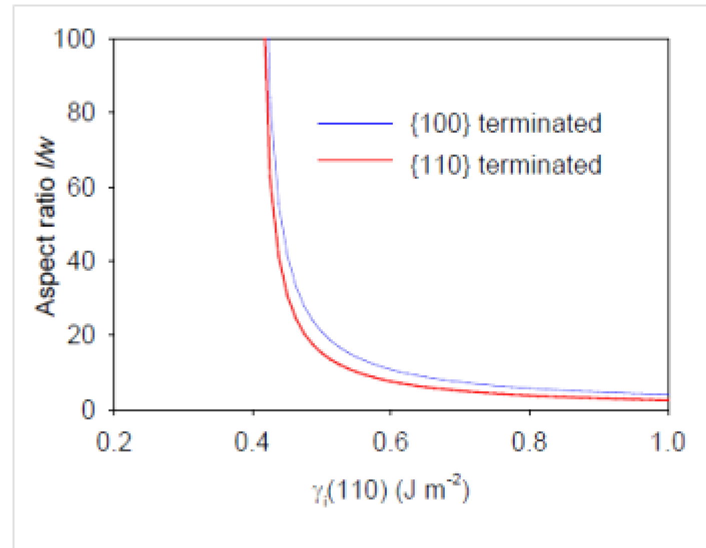

Figure 4.9. Variation of aspect ratio of In_2O_3 nanorods on YSZ substrates as a function of the (110) interface energy.

Figure 4.9 also shows the variation in the aspect ratio assuming that the rods terminate with a vertical {110} end facet. In fact this truncation of the rods is energetically favoured because the (110) surface energy is lower than the (100) surface energy. As such the formation of nanorod islands with a very high aspect ratio between length *l* and width *w* is driven by minimisation of surface energy, provided that the interface energy $\gamma_i(110)$ is small.

It should be noted that elongation of rods along the $[1\bar{1}0]$ direction is also favored by anisotropy in the elastic properties of In_2O_3. Values for the elastic parameters of In_2O_3 have recently been derived by an atomistic modelling procedure giving c_{11} =

297.8 GPa, c_{12} = 141.8 GPa and c_{44} = 76.4 GPa.[41] The energy density associated with uniaxial strain along <100> directions is determined by c_{11} but strain along <110> directions is dependent on $(2c_{11}+2c_{12}+c_{44})/4$ = 238.9 GPa which is less than c_{11}. This mechanism for elongation of the rods is related to that recently proposed by Zabeleta *et al.*[42] who grew (110) oriented Gd-doped CeO_2 rods on cubic (100) $LaAlO_3$ substrates. Elongation along the $[1\bar{1}0]$ direction was attributed to the fact that strain associated with lattice mismatch in the long direction was less than the strain in the orthogonal (001) direction. In the present case the strain is the same in both directions. However because of anisotropy in the elastic constants there is in both cases an anisotropy in the strain energy.

4.4 Concluding remarks

In summary we have been able to rationalise both the distinct growth modes found for In_2O_3 on differently oriented Y-stabilised zirconia surfaces and the propensity for development of islands with {111} facets on (100) and (110) surfaces in terms of relaxed surface energies. The controlled growth In_2O_3 nanostructured materials may offer potential applications in gas sensing, field emission devices and also set-up a model system for fundamental research. The growth of highly oriented nanorods on (110) substrates is of particular note given the growing recent interest in field effect transistors based on nanowires.[5, 43, 44] However most established techniques for preparation of oxide nanowires or nanobelts lead to a tangled mass of interpenetrating structures,[6, 44] in contrast to the perfectly aligned rods prepared in the present work. The use of an anisotropic substrate as in the present work ensures that the rods align spontaneously in one direction. The flat and continuous (111) films prompted by the lowest surface energy is of particular interest to us, since it opens the possibility to fabricate high quality single crystal In_2O_3 thin films by optimizing the growth conditions, which will be topic of next chapter.

4.5 References:

1. C. G. Granqvist, Solar Energy Materials and Solar Cells **91**, 1529 (2007).
2. C. G. Granqvist and A. Hultaker, Thin Solid Films **411**, 1 (2002).
3. P. P. Edwards, A. Porch, M. O. Jones, D. V. Morgan and R. M. Perks, Dalton Transactions 2995 (2004).
4. G. Thomas, Nature **389**, 907 (1997).
5. S. Y. Ju, A. Facchetti, Y. Xuan, J. Liu, F. Ishikawa, P. D. Ye, C. W. Zhou, T. J. Marks and D. B. Janes, Nat. Nanotechnol. **2**, 378 (2007).
6. C. O'Dwyer, M. Szachowicz, G. Visimberga, V. Lavayen, S. B. Newcomb and C. M. S. Torres, Nat. Nanotechnol. **4**, 239 (2009).
7. K. Nomura, H. Ohta, K. Ueda, T. Kamiya, M. Hirano and H. Hosono, Science **300**, 1269 (2003).
8. N. R. Armstrong, P. A. Veneman, E. Ratcliff, D. Placencia and M. Brumbach, Accounts Chem. Res. **42**, 1748 (2009).
9. T. Minami, Semicond. Sci. Technol. **20**, S35 (2005).
10. G. J. Exarhos and X. D. Zhou, Thin Solid Films **515**, 7025 (2007).
11. I. Hamberg, C. G. Granqvist, K. F. Berggren, B. E. Sernelius and L. Engstrom, Phys. Rev. B **30**, 3240 (1984).
12. P. Erhart, A. Klein, R. G. Egdell and K. Albe, Phys. Rev. B **75**, 153205 (2007).
13. A. Walsh, J. L. F. Da Silva, S. H. Wei, C. Korber, A. Klein, L. F. J. Piper, A. DeMasi, K. E. Smith, G. Panaccione, P. Torelli, D. J. Payne, A. Bourlange and R. G. Egdell, Phys. Rev. Lett. **100**, 167402 (2008).
14. S. Lany and A. Zunger, Phys. Rev. Lett. **98**, 045501 (2007).
15. G. Ballabio, M. Bernasconi, F. Pietrucci and S. Serra, Phys. Rev. B **70**, 75417 (2004).
16. M. Marezio, Acta Crystallographica **20**, 723 (1966).
17. P. D. C. King, T. D. Veal, D. J. Payne, A. Bourlange, R. G. Egdell and C. F. McConville, Phys. Rev. Lett. **101**, 116808 (2008).
18. P. D. C. King, T. D. Veal, F. Fuchs, C. Y. Wang, D. J. Payne, A. Bourlange, H. Zhang, G. R. Bell, V. Cimalla, O. Ambacher, R. G. Egdell, F. Bechstedt and C. F. McConville, Phys. Rev. B **79**, 205211 (2009).
19. A. Bourlange, D. J. Payne, R. G. Egdell, J. S. Foord, P. P. Edwards, M. O. Jones, A. Schertel, P. J. Dobson and J. L. Hutchison, Appl. Phys. Lett. **92**, 092117 (2008).
20. A. Bourlange, D. J. Payne, R. G. Palgrave, J. S. Foord, R. G. Egdell, R. M. J. Jacobs, A. Schertel, J. L. Hutchison and P. J. Dobson, Thin Solid Films **517**, 4286 (2009).

21. K. H. L. Zhang, D. J. Payne, R. G. Palgrave, V. K. Lazarov, W. Chen, A. T. S. Wee, C. F. McConville, P. D. C. King, T. D. Veal, G. Panaccione, P. Lacovig and R. G. Egdell, Chem. Mat. **21**, 4353 (2009).
22. K. H. L. Zhang, A. Walsh, C. R. A. Catlow, V. K. Lazarov and R. G. Egdell, Nano Lett. **10**, 3740 (2010).
23. M. Grundmann, H. Frenzel, A. Lajn, M. Lorenz, F. Schein and H. von Wenckstern, Phys. Status Solidi A-Appl. Mat. **207**, 1437 (2010).
24. H. Frenzel, A. Lajn, H. von Wenckstern, M. Lorenz, F. Schein, Z. P. Zhang and M. Grundmann, Adv. Mater. **22**, 5332 (2010).
25. J. V. Barth, G. Costantini and K. Kern, Nature **437**, 671 (2005).
26. J. Stangl, V. Holy and G. Bauer, Rev. Mod. Phys. **76**, 725 (2004).
27. H. Zheng, J. Wang, S. E. Lofland, Z. Ma, L. Mohaddes-Ardabili, T. Zhao, L. Salamanca-Riba, S. R. Shinde, S. B. Ogale, F. Bai, D. Viehland, Y. Jia, D. G. Schlom, M. Wuttig, A. Roytburd and R. Ramesh, Science **303**, 661 (2004).
28. J. P. Perdew, K. Burke and M. Ernzerhof, Phys. Rev. Lett. **77**, 3865 (1996).
29. G. Kresse and J. Furthmuller, Phys. Rev. B **54**, 11169 (1996).
30. G. Kresse and D. Joubert, Phys. Rev. B **59**, 1758 (1999).
31. A. Bourlange, D. J. Payne, R. M. J. Jacobs, R. G. Egdell, J. S. Foord, A. Schertel, P. J. Dobson and J. L. Hutchison, Chem. Mat. **20**, 4551 (2008).
32. P. W. Tasker, Journal of Physics C-Solid State Physics **12**, 4977 (1979).
33. C. Noguera, J. Phys.-Condes. Matter **12**, R367 (2000).
34. J. Goniakowski, F. Finocchi and C. Noguera, Rep. Prog. Phys. **71**, 016501 (2008).
35. F. N. Skomurski, R. C. Ewing, A. L. Rohl, J. D. Gale and U. Becker, Am. Miner. **91**, 1761 (2006).
36. G. W. Watson, E. T. Kelsey, N. H. deLeeuw, D. J. Harris and S. C. Parker, J. Chem. Soc.-Faraday Trans. **92**, 433 (1996).
37. F. Lallet, N. Olivi-Tran and L. J. Lewis, Phys. Rev. B **79**, 035413 (2009).
38. Y. F. Hao, G. W. Meng, C. H. Ye and L. D. Zhang, Cryst. Growth Des. **5**, 1617 (2005).
39. J. Tersoff and R. M. Tromp, Phys. Rev. Lett. **70**, 2782 (1993).
40. M. S. J. Marshall and M. R. Castell, Phys. Rev. Lett. **102**,146102 (2009).
41. A. Walsh, C. R. A. Catlow, A. A. Sokol and S. M. Woodley, Chem. Mat. **21**, 4962 (2009).
42. J. Zabaleta, N. Mestres, P. Abellan, M. Gibert, F. Sandiumenge, T. Puig and X. Obradors, Nanotechnology **21**, 025302 (2010).
43. L. J. Lauhon, M. S. Gudiksen, C. L. Wang and C. M. Lieber, Nature **420**, 57 (2002).
44. Z. W. Pan, Z. R. Dai and Z. L. Wang, Science **291**, 1947 (2001).

Chapter 5:

Temperature and Thickness Dependence of Strain, Bandgap and Transport Properties of Epitaxial In_2O_3 Thin Films Grown on YSZ (111)

5.1 Introduction

In the last chapter, it became clear that (111) oriented YSZ is the most promising substrate for heteroepitaxial growth of highly quality In_2O_3 single crystal thin films, owing to the fact that the (111) surface of In_2O_3 has the lowest energy amongst the low index surfaces. The larger energies for (100) and (110) surfaces drive formation of island and nanorod structures on the respective surfaces.[1-5] Thus, the aim of this chapter is to optimize the growth parameters for preparation of high-quality single-crystalline In_2O_3 thin films on YSZ(111).

At present, the transparent conducting oxides used in technological situations are usually in the form of polycrystalline thin films deposited on glass or polymer substrates by sputtering techniques.[6, 7] Compared with other functional metal oxides[8-10] such as high temperature perovskite-related superconductors (e.g.$YBa_2Cu_3O_{7-x}$), ferromagnetic conductors and oxide ferroelectrics, the epitaxial growth of high-quality In_2O_3 thin films is still in its infancy. However recent prospects for development of TCO materials as the active layer in transparent optoelectronic devices have spawned a flurry of recent work in this field.[11, 12] To date most work on growth of epitaxial single crystal In_2O_3 films has concentrated on deposition of In_2O_3 on alumina[13, 14] and YSZ single crystal substrates by pulsed laser deposition (PLD) in ultrahigh vacuum compatible chambers (i.e. "laser"

molecular beam epitaxy), although there are some reports of single crystal growth by metalloorganic chemical vapour deposition and by molecular beam epitaxy (MBE) using conventional indium Knudsen cells and oxygen atom plasma sources.[1, 3, 15-17] This is likely one of the reasons why many fundamental properties of TCOs remain controversial or unexplored, for example the origin of intrinsic *n*-type conductivity and the possibility of preparing *p*-type TCOs.[18, 19]

In heteroepitaxial growth of material A on lattice mismatched B, material A grows pseudomorphically with a misfit strain which can be accommodated elastically below a critical thickness. When the critical thickness is exceeded, it becomes energetically favourable to generate misfit and threading dislocations to relieve the build-up strain within the film. The growth temperature determines the thermal energy required for atom diffusion and the energetic contribution provided by the entropies associated with defect formation. The physical properties of functional oxides can be in principle engineered during epitaxial growth by tuning the crystal chemistry, strain, and other variables.[9, 10, 20, 21] For example, it has been demonstrated that imposition of a biaxial strain in a magnetite thin film through lattice mismatch with a substrate can lead to changes in magnetic and transport properties caused by cation substitution in the bulk.[20, 21] The point defects and screw dislocations formed during epitaxial growth have strong influence on the critical current density of CuO-based high-T superconductors.[22] `

These considerations motivate us to explore the dependence of physical properties of the In_2O_3 epitaxial thin films on YSZ(111) on different growth conditions. The main parameters involved are growth temperatures and film thicknesses. The dependence of the properties of the films on growth temperature and thickness was examined in a systematic way, using a combination of experimental and computational methods. It was found that the optimal growth temperature is 700°C. It was also shown that there is a

clear correlation between film thicknesses, film morphology and transport properties. Further investigation also showed that ultrathin films are highly strained and this strain leads to a small but significant reduction in the value of the optical band gap.

5.2 Experimental Section

5.2.1 Thin Film Growth

The epitaxial In_2O_3 thin films were grown on (111) oriented 1 cm × 1 cm Y-ZrO_2 substrates in an ultrahigh vacuum oxide MBE system (SVT, USA), as described in the previous chapter. The nominal growth rate was 0.035 nms^{-1} calibrated using the thickness from high resolution transmission electron microscopy (HRTEM) measurements and atomic force microscopy (AFM) images. The Y-ZrO_2 substrates were cleaned by exposure to the oxygen atom beam at a nominal substrate temperature of 860 °C. We explored a range of substrate temperatures between 550 ^oC and 860 ^oC, with a fixed deposition time of 3000 seconds. This corresponds to a nominal film thickness of 105 nm assuming a layer by layer growth mode. The films grown at high substrate temperature may be thinner due a reduction in the sticking coefficient of the In and O species. Thin films with different thickness ranging between 35 nm and 420 nm were grown at a fixed temperature of 700 ^oC by varying the deposition time.

5.2.2 Characterizations

High resolution x-ray diffraction (XRD) θ-2θ measurements were performed on a Philips Xpert diffractometer using monochromatic CuKα radiation (λ=1.54060 Å). AFM images were recorded *ex situ* with a Digital Instruments Multimode SPM instrument, as described in the previous chapter.

Specimens for cross-sectional TEM were prepared by cutting and mechanical grinding down to 5-10 μm, followed by thinning to electron transparency by Ar ion beam milling using a Gatan 691 Precision Ion Polishing System (PIPS). Cross-sectional TEM images were collected using a JEOL3000F microscope operating at 300 keV. Cross-sectional TEM images were collected using a JEOL3000F microscope. Digital Micrograph image software was used to process the TEM images. UV-visible optical absorption spectroscopy measurements were performed using a using a Perkin Elmer Lambda instrument. The electrical properties of the In_2O_3 films with different thickness were characterised by Hall effect measurements using the van der Pauw method at room temperature.

5.3 Computational Details

To provide an accurate description of the structural, elastic and electronic properties of In_2O_3 under conditions of epitaxial strain, a combination of classical and quantum computational techniques was employed. This work was carried out by Dr. Aron Walsh from University of College London. A recently developed a pair-wise interatomic potential for In_2O_3 based on the Born Model of the ionic solid was used in this work[23]. The classical electrostatic energy, obtained from an Ewald summation, is combined with a short-range potential of the Buckingham form. The potential model has been successful in describing the high pressure phase transitions of the material[24], in addition to defect formation and diffusion reactions[25]. Full details of the parameterisation can be found elsewhere[24]. The pertinent structural and elastic properties resulting from this model for In_2O_3 are collected in Table 1, as calculated within the code GULP[26].

Property	Experiment	Potential Model
a (Å)	10.117[23]	10.121
ε_0^{11}	8.9 – 9.5[27]	9.05
ε_∞^{11}	4.0[27]	3.90
C_{11} (GPa)		297.75
C_{12} (GPa)		141.78
C_{44} (GPa)		76.42
γ		0.323
E (GPa)		206.29

Table 1. Calculated properties of In_2O_3 in the bixbyite mineral structure: a is the cubic lattice constant, ε_0 and ε_∞ are the static and high frequency dielectric constants and C_{ij} are the elastic constants, γ is Poisson's ratio, and E is Young's modulus.

In order to obtain information regarding the electronic properties, Dr. A. Walsh *et al.* also performed calculations based on Density Functional Theory (DFT)[28, 29]. These calculations were performed using a plane-wave basis set (with a well-converged 500 eV kinetic energy cutoff), within the code VASP[30, 31]. Further details of the computational setup can be found elsewhere[32, 33]. In order to obtain accurate trends in the material's band gap as a function of epitaxial strain, a hybrid density functional (HSE06[34, 35]) was employed, which has demonstrated recent success in describing the electronic properties of oxide materials[36, 37], including the surface work functions of In_2O_3 itself[38]. At this level of theory, the equilibrium lattice constant of a = 10.156 Å is within 0.5 % of the experimental value.

To simulate the effect of epitaxial strain, the cubic bixbyite lattice was reoriented along the [111] direction using a lattice vector transformation of the form:

$$\begin{bmatrix} -1 & 0 & 1 \\ 0 & 1 & -1 \\ 1 & 1 & 1 \end{bmatrix}$$

which results in a hexagonal supercell, in which the epitaxial ($a_e\sqrt{2}$) and uniaxial ($a_e/\sqrt{3}$) lattice constants can be varied independently. The application of strain effectively reduces the lattice symmetry from body-centered cubic ($Ia\bar{3}$) to trigonal ($R\bar{3}$). The same lattice expansion is observed for the ordered compound $In_4Sn_3O_{12}$ [39], which could be regarded as very heavily Sn-doped In_2O_3. Importantly, for optical properties, the centre of inversion is maintained for the lattice expansion within the (111) plane.

5.4 Influence of Temperature on the Epitaxial Growth of In_2O_3

Firstly, we investigated the influence of substrate temperature on the mode of growth of In_2O_3 films over a range of substrate temperatures between 550 °C and 860 °C, in order to optimize the growth temperatures for high-quality In_2O_3 thin films.

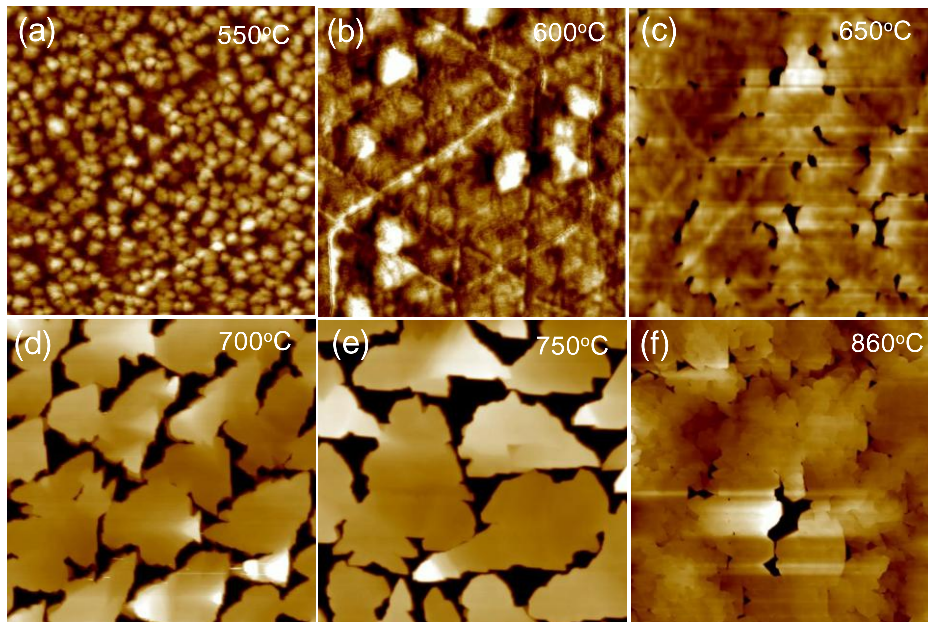

Figure 5. 1. 10 μm × 10 μm topographic AFM images of In_2O_3 epilayers on YSZ (111) grown at different temperatures as indicated in the images. The deposition time was fixed for 3000 seconds for all the samples.

5. 4.1 Surface Morphology: AFM studies

The influence of growth temperature on the In_2O_3 film morphology on a micron length scale was investigated by AFM. Figure 5.1 shows large area (10 µm × 10 µm) AFM images of films with a nominal thickness of 105 nm grown at temperature between 550 °C and 860 °C. The film grown at 550 °C exhibited a rough granular morphology (Figure 5.1a) but with contact between the grains to give a continuous film. The surface grains or columns have lateral dimensions typically of the order of 300 nm, giving a root mean square (RMS) surface roughness of 4.5 nm. A zoom-in AFM image (2 µm × 2 µm) in figure 5.2a shows that the grains have a fractal shape and rugged top surfaces. This suggests the limited surface diffusion length of the In and O ad-atoms during low temperature growth results in poor crystalline quality. This is consistent with Hall effect measurements of films grown at low temperature which reveals a low carrier mobility of around 5-10 $cm^2V^{-1}s^{-1}$. The carrier concentration in these films is typically around 3.0×10^{18} cm^{-3} which is somewhat below the value of about 7×10^{18} cm^{-3} required to exceed the Mott criterion for the onset of metallic behaviour.[4] The film grown at 600 °C (Figure 5.1b) has a smoother surface than that grown at 550 °C with a reduced RMS surface roughness of 1.8 nm. Furthermore the lateral size of the grains grows to around 1 µm, so that the density of grain boundaries decreases. Upon increasing the substrate temperature to 650 °C as shown in Figure 5.1c, the continuous films tend to break up and pinholes are found on the surface of film. This tendency develops further for yet higher growth temperatures as can be easily seen for films grown at 700 °C (Figure 5.1d) and 750 °C (Figure 5.1e). The film microstructure is now based on flat-topped and loosely connected mesa dissected by deep troughs. The mesa have serrated edges with a characteristic angle in many of the serrations of around 60°, reflecting the influence of the three-fold

symmetry of the substrate. The lateral size of the mesa grown at 750 °C is around 5 μm, which is larger than for the film grown at 700 °C. The depth of the troughs is around 150 nm as gauged from AFM line profiles. This is somewhat bigger than the nominal thickness of the films but of course the coverage of the surface is no longer uniform and material from the troughs must be incorporated on the top of the mesa. X-ray photoemission spectra contain substrate Zr 3d and Y 3d peaks, indicating the exposure of bare substrate in the trough area. The tops of the films grown at 700 °C and 750 °C exhibit large flat terraces with occasional steps of height 0.3 ± 0.03 nm, as shown in Figure 5.2b. This distance corresponds to $a/2\sqrt{3}$ = 0.292 nm which reflects the interplanar spacing between atomic layers along the [111] direction of the bixbyite structure of In_2O_3. Overall there seems to be a significant improvement of the crystalline quality at higher temperature. As shown in the next section, upon increasing the deposition time at 700 °C, the mesa grow laterally and ultimately coalesce into a continuous thin film with high crystalline quality.

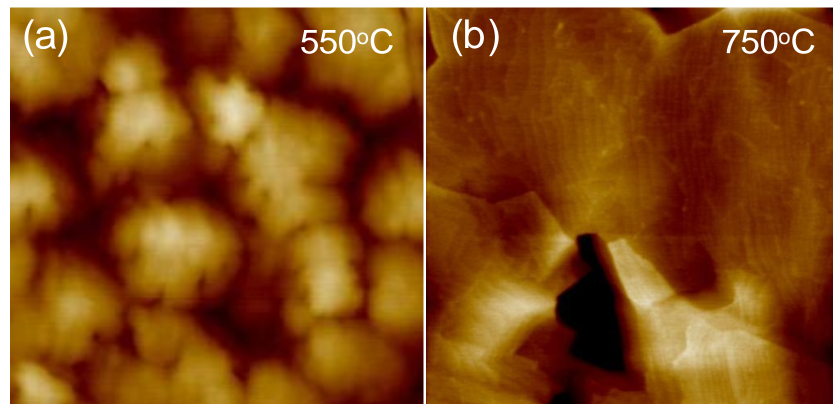

Figure 5. 2. Zoom-in AFM images (2 μm × 2 μm) of In_2O_3 epilayers grown at (a) 550 °C, showing a rough fractal surface; and (b) 750 °C, showing atomic flat terraces on the top islands.

Taken together, the AFM results suggest the improved surface morphology and improved crystalline quality that results from increasing the substrate temperature arises because of the enhanced surface diffusion length of In and O adatoms. At low temperature the dominant kinetic factors give rise to a granular growth mode due to the limited surface mobility, while high substrate temperature progressively drives the growth into a region where there is thermodynamic control.

5.4.2 The Interface: Cross-sectional TEM studies

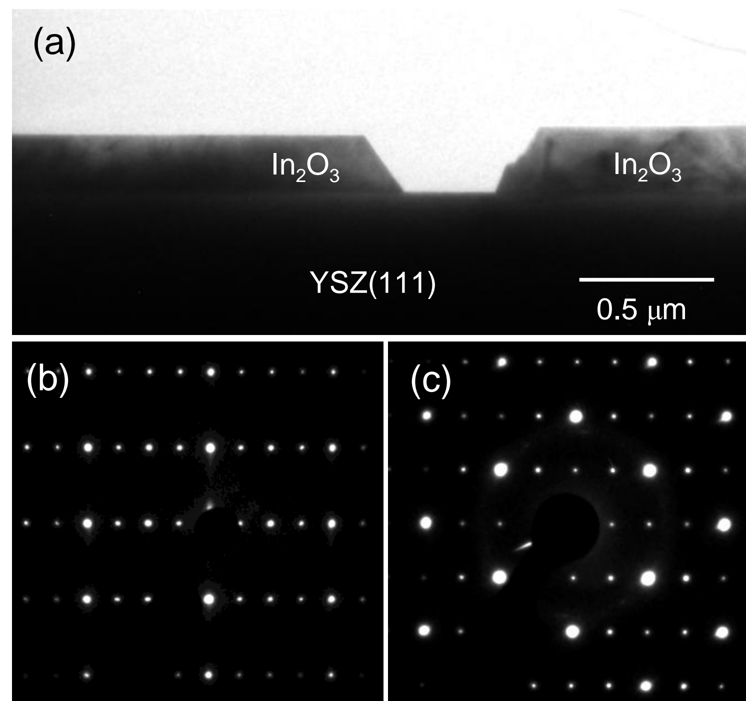

Figure 5. 3. Cross-sectional TEM results on an In_2O_3 epilayer on YSZ (111) grown at 750 °C (a) low magnification image; (b) and (c) Selected area electron diffraction (SAED) viewed down to $[1\bar{1}0]$ and $[1\bar{2}1]$ direction, respectively.

Cross-sectional TEM was used to examine the epitaxial relationship between the In_2O_3 epilayer and the substrate and to probe the interface structure. Figure 5.3a shows a low resolution TEM image of a film grown at 750 °C substrate temperature viewed down th

$[1\bar{1}0]$ direction. This reveals a flat crystalline In_2O_3 film with a well-defined substrate/epilayer interface. It also confirms that the bottoms of the troughs are free of an In_2O_3 wetting layer, in agreement with the XPS measurements. The film exhibits a smooth top surface, consistent with atomic flat surface observed by AFM. Figure 5.3b and c show the selected area electron diffraction (SAED) pattern taken across the interfaces viewed down to $[1\bar{1}0]$ and $[1\bar{2}1]$ direction, respectively. The near coincidence between the epilayer and substrate diffraction spots demonstrates the "cube-on-cube" epitaxial relationship between the In_2O_3 film and the YSZ substrate: $In_2O_3(111)||YSZ(111)$ and $In_2O_3[1\bar{1}0]||YSZ[1\bar{1}0]$.

5.4.3 θ-2θ X-ray Diffraction: Evidence for Strain

Figure 5.4a shows a wide scan *θ-2θ* X-ray diffraction (XRD) profile of a film grown at 550 °C substrate temperature. Two substrate peaks are observed corresponding toY-ZrO_2(111) and Y-ZrO_2(222) reflections. To higher angles of these peaks, epilayer In_2O_3(222) and In_2O_3(444) can be seen. The intermediate (333) epilayer reflection is however forbidden due to the body centering in In_2O_3. All the other films gave similar XRD profiles. X-ray diffraction therefore confirms that all the In_2O_3 films grow epitaxially with the (111) planes of the epilayer parallel to the (111) direction of the YSZ, regardless of the substrate temperature. Figure 5.4b shows more detailed scans across the In_2O_3(222) and YSZ(111) reflections for In_2O_3 films grown at different temperatures presented on a logarithmic scale. It can be seen that the (222) reflections from the In_2O_3 epilayer shift to lower angle with increasing growth temperature, indicating an increase in the out-of-plane *d* spacing. The out-of-plane *d* spacings obtained from the measured

positions of the (222) diffraction peaks are plotted in Figure 5.4c. All the values are lower than the value of a/√3 = 0.5841 nm expected from the bulk lattice constant of In_2O_3 (a = 1.0117 nm). The reduced values of the d spacing can be explained on the basis that the In_2O_3 film is placed under tensile stress due to the 1.6% mismatch between YSZ substrate and the In_2O_3 epilayer. The tensile stress gives rise to a lateral expansion in-plane, which in turn leads to a decrease in the interatomic separations normal to the surface. It can also be seen that the continuous films grown below 600 °C are under higher tensile strain than films grown at temperature above 700 °C. Moreover there is an abrupt relaxation of strain between growth temperatures of 600 °C and 700 °C. These changes parallel those seen in AFM where continuous granular films grown at 600 °C break up to give the characteristic mesa-like structure of films grown at 700 °C. The changes arise because limited thermal energy is available at lower temperatures to overcome the kinetic barrier to formation of the dislocations which allow release of strain. Nonetheless the d spacing for films grown at the highest temperature of 860 °C is still significantly less than the bulk value alluded to above so that release of strain is not complete. The changes found for growth on (111) oriented substrates parallel those seen for films grown on (100) substrates[2, 3]. However on the latter substrates the "break-up" is more complete and films grown at 900 °C consist of an array of isolated truncated square pyramidal islands with typical lateral dimensions of order 1 μm. For films grown on (100) oriented substrates the energy associated with release of strain is augmented by development of {111} side facets on the pyramidal islands, which reduces the overall surface energy.

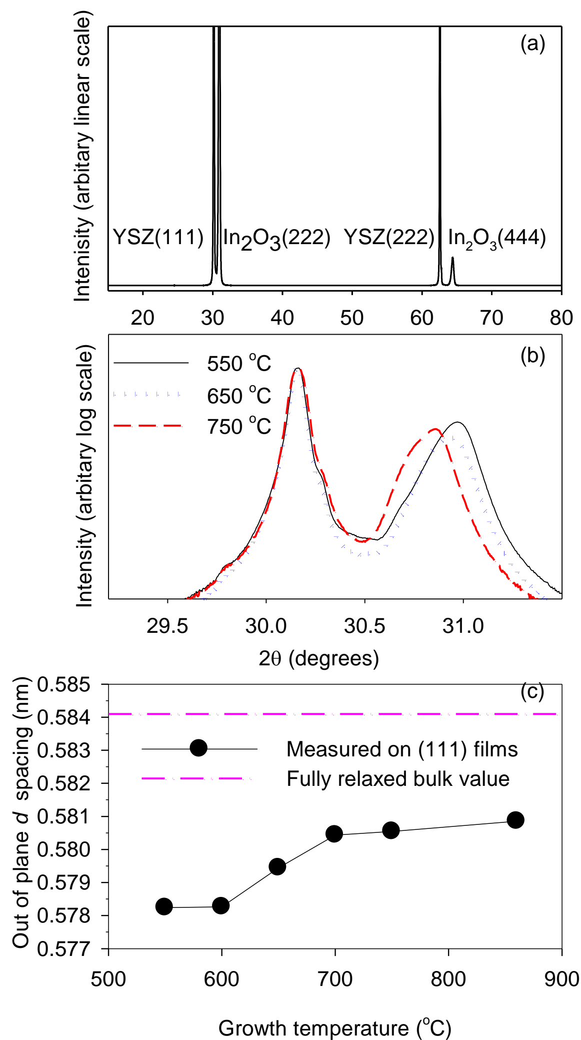

Figure 5.4. (a) Wide scan *θ-2θ* x-ray diffraction profile of In_2O_3 epilayer grown on YSZ (111) at 550 °C; (b) *θ-2θ* x-ray diffraction profiles of In_2O_3 epilayer taken across the substrate (111) peak and the epilayer (222) peaks for three different growth temperature: 550 °C, 650 °C and 750 °C; (b) Out-of-plane *d* spacing for epitaxial In_2O_3 obtained from XRD diffraction peaks as a function of growth temperature.

5.4.4 Post-annealing Effects

Finally we explored the effects of high temperature post-annealing on the film grown at 550 °C. Figure 5.5a shows an AFM image of a film deposited at the lower temperature and then annealed at 750 °C for 1 hour under an oxygen atmosphere. From comparison with Figure 5.1a it can be seen that the film becomes flatter after annealing: the RMS surface roughness decreases from 4.5 nm to 3.8 nm and the size of the grains increase

from 300 nm to about 600 nm, indicating the improved crystalline quality after annealing. Moreover it can be seen in Figure 5.5 b that the In_2O_3(222) XRD peak shifts towards lower angle and the out-of-plane constant moves closer to that of the bulk, indicating the relaxation of tensile strain by thermal treatment.

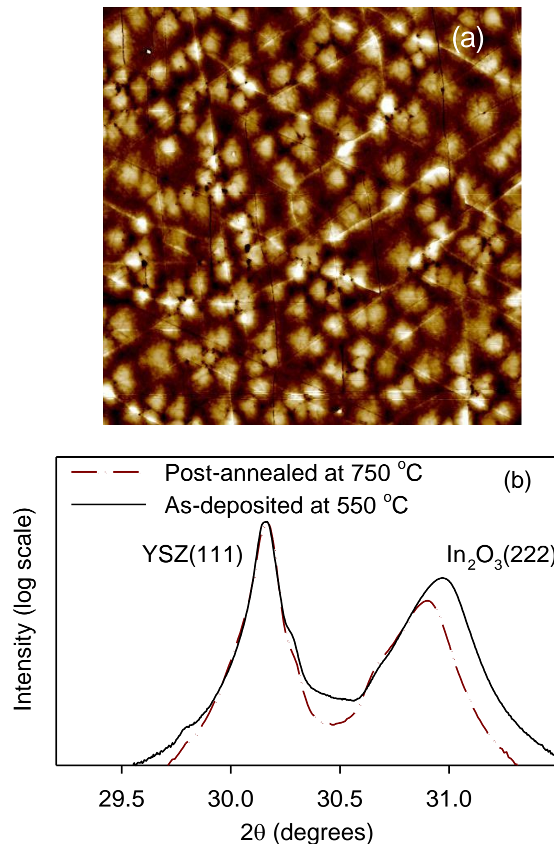

Figure 5.5. (a) 10 μm × 10 μm AFM image of In_2O_3 on YSZ (111) at 550 °C followed by post-annealing at 750 °C for 2 hours; (b) *θ-2θ* x-ray diffraction profiles of for the 550 °C as-grown sample and 750 °C annealed sample.

5.4.5 Summary of Influence of Temperature on the Epitaxial Growth

In this section, we have investigated the influence of the growth temperature on the epitaxial growth of In_2O_3 thin films on YSZ(111). The surface morphology shows strong temperature dependence. Low temperature growth (T < 650 °C) leads to granular and continuous epitaxial thin films. The granular structure degrades the crystalline quality,

thus giving rise to low carrier mobility. However when the growth temperature was increased to 700 °C or above, the films broke up into micron sized mesa. The mesa films exhibited atomic flat surfaces on top, indicating the enhanced crystalline quality resulting from growth at high temperature. The improved surface morphology and improved crystalline quality that results from increasing the substrate temperature arises because of the enhanced surface diffusion length of In and O adatoms. At low temperature the dominant kinetic factors give rise to a granular growth mode due to the limited surface mobility, while high substrate temperature progressively drives the growth into a region where there is thermodynamic control. X-ray diffraction revealed that this change in morphology is associated with release of tensile strain within the epitaxial films. Taken together, the present results indicate that 700 °C is the most promising growth temperature for high-quality thin films. Thus in the next section, we explore the influence of thicknesses on the properties of thin films grown at 700 °C.

5.5 Thickness Dependence of the Strain, Band gap and Transport Properties

It turns out that the films grown at 700 °C have the improved morphology and crystalline quality. In the this section, we will examine the thickness dependence of the strain, band gap and transport properties of epitaxial In_2O_3 thin films over a range between 35 nm and 420 nm, using a combination of experimental and computational methods.

5.5.1 Structure and Morphology

A low magnification TEM image of a 75 nm thick film viewed down the $[1\bar{1}0]$ direction is shown in Figure 5.6 a, revealing a sharp and well defined substrate/epilayer interface.

Figure 5.6b shows a high resolution TEM image taken across the interface, whilst Figure 5.6c is the corresponding selected area electron diffraction (SAED) pattern. The near coincidence between the substrate and the epilayer diffraction spots demonstrates the faithful epitaxial relationship between the In_2O_3 film and the YSZ substrate, whilst HRTEM demonstrates an atomically sharp interface.

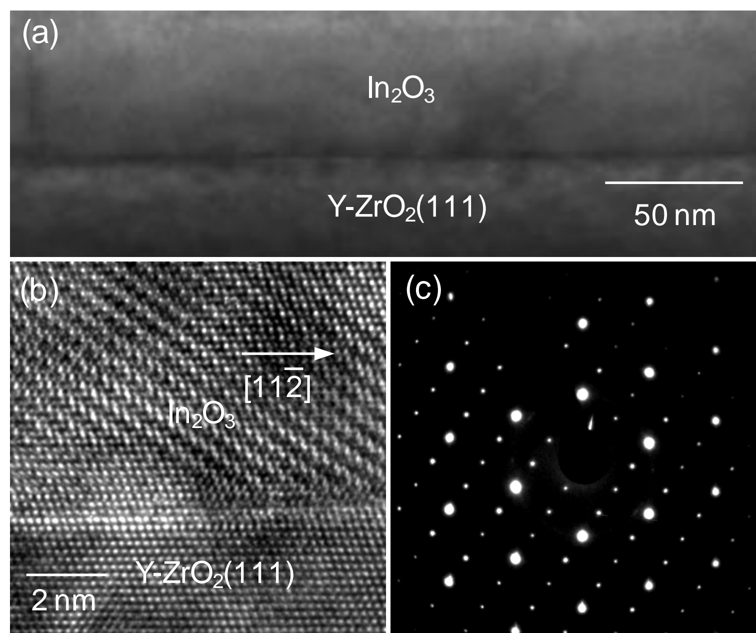

Figure 5.6. Cross-sectional transmission electron microscopy (TEM) results on an In_2O_3 epilayer on YSZ (111), with a thickness of 70 nm: (a) low magnification image, (b) high resolution TEM image viewed down the $[1\bar{1}0]$ direction, and (c) corresponding selected area electron diffraction (SAED).

5.5.2 Evolution of Strain: X-ray Diffraction

Figure 5.7a shows a θ-2θ X-ray diffraction trace for a typical thin film sample with a thickness of 105 nm. Epilayer (222) and (444) reflections appear to a slightly higher angle of the (111) and (222) reflections of the substrate, but no other peaks are observed – the intermediate epilayer (333) reflection is not allowed for a body centred space group.

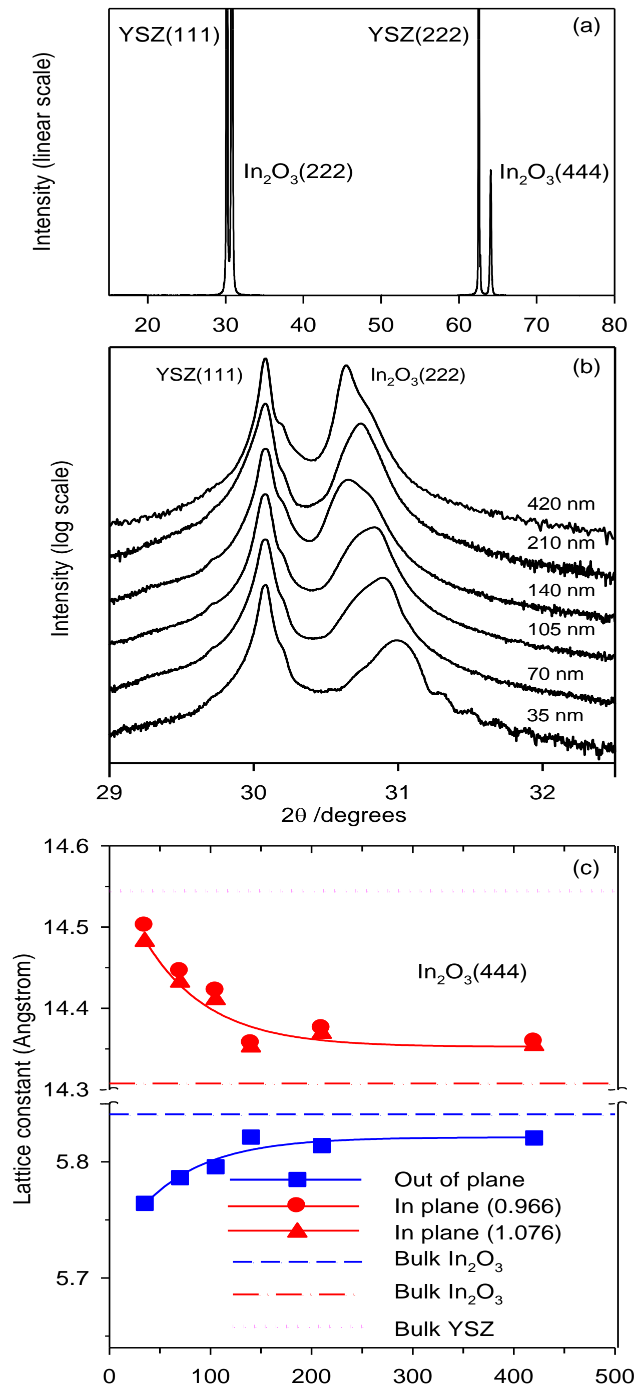

Figure 5.7. (a) θ-2θ x-ray diffraction profile of In_2O_3 a typical epilayer on Y-stabilised ZrO_2 presented on linear scale showing substrate (111) and (222) reflection, along with epilayer (222) and (444) reflections. (b) θ-2θ x-ray diffraction profiles presented on logarithmic scale of In_2O_3 epilayer on Y-stabilised ZrO_2 taken across the substrate (111) peak and the epilayer (222) peak as function of film thickness. (c) Out-of-plane ($c_{\perp}$) and in-plane ($a_{\parallel}$) lattice constants for epitaxial In_2O_3 obtained from XRD diffraction peaks in (b) using the two different values of the ratio between in-plane and out-of-plane strain discussed in the text to derive $a_{\parallel}$. The corresponding values for the substrate and for the unstrained In_2O_3 are shown as horizontal lines.

These results confirm that the In_2O_3 films grow epitaxially, with the (111) planes of the epilayer parallel to the (111) planes of the YSZ substrate across the complete range of thicknesses studied. Figure 5.7b shows scans across the In_2O_3(222) and YSZ(111) reflections for In_2O_3 films of different thickness. The In_2O_3(222) reflection shifts to lower angle with increasing film thickness, indicating an increase in the out-of-plane *d* spacing. The change in *d* spacing can be explained on the basis that the In_2O_3 film is placed under tensile stress due to the 1.6% mismatch between the YSZ substrate and the In_2O_3 epilayer. The tensile stress gives rise to a lateral expansion in-plane, which in turn leads to a decrease in the interatomic separations normal to the surface. The unit cell in the strained layer is therefore hexagonal rather than cubic with an in-plane lattice constant $a_{||}$ that is slightly greater than $\sqrt{2}a_e$ and an out-of-plane constant $c_\perp$ that is slightly less than $a_e/\sqrt{3}$. For a (111) oriented epilayer of a cubic material, the in-plane strain $\varepsilon_{||}$ is related to the out-of-plane strain $\varepsilon_\perp$ through the relationship [40]:

$$\epsilon_\perp = -\epsilon_\parallel \frac{2C_{12} - 2C_0/3}{C_{11} + 2C_0/3}$$

where:

$$C_0 = 2C_{44} - C_{11} + C_{12}$$

The C_{ij} are the elastic constants of the bulk material. Due to the absence of large single crystal samples, reports on experimental values of the elastic properties of In_2O_3 are scarce. However, using the interatomic potential model that Walsh *et al.* have developed[24], the three independent elastic constants were calculated as C_{11} = 297.75 GPa, C_{12} = 141.78 GPa and C_{44} = 76.42 GPa and the derived value for C_0 as defined above is -3.13 GPa. It is thus possible to make the estimate:

$$\epsilon_\perp = -\epsilon_\parallel \times 0.966$$

This equation can be given in an alternative approximate form:

$$\epsilon_{\perp} = -\epsilon_{\parallel} \frac{2\gamma}{1-\gamma}$$

where γ is the Poisson ratio. Based on the Poisson ratio determined using our potential model (γ = 0.323), the uniaxial response remains largely unchanged at 0.954. An empirical estimate of γ = 0.35 is available from X-ray diffraction data [41], which gives:

$$\epsilon_{\perp} = -\epsilon_{\parallel} \times 1.076$$

This value is comfortably close to the potential model (within 10%), when one considers that the potential model represents the limit at T = 0 K and in the absence of any structural defects. The values of $c_{\perp}$ obtained from the θ-2θ diffraction profiles along with the derived values of $a_{\parallel}$ using the two different estimates of the strain ratio are plotted in Figure 5.7c as a function of film thickness. The $c_{\perp}$ values are all lower than the value of $a_e/\sqrt{3}$ = 5.843 Å for bulk In_2O_3, although the values for the thicker films come close to this value. Conversely the value for $a_{||}$ for the thinnest film comes close to matching the substrate value of $2\sqrt{2}a_s$ expected for a coherently strained epilayer. However, even for the thinnest film, the strain does not enable perfect matching. According to Matthews-Blakeslee theory [42], the critical thickness up to which strained pseudomorphic growth mode with perfect lattice matching can be preserved is around 10 nm for 1.6% mismatch. Thus even for the thinnest film (35 nm) studied in the current work, one is above this limit. However, from studies of heteroepitaxial III-V systems, it has been suggested that the Matthews-Blakeslee theory underestimates the critical thickness[43]. Indeed significant lattice relaxation has been found not to occur until layer thicknesses exceed the Matthews-Blakeslee limit by about a factor of ten. When the film thickness is increased

to above 140 nm, the residual strain is almost completely relaxed, consistent with this "Matthews-Blakeslee critical thickness multiplied by ten" rule of thumb.

5.5.3 Surface Morphology: AFM Studies

The surface morphologies of the In_2O_3 films show pronounced thickness dependence as seen in the AFM images of Figure 5.8.

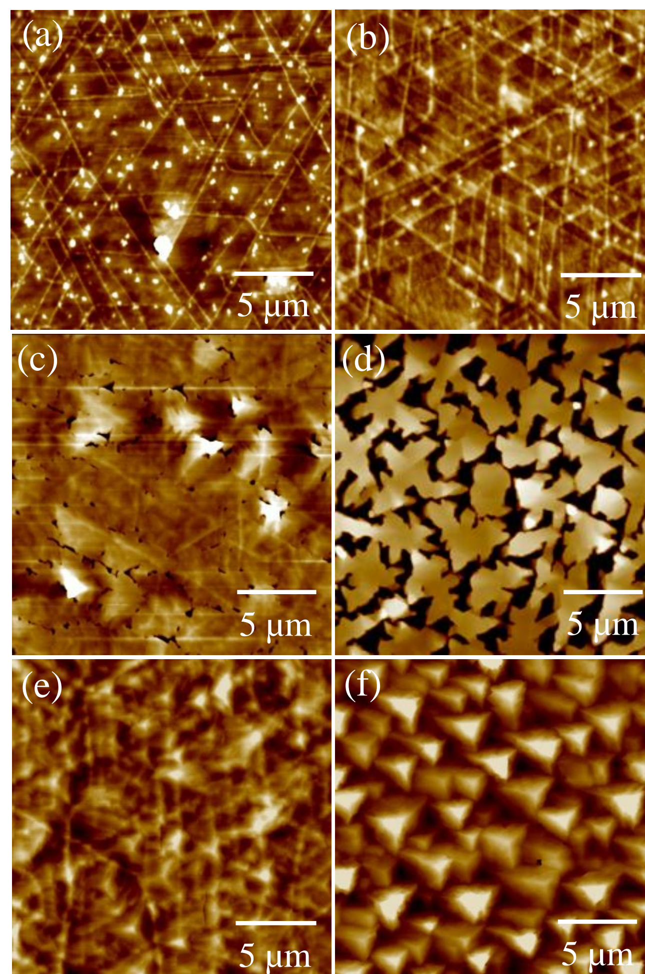

Figure 5.8. AFM images (20 µm × 20 µm) of the surface morphological evolution of the In_2O_3 epilayers on YSZ (111) as function of film thickness: (a) 35 nm; (b) 70 nm; (c) 105 nm; (d) 140 nm; (e) 210 nm; (f) 420 nm.

The film with 35 nm thickness is continuous (Figure 5.8a), with a reasonably flat surface characterised by a root mean square (RMS) roughness of 1.4 nm. The surface is however

crossed by ridges with a height of 1.8 nm and width of 180 nm running along <110> directions. The ridges intersect each other with a characteristic angle of 60° leading to a so-called "cross-hatch" surface morphology. Similar morphology has been observed in other heteroepitaxial growth systems with lattice mismatch less than 2%, such as $GaAs_{1-x}P_x$/GaAs [44] and $Si_{1-x}Ge_x$/Si [45-47]. It has been proposed that the cross-hatch patterns are associated with the formation of a network of dislocations at the interface. The 1.6% mismatch between In_2O_3 and YSZ is in the same regime and it is reasonable to conclude that the cross-hatch morphology is again associated with strain relaxation by generation of misfit dislocations. For slightly thicker films, such as the 70 nm film shown in Figure 5.8b, the density and amplitude of the cross-hatch ridges increases, with a corresponding increase of dislocation density due to dislocation nucleation and multiplication process[48]. This is consistent with the rapid increase of the out-plane lattice constants as the film thickness increases, which has been found in the XRD measurements. However, there is still residual strain and as this accumulates in the In_2O_3 film with further increasing coverage, a "dewetting" process is favoured[49]. Pinholes or trenches are formed on the surface of a film with nominal thickness of 105 nm (Figure 5.8c), whilst after increasing the coverage to 140 nm, the film breaks up into loosely connected mesa with an average size of about 2 μm (Figure 5.8d). The observed "dewetting" transition from 2D to island-like growth indicates the instability of the "cross-hatched" structure above a critical thickness. When the coverage is further increased (Figure 5.8e and f), the In_2O_3 mesa grow laterally and gradually coalesce into a continuous flat thin film with atomic steps. Meanwhile, a sharp unreconstructed In_2O_3(111)-(1×1) diffraction pattern is observed with *in-situ* LEED, indicating the high crystal quality of the thin film after the strain

relaxation process. (The surface structures of the atomically flat film will be discussed in the next chapter)

5.5.4 Electrical Transport Properties

The electrical properties of the In_2O_3 films with different thickness were characterised by Hall effect measurements using the van der Pauw method at room temperature. Figure 5.9 shows the Hall mobility and carrier concentration of In_2O_3 thin films as a function of thickness.

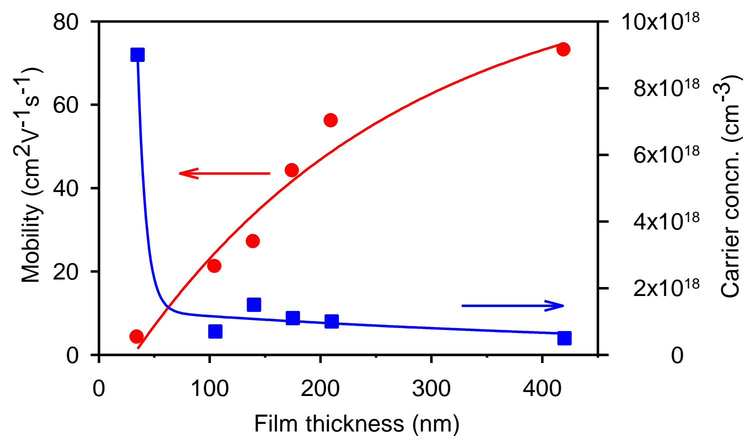

Figure 5.9. Thickness dependent room temperature carrier mobility and carrier concentration of In_2O_3 films measured by the Hall effect using the Van der Pauw method.

The 35 nm thick film exhibits the lowest carrier mobility (4.4 $cm^2V^{-1}s^{-1}$) and highest carrier concentration (9.1 $\times 10^{18}$ cm^{-3}). The 420 nm thick film shows the highest carrier mobility (73 $cm^2V^{-1}s^{-1}$) and a very low carrier concentration (5.0×10^{17} cm^{-3}). The latter is about an order of magnitude lower than the limit for onset of degenerate doping [4]. The optimal mobility is comparable to values of 110 $cm^2V^{-1}s^{-1}$ reported by Koida and Kondo[50] for In_2O_3 grown on YSZ(111) by pulsed laser deposition, although the adventitious carrier concentration in this work was a factor of 10 higher than in the samples grown here. Comparably low doping levels to our own and mobilities of 130

$cm^2V^{-1}s^{-1}$ were reported by Bierwagen et al. for In_2O_3 grown on YSZ(001) under In rich conditions [51].

Analysis of the electronic structure, from explicit DFT calculations of the strained 35nm and 420 nm films, reveals that the dispersion in the conduction band does not change significantly when the system is strained: the isotropic electron effective mass $m^*=(1/\hbar^2)(d^2\varepsilon/dk^2)$ reduces from 0.25 m_e for the bulk material to 0.22 m_e and 0.24 m_e in the 35 nm and 420 nm mismatched films, respectively. The carrier mobility is proportional to $(1/m^*)$; however, the small magnitude of the calculated change suggests that the measured change in electron mobility is not determined by a fundamental change in the host band structure. The corresponding band dispersion diagrams are plotted in Figure 5.10.

In heteroepitaxial thin film growth, dislocations are generally in the form of half-loops comprised of a segment of an edge dislocation parallel to the interface and two threading dislocations (TDs), which are inclined or perpendicular the interface.[17] For the thinner In_2O_3 film, a high density of dislocation half-loops is generated within the film in order to release the misfit strain. The dislocation loops may be associated with non-stoichiometric donor defects. The nature of donor defects in In_2O_3 is however a controversial issue. The widely presumed assumption that oxygen vacancies act as shallow donors has recently been called into question [52] and the oxygen partial pressure dependence of the donor concentration suggests instead that the donors in sputtered thin films may be singly ionised In-O interstitials [53], that is $(In_i^{\bullet\bullet\bullet}O_i^{''})^{\bullet}$ in Kröger-Vink notation; further work to clarify the microscopic nature of the defect chemistry is currently underway. In addition, dislocations may be decorated by interstitial hydrogen, which acts a donor in In_2O_3 and other closely related oxides [54].

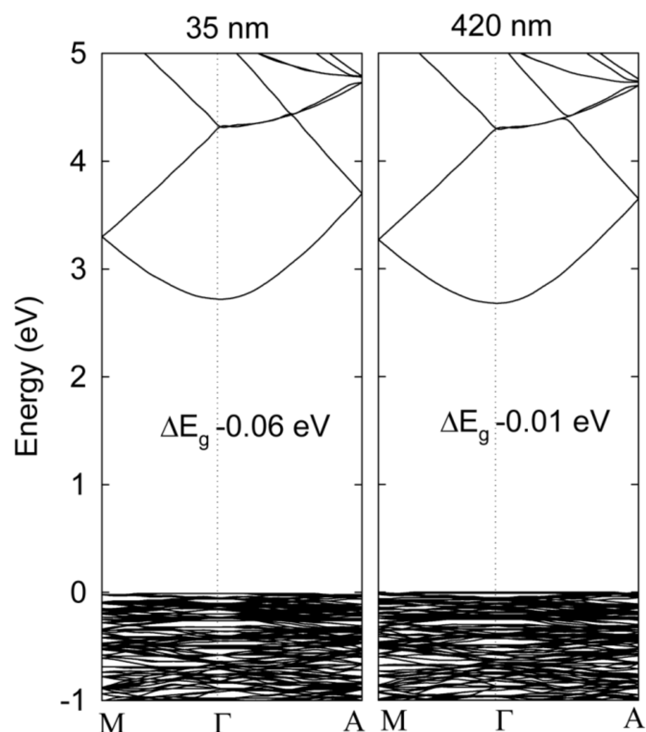

Figure 5.10. Electronic band structure of (111) epitaxially strained In_2O_3 films, as calculated using density functional theory. The highest occupied state is set to 0 eV.

The high density of misfit dislocations that must be present in very thin In_2O_3 films act both as donors and as scattering centre for free electrons, giving rise to low carrier mobility. As the film thickness increases, the dislocation half-hoops may grow and combine together to form long misfit dislocations at the interface. Strain in the films is gradually relaxed by the formation of misfit dislocations at the In_2O_3/YSZ interface. The threading dislocation density, however, decreases with increasing film thickness due to the combination or mutual annihilation of adjacent threading dislocations. Thus after the termination of the strain relaxation process, a high quality In_2O_3(111) single crystal film with 420 nm thickness can be fabricated.

Our results are similar to the recent literature on the thickness dependence of the conductivity of epitaxial InN films [55-58]. There, it was found that the carrier concentration

dropped from 3×10^{19} cm^{-3} for films with a thickness of about 50 nm to 2×10^{17} cm^{-3} for films of thickness 10,000 nm. At the same time the electron mobility of InN films increased by one order of magnitude from about 300 cm^{2}V^{-1}s^{-1} to about 2,000 cm^{2}V^{-1}s^{-1} [56, 57]. These variations were analysed in terms of a model which identified three parallel contributions to the measured carrier density and mobility. The first was associated with an essentially constant background bulk carrier concentration. The second contribution arose from a surface accumulation layer and the third from an interfacial contribution. The last of these contributions is associated with threading dislocation arising from the misfit strain. It was suggested that the dislocations act as *n*-type donors and that the average density of the dislocations decays exponentially with increasing InN film thickness.

5.5.5 Optical Bandgap

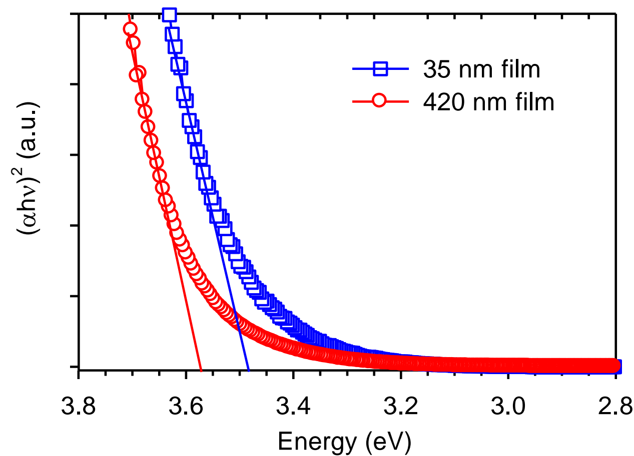

Figure 5.11. Plot of $(\alpha h\nu)^2$ against photon energy ($h\nu$) for In_2O_3 epitaxial films with thicknesses of 35 nm and 420 nm. The curves are extrapolated to $(\alpha h\nu)^2 = 0$, in order to determine the effective direct optical band gap.

Optical absorption spectra for the thickest and thinnest films prepared in the current experiments are shown in Figure 5.11. They are presented as plots of $(\alpha h\nu)^2$ versus photon energy hν, where α is the absorption coefficient. This is the conventional way of using optical data to determine direct allowed energy gaps and is based on the assumption of parabolic bands [59]. The linear extrapolations shown in the figure have intercepts at hν = 3.57 eV for the film with a thickness of 420 nm, and at hν = 3.49 eV for the film with thickness of 35 nm. The optical gap for the thicker film is in general agreement with values reported elsewhere but the small decrease in the band gap for the highly strained 35 nm film is a new observation.

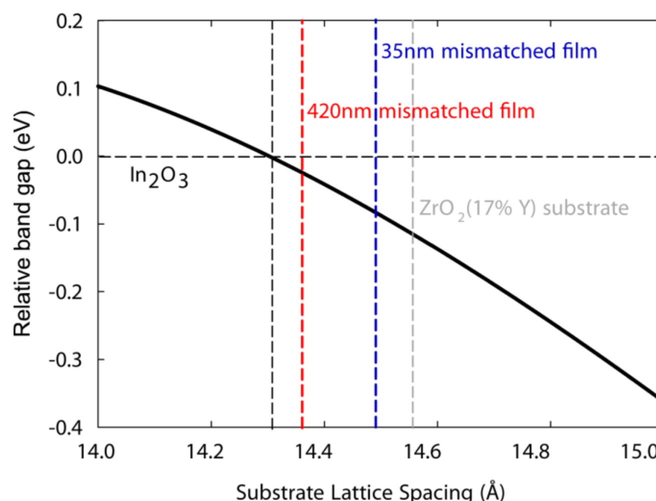

Figure 5.12. Predicted band gap changes for mismatched In_2O_3 films as a function of the epitaxial lattice spacing, and relative to that of bulk In_2O_3.

The effect of epitaxial strain on the band gap of In_2O_3 was also investigated using DFT calculations.[60] The band gap changes are shown in Figure 5.12. for a range of epitaxial lattice spacing; in each case the compensating uniaxial strain is explicitly taken into account. The calculated band gap contraction between the 420 nm and 35 nm films is 0.06 eV, which compares well to the measured value of 0.08 eV. It has been established

that the electronic and optical band gaps are inequivalent due to optically forbidden transitions from the valence to conduction bands, arising from the dipole selection rules associated with the spatial inversion symmetry. In the strained material, these selection rules are maintained and the resulting trends in the optical and electronic band gaps are equivalent, *i.e.* the onset of strong optical transitions still originates from below the top of the valence band.

The observed changes in the band gap arise from the relative energy difference between the valence and conduction bands, but it is instructive to know the absolute contributions in order to understand whether these changes arise from a decrease of the ionisation potential or increase of the electron affinity of the material. The effect of isotropic strain can be characterised through the band gap deformation potential characteristic of the material[61]:

$$\alpha_{V} = \frac{\partial E_g}{\partial lnV}$$

where E_g is the band gap and V is the unit cell volume. For In_2O_3, we calculate α_V to be -4.21 eV, *i.e.* compressing the crystal results in a band gap increase. By breaking α_V down into two component absolute deformation potentials for the band edge states, we obtain:

$$\alpha_V = \alpha_{conduction\ band} - \alpha_{valence\ band}$$

where the valence band deformation potential ($\alpha_{valence\ band}$ = -0.10 eV) is much lower than the corresponding conduction band potential ($\alpha_{conduction\ band}$ = -4.31 eV). These results demonstrate that the band gap changes in response to lattice strain arise primarily from a change in the electron affinity of the materials. The deformation potential found for

In_2O_3 is greater than values close to -1.7 eV calculated for ZnO [62-66], but less than estimates of -7 eV to -8 eV proposed for GaAs and GaN [64, 67]. A deformation potential of -4.21 eV is very close to the values of -3.66 eV [64] and -4.2 eV calculated for InN. Nonetheless, In_2O_3 differs from tetrahedral III-V and II-VI semiconductors in that for the latter $\alpha_{valence\ band}$ typically has a positive value that makes a significant contribution to the overall value of α_V. For In_2O_3 the uppermost flat valence bands are relatively insensitive to volume changes.

5.6 Concluding Remarks

In summary, epitaxial In_2O_3 thin films with thicknesses ranging from 35 nm to 420 nm were grown on YSZ(111) substrates by oxygen plasma assisted MBE. The tensile strain caused by the 1.6% lattice mismatch was gradually relaxed with increasing film thickness. At the same time it was found that the carrier mobility increased with increasing film thickness. High quality (111) oriented films with a low carrier concentration (5.0×10^{17} cm^{-3}) and high mobility (73 $cm^2V^{-1}s^{-1}$) were obtained in the thickest films after strain relaxation. Using a combination of classical and quantum simulation techniques, the uniaxial compression in response of In_2O_3 to the epitaxial tensile strain was quantified, with the former giving rise to a band gap expansion and the latter to a band gap reduction: the net effect is that for thinner highly-mismatched films, the band gap is reduced through a lowering of the conduction band state. These are general effects, which can be exploited in a wider range of metal-oxide systems, either through a judicious choice of growth substrate or through the use of material interfaces and superlattices that introduce coherent lattice strain. It has recently been demonstrated that compressive straining of TiO_2 thin films results in increased visible light absorption[68, 69], which can be explained in the same way as In_2O_3. The implications of this phenomenon are broadly ranging, in particular, strain may be used to control the redox potentials associated with oxide-based electrochemical devices in addition to open-circuit voltages in photovoltaic systems.

The achievement of high quality In_2O_3(111) thin films with atomically flat surfaces is also the basic step to access its structures with atomic-scale details. In following two chapters, we will probe the surface atomic structure (Chapter 6) and

electronic structure (Chapter 7) by surface science techniques such as scanning tunnelling microscopy and synchrotron based photoemission spectroscopy.

5.7 References:

1. A. Bourlange, D. J. Payne, R. G. Egdell, J. S. Foord, P. P. Edwards, M. O. Jones, A. Schertel, P. J. Dobson and J. L. Hutchison, Appl. Phys. Lett. **92**, 092117 (2008).
2. A. Bourlange, D. J. Payne, R. M. J. Jacobs, R. G. Egdell, J. S. Foord, A. Schertel, P. J. Dobson and J. L. Hutchison, Chem. Mat. **20**, 4551 (2008).
3. A. Bourlange, D. J. Payne, R. G. Palgrave, J. S. Foord, R. G. Egdell, R. M. J. Jacobs, A. Schertel, J. L. Hutchison and P. J. Dobson, Thin Solid Films **517**, 4286 (2009).
4. K. H. L. Zhang, D. J. Payne, R. G. Palgrave, V. K. Lazarov, W. Chen, A. T. S. Wee, C. F. McConville, P. D. C. King, T. D. Veal, G. Panaccione, P. Lacovig and R. G. Egdell, Chem. Mat. **21**, 4353 (2009).
5. K. H. L. Zhang, A. Walsh, C. R. A. Catlow, V. K. Lazarov and R. G. Egdell, Nano Lett. **10**, 3740 (2010).
6. C. G. Granqvist and A. Hultaker, Thin Solid Films **411**, 1 (2002).
7. H. Y. Liu, V. Avrutin, N. Izyumskaya, U. Ozgur and H. Morkoc, Superlattices Microstruct. **48**, 458 (2010).
8. J. G. Bednorz and K. A. Muller, Z. Phys. B-Condens. Mat. **64**, 189 (1986).
9. L. W. Martin, Y. H. Chu and R. Ramesh, Mater. Sci. Eng. R-Rep. **68**, III-133 (2010).
10. M. G. Blamire, J. L. MacManus-Driscoll, N. D. Mathur and Z. H. Barber, Adv. Mater. **21**, 3827 (2009).
11. G. Thomas, Nature **389**, 907 (1997).
12. K. Nomura, H. Ohta, K. Ueda, T. Kamiya, M. Hirano and H. Hosono, Science **300**, 1269 (2003).
13. M. Y. Chern, Y. C. Huang and W. L. Xu, Thin Solid Films **515**, 7866 (2007).
14. Z. X. Mei, Y. Wang, X. L. Du, Z. Q. Zeng, M. J. Ying, H. Zheng, J. F. Jia, Q. K. Xue and Z. Zhang, J. Cryst. Growth **289**, 686 (2006).
15. O. Bierwagen, M. E. White, M. Y. Tsai and J. S. Speck, Appl. Phys. Lett. **95**, 072103 (2009).
16. T. Koida and M. Kondo, J. Appl. Phys. **99**, 123703 (2006).
17. E. H. Morales, Y. B. He, M. Vinnichenko, B. Delley and U. Diebold, New J. Phys. **10**, 125030 (2008).
18. S. Lany and A. Zunger, Phys. Rev. Lett. **98**, 045501 (2007).
19. A. Walsh, J. L. F. Da Silva, S. H. Wei, C. Korber, A. Klein, L. F. J. Piper, A. DeMasi, K. E. Smith, G. Panaccione, P. Torelli, D. J. Payne, A. Bourlange and R. G. Egdell, Phys. Rev. Lett. **100**, 167402 (2008).
20. K. H. Ahn, T. Lookman and A. R. Bishop, Nature **428**, 401 (2004).

21. P. K. Muduli, S. K. Bose and R. C. Budhani, J. Phys.-Condes. Matter **19**, 226204 (2007).
22. C. Gerber, D. Anselmetti, J. G. Bednorz, J. Mannhart and D. G. Schlom, Nature **350**, 2790 (1991).
23. M. Born and K. Huang, *Dynamical Theory of Crystal Lattices* (Oxford University Press, Oxford, 1956).
24. A. Walsh, C. R. A. Catlow, A. A. Sokol and S. M. Woodley, Chem. Mat. **21**, 4962 (2009).
25. A. Walsh, S. M. Woodley, C. R. A. Catlow and A. A. Sokol, Solid State Ionics **184** , 52 (2011).
26. J. D. Gale and A. L. Rohl, Molecular Simulation **29**, 291 (2003).
27. I. Hamberg and C. G. Granqvist, J. Appl. Phys. **60**, R123 (1986).
28. W. Kohn and L. J. Sham, Physical Review **140**, 1133 (1965).
29. P. Hohenberg and W. Kohn, Phys. Rev. **136**, B864 (1964).
30. G. Kresse and J. Furthmuller, Physical Review B **54**, 11169 (1996).
31. G. Kresse and J. Furthmüller, Comput. Mater. Sci. **6**, 15 (1996).
32. C. Korber, V. Krishnakumar, A. Klein, G. Panaccione, P. Torelli, A. Walsh, J. L. F. Da Silva, S. H. Wei, R. G. Egdell and D. J. Payne, Physical Review B **81**, 165207 (2010).
33. A. Walsh, J. L. F. Da Silva, Y. F. Yan, M. M. Al-Jassim and S. H. Wei, Physical Review B **79**, 073105 (2009).
34. J. Heyd and G. E. Scuseria, J. Chem. Phys. **121**, 1187 (2004).
35. J. Heyd, G. E. Scuseria and M. Ernzerhof, J. Chem. Phys. **118**, 8207 (2003).
36. M. Marsman, J. Paier, A. Stroppa and G. Kresse, Journal of Physics-Condensed Matter **20**, 064210 (2008).
37. D. O. Scanlon, B. J. Morgan, G. W. Watson and A. Walsh, Physical Review Letters **103**, 096405 (2009).
38. A. Walsh and C. R. A. Catlow, J. Mater. Chem. **20**, 10438 (2010).
39. D. H. O'Neil, A. Walsh, R. M. J. Jacobs, V. L. Kuznetsov, R. G. Egdell and P. P. Edwards, Physical Review B **81**, 085110 (2010).
40. A. Segmuller, Journal of Vacuum Science & Technology a-Vacuum Surfaces and Films **9**, 2477 (1991).
41. D. G. Neerinck and T. J. Vink, Thin Solid Films **278**, 12 (1996).
42. J. W. Matthews and A. E. Blakeslee, Journal of Crystal Growth **27**, 118 (1974).
43. D. R. Bennett and J. R. del Alamo, presented at the Fourth International Conference on Indium Phosphide and Related Materials, 2002 (unpublished).
44. S. Kishino, M. Ogirima and K. Kurata, Journal of the Electrochemical Society **119**, 617 (1972).

45. H. Chen, Y. K. Li, C. S. Peng, H. F. Liu, Y. L. Liu, Q. Huang, J. M. Zhou and Q. K. Xue, Physical Review B **65**, 233303 (2002).
46. M. A. Lutz, R. M. Feenstra, F. K. Legoues, P. M. Mooney and J. O. Chu, Applied Physics Letters **66**, 724 (1995).
47. M. Albrecht, S. Christiansen, J. Michler, W. Dorsch, H. P. Strunk, P. O. Hansson and E. Bauser, Applied Physics Letters **67**, 1232 (1995).
48. D. Hull and D. J. Bacon, *Introduction to Dislocations*, 4th ed. (Butterworth-Heinemann, Oxford, 2001).
49. M. Coll, J. Gazquez, A. Pomar, T. Puig, F. Sandiumenge and X. Obradors, Physical Review B **73**, 075420 (2006).
50. T. Koida and M. Kondo, Journal of Applied Physics **99**, 123703 (2006).
51. O. Bierwagen, M. E. White, M. Y. Tsai and J. S. Speck, Applied Physics Letters **95**, 262105 (2009).
52. S. Lany and A. Zunger, Phys. Rev. Lett. **98**, 045501 (2007).
53. Y. Ohya, T. Yamamoto and T. Ban, Journal of the American Ceramic Society **91**, 240 (2008).
54. P. D. C. King, R. L. Lichti, Y. G. Celebi, J. M. Gil, R. C. Vilao, H. V. Alberto, J. P. Duarte, D. J. Payne, R. G. Egdell, I. McKenzie, C. F. McConville, S. F. J. Cox and T. D. Veal, Physical Review B **80**, 205211 (2009).
55. V. Lebedev, V. Cimalla, T. Baumann, O. Ambacher, F. M. Morales, J. G. Lozano and D. Gonzalez, Journal of Applied Physics **100**, 094903 (2006).
56. L. F. J. Piper, T. D. Veal, C. F. McConville, H. Lu and W. J. Schaff, Applied Physics Letters **88**, 252109 (2006).
57. P. D. C. King, T. D. Veal and C. F. McConville, Journal of Physics-Condensed Matter **21**, 174201 (2009).
58. V. Lebedev, V. Cimalla, J. Pezoldt, M. Himmerlich, S. Krischok, J. A. Schaefer, O. Ambacher, F. M. Morales, J. G. Lozano and D. Gonzalez, Journal of Applied Physics **100**, 094902 (2006).
59. J. I. Pankove, Optical Processes in Semiconductors. (Dover, 1976).
60. A. Walsh, C. R. A. Catlow, K. H. L. Zhang and R. G. Egdell, Phys. Rev. B **83**, 161202 (2011).
61. J. Bardeen and W. Schockley, Physical Review **80**, 72 (1950).
62. A. Janotti and C. G. Van de Walle, Physical Review B **75**, 121201 (2007).
63. Y. Z. Zhu, G. D. Chen, H. G. Ye, A. Walsh, C. Y. Moon and S. H. Wei, Physical Review B **77**, 245209 (2008).
64. Y. H. Li, X. G. Gong and S. H. Wei, Physical Review B **73**, 245206 (2006).

65. Y. Q. Gai, B. Yao, Y. M. Lu, D. Z. Shen, J. Y. Zhang, D. X. Zhao and X. W. Fan, Physics Letters A **372**, 72 (2007).
66. Y. F. Li, B. Yao, Y. M. Lu, C. X. Cong, Z. Z. Zhang, Y. Q. Gai, C. J. Zheng, B. H. Li, Z. P. Wei, D. Z. Shen, X. W. Fan, L. Xiao, S. C. Xu and Y. Liu, Applied Physics Letters **91**, 021915 (2007).
67. C. G. Vandewalle and R. M. Martin, Physical Review Letters **62**, 2028 (1989).
68. T. Shibata, H. Irie and K. Hashimoto, J. Phys. Chem. B **107**, 10696 (2003).
69. W. J. Yin, S. Y. Chen, J. H. Yang, X. G. Gong, Y. F. Yan and S. H. Wei, Appl. Phys. Lett. **96**, 242101 (2010).

Chapter 6:

The Surface Atomic Structure of In_2O_3(111) Determined by STM, LEED and DFT

6.1 Introduction

In the application of ITO as transparent electrodes in liquid crystal displays (LCD) and organic photovoltaics (OPV), the interfaces with other materials are critically important.[1-4] In an OPV, ITO is used as the transparent hole collecting anode and the Fermi level of ITO must be as low as possible to maximize the open-circuit voltage.[1, 4, 5] The surface chemistry of ITO is not easy to control and the material is often chemically incompatible with non-polar organic thin films, leading to delamination of the organic layers and high series resistances in either organic light emitting diodes or OPV cells.[3, 4] Determining the atomic structure of ITO and indium oxide surfaces is a first step towards a molecular understanding of the surface chemistry and is a prerequisite for engineering the interface of ITO with other materials at a molecular scale for ultimate device optimization. Surprisingly little is known about the surface properties of ITO or In_2O_3.[6, 7] There is however some recent work using density functional theory (DFT) calculations.[8, 9] Golovanov *et al.* demonstrated that oxygen atoms on the In_2O_3(100) surface undergo dimerization to stabilize the polar surface.[8] However following progress in the epitaxial growth of high quality In_2O_3 thin films,[10-18] highly ordered (001), (110) and (111) surfaces are now available for investigation by surface science techniques such as scanning tunnelling microscopy (STM) and low energy electron

diffraction (LEED)[19-21]. Experimental results from Diebold's group on Sn-doped In_2O_3(100) sample confirmed the theoretical prediction of oxygen dimerization and also suggested that the Sn doping provides another channel to stabilize this polar surface.[20] STM studies on Sn-doped In_2O_3(111) reveal that the (111) surface is stoichiometric and has a (1×1) termination.[19]

As shown in Chapter 4 and 5 and references therein, the low energy of the (111) surface allows growth of continuous (111) oriented epitaxial thin films which exhibits large atomically smooth terraces.[21, 22] The high-quality surface of the films enables detailed surface structural characterization. In this Chapter, we present a determination of the atomic structure of In_2O_3(111) and Sn-doped In_2O_3(111) by high resolution STM and analysis of intensity/voltage (I/V) curves in LEED, coupled with density functional theory calculations.

6.2 Experimental Details

6.2.1 Thin Film Growth

Epitaxial thin films of undoped In_2O_3 and 3% Sn-doped In_2O_3 (ITO) were grown on 1 cm × 1 cm Y-ZrO_2(111) substrates in the oxide MBE system at a substrate temperature of 700 °C with oxygen plasma pressure of 3×10^{-5} mbar. Both films were then grown to a thickness of 210 nm, with a nominal growth rate was 0.035 nm s^{-1}, as calibrated from the film thickness derived from HRTEM measurements. *In situ* LEED was carried out in an analysis chamber connected to the growth chamber.

6.2.2 Scanning Tunnelling Microscopy

Clean (111) surfaces could be easily regenerated in a second *ex situ* ultra high vacuum (UHV) system in the Surface Science Laboratory 1 (SSL1), National University of Singapore. The undoped In_2O_3 sample was cleaned by repeated cycles of bombardment with 500 eV argon ions followed by annealing at 600 °C for 60 minutes. The STM experiments were carried out in a home-built multichamber UHV system housing an Omicron low temperature STM with a base pressure better than 2×10^{-10} mbar. The STM was operated with a Nanonis controller (Nanonis, Switzerland). STM images were obtained in constant-current mode with a chemically etched tungsten tip at 77 K.

6.2.3 Low Energy Electron Diffraction

The LEED experiments were conducted in a standard UHV surface science chamber in Surface Science Centre, University of Liverpool, containing a PSP Vacuum Technology electron energy analyser, dual anode X-ray source, rear view LEED optics from OCI Vacuum Microengineering and an Omicron STM operating at room temperature. The base pressure of the system was less than 2×10^{-10} mbar, with hydrogen as the main residual gas in the chamber. The In_2O_3 and Sn-doped samples were cleaned by repeated cycles of Ar^+ sputtering at an energy of 500 eV and annealing at 500 °C in UHV. The cleanliness of the final surface was confirmed by XPS, where no C 1s signal could be observed.

6.3 Density Functional Theory Calculations on In_2O_3 (111) Terminated Surface

The relaxed surface structure of In_2O_3 (111) was performed by Dr. A. Walsh using density functional theory, within the generalized gradient approximation (PBE),[23] as implemented in the VASP package.[24, 25] The plane-wave kinetic energy threshold (500

eV) and *k*-point density (4×4×4) were both well-converged for the bulk system. Starting from the relaxed bulk bixbyite lattice (*a* = 1.030 nm), 2D surface models were constructed using a periodic arrangement of slabs, separated with a 20 Å vacuum region. Convergence of the surface energy γ with respect to slab thickness resulted in a model containing 48 formula units (*i.e.* 6 quadrupolar layers) for the (111) surface. Ions in the top two quadrupolar units were allowed to relax, while all other layers were held at their bulk lattice positions. Simulated annealing was performed to assess the stability of the resulting structures at 750 K and no further relaxations or reconstructions were found to occur. Indeed, from a comparison of the low index terminations at the same level of theory, the (111) surface was found to be thermodynamically stable. Lateral relaxations were found to be very small, especially in the second quadrupolar layer where all lateral movements were less than 0.06 Å: in the outer O and In layers most lateral relaxations were less than 0.10 Å, with maximum values of 0.17 Å for O and In with reduced coordination environments. Vertical relaxations were also small, as will be discussed below.

6. 4. Results and Analysis

6.4.1 Surface Geometric Structures

LEED investigation on the (111) surface was performed by *in-situ* immediately after the growth of thin films. Figure 6.1 presents a typical LEED pattern measured with electron beam energy of 80 eV, showing a sharp pattern with 3-fold symmetry. The lattice constant is estimated to be 14.0 Å, which is associated with the bulk terminated (1 × 1) unit cell length of the In_2O_3(111) surface ($\sqrt{2}a$). Morales *et al.* demonstrated the

same (1 × 1) surface termination on Sn-doped $In_2O_3(111)$ thin films.[19] This is associated with the fact that $In_2O_3(111)$ is thermodynamically stable and non-polar surface, as demonstrated in chapter 4.

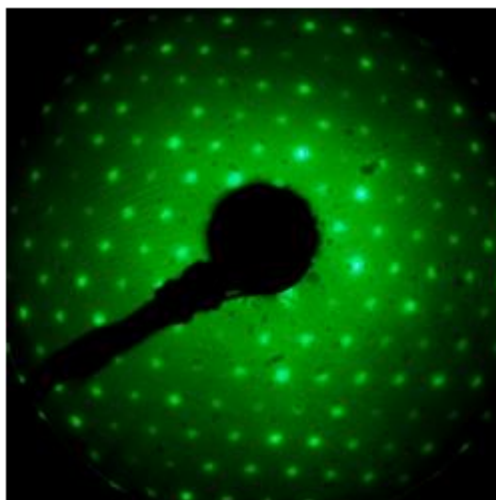

Figure 6.1 A typical *in situ* LEED pattern of the $In_2O_3(111)$-(1 × 1) surface with electron beam energy 80 eV.

The (111) surface contains repeating quadrupolar grouping of anionic and cationic layers (see Figure 6.2b and c). Equal number of In-O and O-In bonds are broken to form the (111) surface, fulfilling the criterion for a stoichiometric surface. It has been shown in chapter 4 that the surface energies of three low index In_2O_3 surfaces follow the order a sequence $\gamma(111) < \gamma(110) < \gamma(100)_{O} < \gamma(100)_{In}$, based on *ab initio* total energy calculations.[22, 26] The bixbyite surfaces of In_2O_3 are very similar in appearance to those of the parent fluorite structure, although there is minor rumpling within the cation layers due to the relaxations in atomic positions associated with the intrinsic vacant oxygen sites within the structure. The bulk-terminated (1 × 1) bixbyite surface of In_2O_3 is similar to the most stable (111) surface of fluorite oxides such as UO_2 and CeO_2, which exhibit stable bulk-terminated (1 × 1) reconstructions.[27-29]

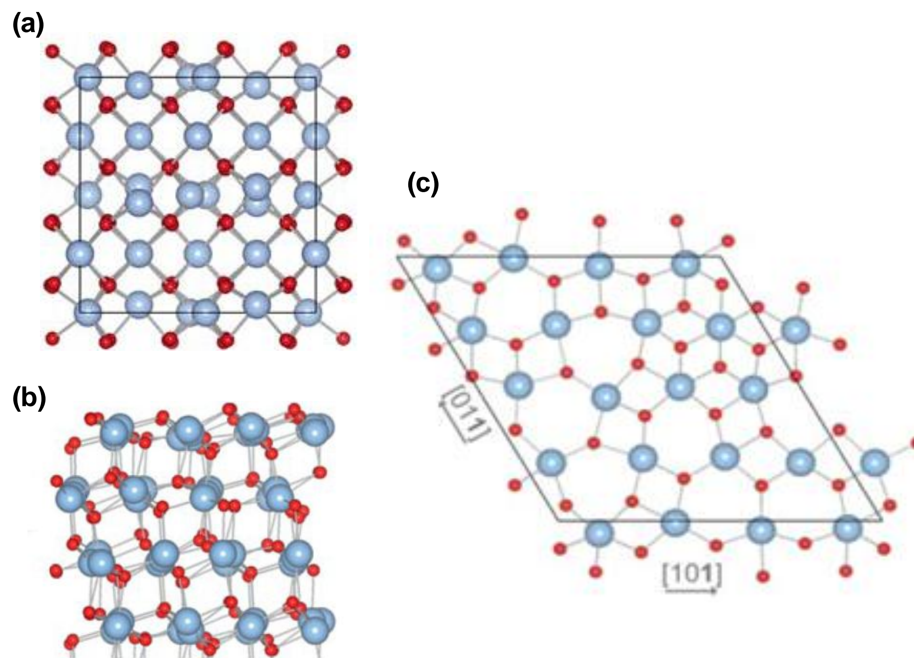

Figure 6.2. (a) Crystal structure representation of the bixbyite In_2O_3 unit cell; (b) side view of the low index (111) surface; (c) top view of (111) surface; In is coloured blue (large balls), with red reserved for oxygen (small balls). (Image adapted from reference[26])

The surface morphologies of the as-grown $In_2O_3(111)$ thin film was examined by *ex-situ* AFM images. Figure 6.3a shows a large area image (5 µm × 5 µm) of 210 nm thick In_2O_3. The surface is very smooth (rms roughness = 3 nm), with triangular spiral hillocks. In the zoom-in image (Figure 6.3b), atomic steps predominantly aligned along the $< 11\overline{2} >$ directions can be clearly resolved. The height of steps is around 3.0 Å which corresponds to the thickness of an O-In-O quadrupolar layer ($a/2\sqrt{3}$). The triangular hillocks are further resolved with a height of ~ 5 nm. A screw dislocation can be seen at the peak of the hillocks (Figure 6.3c). The AFM results thus point towards spiral growth of the In_2O_3 thin film on YSZ (111). It was postulated by Burton, Cabrera, and Frank (is so-called BCF theory) that a screw dislocation emerging on the surface provides a continuous step source for materials growth at low supersaturation, leading to the formation of spiral hilllocks[30]. The spiral growth mode has been observed

in many heteroepitaxial systems such as thin films of superconductors[31], gallium nitrides[32, 33, 32] and even organic materials[34]. As shown in the last Chapter, we have shown that the growth of In_2O_3 films experienced "dewetting" of 2D micron sized mesa followed by coalescence into continuous films (in the present stage) process as the coverage increases. Thus the spiral steps provide the dominant channels for further film growth. Figure 6.3d shows an image of a film with a thickness of 420 nm. The surface clearly features triangular hillocks of lateral dimensions of order 1 μm and 20 nm in height.

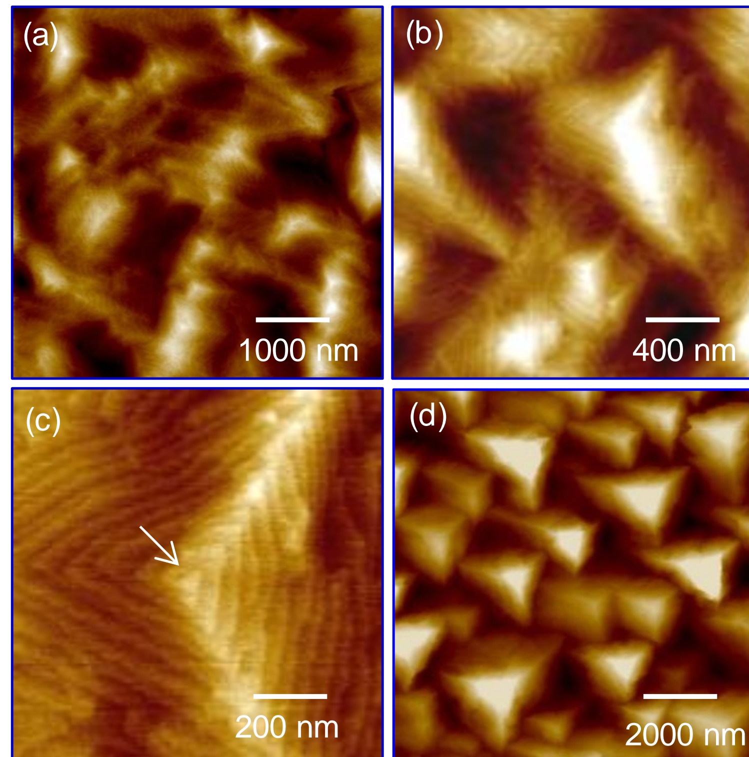

Figure 6.3. (a) A large area image (5 μm × 5 μm) of the 210 nm thick In_2O_3, featuring triangular spiral hillocks. (b) A zoom-in image (Figure 6.3 b), with atomic steps predominantly aligned along $< 11\overline{2} >$ drirections; (c) A zoom-in image on top of a spiral hillock showing a screw dislocation; (d) A large area image (10 μm × 10 μm) of the 420 nm thick In_2O_3, showing the hillocks have a size of 2000 nm.

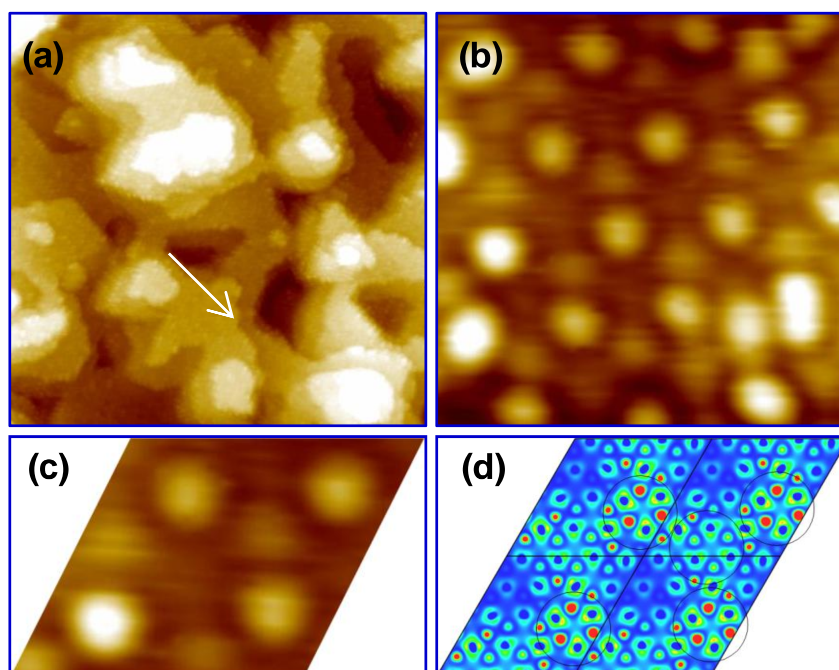

Figure 6.4. (a) A large area (100 nm × 100 nm) STM image of the sputtering and annealed $In_2O_3(111)$-(1×1) surface, revealing flat terraces separated by monatomic steps of 2.9 Å; (b) An atomically resolved empty state STM image (5 nm × 5 nm); V_{sample} = -1.8V, I_t = 300 pA; (c) A high-resolution STM image of the $In_2O_3(111)$-(1×1) unit cell; (d) corresponding DFT simulated density of empty states, showing that the 4 six-fold coordinated In atoms possess the highest density of empty states (red colour).

The flat nature In_2O_3 film motivated us to study the atomic structure with high-resolution STM. The (1 × 1) surface can be regenerated by cycles of Ar^+ sputtering, followed by annealing at 600 °C in UHV. A large area STM image (Figure 6.4a) revealed that the prepared surfaces contained flat terraces separated by monatomic steps of height 2.9 Å. The *ex-situ* prepared surface displays a different morphology from that of the as-grown thin film, probably induced by the disruption produced by the Ar^+ beam. Nevertheless, atomic resolution images can be obtained in empty state imaging (+ 1.8 V sample bias with a tunnelling current of 0.3 nA), see Figure 6.4b. The image clearly shows the (1 × 1) hexagonal arrangement of bright protrusions, as indicated in

Figure 6.4c (side length ~1.4 nm). Since the STM image was obtained by tunnelling empty states, which are mainly derived from In 5s-orbital.[26, 35, 36] This scenario is in line with STM studies of many metal oxides such as TiO_2[37, 38] and CeO_2[39, 40]. The contrast in the STM images of these materials largely originated from surface electronic effects. Thus bright protrusions in the empty state images of TiO_2 reflect the positions of Ti ions, in spite the fact that O atoms are geometrically higher. We thus assign the bright protrusions on the image to In atoms. As shown in reference[19], each unit cell of the (111) surface contains 12 five-fold coordinated In atoms and 4 six-fold coordinated In atoms. The density of states simulated by DFT (Figure 6.4d) shows that the 4 six-fold coordinated In atoms possess the highest density of empty states. This matches well with the current empty state STM images. The bright protrusions are therefore assigned to In atoms with 4 six-fold coordination. The sub-highest empty states originating from the five-fold coordinated In atoms can also be imaged by STM as indicated in the image. Similarly the stoichiometric $TiO_2(110)$-(1×1) surface showed the bright and dark rows along [001] direction in the empty state STM images.[38] Diebold *et al.* have demonstrated based on pseudopotential calculations that the bright rows were attributed to the Ti atoms with five-fold coordination.

It should be noted that our atomically resolved STM images are different to those reported by Morales *et al.* for 4% Sn-doped In_2O_3 (ITO) thin film (12 nm thick).[19] In this study, the unit cell of the ITO(111) was imaged as triangular shaped depressions and protrusions in the empty state image. The authors attributed the contrasts to the In 5s-derived nature as well, but from the five-fold coordinated In atoms. The discrepancy is likely due to the fact that STM images of metal oxide surface are strongly influenced by different sample preparation procedures. The surface stoichiometry, defects and strain within the films can give rise to a variety of STM images even in the same

imaging conditions, for example TiO_2 surfaces.[38, 41] The *ex-situ* prepared surface may have different surface states compared with the *in-situ* STM imaging by Morales *et al.* Furthermore strain in the very thin film (12 nm) used by Morales *et. al.* and Sn doping can be another possibility to induce this discrepancy. Further systematic STM studies are needed to elucidate this issue.

6.4.2 Analysis of LEED Data

STM can only provide information about the in-plane surface atomic structure. To probe the out-plane relaxation, we performed a LEED I–V study, in which the intensity of the diffraction spots as a function of the energy of the incident electrons (LEED I–V spectra) was measured at normal incidence of the primary beam. The surfaces gave sharp (1 × 1) LEED patterns with a low background (Figure 6.5).

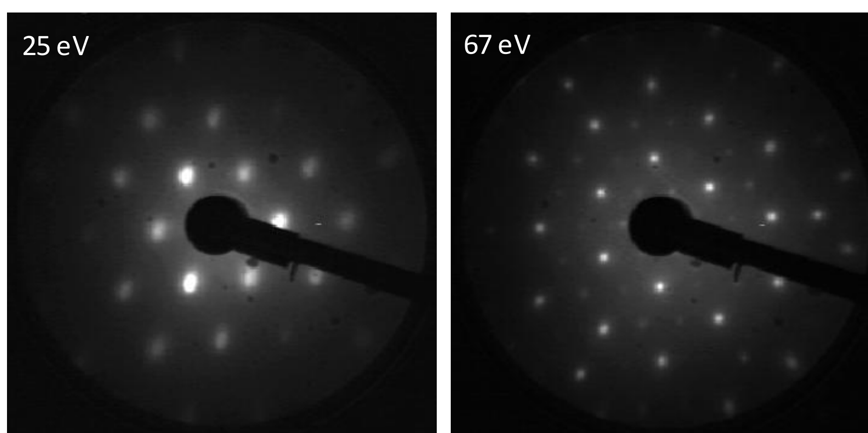

Figure 6.5. LEED patterns from Sn-$In_2O_3(111)$ measured at beam energy indicated.

The I-V spectra were background subtracted and normalised with respect to the primary beam current. The intensities of the symmetrically equivalent spots were averaged in order to reduce experimental noise. The data set that was gathered at 300 K consisted of 8 beams, ranging in energy from 20 eV to a maximum of 250 eV. The cumulative energy range was 1270 eV. The useful energy range was limited by two factors. Firstly owing to the large lateral size of the surface unit cell, low order spots converged into the electron gun at fairly low kinetic energies. Secondly higher order spots rapidly faded into the background for kinetic energies much in excess of 200 eV, thus imposing further limitations on the data range.

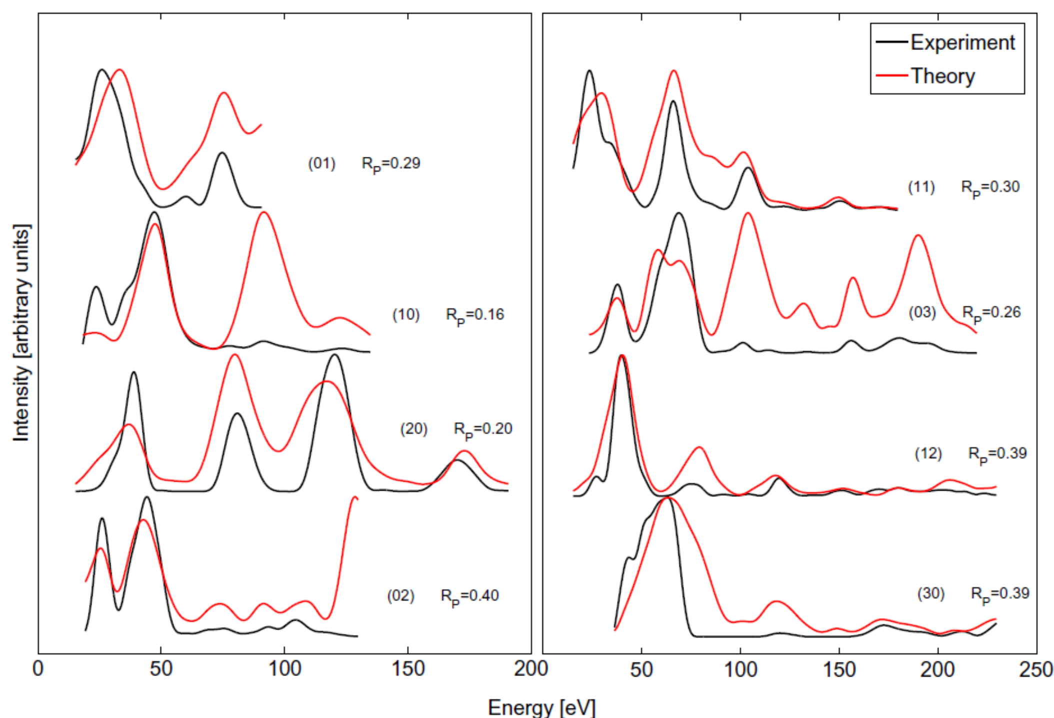

Figure 6.6. Experimental LEED I/V data for the 8 independent beams used to determine the surface structure of Sn-In_2O_3(111) along with I/V curves computed for model structure. The Pendry R-factors for the individual beams are indicated in the figure.

The dynamical LEED calculations were performed by K. Pussi from Lappeenranta University of Technology, Finland using the Tensor-LEED program.[42] The relativistic phase shifts were calculated using the phase shift program[43] that is packaged with Tensor-LEED. The agreement between the theory and the experiment was tested using the Pendry R-factor and the error bars quoted are calculated using the Pendry R-function.[44] Four different sets of phase shifts were used: two for oxygen and two for indium. At the beginning of the analysis the Debye temperatures were set to 1000 K for both O and In. The l_{max} value was set to 8 and the imaginary part of inner potential was set to -5.0 eV. These values were optimised in the final stages of the analysis. The real part of the inner potential is independent of energy and was allowed to relax as is normal in the LEED analysis.

It is customary to use different Debye temperatures for surface and bulk atoms in LEED analysis. This does not usually have any effect on the geometry of the model but it usually makes the agreement (R-factor) better. In this analysis the topmost O atoms and the In atoms in the topmost quadrupole were given different Debye temperature to the values for bulk O and bulk In. The starting values for the Debye temperatures were chosen by "trial and error" starting from the tabulated value of 108 K for In and 500 K for O. Surprisingly high Debye temperature values were favoured for both O and In (1000 K). At the end of analysis the Debye temperature values were optimized to 400 K and 700 K for the "surface" and bulk In respectively and to 1100 K and 1500 K for the surface and bulk O.

The calculation of phase shifts for metal oxides is addressed in detail in the paper of Nascimento *et al.*[45] These authors review the methods that have been used previously and also prescribe a technique for calculating the phase shifts for metal oxides. Because of the charge transfer between the oxygen and metal atoms, the calculation of phase

shifts is less straightforward than is usual. Instead of using empirical muffin tin radii for neutral atoms as is usually the case, one must take account must be taken of the fact that the fact that the In cations have *smaller* radii than neutral In and the oxide ions will have *larger* radii than the neutral O atom. However there is substantial covalency in In_2O_3 so that *a priori* it may be anticipated that the values will be quite close to those for the neutral atoms. In this study, we have chosen to make arbitrary adjustments to the radii for In and O in the phase shift calculation, until the best fit was reached. The final values of the radii were 1.57 Å for In (bulk value 1.625Å) and 0.65 Å for O (bulk value 0.60 Å).

Nascimento *et al.*[45] also discussed the use of energy dependent imaginary and real parts of the inner potential. In the current study, the energy dependence of the real and imaginary components of the inner potential was also considered, but in our case it did not have any effect on the R-factor. This is probably due the fact that the energy range of our study is quite small (20 eV-250 eV) and the changes in the inner potential in this range are also likely to be small. Also our data did not have many peaks. Ignoring the energy dependence of inner potential could cause systematic errors if one had a data set with a large energy range and many peaks in the data (because the Pendry R-factor is most sensitive to the peak positions).

The geometrical parameters are optimized only in the vertical (z) direction, because normal incidence LEED is not very sensitive to the lateral parameters and our data set was limited in range. However, as discussed above, the DFT studies suggest that lateral relaxations are in general very small indeed. The ions in the top two quadrupolar layers were allowed to relax normal to the surface and the deeper layers were kept fixed, as in the DFT calculations. Although 80 atoms were therefore allowed to relax, symmetry constraints dictated that only 28 positional parameters were refined,

along with the real part of the inner potential. This corresponds to 1270/29 eV = 44 eV of raw data per parameter. All parameters were refined simultaneously, starting from an experimental bulk cut structure. Since the DFT calculations had not suggested alternative low energy structures, no alternative structures were refined. However in some preliminary investigations the structural refinement was launched from a starting point where the lattice was expanded by about 8% in the z direction. This structure refined back toward essentially the same the bulk cut structure as found in our final analysis.

The error bars on the oxygen positions are larger and increase with depth below the surface from 0.07 Å and 0.10 Å in the outermost layer through ranges of 0.14 Å - 0.20 Å, 0.20 Å - 0.30 Å and 0.30 Å - 0.30 Å in the next three layers. For some oxygen ions no error bars could be defined, because the R-factor curve was flat around the oxygen position. The final Pendry R-factor is 0.31. Figure 6.6 shows the comparison between the best fit I/V curves and the experimental data for the 8 independent beams that were studied.

The Pendry R factor derived from the fit to experimental data in the present work is comparable to values reported in recent surface structure determinations for oxides by LEED I/V analysis e.g. $Ca_{1.5}Sr_{0.5}RuO_4$ R_P = 0.28[45]; TiO_2(110) (1×1) R_P = 0.29[46] recently improved to R_P = 0.23[47]; Fe_3O_4(001) (√2 × √2) R45° R_P = 0.34[48]; and CoO(001) on Ag(001) R_P = 0.27.[49] It may be noted that in the current study 80 atoms were allowed to relax from their bulk positions so that the complexity of the problem is comparable to that for Fe_3O_4(001) (√2 × √2) where 53 structural parameters were refined: the final R factors in these two structural determinations are very similar.

The structure derived from the LEED experiments is shown in Figure 6.7. The experimental surface structure depicted is very close to the bulk truncated structure although there are very small vertical relaxations with the following ranges in successive ionic layers: $O_{1(outer)}$ -0.18 Å to +0.19 Å; In_1 -0.07 Å to +0.13 Å; $O_{1(inner)}$ -0.04 Å to + 0.21 Å; $O_{2(outer)}$ -0.37 Å to +0.11 Å; In_2 -0.03 Å to +0.11 Å; $O_{2(inner)}$ -0.09 Å to +0.17 Å. In most cases these relaxation are comparable with the error bars. Due to the minor redistributions of the In and O positions within the relevant atomic layers the straddle in ion positions within a single ionic layer close to the surface is slightly different to that in the bulk. This is particularly apparent in the "inner" O layer of the first quadrupole. There is also a small contraction in the distances between the ions in the outermost $\{[O^{2-}]^{24-}_{12}[In^{3+}]^{48+}_{16}[O^{2-}]^{24-}_{12}\}$ quadrupolar unit by a net inward relaxation of the outermost $[O^{2-}]^{24-}_{12}$ layer coupled outward relaxation of the first $[In^{3+}]^{48+}_{16}$ layer and even more pronounced outward relaxation of the next O layer.

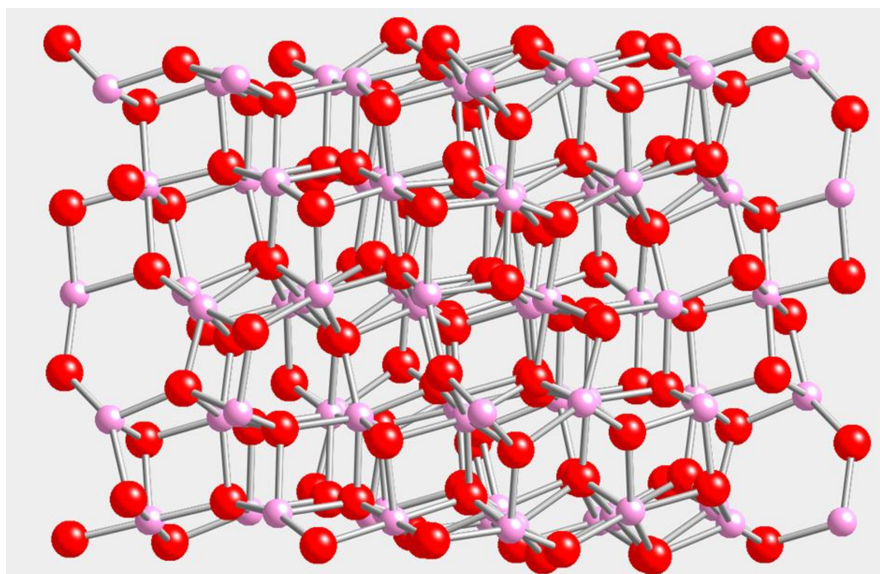

Figure 6.7. The relaxed surface structure of In_2O_3(111) derived from LEED.

Figure 6.8. Schematic representation of the structure for In_2O_3(111) derived from truncation of the bulk structure and from analysis of LEED I/V data. Comparative diagrams for a bulk cut DFT structure and a relaxed DFT structure are also shown. Owing to the complexity of the structures individual atomic positions are not shown but the spread of atomic positions within components of the quadrupolar layers that are characteristic of the (111) surface are represented by the width of the horizontal stripes. The numbers inside the stripes give the straddle of atomic positions within a layer (in Å), while the figures in parentheses for the LEED and relaxed DFT structures give the average vertical relaxation of the atoms within a given layer (also in Å). Positive numbers refer to inward relaxation; while negative refer to outward relaxation.

A schematic of the experimentally determined structure is shown in Figure 6.8 alongside a similar schematic for the bulk truncated structure. This diagram represents the successive O-In-O-O-In-O ionic layers in terms of a series of horizontal stripes. The widths of the stripes in this figure represent the straddle in the distribution of atomic positions within the layers, whilst the numbers within the stripes of the LEED structure indicate the average relaxation in atomic positions within a given stripe. For comparison the figure also includes an analogous schematic representation of the bulk cut and relaxed surface structures derived from DFT calculations. In general there is

good agreement between the magnitudes and directions of the average relaxations as derived from LEED and DFT calculations.

The very small relaxations found in the present study are comparable to those found in a LEED study of the (111) surfaces of the ionic fluorite compounds CaF_2 and BaF_2 [50]. Here the outer fluoride ions were found to have inward relaxations of 0.03 Å and 0.12 Å respectively, but the inward relaxation of the outermost cation layer was only 0.01 Å in each case. Similarly for UO_2(111), potential based models[51] suggest an inward relaxation of 0.11 Å for the outer oxygen layer but an *outward* relaxation of 0.03 Å for the first uranium layer. The relatively small relaxations that seem to be a general feature for fluorite and fluourite-like (111) surfaces are consistent with the fact that this surface is thermodynamically favoured over other terminations.

6.5 Conclusions

In this chapter, the surface structure of In_2O_3 (111) has been determined using a combination of scanning tunnelling microscopy, low energy electron diffraction of single-crystal thin films and first-principles *ab initio* calculations. It turns out that the (111) has a bulk terminated (1 × 1) surface structure, as expected from the low surface energy of the (111) surface. Atomically resolved empty-state STM images are mainly attributed to the In *5s*-derived conduction band, consistent with the electron density isosurface for the lower unoccupied conduction band tate simulated by DFT. Since In_2O_3 has 80 atoms in the unit cell, fitting the LEED data to an experimental structure is not trivial. However, we have achieved an acceptable Pendry R-factor of 0.31. It transpires that bulk terminated In_2O_3(111) have relatively minor relaxations normal to the surface which cause a reduction in the spacings between quadrupolar layers close to the surface. Good agreement is found between the experimental surface structure and that derived from *ab initio* density functional theory calculations. This result emphasises the benefit of a multi-technique approach to resolving surface structure. The same features are expected for other materials adopting the bixbyite crystal structure.

6.6 References:

1. S. Braun, W. R. Salaneck and M. Fahlman, Adv. Mater. **21**, 1450 (2009).
2. H. Ishii, K. Sugiyama, E. Ito and K. Seki, Adv. Mater. **11**, 605 (1999).
3. N. R. Armstrong, C. Carter, C. Donley, A. Simmonds, P. Lee, M. Brumbach, B. Kippelen, B. Domercq and S. Y. Yoo, Thin Solid Films **445**, 342 (2003).
4. N. R. Armstrong, P. A. Veneman, E. Ratcliff, D. Placencia and M. Brumbach, Accounts Chem. Res. **42**, 1748 (2009).
5. H. Hoppe and N. S. Sariciftci, J. Mater. Res. **19**, 1924 (2004).
6. C. G. Granqvist and A. Hultaker, Thin Solid Films **411**, 1 (2002).
7. C. G. Granqvist, Solar Energy Materials and Solar Cells **91**, 1529 (2007).
8. V. Golovanov, M. A. Maki-Jaskari, T. T. Rantala, G. Korotcenkov, V. Brinzari, A. Cornet and J. Morante, Sens. Actuator B-Chem. **106**, 563 (2005).
9. C. G. Zhou, J. Y. Li, S. Chen, J. P. Wu, K. R. Heier and H. S. Cheng, J. Phys. Chem. C **112**, 14015 (2008).
10. O. Bierwagen, M. E. White, M. Y. Tsai and J. S. Speck, Applied Physics Letters **95** (26), 262105 (2009).
11. O. Bierwagen and J. S. Speck, Applied Physics Letters **97** (7), 072103 (2010).
12. O. Bierwagen and J. S. Speck, Journal of Applied Physics **107** (11), 113159 (2010).
13. A. Bourlange, D. J. Payne, R. G. Egdell, J. S. Foord, P. P. Edwards, M. O. Jones, A. Schertel, P. J. Dobson and J. L. Hutchison, Applied Physics Letters **92**, 092117 (2008).
14. A. Bourlange, D. J. Payne, R. G. Palgrave, J. S. Foord, R. G. Egdell, R. M. J. Jacobs, A. Schertel, J. L. Hutchison and P. J. Dobson, Thin Solid Films **517**, 4286 (2009).
15. A. Bourlange, D. J. Payne, R. G. Palgrave, H. Zhang, J. S. Foord, R. G. Egdell, R. M. J. Jacobs, T. D. Veal, P. D. C. King and C. F. McConville, Journal of Applied Physics **106**, 013703 (2009).
16. H. Ohta, M. Orita, M. Hirano, H. Tanji, H. Kawazoe and H. Hosono, Applied Physics Letters **76**, 2740 (2000).
17. H. Ohta, M. Orita, M. Hirano and H. Hosono, Journal of Applied Physics **91**, 3547 (2002).
18. T. Koida and M. Kondo, Journal of Applied Physics **99**, 123703 (2006).
19. E. H. Morales, Y. B. He, M. Vinnichenko, B. Delley and U. Diebold, New J. Phys. **10**, 125030 (2008).
20. E. H. Morales and U. Diebold, Appl. Phys. Lett. **95,** 253105 (2009).

21. K. H. L. Zhang, D. J. Payne, R. G. Palgrave, V. K. Lazarov, W. Chen, A. T. S. Wee, C. F. McConville, P. D. C. King, T. D. Veal, G. Panaccione, P. Lacovig and R. G. Egdell, Chem. Mat. **21**, 4353 (2009).
22. K. H. L. Zhang, A. Walsh, C. R. A. Catlow, V. K. Lazarov and R. G. Egdell, Nano Lett. **10**, 3740 (2010).
23. J. P. Perdew, K. Burke and M. Ernzerhof, Phys. Rev. Lett. **77**, 3865 (1996).
24. G. Kresse and J. Furthmuller, Physical Review B **54**, 11169 (1996).
25. G. Kresse and D. Joubert, Physical Review B **59**, 1758 (1999).
26. A. Walsh and C. R. A. Catlow, J. Mater. Chem. **20**, 10438 (2010).
27. M. R. Castell, C. Muggelberg, G. A. D. Briggs and D. T. Goddard, J. Vac. Sci. Technol. B **14**, 966 (1996).
28. M. R. Castell, Phys. Rev. B **68**, 235411 (2003).
29. J. L. Lu, H. J. Gao, S. Shaikhutdinov and H. J. Freund, Surf. Sci. **600**, 5004 (2006).
30. W. K. Burton, N. Cabrera and F. C. Frank, Nature **163**, 398 (1949).
31. C. Gerber, D. Anselmetti, J. G. Bednorz, J. Mannhart and D. G. Schlom, Nature **350**, 279 (1991).
32. Y. Cui and L. Li, Phys. Rev. B **66**, 155330 (2002).
33. L. Lymperakis, J. Neugebauer, M. Albrecht, T. Remmele and H. P. Strunk, Phys. Rev. Lett. **93**, 196401 (2004).
34. R. Ruiz, D. Choudhary, B. Nickel, T. Toccoli, K. C. Chang, A. C. Mayer, P. Clancy, J. M. Blakely, R. L. Headrick, S. Iannotta and G. G. Malliaras, Chem. Mat. **16**, 4497 (2004).
35. A. Walsh, J. L. F. Da Silva, S. H. Wei, C. Korber, A. Klein, L. F. J. Piper, A. DeMasi, K. E. Smith, G. Panaccione, P. Torelli, D. J. Payne, A. Bourlange and R. G. Egdell, Phys. Rev. Lett. **100**, 167402 (2008).
36. A. Walsh and C. R. A. Catlow, J. Mater. Chem. **20**, 10438 (2010).
37. M. Li, W. Hebenstreit, L. Gross, U. Diebold, M. A. Henderson, D. R. Jennison, P. A. Schultz and M. P. Sears, Surf. Sci. **437**, 173 (1999).
38. U. Diebold, J. F. Anderson, K. O. Ng and D. Vanderbilt, Phys. Rev. Lett. **77**, 1322 (1996).
39. N. V. Skorodumova, M. Baudin and K. Hermansson, Phys. Rev. B **69**, 075401 (2004).
40. S. Fabris, S. de Gironcoli, S. Baroni, G. Vicario and G. Balducci, Phys. Rev. B **71**, 155330 (2005).
41. U. Diebold, Nat. Mater. **9**, 185 (2010).
42. M. A. Vanhove, W. Moritz, H. Over, P. J. Rous, A. Wander, A. Barbieri, N. Materer, U. Starke and G. A. Somorjai, Surface Science Reports **19**, 191 (1993).

43. A. Barbieri and M. A. Vanhove. private communication (http://www.ap.cityu.edu.hk/personal-website/van-Hove.htm)
44. J. B. Pendry, Journal of Physics C-Solid State Physics **13**, 937 (1980).
45. V. B. Nascimento, R. G. Moore, J. Rundgren, J. D. Zhang, L. Cai, R. Jin, D. G. Mandrus and E. W. Plummer, Physical Review B **75**, 035408 (2007).
46. R. Lindsay, A. Wander, A. Ernst, B. Montanari, G. Thornton and N. M. Harrison, Physical Review Letters **94**, 246102 (2005).
47. W. Busayaporn, X. Torrelles, A. Wander, S. Tomic, A. Ernst, B. Montanari, N. M. Harrison, O. Bikondoa, I. Joumard, J. Zegenhagen, G. Cabailh, G. Thornton and R. Lindsay, Physical Review B **81**, 153404 (2010).
48. R. Pentcheva, W. Moritz, J. Rundgren, S. Frank, D. Schrupp and M. Scheffler, Surface Science **602**, 1299 (2008).
49. K. M. Schindler, J. Wang, A. Chasse, H. Neddermeyer and W. Widdra, Surface Science **603**, 2658 (2009).
50. J. Vogt, J. Henning and H. Weiss, Surface Science **578**, 57 (2005).
51. P. W. Tasker, Surface Science **87**, 315 (1979).

Chapter 7

The Surface Electronic Structure of In_2O_3 Probed by Photoemission Spectroscopy

7.1 Introduction

Following development of procedures to achieve high-quality thin films and atomically clean surfaces, this chapter will turn to probing the electronic structures of In_2O_3 and Sn-doped In_2O_3 surfaces by synchrotron-based photoemission spectroscopy (PES) excited with photon energies ranging from the ultraviolet (6-40 eV), through the soft X-ray regime (40-1486.6 eV) to hard X-rays (6000 eV). PES is a widely used technique for studying the electronic structures of solids, specifically the filled valence band and core level states. The variation of intensities of features in the valence band regime with photon excitation energy gives information about the partial densities of states in the valence band and hence the hybridization or mixing of the component atomic orbitals: at sufficiently high photon energies PES basically measures the sum of partial densities of states, each weighted by photon-energy dependent ionization cross-sections.[1] Moreover, the valence electron inelastic mean free path length in soft X-ray PES is probably of the order of 25 Å but under 6000 eV excitation the path length increases to values around 60 Å. This enables one to distinguish surface states from "bulk" electronic states. In this chapter, it is shown that a pronounced electron accumulation layer presents itself at the surfaces of undoped In_2O_3 films with very low carrier concentrations.[2-4] The downward band bending associated with electron accumulation in the near surface region, gives rise

to quantized electron subband states near the Fermi level. The effect of Sn doping on the electronic structures will also be discussed.

7.2 Experimental details

7.2.1 MBE Samples

In_2O_3 and 2% Sn-doped In_2O_3 thin films were grown on 1 cm × 1 cm Y-ZrO_2 substrates in the oxide MBE system with an oxygen plasma pressure of 3 × 10^{-5} mbar. The In_2O_3(111), (110) and Sn-doped In_2O_3 (111) samples were grown at a substrate temperature of 700 °C, while the (100) sample was grown at 650°C. The carrier concentrations (and mobilities) for the In_2O_3(111), (110) and (100) films were determined from single field Hall effect measurements to be 1×10^{18} cm^{-3} (56 $cm^2V^{-1}s^{-1}$), 3×10^{18} cm^{-3} (56 $cm^2V^{-1}s^{-1}$) and 6×10^{18} cm^{-3} (32 $cm^2V^{-1}s^{-1}$), respectively. Since the (111) sample had the lowest level of doping due to defects, most of the PES results in the following chapter are derived from high quality (111) oriented films. The carrier concentrations (and mobility) for the 2% Sn-doped In_2O_3(111) was measured to be 6.8 × 10^{20} cm^{-3} (34 $cm^2V^{-1}s^{-1}$).

7.2.2 Photoemission spectroscopy

High resolution conventional Al Kα X-ray photoemission spectra were measured in a Scienta ESCA 300 spectrometer at the National Centre for Electron Spectroscopy and Surface Analysis (NCESS) at Daresbury Laboratory (UK).[5] The detailed experimental setup has been described in Chapter 3. Gaussian convolution of the analyser resolution with a linewidth of 260 meV for the x-ray source gives an effective instrument resolution

of 400 meV. Energies were referenced relative to Fermi level onsets of Ag samples used to calibrate the spectrometer. The silver Fermi level was found to coincide with weak but well defined Fermi edges found for the doped In_2O_3 samples.

UV photoemission spectra excited with photon energies in the range 6 eV - 40 eV range were measured at the BaDElPh beamline of the Elettra Synchrotron Light Source, Trieste, Italy.[6] The detailed experimental setup has been described in Chapter 3. Measurements were performed at room temperature with pressure better than 5×10^{-11} mbar. The surfaces of In_2O_3 and Sn-doped samples were cleaned by repeated cycles of Ar^+ sputtering (500 eV) and annealing at 700 °C in UHV for 1 hour. Well ordered (1×1) LEED pattern and no trace of C *1s* signal from XPS confirmed the cleanliness of the surfaces.

Further soft X-ray photoemission measurements were performed on beamline I311 of the MAX II synchrotron housed at MAXLAB, Lund, Sweden.[7] The beamline is based on a 48.5 period undulator and operates in an energy range between 40 eV and 1500 eV. The ultrahigh vacuum endstation incorporates facilities for sample heating and rearview LEED optics, whilst the analysis chamber houses a Scienta SES200 spherical sector electron energy analyser. Clean surfaces exhibiting a (1×1) reconstruction were easily regenerated by heating the samples to 700 °C for several hours.

Hard X-ray photoemission measurements at $h\gamma$ = 6000 eV were performed on beamline ID16 of the European Synchrotron Radiation Facility (ESRF) in Grenoble France, using the VOLPE volume photoemission endstation.[8] Photoelectrons were collected in normal emission in the horizontal plane, so that the angle between the offtake direction and both the propagation and polarization vectors of the beam was 45°. The effective beamline resolution was set at 300 meV at 6000 eV photon energy. The

spectrometer resolution was set at 200 meV for most measurements. The total overall energy resolution was 360 meV. The typical time for accumulation valence-band spectra was around 4 hours. No sample degradation was observed at higher photon energies.

7.3 Surface Electronic Structure of In_2O_3: Quantized Electron Accumulation States

7.3.1 Valence Band Structure

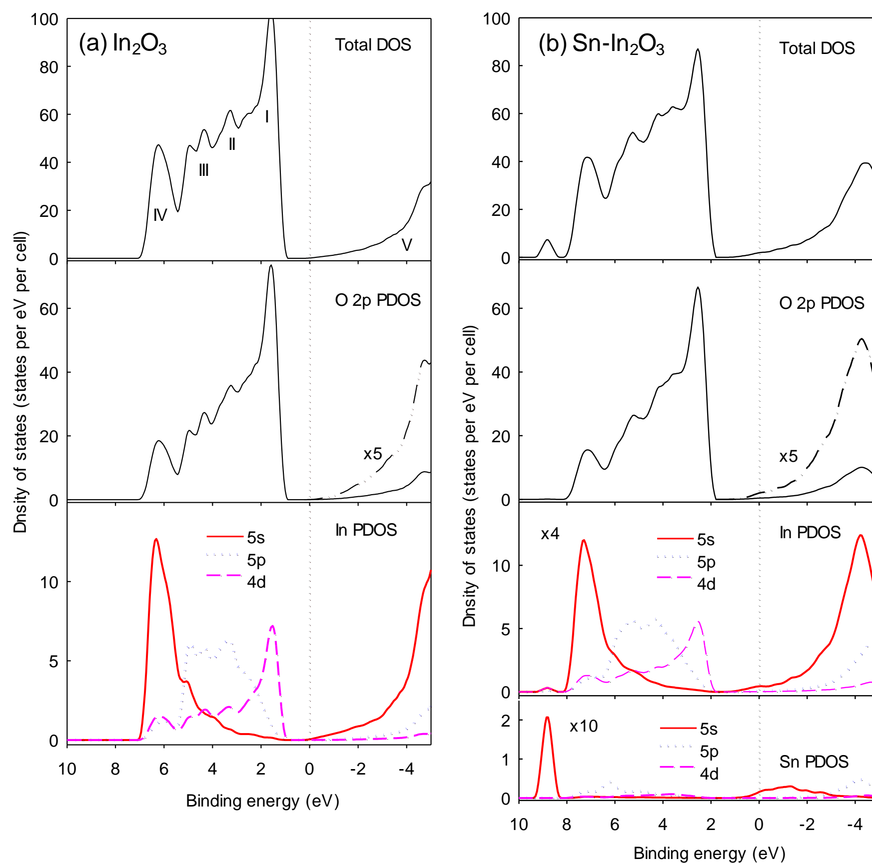

Figure 7.1. Total and partial density of states of (a) In_2O_3 and (b) Sn-doped In_2O_3. Adapted from reference 9[9].

In the ionic model limit the O^{2-} ions of In_2O_3 have an electron configuration $2p^6$ while the electron configuration of In^{3+} is $4d^{10}5s^05p^0$. In terms of this model the valence band is composed of O 2*p* states and the conduction band derives from In 5*s* states. However, band structure calculations suggest that In_2O_3 is a highly covalent material, with pronounced In 5*s* and In 5*p* character found respectively toward the bottom and the middle of the valence band, as shown in Figure 7.1.[9, 10] Conversely there is corresponding O 2*p* character in the conduction band.

PES using a variable incident photon energy provides one means of unravelling the contributions of differing atomic orbitals to the occupied states in a solid and indeed this approach has been used to study the electronic structure of both CdO[11] and SnO_2[12, 13]. Thus photons with energies ranging from 30 eV to 6000 eV were used to excite valence band photoemission spectra of In_2O_3 to assess the extent of mixing between In and O orbitals. The results are shown in Figure 7.2a. For convenience of comparison, the spectra are normalized to the feature of maximum of intensity in the valence band. Four main features may be identified in the spectra labelled as I, II, III, and IV. Peak I has maximum intensity at around 3.8 eV binding energy and dominates most of the spectra but less prominent shoulders at 5.3 eV (II) and 6.8 eV (III), and 8.4 eV (IV) may also be identified.

Partial densities of state calculations in Figure 7.1a shows that peak I is predominantly O 2*p* derived (with around 90% O 2*p* character) but with some mixing with In 4*d* states.[9, 10] In the intermediate region (shoulders II and III), O 2*p* orbitals mix and form bands with In 5*p* orbitals. At the bottom of the valence band in region IV, O 2*p* orbitals mix strongly with In 5*s* states. It is estimated that the states associated with peak IV have around 38% In 5*s* character and 62% O 2*p* character.

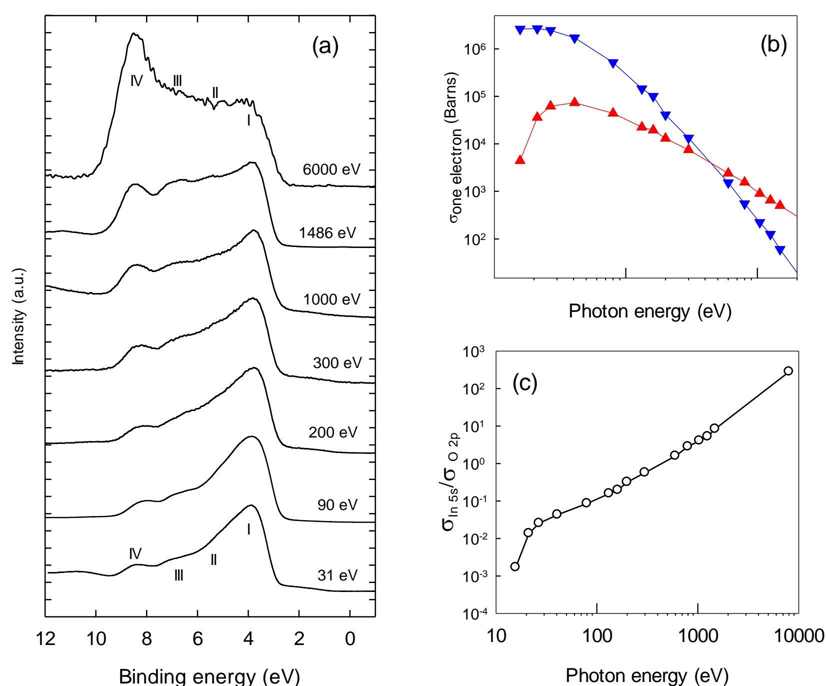

Figure 7.2. (a) Valence band photoemission spectra of $In_2O_3(111)$ excited at the photon energies indicated; (b) One electron ionisation cross sections for O 2*p* and In 5*s* states calculated by Yeh and Lindau as a function of photon energy; (c) One electron cross section ratio $\sigma_{In\ 5s} / \sigma_{O\ 2p}$ as a function of photon energy.

The main changes in the spectra found upon increasing the photon energy are that the intensity of the peak IV and to a lesser extent shoulders II and III increases relative to peak I. For example, at photon energy of 31 eV, peak I is the strongest feature in the valence band. In the reverse way, when the incident photon energy is increased to 6000 eV, the intensity of peak I relative to IV decreases dramatically and peak IV becomes the strongest valence band spectral feature. These striking relative intensity changes arise from photon energy dependent photoionization cross-sections for the orbitals involved in the valence band. The calculated one electron photoionization cross-sections for O 2*p* and In 5*s* states, taken from the tabulations of Yeh and Lindau[14] is shown in Figure 2b. This figure shows that both O 2*p* and In 5*s* one electron cross-sections have maxima below 100 eV and thereafter decrease monotonically with increasing photon energy.

However the decay of the O 2*p* cross-sections is much more pronounced than for the In 5*s* states so that the In 5*s* / O 2*p* cross-section ratio increases with increasing photon energies and above about 500 eV the In 5*s* cross section is bigger than that for O 2*p,* as shown in Figure 7.2c. Somewhat surprisingly the standard tabulation of cross sections due to Yeh and Lindau did not give values for one ionisation cross-sections of In 5*p* states, although from consideration of cross-sections for Sn 5*s* and 5*p* states and from values of cross-sections above 1000 eV tabulated by Scofield[15] we may infer that the In 5*p* cross section is about half that of In 5*s* states in the energy range between 100 eV and 1000 eV, thus explaining the variations in the intensities of shoulders II and III.

7.3.2 Evidence for a Surface Electron Accumulation Layer

Turning now to the empty states of In_2O_3, it may be seen from the calculated density states in Figure 7.1 that the lowest conduction band is primarily of In *5s* derived character with a significant amount of mixing of O *2p* character. Figure 7.3 show detailed valence and conduction spectra excited with photon energies of 1486.6 eV and 6000 eV. Note the conduction band emission near the Fermi energy is magnified. In spectrum excited at 1486.6 eV (7.3a), a well defined conduction band feature (peak V) is observed at the Fermi energy. From the integrated intensity of the conduction band feature relative to that of the valence band and from measurements of plasmon energies on In 3*d* core lines (the calculation will be detailed in section 7.4.3), we can estimate that the carrier concentration probed in the Al Kα XPS experiment is of the order of 2.6×10^{20} cm^{-3}.[16,17] Previously this feature has been assigned to the occupation of In *5s* conduction band resulting from the adventitious donor defects.[18] However the bulk carrier concentration based on Hall effect measurements and confirmed by infrared reflectivity is 1.0×10^{18}

cm^{-3}, two orders lower than the concentration estimated from Al Kα XPS and much lower than the critical Mott criterion concentration (7×10^{18} cm^{-3}) for degenerate doping. Therefore, this suggests there is accumulation of electrons at the near surface region, as reported on the In_2O_3(100) surface by King *et al.*[3, 4]

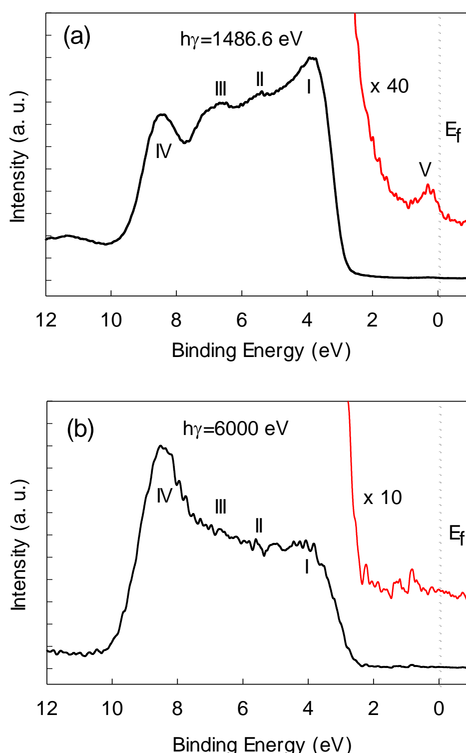

Figure 7.3. Detailed valence band photoemission spectra of the In_2O_3(111) film excited at Al Kα hν =1486.6 eV (a) measured at 45° off-take angle and hard x-ray hν =6000 eV (b) measured at 90° off-take angle. The conduction band emission near Fermi energy is magnified as indicated.

This surface electron accumulation was further confirmed by spectra excited at 6000 eV (Figure 3b), where a much weaker conduction band is observed.[2-4] Assuming a "universal curve" mean free path (λ) of about 2 nm for photoelectrons with a kinetic energy close to 1500 eV it can be shown that 97% of the photoelectron signal derives from the space charge region to be discussed below at 45° offtake angle.[19, 20] Thus Al Kα photoemission is dominated by the space charge region. By contrast in hard X-ray photoemission using 6000 eV photons λ has been estimated to be about 6 nm. Now the

space charge region contributes significantly less (57%) to the total photoelectron signal at normal emission, with significant signal coming from the low carrier density "bulk" of the sample.

The origin of the electron accumulation is linked to the fact that the charge neutrality level (CNL) lies well above the conduction band minimum of this material.[3,4] The CNL is the mid gap energy averaged across all k space. A CNL above the conduction band minimum arises when (as for In_2O_3) the dispersion in the conduction band is significantly bigger than the bandgap and dispersion in the upper valence band is weak. The surface Fermi level pins close to the CNL, leading to a positive surface charge associated with unoccupied donor surface states, and hence an electron accumulation layer near surface region to maintain the charge neutrality. This situation is found for a few other materials, notably InAs[21], InN[22,23] and CdO[24].

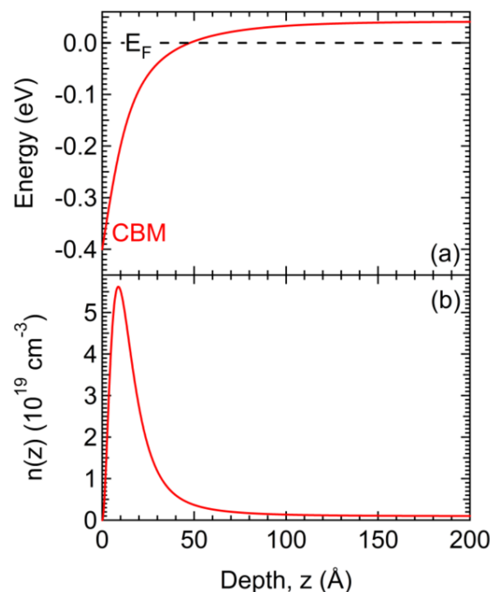

Figure 7.4. Poisson-MTFA calculations of (a) bending of the conduction band minimum with respect to the Fermi level and (b) electron density variation, n(z), as a function of depth, z, below the surface in the $In_2O_3(111)$ electron accumulation layer. The calculations show that the electron accumulation layer extends over a length range of about 5 nm below the surface.

The band bending and carrier-concentration profiles as a function of depth below the surface have been calculated by solving Poisson's equation within a modified Thomas-Fermi approximation (MTFA) incorporating a nonparabolic conduction-band dispersion by Dr. Philip King of the University of Warwick.[4, 25, 26] The results of these calculations are shown in Figure 7.4a (band bending) and b (electron density). Downward band bending of around 0.44 eV is compatible with the position of the valence band edge and arises from a surface state density of 1.3×10^{13} cm^{-2}. The calculations show that there is a pronounced electron accumulation in the near the surface region leading to a maximum carrier density of 5.5×10^{19} cm^{-3}. The accumulation layer takes place over a length range of about 5 nm. The discrepancy between the calculated maximum carrier concentration in the space charge layer and that inferred from XPS will be discussed later.

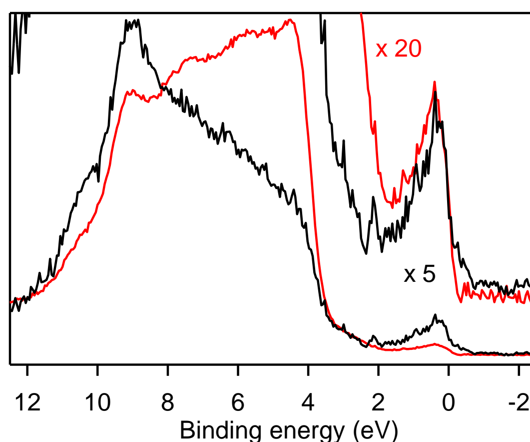

Figure 7.5. Al Kα at hν = 1486.6 eV (red) and hard X ray XPS at hν = 6000 eV (black) valence band spectra of highly degenerate ITO thin film on Si substrate. The carrier concentration is $n = 1.2\times10^{21}$ cm^{-3}. At these very high doping levels any band bending at the surface must take place over a very small length ranges (c.a. 0.5 nm) compared with effective XPS sampling depths so the bands may be regarded as flat. The data show that when the spectra are normalised to the same maximum intensity in the O 2*p* valence band, the conduction band structure in Al Kα XPS must be multiplied by a factor of 4 more than HXPS data to bring the intensities to the same level.

Note that in comparing the conduction band intensities in Figure 7.3, the expansion to the Al Kα data is a factor of 4 higher than to the HXPS data. This is to make allowance for

the fact that the cross-section for ionisation of In 5*s* states, which provide the major contribution to the conduction band, increases dramatically relative to the cross-section for O *2p* states at the higher photon energy.[27] This is supported the measurements for highly doped samples where there is heavily occupied conduction band states and near flat band behaviour. As shown in Figure 7.5, conduction band structure is indeed around a factor of 4 stronger relative to the maximum intensity in the O 2*p* valence band in HXPS at hν = 6000 eV than in Al Kα XPS.

Figure 7.6 show the valence band spectra of the (100) and (110) oriented In_2O_3 thin films excited at $h\nu$ =1486.6. It can be seen that both spectra exhibit a well defined intensity associated with occupied conduction band states, even though the bulk Fermi level is below the conduction band minimum for both samples. This indicates that there is a pronounced electron accumulation layer at the surface of both these samples. Thus it appears that electron accumulation is an intrinsic property of surfaces of undoped In_2O_3 with a low bulk carrier density, regardless of the surface orientation.

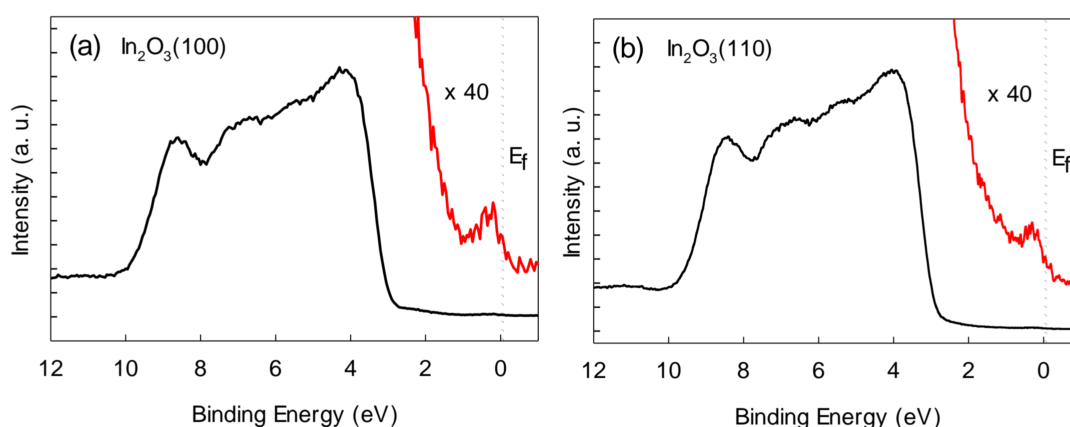

Figure 7.6. Valence (black) and conduction (red) band X-ray photoemission spectra of In_2O_3(100) and (110) films excited at Al Kα hν =1486.6 eV.

7.3.3 *Quantized Electron Sub-states*

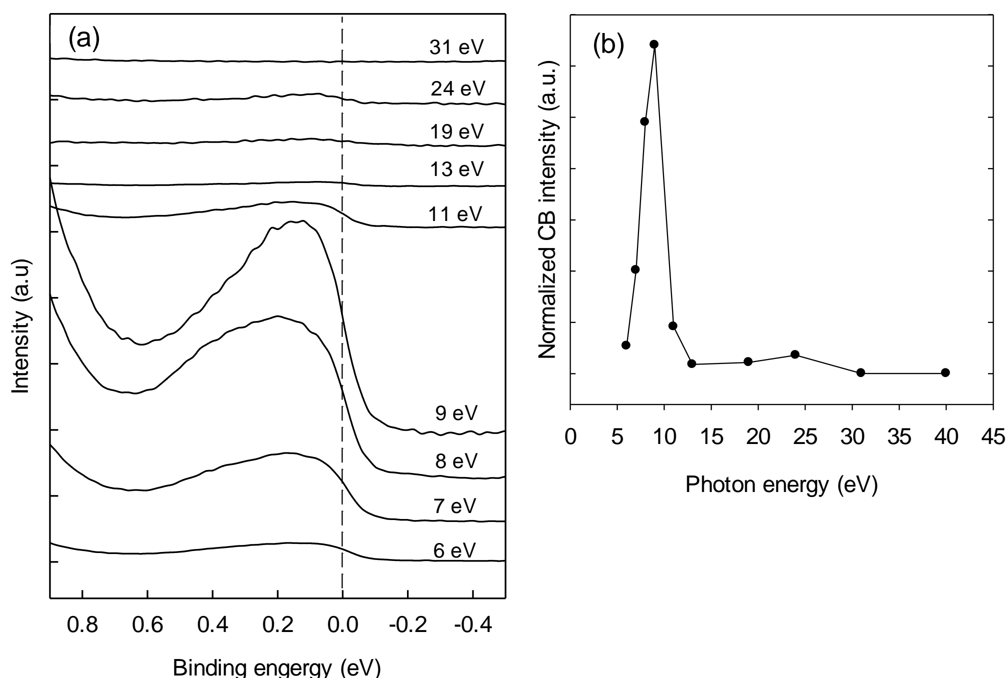

Figure 7.8. (a) Detailed expansion of the conduction band region in photoemission spectra of In_2O_3(111) photoemission spectra excited at the photon energies indicated; (b) The intensity of the conduction band with excitation photon energies.

Figure 7.8 shows expansions of the conduction band region in photoemission spectra of In_2O_3(111) excited with photon energies between 6 eV and 35 eV, as measured at the beamline BaDElPh of the Elettra Synchrotron Light Source, Italy. The intensity of the spectra was normalized relative to the photon beam current measured from a Si diode. It is clearly seen that the intensity of the conduction band strongly depends on the photon energy, as shown in Figure 7.8b. The conduction band shows a very strong maximum at 9 eV photon energy, with a very low intensity around 15 eV. This is presumably due to the occurrence of several Cooper minima in the cross section profile for ionisation of In 5*s* states.

Figure 7.9a presents an angle resolved photoemission spectroscopy (ARPES) photocurrent intensity mapping of states within 0.6 eV of the Fermi level, excited with photon energy of 9 eV at room temperature, where the momentum of the states parallel to the surface ($\boldsymbol{k}_{||}$) is measured as a function of binding energy. Analysis of these data was conducted by Dr. P.D.C. King (University of St. Andrews) based on his earlier work on CdO and InN.

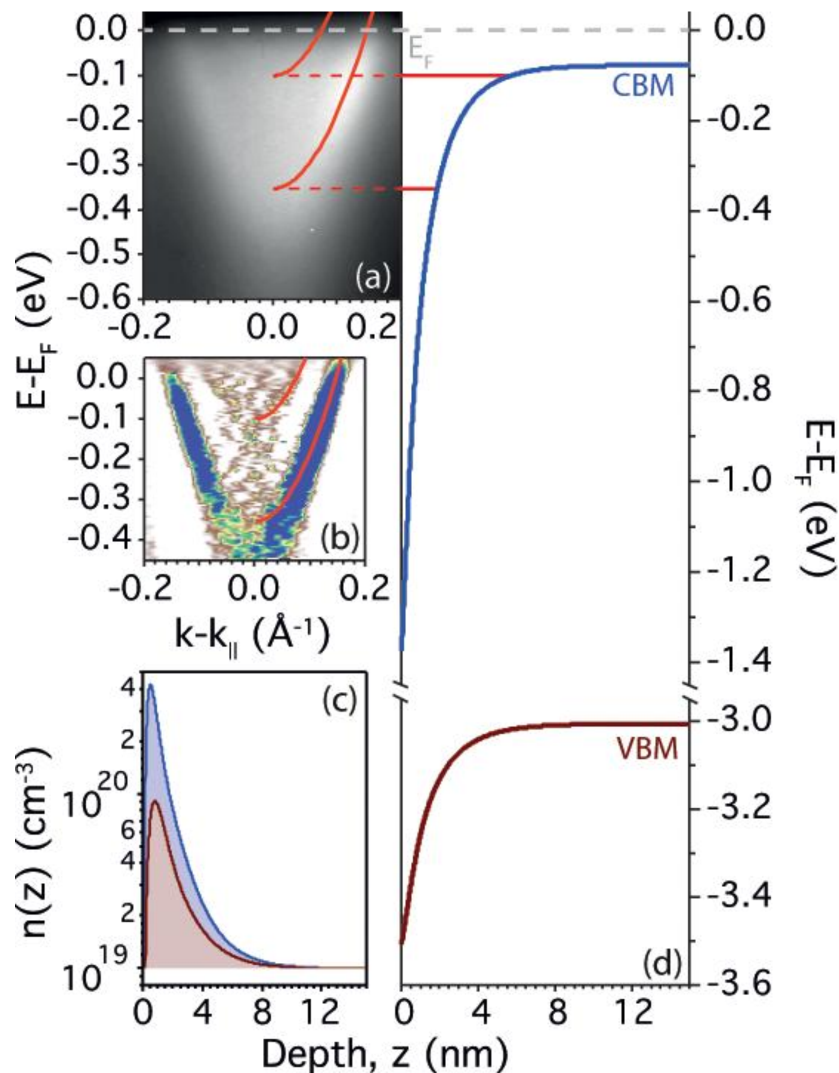

Figure 7.9. (a) Angle resolved PES photocurrent mapping of Fermi surface states of In_2O_3(111) with photon energy of 9 eV, showing two subbands nested below the Fermi level; The red curves indicate two subbands calculated by Poisson-Schrodingers; (b) an MDC second-derivative image of the raw data; (c) Near surface carrier density variation calculated by Poisson-MTFA (Surface density 5.9×10^{13} cm^{-2}); and (d) band bending near surface region.

Two dispersive subbands can be observed, as indicated on the map. It must however be admitted that the inner state is not very well defined and there is high background intensity in the map: nonetheless the overall quasi-quadratic dispersion of the outer state is quite obvious. The quantized states can be observed more clearly by taking the second-derivative of the raw intensity data, as shown in Figure 7.9b. The two subband minima are measured to be located at 0.11 eV and 0.35 eV below the Fermi surface at the Γ point. Both subband states are symmetric in energy (but not intensity) around the Γ point of the surface Brillouin zone and positively dispersed, reflecting the isotropic In *5s* characteristics of the conduction band in the plane parallel to the surface. The discrete subbands result from the quantum confinement effect of the two-dimension quasi-triangular potential created by downward band bending at the surface of In_2O_3(111), as discussed in the last section. Similar quantized electron subbands have been directly observed by ARPES in systems supporting pronounced surface electron accumulation layer, including InAs[21], InN[22] and CdO[24].

The sheet density associated with the electrons in the quantized subband states can also be directly estimated from the measured Fermi wave vectors k_F of the subbands through the relationship $n_{2D}=k_F^2/2\pi$. From the Figure 7.9a and 7.9b, the k_F values for the first and second band are estimated to be 0.10 Å^{-1} and 0.16 Å^{-1}, corresponding to electron densities of 1.6 $\times10^{13}$ cm^{-2} and 4.1 $\times10^{13}$ cm^{-2}, respectively. These give rise to a combined areal density of 5.7 $\times10^{13}$ cm^{-2}. It should be noted that this value is much higher than the value calculated by solving Poisson's equation with MTFA, assuming the same conduction and valence band bending of 0.44 eV as discussed in last section. In fact, the 0.44 eV downward band bending is not large enough to yield two subband states below Fermi level. By solving the Poisson-Schrodinger equations, it was found that a 1.2 eV downward band bending of the conduction band was required to achieve the two

quantized states below Fermi level as well as the much higher carrier concentration, as shown in Figure 7.9c and 7.9d. Given that the valence band bending remains close to 0.44 eV, these results therefore imply that there is a dramatic reduction in the separation between the top of the valence band and the bottom of the conduction band at the surface. King *et al.* have very recently suggested that this shrinkage in the surface band gap arises from the same mechanism that produces bandgap renormalisation in the bulk in heavily doped samples.[28] Here introduction of electrons into the conduction band screens the interaction between conduction and valence electrons through many body effects. However the reduction of the bandgap at the surface is much bigger than can be observed in the bulk at comparable doping levels.

The maximum carrier concentration in the space charge layer derived from these considerations is 4×10^{20} cm^{-3}, i.e. very much higher than discussed in the section 7.3.3. Thus recognition that valence and conduction bands may bend by different amounts helps resolve the XPS intensity dilemma discussed previously. The electron accumulation observed at the surface of the ion bombarded sample discussed in this section is however higher than that of the non-bombarded sample discussed previously. This can be understood in terms of selective sputtering of oxygen during ion bombardment to give surface oxygen vacancies that are not completely healed during subsequent annealing. The areal concentration of oxygen atoms in the outer O plane of $In_2O_3(111)$ is 1.17×10^{15} cm^{-2} . If surface oxygen vacancies act as two electron donors as has been recently suggested, the observed band bending implies that 2.4% of surface O sites are vacant.[29]

7.4 The Influence of Sn Doping on Electronic Structure

This section will deal with the effect of Sn doping on the electronic structure of In_2O_3 as probed by valence band and core level XPS. The essential effect of Sn is to degenerately dope free electrons into the conduction and ultimately move the Fermi level above the conduction band minimum. Photoemission spectra of undoped $In_2O_3(111)$ and of Sn-doped $In_2O_3(111)$ excited at hν = 600 eV in the region of the In 3*d*, Sn 3*d* and O 1*s* core lines are shown in Figure 7.10.

As expected the spectrum of the doped samples contains a weak but well defined Sn 3*d* spin-orbit doublet associated with the In dopant: after correction for ionisation cross-sections the ratio of concentrations Sn/(In+Sn) in the near surface region probed by XPS is estimated to be 2.2%. This corresponds to a carrier concentration of 6.8×10^{20} cm^{-3}, assuming that there is no compensation of Sn by interstitial oxygen.

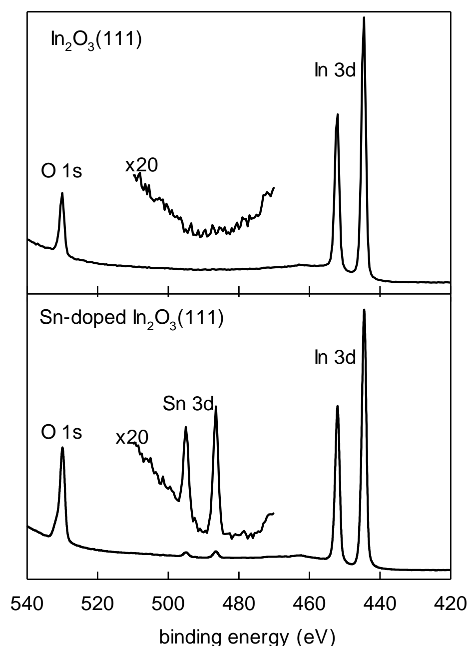

Figure 7.10. Photoemission spectra of undoped $In_2O_3(111)$ and Sn-doped $In_2O_3(111)$ excited at hγ = 600 eV encompassing In 3*d*, Sn 3*d* and O 1*s* core levels.

7.4.1 The Effect of Doping on Valence Band Structures

Figure 7.11 shows a comparison of the valence and conduction band spectra of undoped In_2O_3 and Sn-doped In_2O_3(111) excited at $h\nu$=1486.6 eV.

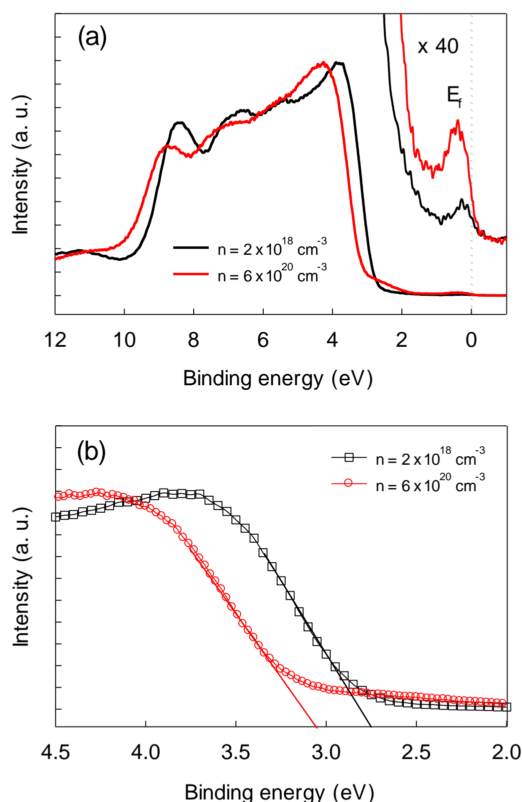

Figure 7.11. (a) Valence and conduction band XPS of undoped In_2O_3 (black) and Sn-doped In_2O_3 (red); the carrier concentrations are indicated. (b) A comparison of shift in valence band onsets.

The most striking effect of Sn doping is that the intensity of the conduction band feature at Fermi level is very strongly enhanced. At the same time the valence band onset shifts 0.25 eV to a higher energy of 3.15 eV ± 0.05 eV, as compared with 2.90 eV ± 0.05 eV for the undoped sample. These observations are consistent with upward movement of the Fermi level with increased filling of the conduction band as the carrier concentration increases. It is interesting to quantitatively analyze the factors that contribution to the

shift of valence band. Using a two band **k·p** model, the position of the Fermi level with a carrier concentration of 6.8 × 10^{20} cm^{-3} can be estimated to be 0.72 eV above the conduction band minimum.[17, 30] As discussed in detail above, the nominally undoped sample has a pronounced electron accumulation layer at the surface, giving rise to downward band bending by about 0.4 eV. A. Walsh *et al.*[31] also showed that bandgap renormalisation or shrinkage with doping, which arises mainly from stabilisation of the lower conduction band states due to the enhanced attractive potential of Sn as compared with In, lowers the bandgap of ITO doped at the present level down the band of ITO by about 0.15 eV. The expected shift of (0.72 - 0.40 - 0.15) = 0.17 eV based on these values matches the valence band shift from the XPS measurement fairly well.

7.4.2 In 3d Core Level

The In $3d_{5/2}$ core lines of undoped In_2O_3 and Sn-doped In_2O_3(111) excited at $h\nu$ =1486.6 eV are shown in Figure 7.12. It should first be noted that the In $3d_{5/2}$ core level of Sn-doped In_2O_3 shifts to higher binding energy due to the shift of Fermi level, as discussed in last section. The core line of the Sn-doped sample also shows a distinctly asymmetric profile, suggesting development of a distinct low binding energy shoulder. In each case the spectra may be fitted with two Voigt components. The low binding energy component is the narrower of the two and is of dominant Gaussian character. The broader high binding energy component is dominantly Lorentzian, hinting at a broadening mechanism associated with life-time effects. Similar core level spectra have been found for related degenerately doped oxide systems including polycrystalline Sn-doped In_2O_3[16, 32], Sb-doped SnO_2[33], PbO_{2-x}[34, 35], and Tl_2O_{3-x}[36].

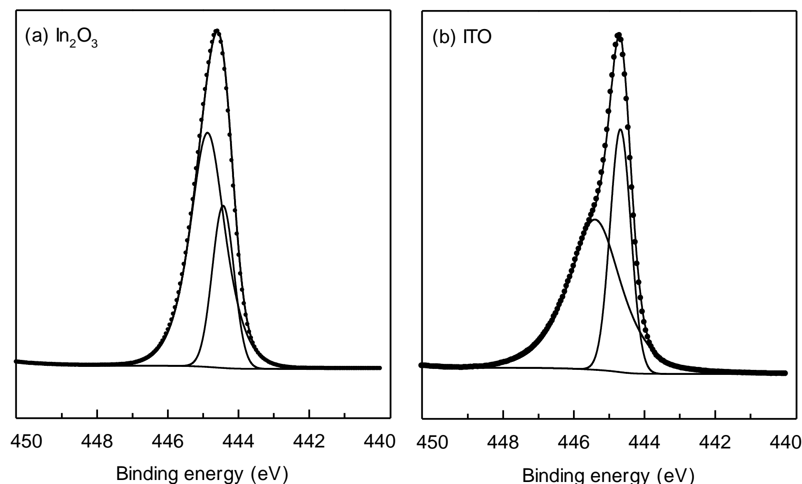

Figure 7.12. Curve fits to the In $3d_{5/2}$ core line for (a) undoped In_2O_3 and (b) Sn-doped In_2O_3.

Two alternative approaches have been used to describe these complex lineshapes. In a model developed by Kotani[37] and Wertheim[38], a screening mechanism was proposed in which the Coulomb potential of the core hole at an ionized atom creates a localized trap state below the conduction band. This is in general possible if the occupied conduction bandwidth is less than the Coulomb interaction between the core hole and the orbital contributing to the conduction band. In this situation, two different final states are then possible depending on whether the localized state is filled by an electron from the conduction band to give a screened final state or remains empty to give an unscreened final state. The core level structure thus comprises a low binding energy component associated with the screened final state and a lifetime broadened high binding energy component with a predominantly Lorentzian lineshape associated with the unscreened final state. Within this model the probability of final state screening is expected to increase as the carrier concentration increases. Indeed it is found that the relative intensity of the low binding energy screened final state peak of the 2.2% Sn-doped In_2O_3 (carrier concentration: 6.8×10^{20} cm^{-3}) is higher than that of In_2O_3.

Sample		BE (eV)	FWHM (eV)	Area (%)	ħω$_p$ (eV)	n (×10^{20}cm^{-3})
In_2O_3	Screened	444.42	0.72	0.27	0.44	2.6
	Unscreened	444.86	1.15	0.73		
2.2% Sn-In_2O_3	Screened	444.68	0.69	0.37	0.72	6.9
	Unscreened	445.40	1.72	0.63		

Table I. Data derived by fitting In $3d_{5/2}$ core line photoemission spectra to two pseudo-Voigt functions: binding energy (BE) (eV), full width at half maximum height (FWHM) (eV), relative areas (%) of the components, plasmon energies ($\hbar\omega_p$) and subsequently derived carrier concentrations (cm^{-3}).

A radically different model for the core line satellites is excitation of the conduction electron plasmon. The high binding energy unscreened final state gives a peak with a broader Lorentzian peak profile whose width reflects the plasmon lifetime, which in turn depends on the conduction electron relaxation rate. It was discovered early in the application of photoemission techniques to simple metallic solids that plasmon satellites make a significant contribution to core level structure in X-ray photoelectron spectra of free electron like metals. The parameters derived from curve fits to the In $3d_{5/2}$ core lines are shown in Table I.

The energy shift between the two components of the In $3d_{5/2}$ peak for undoped In_2O_3 and Sn-doped In_2O_3 is 0.44 eV and 0.72 eV. We can use this energy to estimate the carrier concentration in the near surface region probed by XPS. The plasma energy $\hbar\omega_p$ is determined by carrier concentration n through the relationship:

$$\omega_p^2 = \frac{ne^2}{m^* \varepsilon(\infty)\varepsilon_0}$$

where n is the free carrier density, m* is the electron effective mass, $\varepsilon(\infty)$ is the high frequency dielectric constants and ε_0 is the permittivity of free space. The value for the effective mass is taken to be $0.35m_0$ (where m_0 is the electron rest mass) and a dielectric

constant $\varepsilon(\infty) = 4.0$ is assumed.[32] The carrier concentrations are then estimated to be 2.6 $\times 10^{20}$ cm^{-3} and 6.9 $\times 10^{20}$ cm^{-3} for undoped In_2O_3 and Sn-doped In_2O_3 respectively. The data for undoped In_2O_3 gives a carrier concentration which is clearly very much bigger than the measured bulk carrier concentration and provides again qualitative evidence for surface electron accumulation.

7.4.3 Resonance Effects in Photoemission from Sn-doped $In_2O_3(111)$

Photoemission spectra of the ITO(111) thin film measured at Maxlab are shown in Figure 7.13a, and expansions of the region close to the Fermi energy are shown in Figure 7.13b.

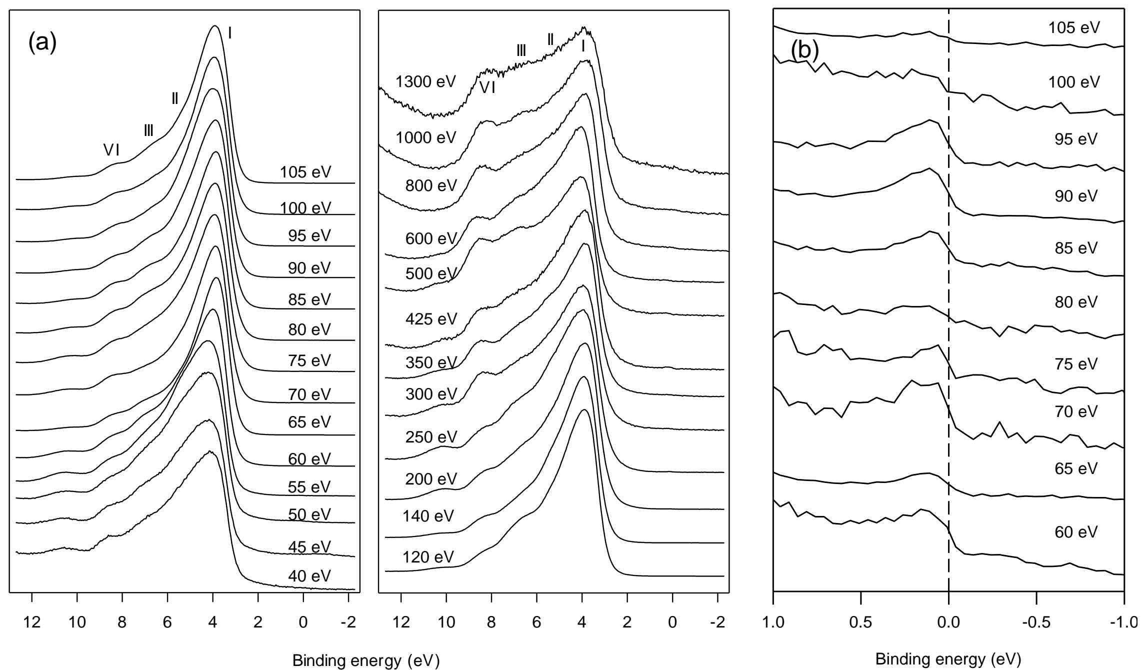

Figure 7.13. (a)Valence band photoemission spectra of Sn-doped $In_2O_3(111)$ excited at the photon energies indicated; (b) expansion of the conduction ban region in photoemission spectra of Sn-$In_2O_3(111)$ in the photon energy regime between 60 eV and 105 eV.

A weak feature straddling the Fermi energy is observed for photon energies between 60 eV and 110 eV: unfortunately at higher photon energies this very weak structure is obscured by photoemission arising from second order synchrotron radiation. This structure declines in intensity between 70 eV and 80 eV photon energies but then shows a pronounced intensity enhancement in the energy range between 85 eV and 95 eV before decreasing again.

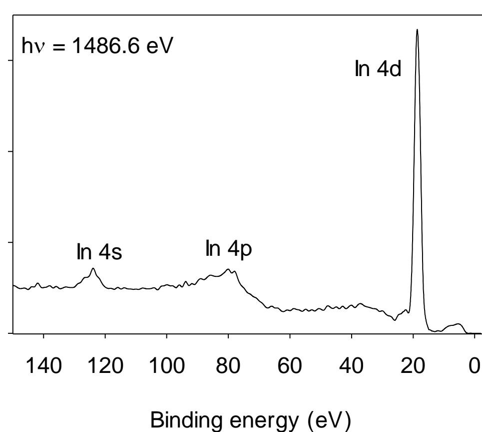

Figure 7.14. Photoemission spectra of Sn-In_2O_3(111) in region of In 4*d*, In 4*p* and In 4*s* core levels measured at hν = 1486.6 eV.

The conduction band states in Sn-doped In_2O_3 are of mixed Sn 5*s*/In 5*s* and O 2*p* character. The rapid variation in intensity is not predicted by the computed one electron ionisation cross sections but is instead attributed to a Fano anti-resonance / resonance line shape linked to the In 4*p* core threshold. The In 4*d*, In 4*p* and In 4*s* core level spectra of the sample excited at 1486.6 eV photon energy are shown in Figure 7.14. The In 4*p* core level appears as a very broad feature centred around 80 eV binding energy. The large width arises from many electron effects which allow 4*p* hole states to mix with excited 4*d* hole state – in the nearby element Te this leads to a complete breakdown in

the one electron picture for a core hole[39]. Using a notional configuration $5s^C$ to represent partial occupancy of the In $5s$ derived conduction band the Fano intensity profile is then attributed to interference between the direct photoemission channel:

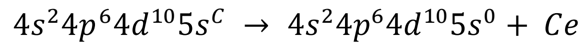

$$4s^2 4p^6 4d^{10} 5s^C \rightarrow 4s^2 4p^6 4d^{10} 5s^0 + Ce$$

and the channel where resonant photoexcitation is followed by Coster-Krönig decay:

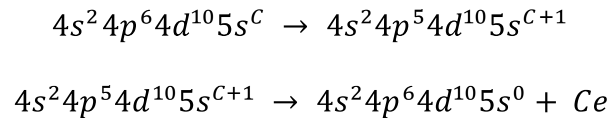

$$4s^2 4p^6 4d^{10} 5s^C \rightarrow 4s^2 4p^5 4d^{10} 5s^{C+1}$$

$$4s^2 4p^5 4d^{10} 5s^{C+1} \rightarrow 4s^2 4p^6 4d^{10} 5s^0 + Ce$$

Very similar resonance structure has been observed[13] in photoemission from bandgap states with significant Sn $5s$ in reduced SnO_2, although as expected the peaks and the dip are shifted to higher photon energy than observed here owing to the greater nuclear charge on Sn as compared with In.

7.5. Conclusions

In summary, it has been shown by photon energy dependent PES that In_2O_3 is a highly covalent material, with significant In 5*s* and In 5*p* character at the bottom and the middle of the valence band and conversely O 2*p* character at the bottom of conduction band. The fact that the charge neutrality level of In_2O_3 lies well above the conduction band minimum leads to a pronounced electron accumulation near to the surface of undoped In_2O_3 films with very low carrier concentrations. The pronounced electron accumulation associated with a downward band bending in the near surface region creates a confining potential well, which causes the electrons in the conduction band become quantized into two subband states, as directly observed by ARPES Fermi surface mapping. The accumulation of high density of electrons near to the surface region was found to shrink the surface band gap through many body interactions, and thus further increase the value of band bending and accumulation electron concentration. The incorporation of Sn introduces free electrons into the conduction and gradually moves the Fermi level above conduction band minimum. Core and valence level spectra shift to higher binding energies. The In 3*d* core line measured at both undoped and Sn-doped In_2O_3 display an asymmetric lineshape, and may be fitted with two components associated with screened and unscreened final states, associated with free electrons in the conduction band.

7.6 References:

1. K. H. L. Zhang, D. J. Payne and R. G. Egdell, Solid State Commun. ((In press)).
2. K. H. L. Zhang, D. J. Payne, R. G. Palgrave, V. K. Lazarov, W. Chen, A. T. S. Wee, C. F. McConville, P. D. C. King, T. D. Veal, G. Panaccione, P. Lacovig and R. G. Egdell, Chem. Mat. **21**, 4353 (2009).
3. P. D. C. King, T. D. Veal, D. J. Payne, A. Bourlange, R. G. Egdell and C. F. McConville, Phys. Rev. Lett. **101**, 116808 (2008).
4. P. D. C. King, T. D. Veal, F. Fuchs, C. Y. Wang, D. J. Payne, A. Bourlange, H. Zhang, G. R. Bell, V. Cimalla, O. Ambacher, R. G. Egdell, F. Bechstedt and C. F. McConville, Phys. Rev. B **79**, 205211 (2009).
5. G. Beamson, D. Briggs, S. F. Davies, I. W. Fletcher, D. T. Clark, J. Howard, U. Gelius, B. Wannberg and P. Balzer, Surface and Interface Analysis **15**, 541 (1990).
6. L. Petaccia, P. Vilmercati, S. Gorovikov, M. Barnaba, A. Bianco, D. Cocco, C. Masciovecchio and A. Goldoni, Nucl. Instrum. Methods Phys. Res. Sect. A-Accel. Spectrom. Dect. Assoc. Equip. **606**, 780 (2009).
7. R. Nyholm, J. N. Andersen, U. Johansson, B. N. Jensen and I. Lindau, Nucl. Instrum. Methods Phys. Res. Sect. A-Accel. Spectrom. Dect. Assoc. Equip. **467**, 520 (2001).
8. P. Torelli, M. Sacchi, G. Cautero, M. Cautero, B. Krastanov, P. Lacovig, P. Pittana, R. Sergo, R. Tommasini, A. Fondacaro, F. Offi, G. Paolicelli, G. Stefani, M. Grioni, R. Verbeni, G. Monaco and G. Panaccione, Rev. Sci. Instrum. **76**, 023909 (2005).
9. P. Erhart, A. Klein, R. G. Egdell and K. Albe, Phys. Rev. B **75** , 153205 (2007).
10. C. Korber, V. Krishnakumar, A. Klein, G. Panaccione, P. Torelli, A. Walsh, J. L. F. Da Silva, S. H. Wei, R. G. Egdell and D. J. Payne, Physical Review B **81**, 165207 (2010).
11. Y. Dou, R. G. Egdell, D. S. L. Law, N. M. Harrison and B. G. Searle, J. Phys.: Condens. Matter **10**, 8447 (1998).
12. J. M. Themlin, R. Sporken, J. Darville, R. Caudano, J. M. Gilles and R. L. Johnson, Physical Review B **42**, 11914 (1990).
13. M. Sinner-Hettenbach, M. Gothelid, T. Weiss, N. Barsan, U. Weimar, H. von Schenck, L. Giovanelli and G. Le Lay, Surface Science **499**, 85 (2002).
14. J. J. Yeh and I. Lindau, At. Data Nucl. Data Tables **32** (1), 1 (1985).
15. J. H. Scofield.
16. V. Christou, M. Etchells, O. Renault, P. J. Dobson, O. V. Salata, G. Beamson and R. G. Egdell, J. Appl. Phys. **88**, 5180 (2000).

17. A. Bourlange, D. J. Payne, R. G. Palgrave, H. Zhang, J. S. Foord, R. G. Egdell, R. M. J. Jacobs, T. D. Veal, P. D. C. King and C. F. McConville, J. Appl. Phys. **106**, 013703 (2009).
18. Y. Gassenbauer, R. Schafranek, A. Klein, S. Zafeiratos, M. Havecker, A. Knop-Gericke and R. Schlogl, Phys. Rev. B **73**, 245312 (2006).
19. A. Zangwill, P*hysics at Surfaces* (Cambridge University Press, England, 1988).
20. M. Sacchi, F. Offi, P. Torelli, A. Fondacaro, C. Spezzani, M. Cautero, G. Cautero, S. Huotari, M. Grioni, R. Delaunay, M. Fabrizioli, G. Vanko, G. Monaco, G. Paolicelli, G. Stefani and G. Panaccione, Phys. Rev. B **71**, 155117 (2005).
21. M. Noguchi, K. Hirakawa and T. Ikoma, Phys. Rev. Lett. **66**, 2243 (1991).
22. L. Colakerol, T. D. Veal, H. K. Jeong, L. Plucinski, A. DeMasi, T. Learmonth, P. A. Glans, S. C. Wang, Y. F. Zhang, L. F. J. Piper, P. H. Jefferson, A. Fedorov, T. C. Chen, T. D. Moustakas, C. F. McConville and K. E. Smith, Phys. Rev. Lett. **97**, 237601 (2006).
23. I. Mahboob, T. D. Veal, C. F. McConville, H. Lu and W. J. Schaff, Phys. Rev. Lett. **92**, 036804 (2004).
24. L. F. J. Piper, L. Colakerol, P. D. C. King, A. Schleife, J. Zuniga-Perez, P. A. Glans, T. Learmonth, A. Federov, T. D. Veal, F. Fuchs, V. Munoz-Sanjose, F. Bechstedt, C. F. McConville and K. E. Smith, Phys. Rev. B **78**, 165127 (2008).
25. G. Paasch and H. Ubensee, Phys. Status Solidi B-Basic Res. **113**, 165 (1982).
26. P. D. C. King, T. D. Veal and C. F. McConville, Phys. Rev. B **77**, 125305 (2008).
27. J. H. Scofield, Lawrence Livermore National Laboratory Report **UCRL-51326** (1973).
28. P. D. C. King, T. D. Veal, C. F. McConville, J. Zuniga-Perez, V. Munoz-Sanjose, M. Hopkinson, E. D. L. Rienks, M. F. Jensen and P. Hofmann, Physical Review Letters **104**, 256803 (2010).
29. A. Walsh, Appl. Phys. Lett. **98**, 261910 (2011).
30. E. O. Kane, J. Phys. Chem. Solids **1**, 249 (1957).
31. A. Walsh, J. L. F. Da Silva and S. H. Wei, Phys. Rev. B **78**, 075211 (2008).
32. C. Korber, V. Krishnakumar, A. Klein, G. Panaccione, P. Torelli, A. Walsh, J. L. F. Da Silva, S. H. Wei, R. G. Egdell and D. J. Payne, Phys. Rev. B **81**, 165207 (2010).
33. R. G. Egdell, J. Rebane, T. J. Walker and D. S. L. Law, Phys. Rev. B **59**, 1792 (1999).
34. D. J. Payne, G. Paolicelli, F. Offi, G. Panaccione, P. Lacovig, G. Beamson, A. Fondacaro, G. Monaco, G. Vanko and R. G. Egdell, J. Electron Spectrosc. Relat. Phenom. **169**, 26 (2009).
35. D. J. Payne, R. G. Egdell, D. S. L. Law, P. A. Glans, T. Learmonth, K. E. Smith, J. H. Guo, A. Walsh and G. W. Watson, J. Mater. Chem. **17**, 267 (2007).

36. P. A. Glans, T. Learmonth, K. E. Smith, J. Guo, A. Walsh, G. W. Watson, F. Terzi and R. G. Egdell, Phys. Rev. B **71**, 235109 (2005).

37. A. Kotani and Y. Toyozawa, J. Phys. Soc. Jpn. **37**, 912 (1974).

38. G. K. Wertheim, Chem. Phys. Lett. **65**, 377 (1979).

39. G. Wendin and M. Ohno, Physica Scripta **14**, 148 (1976).

Chapter 8

Domain Matching Epitaxial Growth of In_2O_3 Films on α-Al_2O_3(0001)

8.1 Introduction

In chapters 4 and 5 we showed that fluorite Y-stabilized ZrO_2 provides an ideal substrate for growth of high quality thin films of bixbyite In_2O_3 due to the small 1.6% mismatch with *bcc*-In_2O_3 and the similarity in the crystal structure. In particular, atomically flat In_2O_3(111) films could be grown on Y-stabilized ZrO_2(111) substrates due to the fact that (111) has the lowest surface energy amongst the low index surfaces.[1, 2] The high quality of the In_2O_3 surfaces allowed us to investigate various aspects of the surface physics of In_2O_3. In particular it was found that a pronounced electron accumulation layer is present in the near the surface region of undoped In_2O_3(111).[3]

As has been discussed extensively in this thesis, the phase of In_2O_3 thermodynamically stable under ambient conditions adopts the body-centred cubic (*bcc*) bixbyite structure, with space group $Ia\bar{3}$ and lattice parameter a = 10.1170 Å.[4] The structure may be regarded as a 2×2×2 superstructure of fluorite with ordered removal of O from ¼ of the anion sites. Under high pressure conditions a rhombohedral (*rh*) phase is stabilised.[5] The rhombohedral cell belongs to the $R\bar{3}c$ space group but can also be described in terms of a hexagonal cell with $a = b = 5.478$ Å and $c = 14.51$ Å. The structure is based on a hexagonally close packed array of O ions with occupation of 2/3 of the octahedral holes by In ions: this structure is also adopted by a number of other compounds with stoichiometry M_2O_3.

An alternative substrate to YSZ is α-Al_2O_3. This material is much cheaper than YSZ and is widely used for epitaxial growth of ZnO and GaN.[6-9] Like *rh*-In_2O_3, α-alumina or corundum belongs to the rhombohedral space group $R\bar{3}c$ and the structure is usually defined in terms of a hexagonal cell with $a = b =$ 4.759 Å and $c =$ 12.991 Å.[10, 11] Using the subscripts *s* and *e* to distinguish between the *e*pilayer and the *s*ubstrate it can be seen that there is a close match between $3a_s$ = 14.277 Å and $\sqrt{2}a_e$ = 14.308 Å for *bcc*-In_2O_3 since:

$$m = (\sqrt{2}a_e - 3a_s)/3a_s = 0.00217$$

i.e. the mismatch m defined in this way is only +0.217%. However ionic positions within the unit cells do not coincide optimally when bcc-$In_2O_3[1\bar{1}0]$ ‖ $Al_2O_3[11\bar{2}0]$. Indeed Mei et al. found that an In_2O_3 epilayer grown on $Al_2O_3(0001)$ by O-plasma MBE[12] at 680 °C was rotated by 30° so that bcc-$In_2O_3[1\bar{1}0]$ ‖ $Al_2O_3[10\bar{1}0]$ with a mismatch m defined by a 2/3 coincidence structure:

$$m = (\sqrt{2}a_e - 2\sqrt{3}a_s)/2\sqrt{3}a_s = -0.132$$

It can be seen that $|m|$ is now much bigger. However as will be discussed later, this orientation allows the hexagonal mesh of In ions to lie in reasonable registry with the O ions in the Al_2O_3 substrate. As with YSZ substrates, the epilayer is under tensile stress. A Hall mobility of 30 $cm^2V^{-1}s^{-1}$ for these films was somewhat disappointing.

Elsewhere Yang *et al.* have reported an in-plane epitaxial relationship bcc-$In_2O_3[\bar{1}\bar{1}0]$ ‖ $Al_2O_3[11\bar{2}0]$ for (111) oriented films grown by metallo-organic chemical vapour deposition (MOCVD) using $In(CH_3)_3$ and O_2 precursors at substrate temperatures between 550 °C and 750 °C.[13] This is a puzzling result because the $[\bar{1}\bar{1}0]$ direction is not

orthogonal to $[111]$. The result is also at variance with the work of Ambacher and co-worker, who have made extensive studies of the growth of In_2O_3 on Al_2O_3(0001) by MOCVD using $In(CH_3)_3$ and H_2O as precursors [14-19]. At high flow rates of the $In(CH_3)_3$ precursor and at low substrate temperatures the *bcc* polymorph of In_2O_3 grows with (001) orientation, giving the out of plane epitaxial relationships bcc - $\mathrm{In_2O_3}[001] \parallel \mathrm{Al_2O_3}[0001]$ [14-18]. This is a surprising result as the (001) surface of In_2O_3 is a polar Tasker type III surface[20] with a higher surface energy than the quadrupolar (111) surface.[1, 2] In-plane, the films were found to be built up from square or rectangular domains rotated by 30° relative to each other[14] with $bcc - \mathrm{In_2O_3}[100] \parallel \mathrm{Al_2O_3}[11\bar{2}0]$ etc. However at higher temperatures and lower flow rates a biphasic mixture of *bcc*- and rh-In_2O_3 was obtained: phase pure rh-In_2O_3(0001) could be grown at 600 °C with $In(CH_3)_3$ flow rates of around 4 µmole / minute [14, 16, 19]. Simple epitaxy with rh-$\mathrm{In_2O_3}[0001] \parallel \mathrm{Al_2O_3}[0001]$ and rh-$\mathrm{In_2O_3}[10\bar{1}0] \parallel \mathrm{Al_2O_3}[10\bar{1}0]$ was observed. This gives a mismatch:

$$m = (a_e - a_s)/a_s = +0.151$$

The rh-In_2O_3 epilayer is under pronounced compressive stress which may help account for stabilisation of a phase which can be obtained in the bulk only at very high pressures.[5]

In this chapter, we present an investigation into the epitaxial growth of *bcc*- and *rh*-In_2O_3 on α-Al_2O_3(0001) by oxygen plasma assisted molecular beam epitaxy. We show that despite the large mismatches between the epilayer and the substrate for both phases, it is possible to maintain epitaxial growth in both cases by matching different integral multiples of lattice planes of the In_2O_3 and the substrate.

8.2. Experimental details

In_2O_3 films were grown on 1 cm × 1 cm α-$Al_2O_3(0001)$ substrates in an ultrahigh vacuum oxide MBE system (SVT, USA) system with a base pressure of 5×10^{-9} mbar. This incorporated a hot lip indium effusion cell and a radio frequency (RF) oxygen plasma atom source operated at 200 W RF power with an oxygen background pressure of 3×10^{-5} mbar. Substrates were held by gravity in a recessed Mo mounting plate and heated radiatively using a graphite filament. The growth temperature was measured by a chromel-alumel thermocouple mounted immediately behind the substrate. The $Al_2O_3(0001)$ substrates were cleaned by exposure to the oxygen atom beam with a measured substrate temperature of 900°C. Films were then grown over a range of substrate temperatures (T_s) between 300 °C and 750 °C in growth runs whose duration extended over a time of 3×10^3 s (50 minutes). The nominal growth rate was 0.035 nm s^{-1} calibrated using the thickness from HRTEM measurements and AFM images.

High resolution x-ray diffraction (XRD) θ-2θ measurements were performed on a Philips Xpert diffractometer using monochromatic CuKα radiation (λ=1.54060 Å). Specimens for cross-sectional transmission electron microscopy (TEM) were prepared by cutting and mechanical grinding down to 5-10 μm, followed by thinning to electron transparency by Ar ion beam milling using a Gatan 691 Precision Ion Polishing System (PIPS). Cross-sectional TEM images were collected using a JEOL3000F microscope operating at 300 keV. The effect of epitaxial strain at the interface was analyzed using geometric phase analysis (GPA) of HRTEM images.[21] GPA strain measures were obtained after using a large area of the substrate as a reference. A Gaussian mask with standard deviation equal to 7.33 pixels was applied in Fourier space, corresponding to a spatial resolution of 0.43 nm. The axes were chosen along the principal directions of

elastic symmetry, taking the x-axis parallel to the interface and the z-axis normal to the interface.

The electrical properties of the In_2O_3 films with different thickness were characterised by Hall effect measurements using the van der Pauw method at room temperature. Optical absorption spectroscopy measurements were performed at room temperature on an ultraviolet-visible Varian Cary 5000 spectrometer.

8.3 Results and discussion

8.3.1 Overview of the Growth Morphology

The crystal structures of the In_2O_3 films grown at different temperatures were initially examined by simple θ-2θ diffraction measurements. Typical XRD profiles are shown in Figure 8.1.

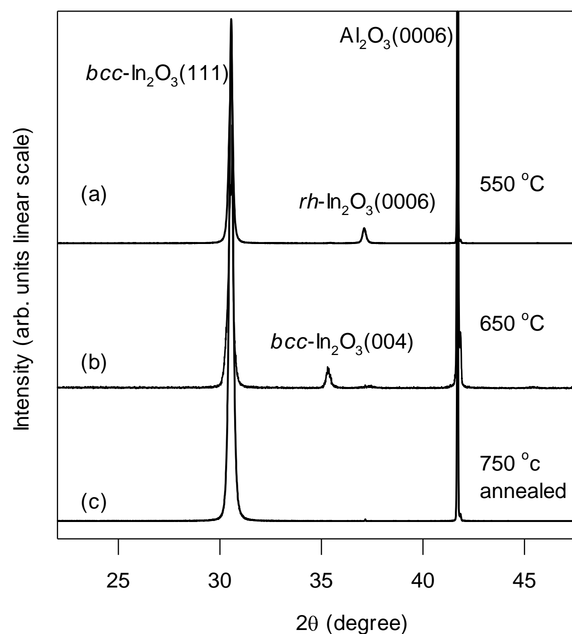

Figure 8. 1. Wide scan θ-2θ x-ray diffraction profile of In_2O_3 epilayer grown on α-Al_2O_3(0001) substrates at growth temperatures of (a) 450 °C, (b) 650 °C (c) grown at 550 °C followed by annealing at 750 °C for 30 minutes.

It is clear that the thermodynamically stable *bcc*-In_2O_3 phase predominates in all films with the *bcc*-In_2O_3(111) plane parallel to the basal (0001) planes of the Al_2O_3 substrate. For films grown at T_s < 550 °C, a minority *rh*-In_2O_3 phase is also present with a signature provided by the (0006) peak located at 2θ = 37.11°. The *rh*-In_2O_3 phase was unstable against thermal treatment. As shown in Figure 8.1c, thermal annealing a film grown at T_s=550 °C by heating at 750 °C for 30 minutes promotes the complete transformation of the minority *rh*-In_2O_3 phase into *bcc*-In_2O_3 to give single phase *bcc*-In_2O_3(111) thin films. Films grown at a substrate temperature higher than 650 °C only exhibit the stable *bcc*-In_2O_3 phase, with predominant *bcc*-(111) orientation but a small fraction of (001) oriented material.

AFM was used to examine the film morphology. Figure 8.2a shows large area AFM image (2000 nm × 2000 nm) of a film grown at 550°C. The films are rough and granular with interconnected trigonal or hexgonal islands, reflecting the rotational symmetry of the substrate. The influence of the 3-fold symmetry is less obvious after post annealing a film grown at 550 °C at 750 °C (Figure 8.2b).

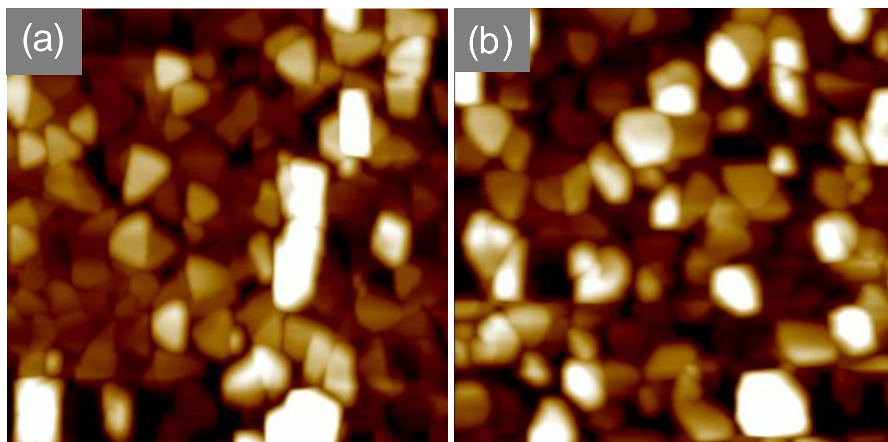

Figure 8. 2. (a) 2000 nm × 2000 nm AFM image of In_2O_3 sample grown at 550 °C (b) similar image after annealing at 750 °C for 30 minutes.

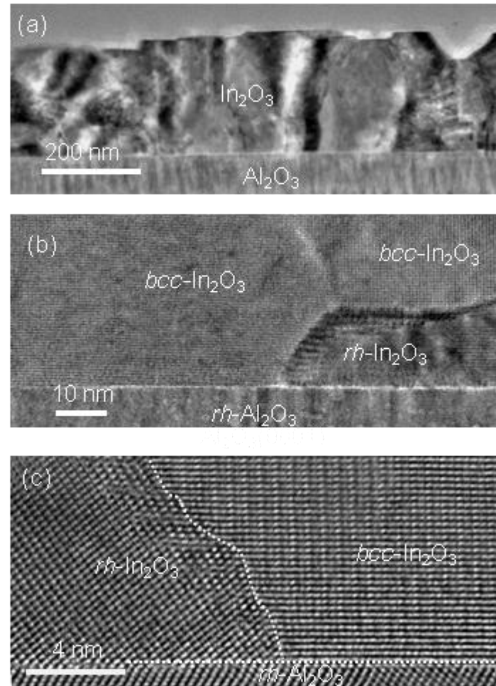

Figure 8.3. (a) Large area TEM image of In_2O_3 layer on Al_2O_3(0001) grown at 550 °C (b) expanded image showing *rh* inclusion close to the interface surrounded by *bcc*-In_2O_3 (c) further expanded high resolution image showing contrasting structures of *rh* and *bcc* phases of In_2O_3.

Cross-sectional high resolution TEM was also used to examine the film morphology as well as the interfacial structure and epitaxial relationship between the In_2O_3 and Al_2O_3(0001). Figure 8.3a shows a low magnification image of a biphasic film grown at 550 °C viewed down the $[1\bar{2}10]$ direction of the substrate. The film has a rough and irregular surface and several obvious boundaries between different domains. Higher resolution images such as that shown in 8.3b in combination with selected area electron diffraction allowed us to establish that within the epilayer it was possible to distinguish between domains of the *bcc* and *rh* polymorphs of In_2O_3: the latter often appeared as inclusions within the *bcc* phase and usually confined to the interface. The meandering boundary between *bcc*-In_2O_3 and *rh*-In_2O_3 is identified in the higher resolution image of 8.3c which more clearly distinguishes between the two phases. For the *bcc* phase the epitaxial relationships are confirmed to be *bcc*-In_2O_3 $[111]$ ||Al_2O_3 $[0001]$ and *bcc*-$In_2O_3$$[1\bar{1}0]$||$Al_2O_3$$[10\bar{1}0]$ i.e. the $[1\bar{1}0]$ direction of the unit cell for the In_2O_3 epilayer is

rotated by 30° from the $[11\bar{2}0]$ direction for the substrate; whilst for the *rh* phase as expected we have rh-$In_2O_3[0001] \parallel Al_2O_3[0001]$ and rh-$In_2O_3[10\bar{1}0] \parallel Al_2O_3[10\bar{1}0]$ i.e. the structure is unrotated.

8.3.2 Characterisation of bcc-In_2O_3

The hexagonal crystal structure of α-Al_2O_3 is based on a hexagonally close packed array of oxide ions with the close packed planes alternating in an ABABAB---- sequence. Between each pair of AB layers, 2/3 of the available octahedral holes are occupied by Al leaving 1/3 of the holes vacant. The Al ions do not occupy the centres of the holes but are displaced alternately up and down toward A and B layers respectively. The positions of the empty sites rotate between the 3 available positions within successive layers, which coupled with the up/down displacements leads to a c-axis repeat containing 6 close packed O layers, that is 3 AB bilayers. By contast in the bixbyite structure of In_2O_3 the In ions form an approximately cubic close packed array with ¾ occupancy of the available tetrahedral holes by O.

An idealised view of the interfacial epitaxial relationship between Al_2O_3(0001) and *bcc*-In_2O_3(111) is shown in Figure 8.4. This schematic ignores the -13.2% mismatch discussed above and involves a 2/3 coincidence structure between the rotated surface unit cell for In_2O_3(111) and the substrate. The coordinate system for Al_2O_3 in this figure corresponds to that used by Lee and Lagerlof.[10] The separation between In atoms in the close packed (111) planes of In_2O_3 is $d_{In-In} = \sqrt{2}a_e/4$ = 3.577 Å, whilst the separation between O atoms is the close packed planes of Al_2O_3(0001) is $d_{O-O} = a_s/\sqrt{3} = 2.748$ Å. The mismatch between these distances is given by:

$$m = (d_{In-In} - d_{O-O})/d_{O-O} = 0.302$$

Whereas for a 2/3 coincidence structure we have a smaller mismatch defined by:

$$m = (2d_{In-In} - 3d_{O-O})/3d_{O-O} = -0.132$$

Within the idealised coincidence structure depicted in Figure 8.4, ¼ of the In ions sit on top of O atoms in the basal close packed plane of alumina(0001), whilst the other In ions occupy two-fold bridging sites. Alternatively, and more likely, by shifting the whole epilayer cell upward along the $[1\bar{2}10]$ direction of the substrate, half of the In atoms are brought into 3-fold hollow sites, although it is then impossible to avoid some of the In ions sitting above a subsurface Al atom. Note that the structure shown in Figure 8.4 differs from that proposed by Mei *et al.*[12] whose structure suggested that $d_{In-In} \approx d_{O-O}$.

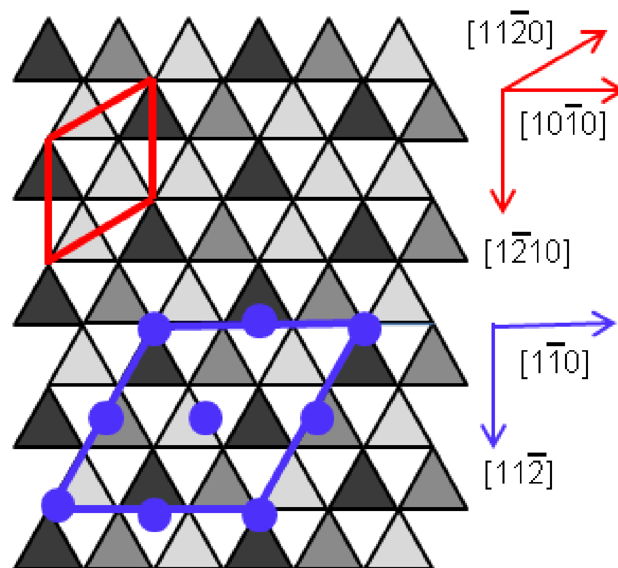

Figure 8.4. Schematic representation of epitaxial relationship between Al_2O_3(0001) and In_2O_3(111). The points of intersection of the mesh of triangles represent oxygen positions in the basal plane of Al_2O_3. The shaded triangles indicate that an octahedral hole lies under the triangle and the three levels of shading distinguish between octahedral holes that are (i) occupied by an upwardly displaced Al ion (ii) occupied by a downwardly displaced Al ion and (iii) empty. The hexagonal surface unit cell of alumina is shown in the top left hand corner with the directions in a hexagonal coordinate system to the right (both red). The In positions in ¼ of an idealised $\sqrt{2}a_e \times\sqrt{2}a_e$ cell of In_2O_3(111) commensurate with the substrate are shown as closed circles (blue online) in the lower part of the figure with the $\sqrt{2}/2a_e \times\sqrt{2}/2a_e$ cell highlighted (blue). The directions for this cell in a cubic coordinate system are shown to the right (blue).

Figure 8.5a shows a higher resolution image of a *bcc*-In_2O_3 film viewed down the $[11\bar{2}]$ direction of the In_2O_3 epilayer, corresponding to the $[11\bar{2}0]$ direction of the substrate. The atomic structure and interplanar separations in the epilayer are consistent with the bixbyite structure of In_2O_3 with spacings of 0.72 nm and 0.29 nm that are close to $a_e/\sqrt{2}$ and $a_e/2\sqrt{3}$ respectively. Further expanded images of the epilayer and substrate are shown in 8.5b and 8.5c. This pair of images confirms the near 2/3 coincidence in atomic spacings parallel to the substrate surface along the $[10\bar{1}0]$ direction of the substrate and also confirms that the coincidence structure leaves residual tensile strain in the epilayer.

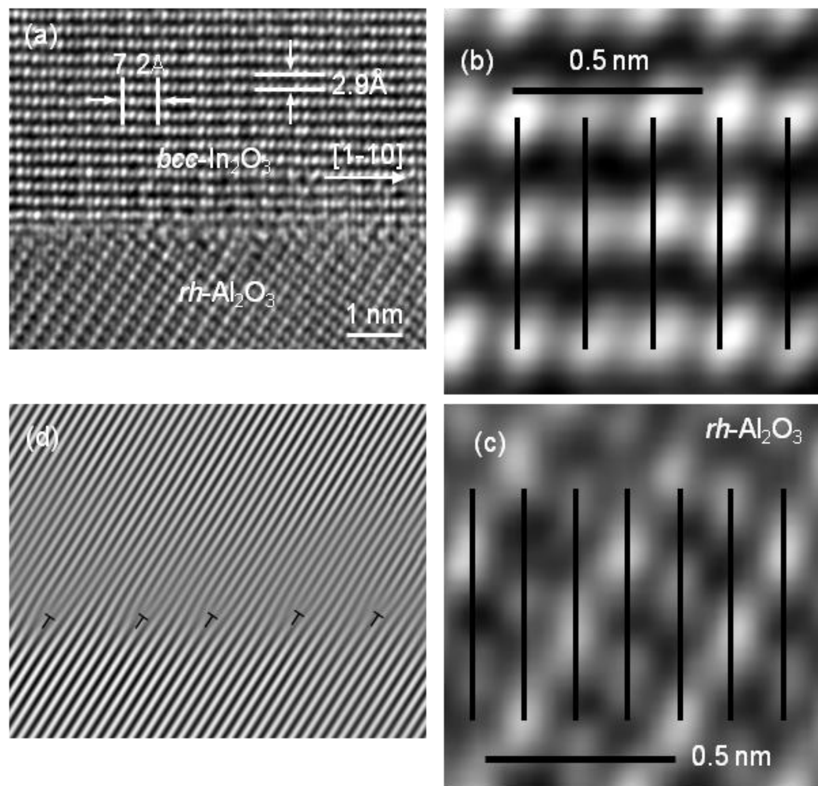

Figure 8.5. (a) High resolution TEM image of the interface region of *bcc*-In_2O_3 on Al_2O_3(0001) viewed down the $[1\bar{2}10]$ direction of Al_2O_3. (b) Expanded view of part of the image of the epilayer. (c) Expanded view of part of the image of the substrtate, which in comparison with (b) highlights the near 2/3 coincidence in atomic separations. (d) Fourier filtered image of the interface showing periodic misfit dislocations.

As mentioned above there is a mismatch of -13.2% between $\sqrt{2}a_e$ and $2\sqrt{3}a_s$. With misfits of less than 7%-8% thin films, can grow pseudomorphically with simple lattice matching epitaxy up to a critical thickness, beyond which it becomes energetically favourable to generate dislocations which release the strain induced by the substrate.[22-24] The smaller the lattice mismatch, the thicker the layer within which coherent strained epitaxy can be maintained. However for very large mismatches, as in the current study, domain matching epitaxy is favoured. Here different integral multiples of lattice planes containing densely packed rows are matched across the interface with introduction of periodic misfit dislocations. Figure 8.5d shows a Fourier-transform filtered image of the interface derived from in-plane In_2O_3 and Al_2O_3 reflections, so that only the lattice planes perpendicular to the interface are imaged. Quasi-periodic dislocations can be seen at the interface, with every 7 or 8 planes of $In_2O_3(1\bar{1}0)$ matching with 6 or 7 planes of $Al_2O_3(10\bar{1}0)$. Taking the $8 \times d\{In_2O_3(1\bar{1}0)\} + 7 \times d\{Al_2O_3(10\bar{1}0)\}$ domain matching structure we have a residual mismatch defined by:

$$m = (8\sqrt{2}a_e - 7 \times 2\sqrt{3}a_s)/7 \times 2\sqrt{3}a_s = -0.0081$$

whilst for $7 \times d\{In_2O_3(1\bar{1}0)\} + 6 \times d\{Al_2O_3(10\bar{1}0)\}$ we have:

$$m = (7\sqrt{2}a_e - 6 \times 2\sqrt{3}a_s)/6 \times 2\sqrt{3}a_s = +0.0215$$

In principle, the 8/7 domain matching structure effectively accommodates the -13.2% mismatch by the introduction of periodic dislocations localized at the interface leaving a

residual -0.8% tensile strain in the In_2O_3 films. Introduction of some regions with a 7/6 matching can lead to complete release of the mismatch.

Accommodation of mismatch by periodic dislocations in domain matching epitaxy contrasts with layer matching epitaxy where pseudomorphic growth is followed by strain relaxation process giving rise to formation of a high density of threading dislocations. These dislocations can act as scattering centre for free electrons, degrading the transport properties of the thin films. In contrast, despite of the large mismatch between $In_2O_3(111)$ and $Al_2O_3(0001)$, mismatch accommodation by domain matching epitaxy can result in periodic dislocations localized at interface as soon as the material nucleates on the substrate, leaving the film on top of the interface nearly free of threading dislocation. Therefore domain matching epitaxy in systems with a large mismatch may open up new routes to fabrication of high-quality crystalline thin films.[23]

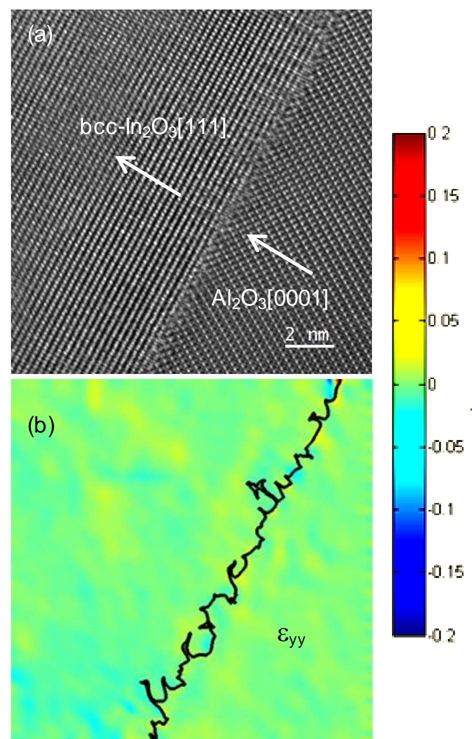

Figure 8.6. (a) Large area atomically resolved HRTEM image of interface between $Al_2O_3(0001)$ and *bcc*-$In_2O_3(111)$ (b) interface strain map showing ε_{yy} component (normal to surface) as derived from geometric phase analysis.

To explore this idea, the distribution of strain at the interface between Al_2O_3(0001) and In_2O_3(111) was further characterised by geometric phase analysis of HRTEM images. Figure 8.6a shows a large area real space HRTEM image, while 6b shows a strain map for ε_{yy} i.e. for atomic separations normal to the interface. Here reference vectors are taken independently and separately for the substrate and the epilayer well away from the interface. With such a vector basis all displacements in the epilayer and in the substrate toward the interface are found and then the strain is calculated. The displacements of atomic planes from the positions away from the interface are represented in terms of a chromatic scale where colours at the red end of the spectrum indicate an expansion of interplanar separations and colours at the blue end of the spectrum indicate a corresponding compression. An intermediate pale green colour is associated with unchanged substrate separations. The black line links points where the strain between substrate and epilayer is equal. The rugged shape of the line is due to the presence of the strain around the network of misfit dislocations. It is clear from the map that strain is localised close to the interface.

8.3.3 Characterisation of rh-In_2O_3

Finally we turn to the minority *rh*-In_2O_3 phase found in some of the films. Figure 8.7a shows a HRTEM image of the interface between *rh*-In_2O_3 and Al_2O_3(0001). As expected, simple epitaxial relationships *rh*-In_2O_3 $[0001]$ $||Al_2O_3$ $[0001]$ and *rh*-$In_2O_3[10\bar{1}0]||Al_2O_3[10\bar{1}0]$ are found. As mentioned previously in this system the in-plane mismatch is +15.1%, i.e. the epilayer is under compressive stress. In a fashion similar to that found for the *bcc* phase, this large mismatch can be accommodated by domain matching epitaxy involving $6 \times a_e[10\bar{1}0] + 7 \times a_s[10\bar{1}0]$ which leads to:

$$m = (6a_e - 7a_s)/7a_s = -0.013$$

i.e. the residual tensile strain is only 1.3%. Fourier filtered images using either $[22\bar{4}4]$ or $[33\bar{6}0]$ diffraction features to reconstruct the real space image are shown in figure 7b and 7c. These images confirms that again there are a series of periodic misfit dislocations analogous to those shown in figure 5d. However in this case dislocations and strain propagate further into the epilayer away from the interface.

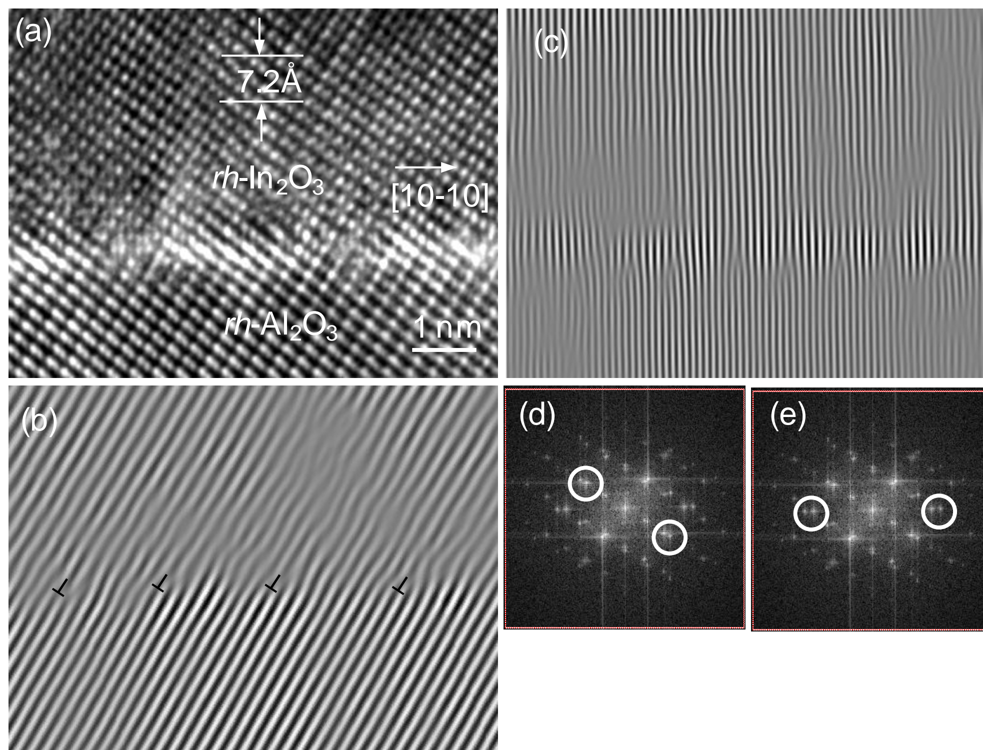

Figure 8.7. (a) High resolution TEM image of the interface region of *rh*-In_2O_3 on Al_2O_3(0001) viewed down to $[1\bar{2}10]$ direction of Al_2O_3, showing the *rh*-on-*rh* epitaxial relationship (b) Fourier filtered image using the $[22\bar{4}4]$ diffraction features from the substrate and epilayer respectively to reconstruct the real-space image of the interface. Periodic misfit dislocations loaclised at the interface are highlighted. (c) Fourier filtered image using the $[33\bar{6}0]$ diffraction features from the substrate and epilayer respectively to reconstruct the real-space image of the interface. (d) and (e) show diffraction patterns taken across the interface with the regions used to reconstruct the images in (b) and (c) highlighted.

The large area HRTEM image and strain map corresponding to figure 8.6 are shown in figure 8.8. Again it can be seen that strain in the epilayer is mainly confined to the interface region, although a crescent of alternating compressive and tensile strain is apparent in the lower part of the epilayer.

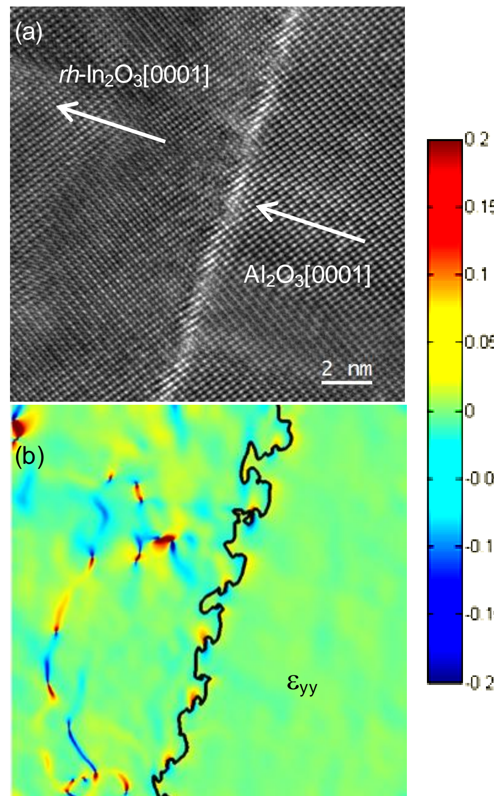

Figure 8.8. (a) Large area atomically resolved HRTEM image of interface between Al_2O_3(0001) and *rh*-In_2O_3(111) (b) interface strain map showing ε_{yy} component (normal to surface) as derived from geometric phase analysis.

The stabilization of metastable phases by growth of thin films on substrates with a matched crystal structure and lattice parameter is a well-known phenomenon, providing a valuable tool for synthesis of new thin film oxide materials not easily accessible by other techniques. Epitaxial stabilization is based on the favourable free-energy associated with structural coherence at the film/substrate interface.[25] In present case the metastable *rh*-In_2O_3 is stabilized due to the identical space groups of the epilayer and substrate.

Moreover the substrate places the epilayer under compressive stress, thus promoting formation of the high pressure *rh* phase.

8.3.4 Optical Absorption Spectra

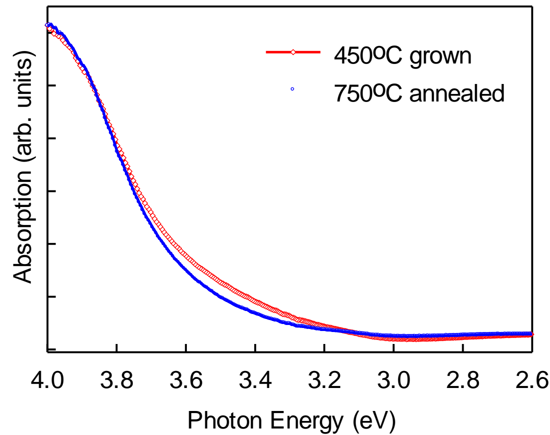

Figure 8.9. Optical absorption coefficient against photon energy for In_2O_3 film grown at 450 °C (red) and film grown at 550 °C followed by annealing at 750 °C for 30 minutes (blue).

Figure 8.9 shows optical absorption spectra of for In_2O_3 films deposited at 450 °C and at 550 °C, followed by annealing at 750 °C. For the pure *bcc*-In_2O_3 film obtained after annealing at 750 °C significant the main absorption onset can be observed at around 3.6 eV, with a weaker low energy absorption tail extending down to below 3.0 eV. These spectra are consistent with previous optical measurements for *bcc*-In_2O_3.[26] It is now known that bcc-In_2O_3 has a direct but dipole forbidden bandgap of around 2.9 eV,[27-30] with the onset of dipole allowed transitions at about 0.8 eV higher energy. Thus the weak onset corresponds to the dipole forbidden gap and the strong onset to allowed transitions. For the sample grown at 450°C, the relatively stronger low energy absorption around 3.2-3.6 eV results from the small fraction of *rh*-In_2O_3 phase stabilized at the interface region. As has been discussed in detail elsewhere,[28] the lower symmetry of the *rh* phase does not result in dipole forbidden transitions at the band edge so that there is stronger absorption

around 3 eV even though the bandgap of the *rh* phase is estimated to be about 0.1 eV bigger than for the bcc phase.[14]

8.4 Conclusions

In summary, we have shown both *bcc*- and *rh*-In_2O_3 can be grown epitaxially $Al_2O_3(0001)$ despite very different lattice parameters by matching different integral multiples of lattice planes of In_2O_3 with those of Al_2O_3. Residual strain is released by periodic misfit dislocations localized at in the interface. The growth of thermodynamically stable *bcc*-$In_2O_3(111)$ phase involves a 2/3 coincidence structure where the unit cell in the epilayer is rotated by 30° from the unit cell of the Al_2O_3. This allows In ions to come into coincidence with high symmetry sites of the close packed basal O layer of $Al_2O_3(0001)$, giving rise to an epitaxial relationships of $In_2O_3(111)||Al_2O_3(0001)$ and $In_2O_3[1\bar{1}0]||Al_2O_3[10\bar{1}0]$. Further work is however needed to establish whether In ions have a preference for 3-fold hollow sites or bridging and on-top sites. The similarity in the bonding symmetry between *rh*-In_2O_3 and *rh*-Al_2O_3 allows the stabilization of a metastable *rh*-$In_2O_3(0001)$ phase with a simple *rh*-on-*rh* configuration during low temperature growth. The epitaxial stabilisation of the high pressure *rh* phase observed may also be promoted by the fact that *rh*-$Al_2O_3(0001)$ places *rh*-$In_2O_3(0001)$ under compressive stress. Domain matching epitaxy during growth of oxide layers on highly mismatched substrates offers exciting possibilities for fabrication of high quality thin films.

8.6 References:

1. K. H. L. Zhang, A. Walsh, C. R. A. Catlow, V. K. Lazarov and R. G. Egdell, Nano Lett. **10**, 3740 (2010).
2. A. Walsh and C. R. A. Catlow, J. Mater. Chem. **20**, 10438 (2010).
3. K. H. L. Zhang, D. J. Payne, R. G. Palgrave, V. K. Lazarov, W. Chen, A. T. S. Wee, C. F. McConville, P. D. C. King, T. D. Veal, G. Panaccione, P. Lacovig and R. G. Egdell, Chem. Mat. **21**, 4353 (2009).
4. M. Marezio, Acta Crystallographica **20**, 723 (1966).
5. R. D. Shannon, Solid State Commun. **4**, 629 (1966).
6. Y. F. Chen, D. M. Bagnall, H. J. Koh, K. T. Park, K. Hiraga, Z. Q. Zhu and T. Yao, J. Appl. Phys. **84**, 3912 (1998).
7. Y. F. Chen, H. J. Ko, S. K. Hong and T. Yao, Appl. Phys. Lett. **76**, 559 (2000).
8. S. Strite and H. Morkoc, J. Vac. Sci. Technol. B **10**, 1237 (1992).
9. Q. Zhu, A. Botchkarev, W. Kim, O. Aktas, A. Salvador, B. Sverdlov, H. Morkoc, S. C. Y. Tsen and D. J. Smith, Appl. Phys. Lett. **68**, 1141 (1996).
10. W. E. Lee and K. P. D. Lagerlof, Journal of Electron Microscopy Technique **2**, 247 (1985).
11. F. Fuchs and F. Bechstedt, Phys. Rev. B **77**, 155330 (2008).
12. Z. X. Mei, Y. Wang, X. L. Du, Z. Q. Zeng, M. J. Ying, H. Zheng, J. F. Jia, Q. K. Xue and Z. Zhang, J. Cryst. Growth **289**, 686 (2006).
13. C. Y. Wang, V. Cimalla, H. Romanus, T. Kups, G. Ecke, T. Stauden, M. Ali, V. Lebedev, J. Pezoldt and O. Ambacher, Appl. Phys. Lett. **89**, 011904 (2006).
14. C. Y. Wang, V. Cimalla, H. Romanus, T. Kups, G. Ecke, T. Stauden, M. Ali, V. Lebedev, J. Pezoldt and O. Ambacher, Applied Physics Letters **89**, 011904 (2006).
15. J. G. Lozano, F. M. Morales, R. Garcia, D. Gonzalez, V. Lebedev, C. Y. Wang, V. Cimalla and O. Ambacher, Applied Physics Letters **90**, 3 (2007).
16. C. Y. Wang, V. Cimalla, H. Romanus, T. Kups, M. Niebelschutz and O. Ambacher, Thin Solid Films **515**, 6611(2007).
17. M. Ali, C. Y. Wang, C. C. Roehlig, V. Cimalla, T. Stauden and O. Ambacher, Sens. Actuator B-Chem. **129**, 467 (2008).
18. C. Y. Wang, V. Cimalla, V. Lebedev, T. Kups, G. Ecke, S. Hauguth, O. Ambacher, J. G. Lozano, F. M. Morales and D. Gonzalez, in *Physica Status Solidi C - Current Topics in Solid State Physics, Vol 5, No 6*, edited by T. Palacios and D. Jena (Wiley-V C H Verlag Gmbh, Weinheim, 2008), Vol. 5, pp. 1627-1629.

19. C. Y. Wang, Y. Dai, J. Pezoldt, B. Lu, T. Kups, V. Cimalla and O. Ambacher, Crystal Growth & Design **8**, 1257 (2008).
20. P. W. Tasker, Journal of Physics C-Solid State Physics **12**, 4977 (1979).
21. P. L. Galindo, S. Kret, A. M. Sanchez, J. Y. Laval, A. Yanez, J. Pizarro, E. Guerrero, T. Ben and S. I. Molina, Ultramicroscopy **107**, 1186 (2007).
22. M. Grundmann, T. Bontgen and M. Lorenz, Phys. Rev. Lett. **105**, 146102 (2010).
23. J. Narayan and B. C. Larson, J. Appl. Phys. **93**, 278 (2003).
24. G. Saint-Girons, J. Cheng, P. Regreny, L. Largeau, G. Patriarche and G. Hollinger, Phys. Rev. B **80**, 155308 (2009).
25. O. Y. Gorbenko, S. V. Samoilenkov, I. E. Graboy and A. R. Kaul, Chem. Mat. **14**, 4026 (2002).
26. I. Hamberg, C. G. Granqvist, K. F. Berggren, B. E. Sernelius and L. Engstrom, Phys. Rev. B **30**, 3240 (1984).
27. A. Bourlange, D. J. Payne, R. G. Egdell, J. S. Foord, P. P. Edwards, M. O. Jones, A. Schertel, P. J. Dobson and J. L. Hutchison, Appl. Phys. Lett. **92**, 092117 (2008).
28. P. D. C. King, T. D. Veal, F. Fuchs, C. Y. Wang, D. J. Payne, A. Bourlange, H. Zhang, G. R. Bell, V. Cimalla, O. Ambacher, R. G. Egdell, F. Bechstedt and C. F. McConville, Phys. Rev. B **79**, 205211 (2009).
29. P. D. C. King, T. D. Veal, D. J. Payne, A. Bourlange, R. G. Egdell and C. F. McConville, Phys. Rev. Lett. **101**, 116808 (2008).
30. A. Walsh, J. L. F. Da Silva, S. H. Wei, C. Korber, A. Klein, L. F. J. Piper, A. DeMasi, K. E. Smith, G. Panaccione, P. Torelli, D. J. Payne, A. Bourlange and R. G. Egdell, Phys. Rev. Lett. **100**, 167402 (2008).

Chapter 9:

Concluding Remarks and Outlook

9.1 Thesis Summary

This thesis has focussed on the epitaxial growth of high-quality thin films of pure or Sn-doped In_2O_3 by molecular beam epitaxy, and experimental investigation of their structures and morphologies, electronic properties and surface physics. The experimental work was supplemented *by ab inito* DFT calculations carried out by Dr. Aron Walsh. A brief summary of the work completed is presented below.

In Chapter 4 it was shown that highly ordered In_2O_3 nanoislands and nanorods could be grown epitaxially on (100) and (110) oriented Y-stabilized ZrO_2 substrates, as shown in Figure 9.1.[1] On (111) substrates continuous thin films are obtained. On the basis of *ab initio* density functional theory calculations, it was shown that the striking influence of substrate orientation on the distinctive growth morphology is linked to the fact that the energy for the (111) surface is much lower than for either polar (100) or non-polar (110) surfaces. This explains the growth of atomically flat In_2O_3 thin films on (111) substrate, as well as the self-assembly of nanoislands and nanorods on the other two surfaces, with development of low energy {111} side facets.[1, 2] These results provide a model system for the rational design of oxide nanostructures in systems where there is a large anisotropy in surface energies.

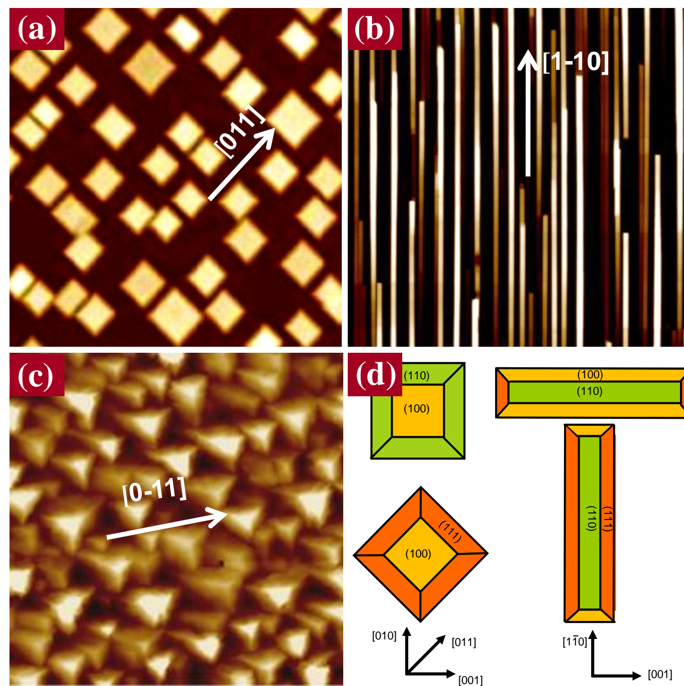

Figure 9.1. The lowest energy of $In_2O_3(111)$ surface is thermodynamically favorable termination, promoting self-assembly of: (a) nanoislands and (b) nanorods on the YSZ (100) and (110) substrates, (c) while atomically flat $In_2O_3(111)$ thin film on YSZ (111).

In Chapter 5, the growth of $In_2O_3(111)$ thin films was further investigated and the influence of growth temperature and film thickness was studied in detail.[3, 4] It was shown that very thin In_2O_3 epilayers (35 nm) are under high tensile strain caused by the 1.7% lattice mismatch with the substrate, while the tensile strain was gradually relaxed with increasing film thickness. High-quality films with a low carrier concentration (5.0×10^{17} cm^{-3}) and high mobility (73 $cm^2V^{-1}s^{-1}$) were obtained in the thickest films (420 nm) after strain relaxation. The optical bandgap of the thinnest In_2O_3 film was around 0.1 eV smaller than that of bulk, as shown in Figure 9.2. Using a combination of classical and quantum simulation techniques, the uniaxial compression of In_2O_3 in response to the epitaxial tensile strain was quantified, with the former giving rise to a band gap expansion and the latter to a band gap reduction: the net effect is that for thin highly-

mismatched films, the band gap is reduced through a lowering of the conduction band states arising from a reduction of bonding-antibonding interactions.[4, 5] These are general effects, which can be exploited in a wider range of metal-oxide systems, either through a judicious choice of growth substrate or through the use of material interfaces and superlattices that introduce coherent lattice strain.

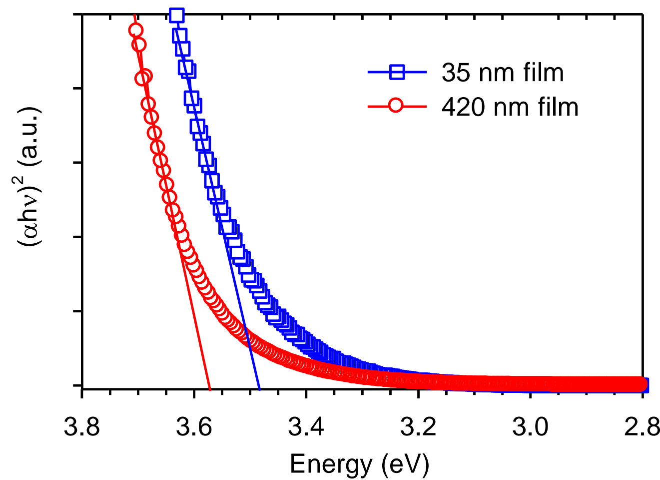

Figure 9.2. Plot of $(\alpha h\nu)^2$ against photon energy ($h\nu$) for In_2O_3 epitaxial films with thicknesses of 35 nm and 420 nm. The curves are extrapolated to $(\alpha h\nu)^2 = 0$, in order to determine the effective direct optical band gap.

The achievement of high-quality In_2O_3(111) thin film with atomically flat surfaces also enabled us to explore surface structural properties and surface electronic structure, as described in Chapter 6 and Chapter 7. In Chapter 6, the atomic structure of In_2O_3 (111) surface was determined using combination of scanning tunnelling microscopy, analysis of intensity/voltage curves in low energy electron diffraction and first-principles *ab initio* calculations. The (111) surface has a bulk terminated (1 × 1) structure, as expected from the low energy of the (111) surface. There are very small vertical relaxations in the outermost of the $\{[O^{2-}]_{12}^{24-}[In^{3+}]_{16}^{48+}[O^{2-}]_{12}^{24-}\}$ quadrupolar units that define the (111)

surface, which reduces the average separation between In and O. Good agreement was found between the experimental surface structure and that derived from *ab initio* density functional theory calculations. This result emphasises the benefit of a multi-technique approach to resolving surface structure. The same features are expected for other materials adopting the bixbyite crystal structure.

Chapter 7 probed the electronic properties of $In_2O_3(111)$ surface using synchrotron-based photoemission spectra excited with photon ranging from the UV (6 eV - 40 eV), through the soft X-ray regime (40 eV -1486.6 eV) to hard X-rays (6000 eV). It has been shown that In_2O_3 is a highly covalent material, with significant hybridization of In 5*s* and In 5*p* states with the O 2*p* states at the bottom of and in the middle of the valence band. Conversely O 2p states mix strongly with In 5s states in the lowest conduction band. By comparing valence band spectra excited by soft and hard X-rays as shown in Figure 9.3, it was inferred that there is a pronounced electron accumulation layer at the surface of In_2O_3 films with very low carrier concentrations. This is ultimately determined by the fact the charge neutrality level of In_2O_3 lies well above the conduction band minimum.[6] The electron accumulation layer results in downward band bending, giving rise to quantized electron subband states near the Fermi level. The incorporation of Sn introduces free electrons into the conduction band and the Fermi level moves up above the conduction band minimum.[7] Both core and valence levels shift to higher binding energies. The In 3*d* core line measured for both undoped and Sn-doped In_2O_3 display an asymmetric lineshape, and may be fitted with two components associated with screened and unscreened final states. The final state screening is in turn associated with free electrons in the conduction band.

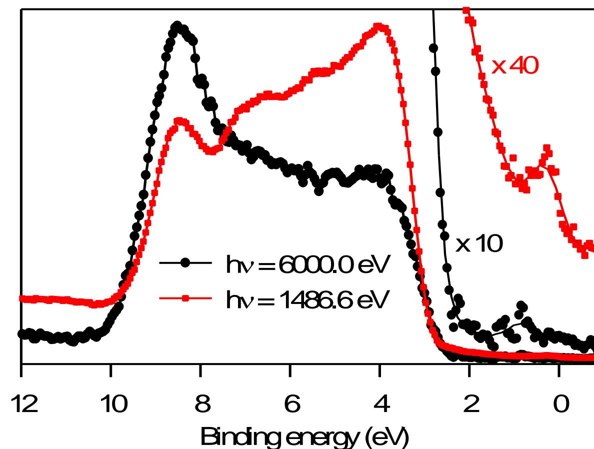

Figure 9.3. Valence band photoemission spectra measured hγ =1486.6 eV (red) and hard X- ray (ESRF) hγ =6000 eV (black). Comparison of conventional XPS and hard XPS provides evidence of a pronounced electron accumulation layer at surface regions.

Finally the epitaxial growth of In_2O_3 thin films on α-Al_2O_3(0001) substrates with very large lattice mismatch (15%) was considered. Both the stable body centred cubic phase and metastable corundum In_2O_3 phases can be stabilized in epitaxial thin films by the domain matching epitaxy mechanism by matching the integral multiples of lattice planes of the In_2O_3 and substrate.

9.2 Ongoing and Future Work and Outlook

The growth of high-quality In_2O_3 thin films and the investigation of their structures, morphologies and electronic properties are just the first steps toward understanding the fundamental science of ITO surfaces. Many of the procedures developed here are obviously transferable to other TCOs. The relatively mature field of conventional semiconductor science provides a paradigm for further exploration of the growth, structural characteristics, electronic properties and surfaces/interfaces of these materials. Ongoing and future work is discussed briefly below.

9.2.1 High Resolution X-ray Diffraction of In_2O_3 Nanostructures and Thin Films

Epitaxial growth may be accompanied by generation of dislocations or points defects, strain relaxation, shape and phase transition and local misorientation of atomic planes. High resolution X-ray diffraction, especially reciprocal space mapping (RSM), provides information on lattice parameters (from which strain and composition are determined), misorientation and crystallographic tilting (from which defects types and dislocation densities may be deduced), crystallite size and microstrain, phase separation and superlattice thickness *etc*.[8] Thus it is a widely used technique in semiconductor materials for the analysis of the structural characteristics of epitaxial thin films and devices.[9]

We accordingly have begun to apply RSM in combination with atomic force microscopy (AFM) to investigate the crystallographic orientation, strain and growth modes of In_2O_3(100) nanoislands (introduced in Chapter 4), (110) nanorods (introduced in Chapter 4) and (111) thin films (introduced in Chapter 5) in greater detail. In-house work carried out in the Department of Physics by Dr. Anne Bourlange in collaboration with Professor Roger Cowley has shown that crystallographic tilting of the atomic planes of micron sized In_2O_3(100) islands helps to relieve tensile strain arising from a -1.7% lattice mismatch between the epilayer and the Y-ZrO_2 substrate.[10] The same tilt phenomena was also observed in the self-assembled (110) nanorods introduced in Chapter 4: this work was completed on a run on the XMaS beamline of the ESRF completed in April 2011, but further analysis is needed to complete this work and it is not included in this thesis. In addition it has been established that there was is clear In_2O_3(100) island shape and tilt transition as the function of island size. The synchrotron work that identifies the tilt transition was completed in May 2011 but again further analysis is needed to complete the work. As shown in Figure 9.4, very small islands (with dimensions of order 60 nm) have edges aligned along <010> directions. RSM

reveals these islands have no tilt. Larger islands with edge dimensions in excess of 300 nm have edges aligned along <110> directions and are also tilted in these directions, as discussed in reference 10. The shape and tilt transition is analogous to the well-known shape transition in self-organized semiconductor nanoislands found in systems such as Ge on Si(100) and InAs on GaAs.[11, 12] Ongoing work is analysing these data using a thermodynamic model borrowed from the literature concerned with self-organization of semiconductor systems. This assumes that the growth mode is determined by the size-dependent energy minimisation resulting from an interplay between elastic strain and surface/interface energies. It is worth noting that the anisotropy in surface energies for oxides may be up to around 100%, which is much larger than that for conventional semiconductor materials where the anisotropy is normally around 10%.

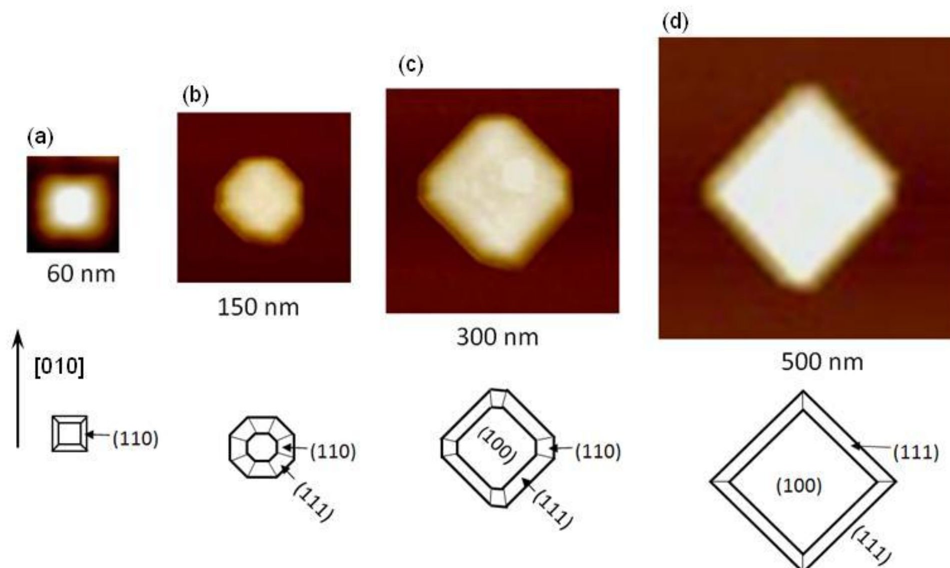

Figure 9.4. (a)-(d) morphologies of the (100) nanoislands as function of size: the edges of the nanoislands are aligned along [010] direction when the islands are small (e.g. 60 nm), and transit to be aligned along [011] direction for large size islands (e.g.300 nm); The shape-transition accompanies with the tilting of the islands.

The structural properties of the $In_2O_3(111)$ strained thin films introduced in Chapter 5 have also been examined by high resolution X-ray diffraction. The results allow direct measurements on the in-plane and out-of-plane lattice parameters of the strained thin films and hence the strain status and Poisson ratio of this material. The experiments confirm that the Poisson ratio is around 0.3, as assumed in chapter 5. Secondly, quantitative analysis on the RSMs can provide dislocation densities within the films, which can be directly correlated with the electrical properties of the films. This in turn shines light on attempts to improve the quality of $In_2O_3(111)$ films grown by MBE.

9.2.2 Surface Physics of Low Index ITO Surface

The understanding of the surface physics of In_2O_3 developed in Chapters 6 and 7 in conjunction with literature data[13, 14] also paves the way for further work. Only the atomic structure of the (111) surface has been determined in Chapter 6. The multi-technique approach employed here will be used in future work on the more interesting polar (100) and (110) surfaces, as well as on other metal oxide TCO surfaces. Photoemission spectroscopy as discussed in Chapter 7 provides the methodology to study and compare the electronic properties the other low index surfaces.

It is well known that surface point defects such as oxygen vacancies or adsorbed hydroxyl ions, as well as shear plane defects or other defect clusters have a strong influence on the chemistry of oxide surfaces. For example defects are critical in determining the reactivity of $TiO_2(110)$ for water splitting[15] and the surface conductivity of SnO_2 as sensor material[16]. The most likely surface defects in In_2O_3 are oxygen vacancies, which probably provide the microscopic basis for electron accumulation in the

near surface region. Thus there is scope for further work using surface science techniques to study local defects and reactivity of In_2O_3 surfaces.

9.2.3 Optimizing the energy level alignment at organic layer/ITO interface

As discussed in Chapter 1, ITO is the essential transparent anode for collection of hole in organic photovoltaic (OPV) devices. It is well-known that the alignment of energy levels at organic layer/ITO and donor/acceptor interfaces is a key factor influencing photo-induced charge separation, the charge injection barrier, open circuit voltage (V_{oc}) and ultimately the overall OPV device performance.[17] A detailed understanding of the interfacial properties can provide strategies to enhance OPV efficiency through interface engineering. The basic principle of interface engineering is to optimize the energy level alignment between organic active layers and transparent electrodes by surface functionalisation. Techniques that have been used include inserting very thin layers of transition metal oxides such as MoO_3 and NiO or self-assembled monolayers (SAM).[18]

The high-quality In_2O_3 and ITO single crystal thin films produced in this thesis provide ideal model surfaces for further study of molecular absorption and energy-level alignments at the interfaces between organic active layers and ITO. Donor type molecules like copper pthalocyanine (CuPc) can work as a probe to study the evolution of work function, band bending and energy-level alignment at the interface between organic layers and ITO by photoemission spectroscopy. With a full understanding of interfaces between CuPc and ITO, the surface of ITO can be modified by ultrathin (1-5 nm) metal oxides (such as MoO_3 and NiO) and self-assembled organic monolayer (SAM) to obtain optimized parameters for enhancing the efficiency of OPV devices.

9.3 Reference:

1. K. H. L. Zhang, A. Walsh, C. R. A. Catlow, V. K. Lazarov and R. G. Egdell, Nano Lett. **10**, 3740 (2010).
2. A. Walsh and C. R. A. Catlow, J. Mater. Chem. **20**, 10438 (2010).
3. K. H. L. Zhang, V. K. Lazarov, H. H. C. Lai and R. G. Egdell, J. Cryst. Growth **318**, 345 (2011).
4. K. H. L. Zhang, V. K. Lazarov, T. D. Veal, F. Oropeza, C. McConville, R. G. Egdell, A. Walsh and R. Catlow, Journal of Physics Condensed Matter **23**, 334211 (2011).
5. A. Walsh, C. R. A. Catlow, K. H. L. Zhang and R. G. Egdell, Phys. Rev. B **83**, 161202 (2011).
6. K. H. L. Zhang, D. J. Payne, R. G. Palgrave, V. K. Lazarov, W. Chen, A. T. S. Wee, C. F. McConville, P. D. C. King, T. D. Veal, G. Panaccione, P. Lacovig and R. G. Egdell, Chem. Mat. **21**, 4353 (2009).
7. K. H. L. Zhang, D. J. Payne and R. G. Egdell, Solid State Commun. (Accepted).
8. B. D. Cullity and S. R. STOCK, Elements of X-Ray Diffraction 3rd edn (Englewood Cliffs, NJ: Prentice-Hall, 2001).
9. M. A. Moram and M. E. Vickers, Rep. Prog. Phys. **72**, 036502 (2009).
10. R. A. Cowley, A. Bourlange, J. L. Hutchison, K. H. L. Zhang, A. M. Korsunsky and R. G. Egdell, Phys. Rev. B **82**, 165312 (2010).
11. G. Medeiros-Ribeiro, A. M. Bratkovski, T. I. Kamins, D. A. A. Ohlberg and R. S. Williams, Science **279**, 353 (1998).
12. J. Stangl, V. Holy and G. Bauer, Rev. Mod. Phys. **76**, 725 (2004).
13. E. H. Morales and U. Diebold, Appl. Phys. Lett. **95**, 253105 (2009).
14. E. H. Morales, Y. B. He, M. Vinnichenko, B. Delley and U. Diebold, New J. Phys. **10**, 125030 (2008).
15. O. Bikondoa, C. L. Pang, R. Ithnin, C. A. Muryn, H. Onishi and G. Thornton, Nat. Mater. **5**, 189 (2006).
16. M. Batzill and U. Diebold, Prog. Surf. Sci. **79**, 47 (2005).
17. S. Braun, W. R. Salaneck and M. Fahlman, Adv. Mater. **21**, 1450 (2009).
18. M. D. Irwin, B. Buchholz, A. W. Hains, R. P. H. Chang and T. J. Marks, Proc. Natl. Acad. Sci. U. S. A. **105**, 2783 (2008).